CHEMICAL REVIEWS

pubs.acs.org/CR

Review

From Solution to Thin Film: Molecular Assembly of π-Conjugated Systems and Impact on (Opto)electronic Properties

Published as part of the Chemical Reviews virtual special issue "Emerging Materials for Optoelectronics".

Azzaya Khasbaatar,[⊥] Zhuang Xu,[⊥] Jong-Hoon Lee,[⊥] Gonzalo Campillo-Alvarado, Changhyun Hwang, Brandon N. Onusaitis, and Ying Diao*

Cite This: *Chem. Rev.* 2023, 123, 8395–8487

Read Online

ABSTRACT: The assembly of conjugated organic molecules from solution to solid-state plays a critical role in determining the thin film morphology and optoelectronic properties of solution-processed organic electronics and photovoltaics. During evaporative solution processing, π-conjugated systems can assemble via various forms of intermolecular interactions, forming distinct aggregate structures that can drastically tune the charge transport landscape in the solid-state. In blend systems composed of donor polymer and acceptor molecules, assembly of neat materials couples with phase separation and crystallization processes, leading to complex phase transition pathways which govern the blend film morphology. In this review, we provide an in-depth review of molecular assembly processes in neat conjugated polymers and nonfullerene small molecule acceptors and discuss their impact on the thin film morphology and optoelectronic properties. We then shift our focus to blend systems relevant to organic solar cells and discuss the fundamentals of phase transition and highlight how the assembly of neat materials and processing conditions can affect blend morphology and device performance.

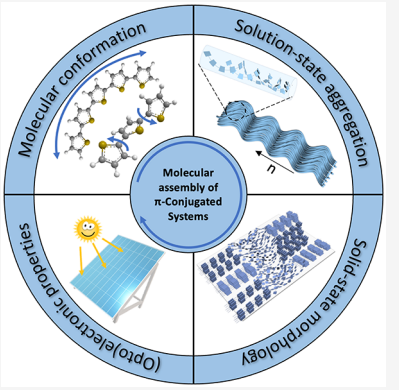

CONTENTS

Received: December 28, 2022
Published: June 5, 2023

https://doi.org/10.1021/acs.chemrev.2c00905
Chem. Rev. 2023, 123, 8395–8487

1. INTRODUCTION

The discovery of the semiconducting property of organic molecules dates back to the year 1950 when Akamatu and Inokuchi found the resistivity of violanthrone to decrease with increased temperature due to the semiconducting nature of the material.[1,2] Following this breakthrough, electroluminescent molecular crystals and conducting polymers were introduced in the 1960–1970s ushering a new era in the field of organic electronics.[3] In particular, the breakthrough in 1977 by Shirakawa, Heeger, and MacDiarmid, later awarded the Nobel Prize in 2000,[4] demonstrated that the conductivity of polyacetylene can be enhanced by ten million times when doped with iodine, nearly matching the conductivity of metals.[5,6] These scientific discoveries in the field have inspired many researchers to pursue fundamental and applied research and led to the development of the first organic solar cells (OSCs) and organic field-effect transistors (OFETs) in the 1980s.[7−9] These technological advancements, in addition to many others from the past 70 years, have paved the way to the rapid progress of organic electronic devices including OFETs, OSCs, and organic light-emitting diodes (OLEDs) which have already become a multibillion dollar industry today.[10] OFETs and OSCs are also nearing commercialization and offer many unique advantages over their inorganic counterparts, such as solution processability at ambient conditions, flexibility, foldability, and transparency, which could lead to many more emerging new technologies that one could imagine.

The first OFET device, which utilized polythiophene as the active semiconducting material with a charge carrier mobility of 10^{-5} cm^2 V^{-1} s^{-1}, was introduced in 1987.[9] Since then, the charge carrier mobility of OFETs has increased over 6 orders of magnitude owing to materials and processing innovations. The main property which allows conjugated organic molecules to transport electronic charge is their conjugation along the backbone, which causes delocalization of electrons, allowing efficient charge transport. Charge transport also occurs between different molecules connected via van der Waals interactions, particularly $\pi-\pi$ stacking, which is highly sensitive to intermolecular packing in the solid-state. This $\pi-\pi$ stacking interaction plays a crucial role in the charge transport of conjugated organic materials, leading to a significant enhancement of charge carrier mobility. Although material design has enabled a drastic improvement in the device performance of OFETs, recent studies have emphasized the importance of thin film morphology and microstructures on the charge carrier mobility of OFETs.[11] Since most organic electronic devices are fabricated by solution processing, understanding molecular assembly processes is, therefore, crucial for controlling the thin film morphology of OFETs. The molecular assembly of conjugated organic molecules, however, can be highly complex, involving various possible assembly pathways traversing multiple length scales. In Figure 1(top), we show various assembly pathways for conjugated polymers discussed in this review: single polymer chains of various conformations form primary and secondary aggregates in solution during evaporative assembly which ultimately determine the thin film morphology. Conjugated polymers are typically aggregated in solution, leading to primary solution-state aggregates driven by $\pi-\pi$ interactions between polymer backbones and/or London-dispersion interactions between alkyl side chains. Studies have shown that these solution-state aggregates strongly affect the neat film morphology and electronic properties of OFETs.[12,13] In particular, solution aggregation can enhance thin film crystallinity,[14,15] in-plane alignment,[12,15,16] and tune out-of-plane molecular orientation,[17,18] leading to improved charge carrier mobilities as compared to nonaggregated solutions. However, not all solution-state aggregates are conducive to improving the film morphology, and different types of primary aggregates can lead to distinct morphologies and electronic properties.[16,19] Besides primary aggregate structures, secondary structures can form during solvent evaporation, such as liquid crystals (LCs) and fiber network aggregates which ultimately template the final film morphology and device properties of organic electronic devices.

https://doi.org/10.1021/acs.chemrev.2c00905
Chem. Rev. 2023, 123, 8395−8487

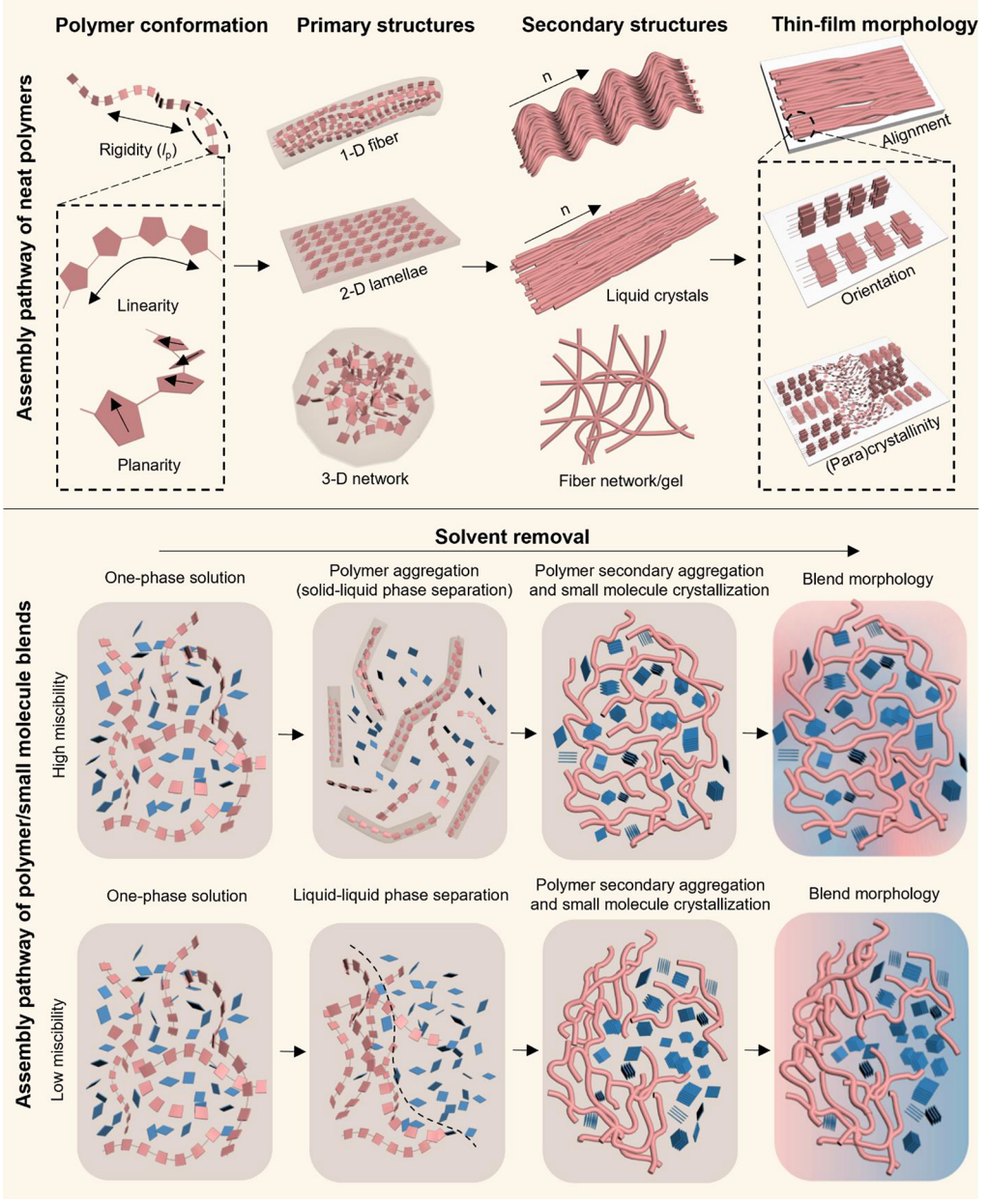

Figure 1. Schematic representations of assembly pathways of neat polymers and polymer/small molecule blends. Top panel: Neat polymer assembly. The single-strand polymer conformation is largely affected by the overall stiffness quantified by its persistence length *l*p, which is further dictated by the chain linearity and planarity. Polymers readily aggregate in ink solution with possible primary structures including 1-D fiber, 2-D lamellae, and 3-D networks as suggested by the current body of literature. Primary structures may further assemble into secondary liquid crystals or gel networks driven by concentration during evaporative assembly. The overall solution-state assembly significantly impacts the thin-film morphology including alignment, molecular orientation, and (para)crystallinity. Bottom panel: Assembly pathway of polymer/small molecule blends. The initial mixed one-phase solution containing the donor polymer and small molecule acceptor undergoes solid−liquid or liquid−liquid phase separation depending on the miscibility of the donor and acceptor materials. Following the phase separation is further aggregation of the donor polymer and crystallization of the small molecule leading to the distinct phase-separated blend morphologies largely determined by the phase separation and assembly processes.

As for OSCs, they were first introduced in 1986 by Tang and co-workers and have rapidly progressed from exhibiting less than 1% efficiency to over 19% efficiency for a single junction cell today.[8,20−22] This drastic progress can be associated with several pioneering works, starting from the invention of bulk heterojunction (BHJ) structures exhibiting interpenetrating network-like morphology from a phase-segregated mixture of two semiconducting polymers.[23,24] This structure has been adopted to overcome the short exciton diffusion length (typically, ≈10 nm) and low charge carrier mobility of organic semiconductors.[25] The BHJ structure and the development of fullerene based electron acceptor[26] have since driven the field, steadily increasing the efficiency of OSCs to ∼12% by 2016.[27] Since 2017, polymer donor and nonfullerene acceptor (NFA) based OSCs have begun to outperform fullerene based OSCs,[28] shifting the focus of the research community toward molecular design of NFA based OSCs. The rapid development of NFAs has boosted the efficiency of OSCs to over 19% only within the past few years.[20−22] Compared to fullerene-based acceptors, one of the key advantages of NFAs is their easily tunable energy

https://doi.org/10.1021/acs.chemrev.2c00905
Chem. Rev. 2023, 123, 8395−8487

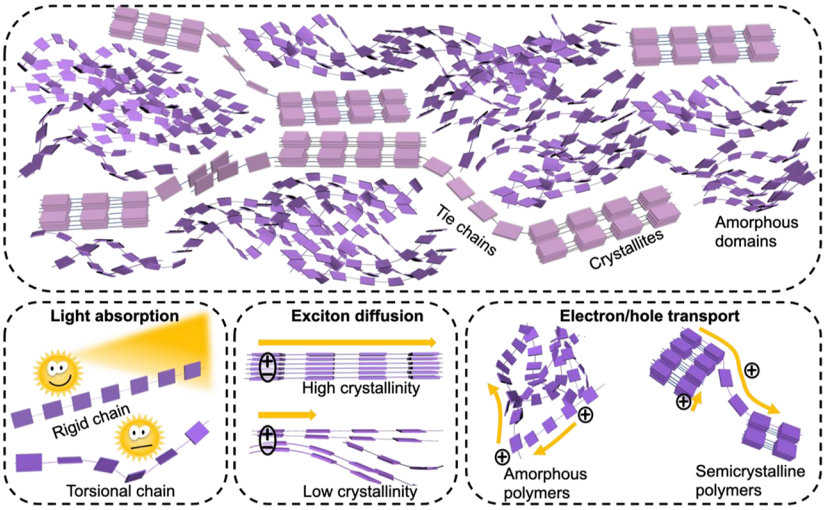

Figure 2. Schematic representation of the impact of film morphology on the photophysical processes in conjugated polymers. (Top) A typical semicrystalline morphology of conjugated polymers. (Bottom) (Left) Stiffer chain conformation conducive to higher absorbance. (Middle) Higher crystallinity leading to longer exciton diffusion length. (Right) Charge carrier transport in amorphous and semicrystalline polymers.

levels, leading to higher open-circuit voltages (V_{OC}) than those of fullerene-based devices.[29] NFAs can also be tailored to broaden the absorption range in the visible and near-infrared range, which is essential for achieving high short-circuit current density (J_{SC}). Another key advantage for the tunable molecular design of NFAs is the ability to control the morphology, particularly the crystallinity, molecular packing and orientation which drastically influence the charge transport properties in OSCs.[29−31] Besides acceptor molecules, donor polymer design is also critical for the blend film morphology and device properties.[32,33] Similar to OFETs, the morphology of OSCs is also critical for the device performance and stability of OSCs, which is in turn determined by the molecular assembly of donor and acceptor molecules from solution to solid-state during processing. However, in OSCs, where the donor and acceptor materials are blended, the BHJ morphology is not only dependent on the assembly properties of the neat materials but also on their miscibility, relative rate of aggregation and crystallization behaviors, and processing conditions.[34,35] Figure 1 (bottom) illustrates how the miscibility between the donor and acceptor materials can lead to two types of phase separation pathways, liquid−liquid (L−L) and solid−liquid (S−L) phase separation. The interplay between phase separation processes and molecular assembly pathways, thus, ultimately determine the BHJ morphology of OSCs.

In this review, we will provide an in-depth summary of molecular assembly processes of neat conjugated polymers, neat NFAs, and their blends during evaporative solution processing, and we will provide insights into how these assembly processes impact the solid-state morphology and (opto)electronic properties in both OFETs and OSCs. Before discussing the molecular assembly pathways, we will first review how multiscale morphology of OFETs and OSCs influence their optoelectronic properties and device performance. In the subsequent sections, we will discuss how molecular assembly pathways of conjugated polymers, NFAs, and blend systems determine these multiscale morphologies and device properties. Finally, we will provide a summary and an outlook in Section 5, emphasizing challenges and future directions for understanding molecular assembly pathways, highlighting the need for machine-learning-guided high-throughput experimentations to develop the structure−property relationship in organic electronics.

1.1. Fundamental Optoelectronic Properties of π-Conjugated Materials and Their Relation to Multiscale Morphology

In this section, we will briefly summarize how morphology of π-conjugated materials at different levels (molecular, mesoscale, and macroscale) affect their optoelectronic properties. As shown in Figure 2, conjugated polymers typically exhibit a hierarchical morphology, which encompasses conformation (planarity, linearity) and intermolecular packing (π−π and lamellar stacking) at molecular scale, crystalline domain size, orientation and connectivity at mesoscale, and alignment and (para)-crystallinity at macroscale. This multiscale morphology plays a critical role in determining the optoelectronic properties of these materials in neat domains. In this section, we will specifically focus on how morphology affects charge transport, light absorption, and exciton diffusion (Figure 2). For a more comprehensive discussion of electronic and optoelectronic properties of conjugated polymers, we refer readers to other excellent reviews.[36−39]

1.1.1. Hole and Electron Transport. In this section, our primary focus will be on discussing how the multiscale morphology of conjugated polymers relates to their charge transport properties. For a discussion on charge transport in small molecule crystals, we refer readers to several outstanding reviews.[37,38,40] Charge transport process is essential for conjugated polymer-based devices which rely on efficient movement of charge carriers (holes or electrons) through the polymer material to generate sufficient electrical current. For example, in OFETs, the field-effect mobility (μ) is one of the most important parameters to benchmark the electrical properties of the channel materials, which is crucial for fast device operation and overall device performance.[41] In OSCs, upon exciton dissociation, high and balanced electron and hole mobilities are essential for efficient charge transport in blend films and subsequent collection at electrodes, and slow or inefficient transport can lead to a loss of energy and reduced device efficiency.[42] In OLEDs, the charge carrier mobility serves as an important parameter affecting the efficiency, brightness, and lifetime of the devices.[43,44] In organic electrochemical

https://doi.org/10.1021/acs.chemrev.2c00905
Chem. Rev. 2023, 123, 8395−8487

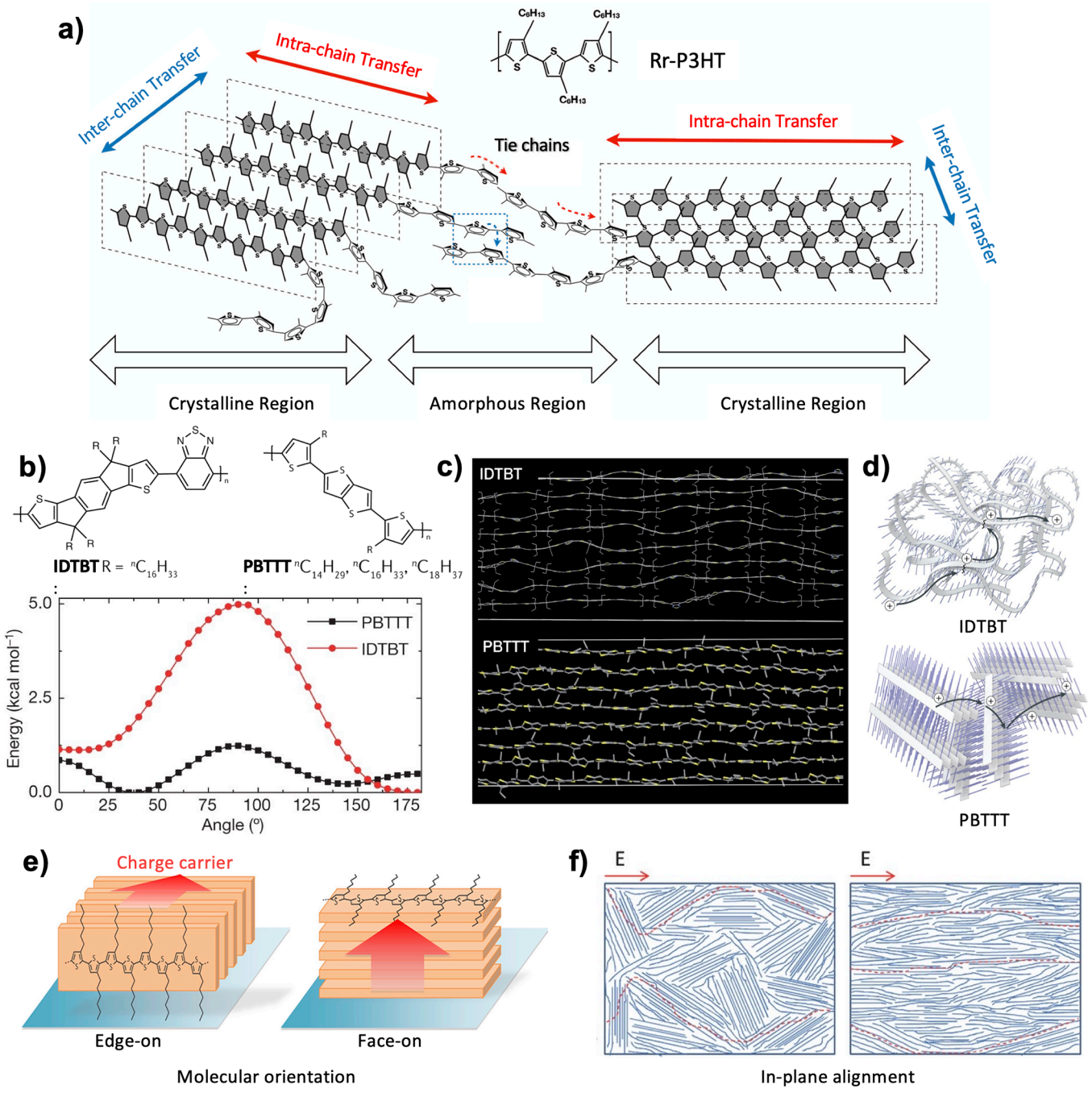

Figure 3. Important factors that govern the charge transport property. a) Charge transport processes at different length scales in a semicrystalline thin film comprising edge-on regioregular P3HT. b) Chemical structure of IDTBT and PBTTT polymers (top) and their calculated gas-phase torsion potentials (bottom). For PBTTT, the potential for torsion between thiophene and thienothiophene units is shown. c) Simulations of the backbone conformation of IDTBT and PBTTT in side-chain-disordered and noninterdigitated structures. d) Schematic illustration of amorphous and semicrystalline packing structure of IDTBT and PBTTT, respectively. e) Representative motifs of molecular orientation for semiconducting polymers with respective to the substrate surface. f) Schematic illustration of semicrystalline polymer films with nonorientated and orientated domains. Figure reproduced with permission from ref 77, Copyright 2015 American Chemical Society (a); ref 50, Copyright Springer Nature (b-top, d); ref 49, Copyright 2020 Springer Nature (b-bottom, c); ref 78, Copyright 2015 Elsevier (e); ref 72, Copyright 2018 John Wiley and Sons (f).

transistors (OECTs), the charge carrier mobility of the channel materials jointly determines the device transconductance and thus the overall OECT signal amplification.[45,46] Therefore, understanding the charge transport process in conjugated polymers and its relationship to solid-state morphology is imperative to optimize the performance of a wide range of devices in a controlled fashion.

Due to the presence of complex, hierarchical morphology, charge transport in conjugated polymers takes place at multiple length scales.[36,37,39] At molecular scale, transport relies on delocalization of π-electrons along the backbones (intrachain) and between the chains (interchain) (Figure 3a) and chain conformation is the determining factor that dictates the transport properties. It is well-known that intrachain charge transport is sensitively affected by the planarity defined by the

https://doi.org/10.1021/acs.chemrev.2c00905
Chem. Rev. 2023, 123, 8395−8487

relative dihedral angles of monomers of the conjugated backbone: overlap of neighboring carbon p-orbitals along the chain needs to be maximized for efficient transport; if adjacent monomers are twisted from coplanarity, p-orbital overlap is reduced giving rise to charge trapping. An intrachain mobility close to 600 $cm^2 V^{-1} s^{-1}$ has been demonstrated in ladder-type poly(*p*-phenylenes) where the neighboring phenylene monomers are restricted to a planar geometry by a bridging carbon atom.[47] Similarly, the intermolecular transport requires p-orbital overlap among the neighboring chains dictated by intermolecular ordering via $\pi-\pi$ stacking; a planar backbone conformation is conducive to strong cofacial stacking maximizing the orbital overlap.[36] The importance of chain conformation (i.e., rigidity) for charge transport is further amplified by recent research on donor−acceptor (D−A) polymers with alternating electron-rich and electron-deficient units along the polymer backbone. Compared to the traditional thiophene-based conjugated polymers such as poly(3-hexylthiophene) (P3HT) and PBTTT, modern D−A polymers feature more rigid fused-ring building blocks. Those D−A polymers show certain degree of crystalline order as revealed by X-ray diffraction, but they are in general less crystalline than thiophene-based polymers: most D−A polymers show fewer observable, high-order diffraction peaks compared to PBTTT, and the peaks are usually broader, suggesting a higher degree of paracrystalline disorder ($g \approx 10-15\%$) compared to P3HT/PBTTT ($g \approx 6-8\%$).[41,48] However, compared to P3HT/PBTTT which typically exhibit mobilities up to 0.1−1 $cm^2 V^{-1} s^{-1}$ in OFET, D−A polymers show significantly higher mobilities which commonly exceed 1 $cm^2 V^{-1} s^{-1}$ and can reach up to ∼20 $cm^2 V^{-1} s^{-1}$.[37,41] This is in part attributable to the more rigid backbone of D−A polymers which is more resilient to disorder critical to efficient intrachain charge transport.[37] For instance, the indacenothiophene-benzothiadiazole (IDTBT) copolymers consist of extended rigid, fused-ring conjugated units which are connected by only a few torsion-susceptible linkages (Figure 3b).[49] Besides, the linkages exhibit steep torsion potentials (Figure 3b) due to a H-bond between the N atom of the benzothiadiazole and α-H atom of the adjacent indacenodithiophene.[50] As a result, in the solution-state, high planarity gives exceptionally high persistence length of l_p = 131 nm,[51] which is significantly higher than that of regioregular P3HT ($l_p \approx 3$ nm)[52] and PBTTT (l_p = 9 nm).[53] In solid-state, IDTBT exhibits a largely torsion-free, planar backbone conformation as demonstrated by Venkateshvaran and Sirringhaus et al. using quantum chemical and molecular dynamic (MD) calculations.[49] The backbone planarity is also evidenced by pressure-dependent Raman spectroscopy which shows the absence of pressure dependence of the stretching mode on IDT and BT units, indicating the IDTBT backbone is highly planar in the solid-state. Owing to the superior backbone rigidity, all molecular sites are thermally accessible in IDTBT shown in temperature-dependent transistor measurements and field-effect-modulated Seebeck measurements.[49] Moreover, the IDTBT backbone is highly disorder-resilient (Figure 3c): IDTBT adopts remarkably planar (torsion angle of 5.2 ± 4.0°), largely torsion-free backbone even in the presence of simulated side chain disorder. The PBTTT chains, in contrast, exhibit a twisted backbone with a broader range of torsion angles (27.2 ± 14.6°). Owing to its highly rigid chain conformation, IDTBT exhibits an OFET mobility of 3.6 $cm^2 V^{-1} s^{-1}$, despite its quasi-amorphous nature without detectable long-range order (Figure 3d).[54]

At mesoscale (typically tens of nanometers), for torsional polymers (e.g., P3HT and PBTTT), efficient charge transport requires a high degree of crystallinity with sufficient crystalline domain connectivity and usually benefits from a preferential edge-on orientation for OFETs[36] and face-on orientation for OSCs. Crystalline domains usually feature a longer conjugation length and improved intermolecular coupling compared to amorphous regions, and thus provide efficient charge transport pathways (Figure 3a).[37] Therefore, a boost in charge-carrier mobility is usually observed concomitantly with increased film crystallinity through controlling the solution-state structures.[14−16,19,55−58] The semicrystalline nature of most conjugated polymers, however, sets an injection barrier as charges traverse from crystallites into intercrystallite amorphous regions.[37,39] This barrier, together with the inherently low charge-transport efficiency imparted by amorphous microstructures, can significantly reduce charge-transport efficiency.[37] Therefore, establishing percolation of charge transport between crystallites through tie-chains is crucial (Figure 3a).[59] It has been suggested that effective percolation requires the crystallites/aggregates to be separated at a short distance on the order of the persistence length of the tie chains.[60] Meanwhile, several studies have shown a rigid backbone conformation featuring high persistence lengths indeed facilitates charge percolation through the formation of tie-chains.[36,59,61] Therefore, backbone rigidity is also important for achieving charge percolation at mesoscale. Moreover, as charge transport mainly occurs along the conjugated backbone and π-stacking direction and is essentially absent along the lamellar stacking direction, an edge-on backbone orientation can facilitate the in-plane migration of charge carriers and consequently give rise to high device performance for OFETs (Figure 3e).[18,36,62,63] An early work by Sirringhaus and co-workers has demonstrated that P3HT films showing preferentially edge-on molecular orientation exhibit OFET mobilities 3 orders of magnitude higher than those with crystallites that are preferentially oriented face-on.[64] Controlling the solution-state aggregation enables tuning molecular orientation in corresponding films and consequently improving OFET transport properties.[15,17,18,62] For example, Li, Müllen, and Pisula et al. have obtained a two orders of magnitude increase in OFET mobility for difluorobenzothiadiazole-based polymers when tuning the molecular orientation from face- to edge-on by enhancing aggregation extent in solution;[18] Chen and Fréchet et al. have increased hole mobility of PDPP3F from 0.56 to 2.25 $cm^2 V^{-1} s^{-1}$ by changing orientation from face- to edge-on through replacing the branched (2-butyloctyl) to a more aggregating, linear (*n*-hexadecyl) side chain, although the concomitant increase in crystallinity may also contribute to mobility enhancement.[15] In some cases, a face-on/edge-on bimodal orientation is preferable due to the formation of three-dimensional charge-transport pathways that efficiently boost transistor performance.[62,65−70] As we shall discuss in Section 2, tuning solution-state aggregation enables delicate control over the face-on/edge-on ratio,[15,17,67,71] which can potentially lead to an optimal bimodal distribution.[67] On the other hand, a preferential face-on orientation is desirable for devices requiring high levels of out-of-plane transport, such as OSCs (detailed in Section 1.2) and light emitting diodes.[63]

At larger length scales (hundreds of nanometers to micrometers), charge transport can benefit from long-range ordering, where uniaxially aligned polymers adopt a rigid conformation. It has been reported that highly aligned films give rise to a significant improvement in charge carrier mobility.[72] For

https://doi.org/10.1021/acs.chemrev.2c00905
Chem. Rev. 2023, 123, 8395−8487

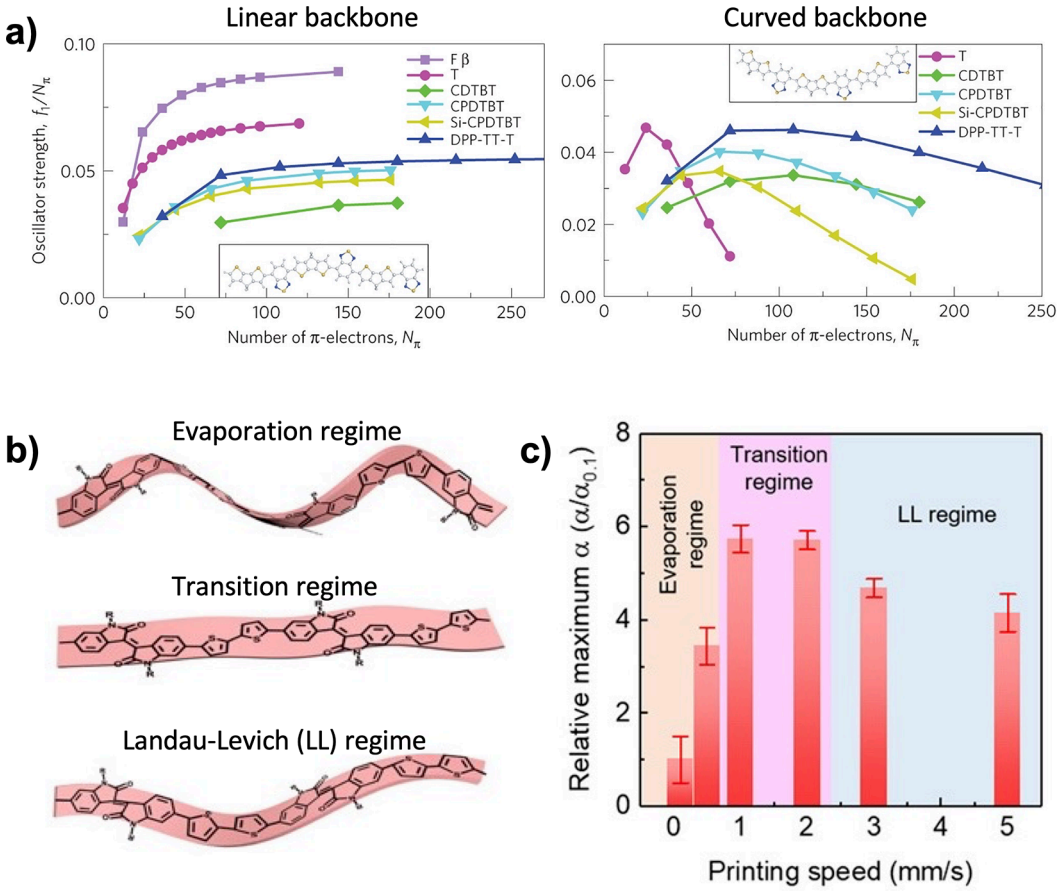

Figure 4. Conformation−light absorption relationship. a) Normalized oscillator strength f_1 of the lowest energy transition as a function of the number of π-electrons N_π for several oligomers with all-trans linear conformation (left) and all-cis curved conformation. b) Schematic illustration of backbone planarity for isoindigo-bithiophene based polymer PII2T printed in different regimes. c) PII2T film absorption coefficient (α) as a function of printing speed. All α values are obtained at ∼720 nm corresponding to the 0−0 transition and are normalized by that of film printed at 0.1 mm/s. Figure reproduced with permission from ref 79, Copyright 2016 Springer Nature (a); ref 83, Copyright 2019 American Association for the Advancement of Science (b, c).

instance, Tseng and Heeger et al. have acquired an exceptionally high hole mobility of 23.7 $cm^2\ V^{-1}\ s^{-1}$ from PCDTPT films owing to long-range alignment obtained by slow solution drying in tunnels atop nanogrooved substrates.[73] Jimison and Salleo et al. have suggested that in-plane alignment of P3HT produces relatively straight polymer chains, which results in gradual, low-angle grain boundaries in the alignment direction.[74] This consequently increases the coherence of crystallite orientations and reduces abrupt backbone direction shifts that occur at grain boundaries, leading to higher mobility along the alignment direction (Figure 3f).[74] This is consistent with the observation by Crossland and Ludwigs et al. that a sharp reduction in P3HT OFET mobility is obtained when increasing the nonaligned grain boundaries using a self-seeding crystallization method.[75] O'Connor and Rumbles et al. have further demonstrated that the improved charge transport of P3HT along the alignment direction can be ascribed to preferentially aligned tie-chains at grain boundaries.[76] This is inferred from the fact that the macroscopic charge-transport anisotropy in highly aligned P3HT films is substantially higher than the local charge-transport anisotropy. Further removal of aligned tie chains through thermal annealing results in sharp grains and thus leads to an order of magnitude drop in OFET mobility. Given the significant impact of polymer unidirectional alignment on charge-transport properties, a wide array of approaches has been developed to achieve highly aligned polymer films.[73] In Section 2, we will delve into the details of how exerting precise control over solution-state aggregation and promoting the formation of lyotropic liquid crystals can serve as promising strategies for achieving highly aligned thin film morphology.

1.1.2. Light Absorption. The optical absorption of π-conjugated materials is critical to the performance of organic optoelectronic devices. For example, the first photophysical process in OSCs is the absorption of photons from the incident light in both donor and acceptor phases, which is the primary step toward charge generation that is strongly related to the short-circuit current J_{SC} of OSC devices.[79,80] Organic photodetectors with a higher absorption coefficient can exhibit higher responsivity and sensitivity during the conversion of light energy into a detectable electrical signal.[46]

The optical absorption strength of π-conjugated molecules has proven to be strongly correlated with the molecular conformation.[79−82] Several studies have shown that highly absorbing molecules usually possess a planar, linear molecular conformation due to enhanced oscillator strength (f), giving a higher absorption coefficient.[79,80] Assuming a random orientation of transition dipoles relative to the direction of exciting electromagnetic field, f (for an electronic transition from state $|i\rangle$ of energy E_i to state $|j\rangle$ of energy E_j) can be defined as[79]

https://doi.org/10.1021/acs.chemrev.2c00905
Chem. Rev. 2023, 123, 8395−8487

$$f_{ij} = \frac{2}{3}\frac{m_e}{\hbar^2 e^2}(E_j - E_i)m_{ij}^2 \quad (1)$$

where m_e is the mass of electron, $\hbar$ is the Planck's constant, $m_{ij} = e\langle j|\hat{r}|i\rangle$ is the transition dipole with electronic charge e and position operator $\hat{r}$. f can be further related to the linear absorption coefficient α through the imaginary part of the complex dielectric function ($\varepsilon = \varepsilon_1 + i\varepsilon_2$):

$$\alpha = \frac{\omega}{nc}\varepsilon_2(\omega) = \frac{\omega}{nc}\frac{2\pi N_m e^2}{\varepsilon_0 m_e}\sum_{i,j}\frac{f_{ij}}{\omega}\delta\left(\omega - \frac{E_{ij}}{\hbar}\right) \quad (2)$$

where c is the speed of light in vacuum, ω is the angular frequency of light, N_m stands for the volume density of monomers from which f is calculated. Therefore, a higher oscillator strength f is conducive to enhancing the absorption strength. Demonstrated by Vezie and Nelson et al., the linearity of the polymer backbone, which is dictated by relative population of trans and cis conformers, can significantly impact the absorption by affecting the oscillator strength f of the electronic transition.[79] Figure 4a shows the calculated oscillator strength in the lowest-energy transition (f_1) of several oligomers as a function of the number of π-electrons (N_π) controlled by the oligomer length. To decipher its dependence on linearity, the calculation is performed with all-trans linear and all-cis curved conformation. All polymer systems show an initial rising of f_1 with N_π, which is ascribed to an increase in polarizability with oligomer length. At large N_π, however, the f_1 values of all-trans oligomers reach a plateau whereas those of all-cis oligomers decrease with N_π upon reaching a maximum regardless of the chemical versatility of the oligomers. This decrease in oscillator strength and thus loss in absorption is ascribed to the oligomer curvature along the backbone rooted in an all-cis conformation. In reality, however, many conformers coexist with chain end-to-end distance residing between the all-trans and all-cis limits. The relative distribution of trans and cis conformations is registered in the persistence length. By comparing over 40 conjugated polymers, the authors have found that polymers with a relatively longer persistence length show remarkably high optical absorption in the visible range. Specifically, the thieno[3,2-*b*]thiphene-diketopyrrolopyrrole (DPP-TT-T) polymer exhibits the highest theoretical persistence length among the polymers studied in this work due to a preference for trans alignment, relatively long monomer, and high coplanarity. As a result, this polymer shows an optical absorption strength much higher than the typical values observed for conjugated polymers. In addition to linearity, planarity also contributes to chain stiffness and is crucial to absorption strength of conjugated polymers. Our recent study has shown that, by achieving flow-induced planarization of PII-2T D−A polymer, a 6-fold increase in α value is obtained in thin films with planarized backbones compared to those composed of twisted polymer chains (Figure 4b, c).[83] The correlation between high absorption strength and planar/linear conformation also applies to smaller π-conjugated molecules like NFAs.[80−82] For instance, Yan and Nelson et al. have investigated the absorption strength of NFAs using a database of time-dependent density functional theory (TDDFT) calculations of ∼500 π-conjugated molecules.[80] They have identified that the linearity and planarity of the NFAs are strongly correlated with the absorption coefficient. Besides, a fully conjugated backbone with more polarizable heteroatoms is also conducive to high absorption strength.

In addition to single chain conformation, several other factors, such as molecular weight (MW), crystallinity, and types of aggregation, have been observed to impact the absorption of conjugated polymers. Vezie and Nelson et al. have found that a higher MW of the polymer results in a higher absorption coefficient in solution.[79] They surmised that the MW increases the relative fraction of linear conformers due to the increased strength of chain−chain interactions for high MW polymers. Additionally, the chain planarity in high MW polymers can be another factor contributing to stronger absorption due to aggregation-induced chain planarization.[84] Zhokhavets and Ambacher et al. have shown that the optical absorption of P3HT/PCBM films increases with P3HT crystallinity.[85] Although not explained by the authors, the enhanced absorption in films with high crystallinity likely results from a larger fraction of planarized chain within crystalline domains. Besides, the absorption profile can be influenced by various types of aggregation. For instances, the ratio of 0−0 and 0−1 vibronic peaks are sensitively affected by H vs J aggregation depending on the dominance of intrachain or interchain exitonic coupling;[86] the absorption range can be tuned by controlling the polymorphism of the aggregates as ordered polymorphs can exhibit a low-energy absorption peak that is not present in disordered aggregates.[87]

1.1.3. Exciton Behavior. Understanding the exciton behavior including generation, diffusion, dissociation, and recombination is also crucial for improving the performance of organic optoelectronic devices such as OSCs, OLEDs, organic photodetectors, and light modulators.[25,88−92] Excitons can be generated by absorption of photons or by injection of electrons and holes, and can contribute to photocurrent via exciton dissociation as in OSCs and organic photodetectors or to electroluminescence via radiative recombination as in OLEDs. All the exciton behavior are important to determine the exciton conversion yields and device performance parameters (e.g., J_{SC} for OSCs,[25,89] photoresponsivity for organic photodetectors,[46,90] luminance or brightness for OLEDs[91,93]), and strongly dominated by film morphology.[88,89] In this section, we will focus on the impact of morphology on exciton behaviors, especially exciton diffusion and dissociation in donor and acceptor blend films.

In general, it is highly improbable for excitons to thermally dissociate into free charge carriers in pure π-conjugated materials, because the excitons have a much stronger binding energy ($E_b \approx c^2/4\pi r\varepsilon_0\varepsilon_r$) of 300−500 meV than thermal energy (k_BT) of ∼25 meV at room temperature, where c is the speed of light; r, the Coulombic radius; ε_0, the vacuum permittivity; ε_r, the relative dielectric constant; k_B, the Boltzmann constant; T, the temperature).[94,95] This means that excitons in a single π-conjugated material hardly contribute to photocurrent by themselves. To dissociate into free charge carriers, excitons must first reach the donor−acceptor interface within their lifetime (τ), which is called exciton diffusion, otherwise excitons will be lost via recombination. The details in recombination during photophysical processes are well described in previous review papers.[31,96,97] Figure 5a illustrates exciton diffusion processes, fast and short downhill migration followed by slow and long thermally activated hopping, showing that exciton diffusion length (L_D) is strongly dependent on distribution of excitonic states and energetic disorders at room temperature.[88] The excitonic states and energetic disorder are greatly affected by crystallinity of film, which is defined as the proportion of ordered regions in the film. Highly crystalline films have high

https://doi.org/10.1021/acs.chemrev.2c00905
Chem. Rev. 2023, 123, 8395−8487

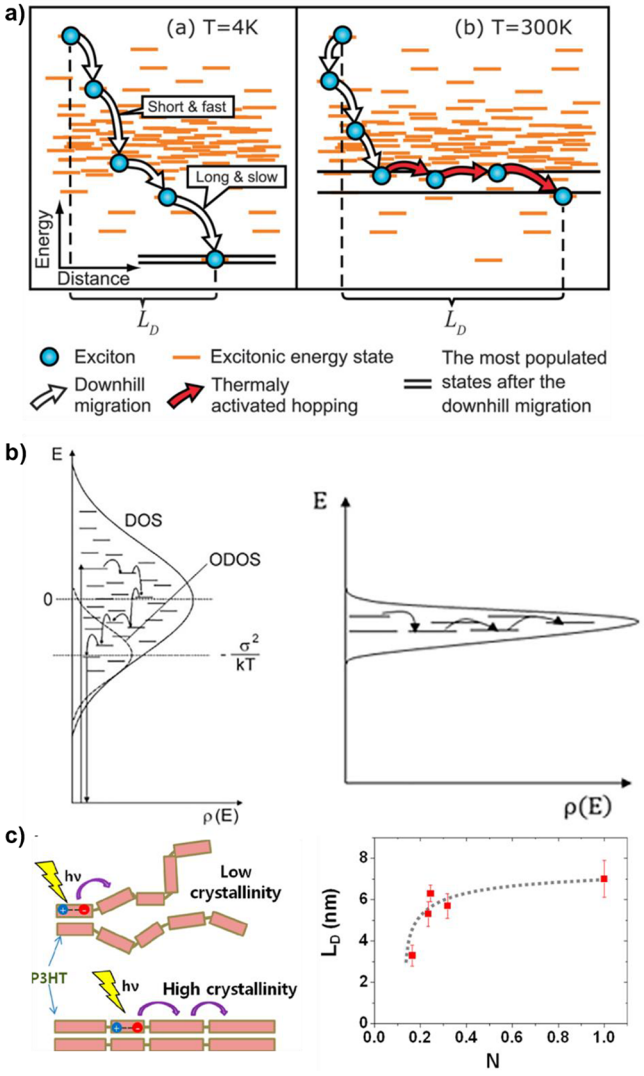

Figure 5. Impact of temperature and crystallinity on exciton diffusion. a) Exciton diffusion processes via downhill migration and thermally activated hopping at T = 4 K vs 300 K. b) Density of states representing distribution of excitation energies in disordered and ordered materials. c) Illustration of exciton diffusion in P3HT films with low and high crystallinity and exciton diffusion length (L_D) as a function of the crystallinity (N) of P3HT films. Figure reproduced with permission from ref 88, Copyright 2015 Royal Society of Chemistry (a); ref 25, Copyright 2020 Cell Press (b); ref 103, Copyright 2014 American Chemical Society (c).

molecular packing density and thus the increased density of states (DOS) with narrow half-width of Gaussian energy distribution (σ), and the equilibrium energy of the excitons is offset by σ^2/kT with respect to the center of DOS as shown in Figure 5b.[25,98] Thus, smaller σ gives a higher chance for excitons to hop, extending L_D, which is beneficial for enhancing the efficiency of exciton dissociation at the donor/acceptor interface. For the π-conjugated materials, the rigid planar conformation of conjugated backbone can lead to strong intra- and intermolecular coupling and induce high crystallinity in the solid-state thin film, resulting in reduced energetic disorder and preventing the structural relaxation in the excited state.[25,98] Figure 5c shows the effect of crystallinity on L_D in P3HT films, confirming that as the degree of crystallinity increases, L_D becomes lengthened.

Excitons can be relocated via a nonradiative process of energy transfer, such as Förster resonant energy transfer, Dexter energy transfer, and electron transfer, which is called exciton diffusion. Considering that Förster resonant energy transfer facilitates singlet exciton diffusion, the L_D is expressed as[88]

$$L_D = \frac{1}{d^2\sqrt{6}}\sqrt{\frac{9\Phi_{PL}\kappa^2}{128\pi^5 n^4}\frac{\tau_f}{\tau_0}J} \tag{3}$$

where d is the intermolecular spacing or the distance between the chromophores; Φ_{PL}, the photoluminescence (PL) quantum yield; κ^2, the dipole−dipole orientation factor ($0 \le \kappa^2 \le 4$); n, the refractive index; τ_f, the PL lifetime in a solid; τ_0, the intrinsic exciton lifetime that is not limited by diffusion limited quenching at defects; J, the spectral overlap between the area-normalized PL spectrum of donor and the absorption spectrum of acceptor. According to this expression, we could expect how molecular assembly can impact the exciton diffusion in the π-conjugated materials. The d value can vary in the range of 0.35−5 nm, defined by the $\pi-\pi$ stacking distance (lower limit) and the Förster radius (upper limit) and inducing a large variation of L_D by two orders of magnitude.[99−101] The dipole orientation factor κ^2 can have a maximum value ($\kappa^2 = 4$) when all transition dipoles are aligned (e.g., single crystal), whereas the κ^2 value becomes much smaller (0.476) for amorphous films with randomly oriented dipoles,[89,102] pointing to the importance of crystallinity on exciton diffusion[103] as discussed above. However, it is challenging to align the dipoles especially for the π-conjugated polymer films formed via solution processing.[102] The ratio of τ_f/τ_0 is determined by the amount of exciton quenching defects and becomes unity when the material is highly pure. The spectral overlap J is strongly correlated with the Stokes shift. For achieving longer L_D, the π-conjugated materials should have smaller red-shift of emission compared to the absorption spectrum, which is strongly influenced by molecular assembly such as the type of aggregation, determining intrachain and interchain excitonic coupling.[89]

For efficient exciton dissociation, we also need to consider domain size or spacing, the characteristic length of periodic modulation of composition in the BHJ blend film. The factors determining domain properties will be discussed further in Section 4.1. Exciton harvesting efficiency (η_{EH}) at the interface is roughly estimated by

$$\eta_{EH} = 1 - \frac{\tau_b}{\tau_n} = 1 - \frac{L^2}{L_D^2} \tag{4}$$

where τ_b and τ_n stand for exciton lifetime of the blend and neat films, respectively, and L is the exciton travel distance in the duration τ_b corresponding to half the domain size. The domain size needs to be close to $2L_D$ to prohibit exciton recombination. However, typical L_D of π-conjugated materials is ~10 nm.[88] Thus, decreasing domain size (or L) can enhance η_{EH}. On the other hand, increasing energetic disorders in the blend film induces charge trapping because of longer pathway of charges to electrodes, thus reducing charge collection efficiency. Therefore, for achieving higher η_{EH}, L_D needs to be increased as much as possible, allowing larger domain size in the blend film which is necessary for efficient charge transport while minimizing recombination.

The exciton arriving at the donor−acceptor interface can relax to a singlet charge transfer (CT) exciton via electron and hole transfer. The electron transfer is mainly driven by the offset of

https://doi.org/10.1021/acs.chemrev.2c00905
Chem. Rev. 2023, 123, 8395−8487

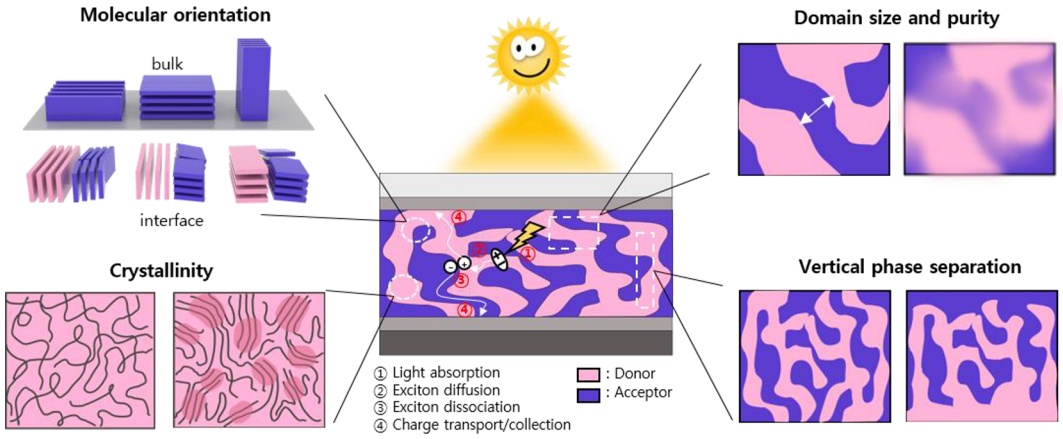

Figure 6. Schematic illustration of photophysical processes in BHJ film of OSC device (middle) and morphological parameters: crystallinity, molecular orientation, domain size and purity, and vertical phase separation, which affect the OSC device properties.

the lowest unoccupied molecular orbitals (LUMOs) between the donor and acceptor, and the hole transfer by offset of the highest occupied molecular orbitals (HOMOs). However, the CT state is still bound with a binding energy (E_b). For dissociation into free charge carriers, it requires an external energy to overcome the binding energy, which comes from the excess vibrational energy released when hot CT exciton forms, and the built-in electric field generated by the difference in the effective work function of two electrodes.[94] In organic solids, the intramolecular vibration can give more significant effect on the exciton dissociation than the intermolecular vibration because of the larger spacing between molecules. According to the Braun-Onsager model, the CT exciton dissociation rate k_{diss} can be described as[104]

$$k_{diss}(F) = \frac{3\mu e}{4\pi\varepsilon_0\varepsilon_r {r_0}^3} \exp\left(\frac{-E_b}{k_B T}\right)\left(1 + b + \frac{b^2}{3} + \frac{b^3}{18} + \cdots\right) \tag{5}$$

where F is the electric field; μ, the sum of the charge carrier mobilities; r_0, the initial intrapair separation; E_b, the binding energy of the CT state; b, the reduced electric field ($b = e^3F/8\pi\varepsilon_0\varepsilon_r k_B^2 T^2$). The last factor in the bracket is the Taylor expansion of a first-order Bessel function for the reduced electric field (b).[105] It is obvious that the dissociation rate is strongly dependent on the electrical field (F), and thus thin film architecture is necessary for a high exciton dissociation yield. In addition, μ, ε_r and E_b are also important factors that are correlated with molecular assembly such as types of aggregation, molecular packing, and molecular orientation at the interface.[106−108] It was reported that molecular packing motifs and intermolecular interaction affect solid-state polarization nearby excitons and consequently exciton dissociation rate. In addition, the ratio between molecular polarizability and molecular volume has a linear relationship with ε_r, indicating high molecular polarizability as well as high molecular packing density is necessary for high ε_r (low E_b) and consequently efficient exciton dissociation.[109] Furthermore, molecular packing configuration plays a crucial role of determining electronic coupling and charge-transfer rate between donor and acceptor. Proper molecular packing configuration can induce a low energy difference between the CT and local excitons states, resulting in faster exciton dissociation and thereby higher J_{SC}.[110] According to Monte Carlo simulation of CT dissociation yield in polymer−fullerene blend, the delocalization of charge carriers along the effective conjugated segments of donor polymer promotes the CT dissociation by improving the local mobility as well as reducing the effective Coulomb binding energy because of the larger Coulombic radius.[94,111]

1.2. Device Properties of OSCs and Their Relation to the Microstructures

The fundamental optoelectronic properties discussed in Section 1.1 collectively determine the solar cell device properties, namely, power conversion efficiency (PCE), V_{OC}, J_{SC}, and fill factor (FF). The PCE of OSC devices under illumination (P_{in}) of 100 mW cm^{-2} (AM 1.5G condition) is expressed by

$$PCE\ (\%) = \frac{P_{out}}{P_{in}} \times 100 = V_{OC} \times J_{SC} \times FF \tag{6}$$

where P_{in} and P_{out} are the input power and the output power ($P_{out} = V_{MPP} \times J_{MPP}$, $FF = (V_{MPP} \times J_{MPP})/(V_{OC} \times J_{SC})$ where V_{MPP} and J_{MPP} are the voltage and current density at maximum power point in $J-V$ characteristics of OSCs). Among these device parameters, J_{SC} is closely related to the optoelectronic properties of π-conjugated materials because the overall efficiency of converting incident light into electrical current is determined by four main photophysical processes as illustrated in Figure 6: 1) photon absorption/exciton generation, 2) exciton diffusion, 3) exciton dissociation (charge transfer/separation), and 4) charge transport/collection,[30,31] which can be described by the external quantum efficiency (EQE):

$$EQE = \eta_{abs}\eta_{ED}\eta_{CT}\eta_{CC} \tag{7}$$

where η_{abs} is the absorption efficiency: η_{ED}, the exciton diffusion efficiency; η_{CT}, the charge transfer and separation efficiency; η_{CC}, the charge transport and collection efficiency.[112] These photophysical processes are briefly covered in Section 1.1. For an in-depth discussion, we refer the readers to prior excellent reviews on this topic.[94,96,113] The photocurrent density of OSCs can be calculated by using EQE spectra as follows:

$$J_{SC,EQE} = \frac{q}{hc}\int EQE(\lambda)E(\lambda)\lambda\ \mathrm{d}\lambda \tag{8}$$

where q is the elementary charge, h is Planck's constant, c is the speed of light, λ is the wavelength, and $E(\lambda)$ is the spectral irradiance.[114] The total photocurrent density, $J_{SC,EQE}$, from the EQE spectra should match the J_{SC} from the $J-V$ characteristics. The V_{OC} of OSCs, which is the maximum voltage that a solar cell can generate, is mainly governed by the energy gap between

https://doi.org/10.1021/acs.chemrev.2c00905
Chem. Rev. 2023, 123, 8395−8487

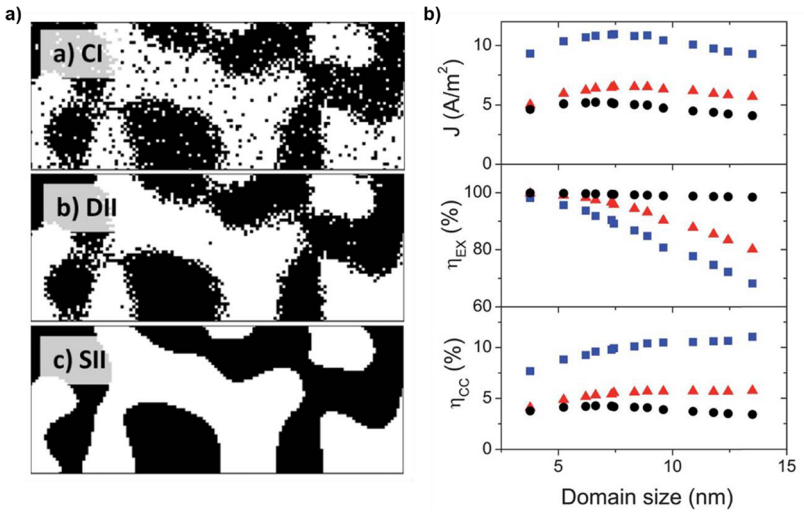

Figure 7. a) 2D images of an $x-y$ slice through a morphology, the compositional interpretation (CI, top), the diffuse interface interpretation (DII, middle) and the sharp interface interpretation (SII, bottom). Black and white represent donor and acceptor, respectively (the size of figures is 127 nm × 50 nm). b) Simulated current density (J, top), exciton dissociation efficiency (η_{EX}, middle) and carrier collection efficiency (η_{CC}, bottom) as a function of domain size for morphologies of CI (black circles), DII (red triangles) and SII (blue squares). Figure reproduced with permission from ref 143, Copyright 2012 Royal Society of Chemistry (a, b).

HOMO of the donor and LUMO of the acceptor molecule.[115−117] Large energy gap is expected to induce high V_{OC}, but the resulting small HOMO or LUMO offset of donor and acceptor can reduce the driving force for exciton dissociation, which could reduce *FF*.[117,118] Although V_{OC} of OSCs is mainly determined by the energy levels of the donor and acceptor materials, it can also be influenced by the morphology of the blend film, particularly, the molecular orientation at the interface between donor and acceptor phases[119] and their crystallinity.[120] Similarly, the *FF* of OSCs, which represents how easily photogenerated charges can be extracted upon forward bias, is also strongly influenced by the blend film morphology, including the crystallinity, domain size, domain purity, and molecular packing.[121,122] Figure 6 illustrates the interplay between the photophysical processes and the blend film morphology parameters, namely the crystallinity of the donor and acceptor phases, their molecular orientation in the bulk and at the interface, domain size and purity, and vertical phase separation. In this section, we will summarize these key BHJ morphological features that impact the device properties. For a comprehensive discussion, we refer the readers to previous reviews on this topic.[35,123−125]

1.2.1. Crystallinity. Crystallinity is an important morphological parameter which influences not only the device performance but also the stability of OSCs. As discussed in Section 1.1, optoelectronic properties such as light absorption, exciton behavior and charge transport are also affected by the crystallinity of the blend film. As previously shown in Figure 5, a more crystalline film is expected to have a longer L_D and lower density of trap sites that enhance exciton dissociation yields and reduce charge trapping during charge transport, which consequently improves J_{SC} and *FF* of OSC devices. Therefore, it is desirable to enhance the crystallinity of donor and acceptor phases in the blend films for efficient charge transport. At the same time, it is critical to balance the crystallinity of the donor and acceptor phases in the blend films. Because electron and hole mobilities are strongly dominated by the crystallinity of the donor and acceptor phases, respectively; balanced electron and hole mobilities is important for attaining high J_{SC} and *FF* in OSCs.[126−130] Therefore, a delicate control of crystallinity in the blend films is the key to optimize the device performance in OSCs. In addition, improving the crystallinity at the donor/acceptor interface is essential for achieving high V_{OC} in OSCs, which helps to reduce the energy loss via trap-assisted recombination by realizing band-to-band recombination.[120,131] One possible origin of trap states is tailing of density of states induced by thermal motion.[132] For crystalline materials, the highly ordered nature of molecules at the donor−acceptor interface can suppress the thermal motion of the π−conjugated cores and reduce the energetic disorder near the donor−acceptor interface. In addition, crystallinity is also closely related to the photostability of OSCs during operation under continuous illumination.[131] In case of OSCs with an amorphous donor polymer, illumination can induce a significant drop of V_{OC} by the formation of localized trap states by the light-induced degradation, which promotes trap-assisted recombination. On the other hand, a donor polymer with high crystallinity can prohibit light-induced degradation and reduce the burn-in loss at the initial period of operation. Therefore, it is favorable to achieve high crystallinity at the donor−acceptor interface to prolong the photostability of the OSC devices, which will be discussed in Section 1.3.

1.2.2. Domain Size and Purity. Domain size or spacing is one of the most straightforward morphological parameters affecting exciton diffusion and charge transport behavior in the BHJ blend film[125] as discussed in Section 1.1.3. In the BHJ OSCs, to efficiently convert the absorbed photons into photocurrent, the domain size needs to be close to $2L_D$ (typically, $L_D \approx 10$ nm), which provides large donor/acceptor interfacial area facilitating efficient exciton dissociation and charge generation at the interface. On the other hand such small domain size lengthens the charge transport pathway, thus increasing probability of charge trapping during charge transport.[25,125,133] For blend with short L_D, there should be a trade-off between exciton dissociation that determines J_{SC} and charge transport that affects *FF*. Recently, RSoXS measurements have shown that high performance OSCs with NFAs have relatively larger donor and acceptor domains of 20−50 nm with high

https://doi.org/10.1021/acs.chemrev.2c00905
Chem. Rev. 2023, 123, 8395−8487

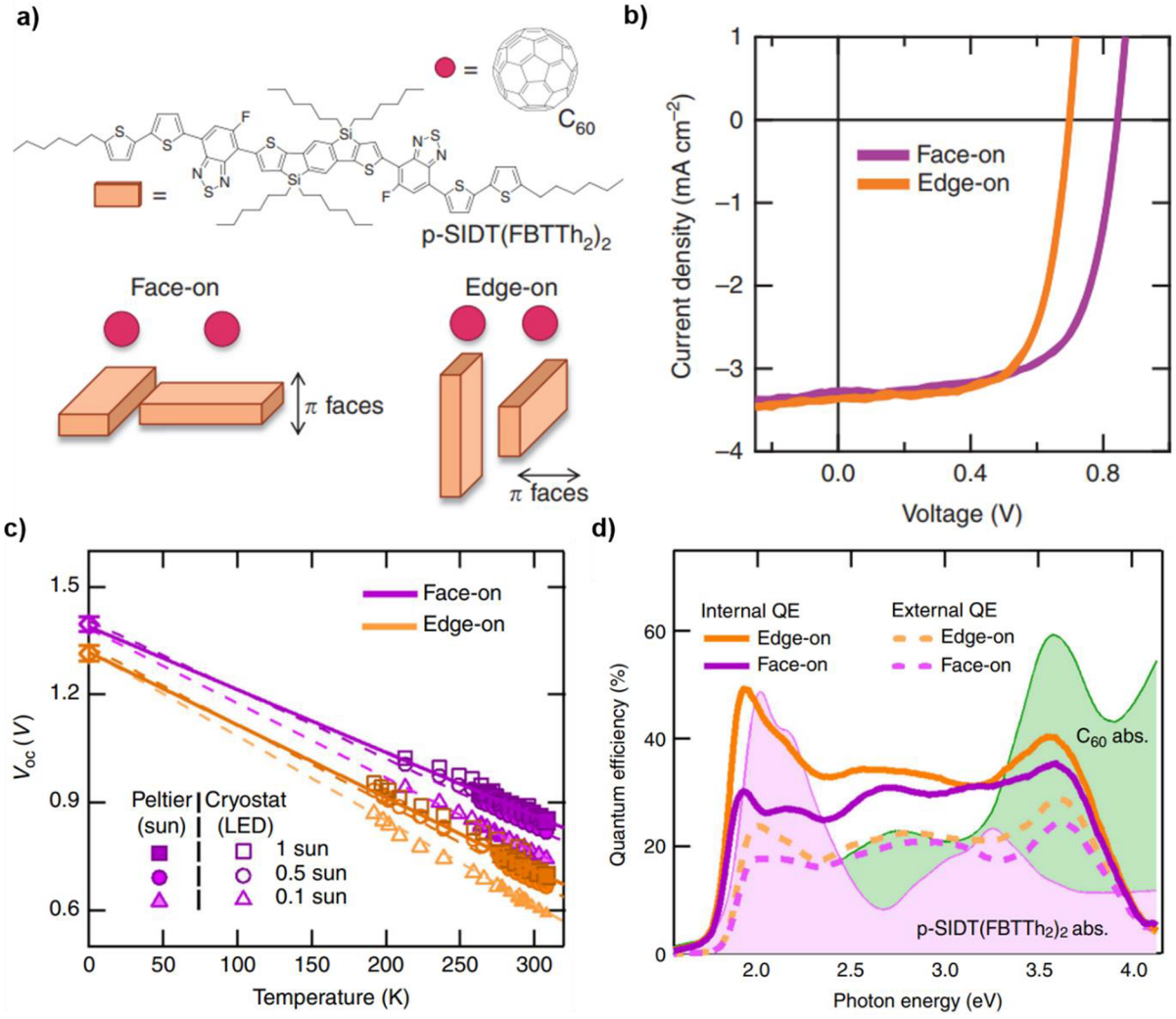

Figure 8. Molecular orientation and the resulting OSC device performance. a) Chemical structures of donor and acceptor and their molecular orientation at the interface. b) *J*−*V* characteristics of OSCs with face-on or edge-on bilayer. c) Temperature dependency of V_{OC} of OSCs under 1, 0.5, and 0.1 sun. d) Internal and external quantum efficiency (*QE*) of OSCs. Figure reproduced with permission from ref 155, Copyright 2017 Springer Nature (a−d).

domain purity compared with fullerene-based OSCs.[134] Moreover, according to recent studies, some of the high performance NFAs such as ITIC series and Y series have exhibited much longer exciton diffusion length between 30 and 50 nm than those of fullerene derivatives (<10 nm),[21,135] which results from their high crystallinity and opened a way to achieve high *PCEs* toward 20% by using NFA.[20−22] The correlation between domain size and device performance has been investigated in many high performance OSC systems.[136−139] Considering the exciton diffusion length of photoactive materials, their domain size needs to be controlled and optimized for achieving high performance by various methods such as molecular engineering,[137,139,140] modulation of solutions,[138,141] process engineering and post-treatment.[139,142]

Depending on the miscibility of the donor and acceptor, their phase separation behaviors in the BHJ films, especially domain purity, are greatly affected, which will be discussed further in Section 4.1. Due to the partial miscibility of the donor and acceptor materials in most of BHJ blends, completely pure domains are rarely observed (Figure 7a). Thus, the domain purity has been considered as another critical morphological factor that describes domain composition variation,[143,144] which can improve the connectivity to the electrode and thereby impacts nongeminate recombination. Strong intermixing between donor and acceptor materials results in low average domain purity, leading to severe geminate and nongeminate recombination in OSCs. In contrast, higher average domain purity suppresses charge recombination and leads to enhanced charge transport and high device performance, provided that percolation is maintained at high domain purity. Among the solar cell parameters, *FF* is closely related to the average domain purity. According to Monte Carlo modeling, varying the domain size of the blend films with impure domains has limited effect on the device performance because the good connectivity imparted by impure domains largely overrides the increase in charge trapping (Figure 7b).[143,144] In addition, sharp interface and well-connected domains out-perform the domains with diffusive interfaces. Therefore, domain size, purity and interface should be simultaneously considered for achieving high performance OSCs.

1.2.3. Molecular Orientation. In Section 1.1, we discussed the role of molecular orientation on charge transport in OFET devices. In this section, we will focus on its role in OSC devices. Unlike fullerene derivatives with isotropic geometry, NFAs have

https://doi.org/10.1021/acs.chemrev.2c00905
Chem. Rev. 2023, 123, 8395−8487

inherent asymmetric geometry, leading to anisotropic assembly with donor polymers to produce anisotropic optoelectronic properties.[81,145] Due to this asymmetry, the control of molecular orientation of donor and acceptor materials in the blend films is critical to realize high performance of OSCs. Many works have been conducted to understand the effect of molecular orientation of donor and acceptor materials in the bulk and at their interfaces on the photophysical processes in the BHJ OSCs.[81,145−153] By side chain engineering, different molecular orientation of NFAs such as face-on, edge-on and flat-on can be induced.[147] It has been found that a face-on orientation, with the conjugated backbone of the molecule lying parallel to the substrate, is essential for photoactive materials to have strong orbital overlap via $\pi-\pi$ stacking along the vertical direction.[81,147,149,150,152,153] On the other hand, flat-on and edge-on are preferred for for lateral charge transport in OFETs but not conducive to vertical charge transport for OSCs, as discussed in Section 1.1. The interfacial molecular orientation at the donor−acceptor interface is also crucial for high performance OSCs. Although several studies reported that molecular orientation at the donor−acceptor interface significantly influences the solar cell parameters in fullerene-based OSCs,[145,149,150,154,155] only a few studies with NFA-based OSCs have been conducted so far.[149,154,156] According to the previous studies, the orientation distribution of the donor and acceptor materials affects energy levels of the charge transfer states at the interface, resulting in different photoresponses, such as charge generation, radiative and nonradiative recombination.[145,146,155] For a small molecule donor-fullerene bilayer system shown in Figure 8a, donor molecules face-on to the acceptor interface lead to a higher charge transfer state energy and less nonradiative recombination, resulting in higher V_{OC} as well as higher radiative efficiency (Figure 8b,c). On the other hand, donor molecules edge-on to the acceptor interface exhibited more efficient charge generation, attributed to smaller electronic coupling between the charge transfer states and the ground state, and lower activation energy (lower E_b) for charge generation, which was confirmed by comparing internal and external quantum efficiencies (Figure 8d). This result indicates that there is a trade-off between V_{OC} and charge generation depending on the interfacial molecular orientation.[155] With regard to the role of molecular design, it has been reported that molecular orientation at the small molecule donor−NFA interface can vary by controlling the alkyl side chain length of the donors.[149,156] Donor molecule with short side chains was edge-on oriented with strong self-interaction in the neat film and maintained its orientation even after being blended with the face-on oriented NFA, inducing face-to-edge interface.[160] On the contrary, when the alkyl side chain of the donor molecule increased, the grazing incident wide-angle X-ray scattering (GIWAXS) measurements on the blend film indicated that NFA changes its orientation from face-on to edge-on, leading to face-to-face interface. As a result, the system with favorable face-to-face orientation enhances charge transport as well as coherence length of $\pi-\pi$ stacking, inducing a considerable increase in *PCE*s compared to those with face-to-edge orientation. Although these studies indicate that molecular orientation at the donor and acceptor interface is critical to device properties, understanding the exact formation mechanism of interfacial molecular orientation requires further investigation.

1.2.4. Vertical Phase Separation. In OSCs, selective charge transport toward respective electrodes is essential to improve charge extraction and collection efficiency. Since the network of donor and acceptor domains in the blends act as the transport channels for holes and electrons, their distribution along the vertical direction has a great impact on the device performance. In general, donor-rich and acceptor-rich layers need to be located at the respective electrodes, which can reduce the nongeminate recombination by preventing back transport of countercharges. However, vertical stratification of donor and acceptor is a complex process during film formation resulting from various factors such as thermodynamics, kinetics, and interfacial effects.[157] Interactions among light absorbing materials, solvent, surfaces of substrate and air during film formation and post-treatment is decisive for vertical component distribution. There have been many attempts to control the vertical component distribution by a variety of methods, including thermal annealing,[158,159] solvent vapor annealing,[160] washing or evacuation,[161] adding additives[162] or a third component,[163] and modulating surface energies of components or substrate.[164] A prior review reported the mechanism for controlling vertical distribution in the fullerene systems, describing the main contributing factors to be solubility, film drying kinetics, along with the surface free energies of the different materials.[157] Even though there have been many studies and achievements on vertical phase separation, it is still challenging to control in a new material system. Recently, to tailor vertical phase distribution efficiently, a pseudo bilayer structure has been introduced via a two-step deposition of donor and acceptor in sequence, sequential deposition method, resulting in a favored vertical phase distribution as well as improved film morphology.[165−167] This film deposition method enables delicate control of the morphology for each photoactive material separately, which is advantageous for efficient exciton dissociation and charge transport.

1.3. Stability of π-Conjugated Materials and Blends

Despite impressive improvements of device performance of organic optoelectronics in the last few decades, the poor operational lifetime of many high performing organic electronic materials limits their use for practical applications.[168] Therefore, it is required to understand the degradation mechanism of organic optoelectronic materials to provide guidance on designing molecular structures and controlling molecular assembly and morphology in the film to attain a more stable operation. There have been many relevant review papers summarizing the degradation mechanism and various solutions to overcome the stability issues.[169−172] In this section, we will briefly discuss how morphology can affect the stability of π-conjugated materials and blends.

1.3.1. Photostability. As we discussed in Section 1.1, film morphology greatly affects the optoelectronic properties of the π-conjugated materials, such as light absorption, charge transport and exciton behavior. In addition, morphology is also closely related with the stability of the organic optoelectronic devices during their operation. Depending on the morphology of the film, its photochemical stability is influenced when the π-conjugated materials are exposed to air and light, inducing chemical changes and disruptions of π-conjugation, and thereby resulting in reduction of optical absorption strength in a process called photobleaching. Further, such chemical structural change increases defects and disorders which act as charge trap sites or exciton quenching sites—this effect is termed photo-oxidation. Since π-conjugated materials are inevitably exposed to air and light during large-scale fabrication such as roll-to-roll printing processes, developing

https://doi.org/10.1021/acs.chemrev.2c00905
Chem. Rev. 2023, 123, 8395−8487

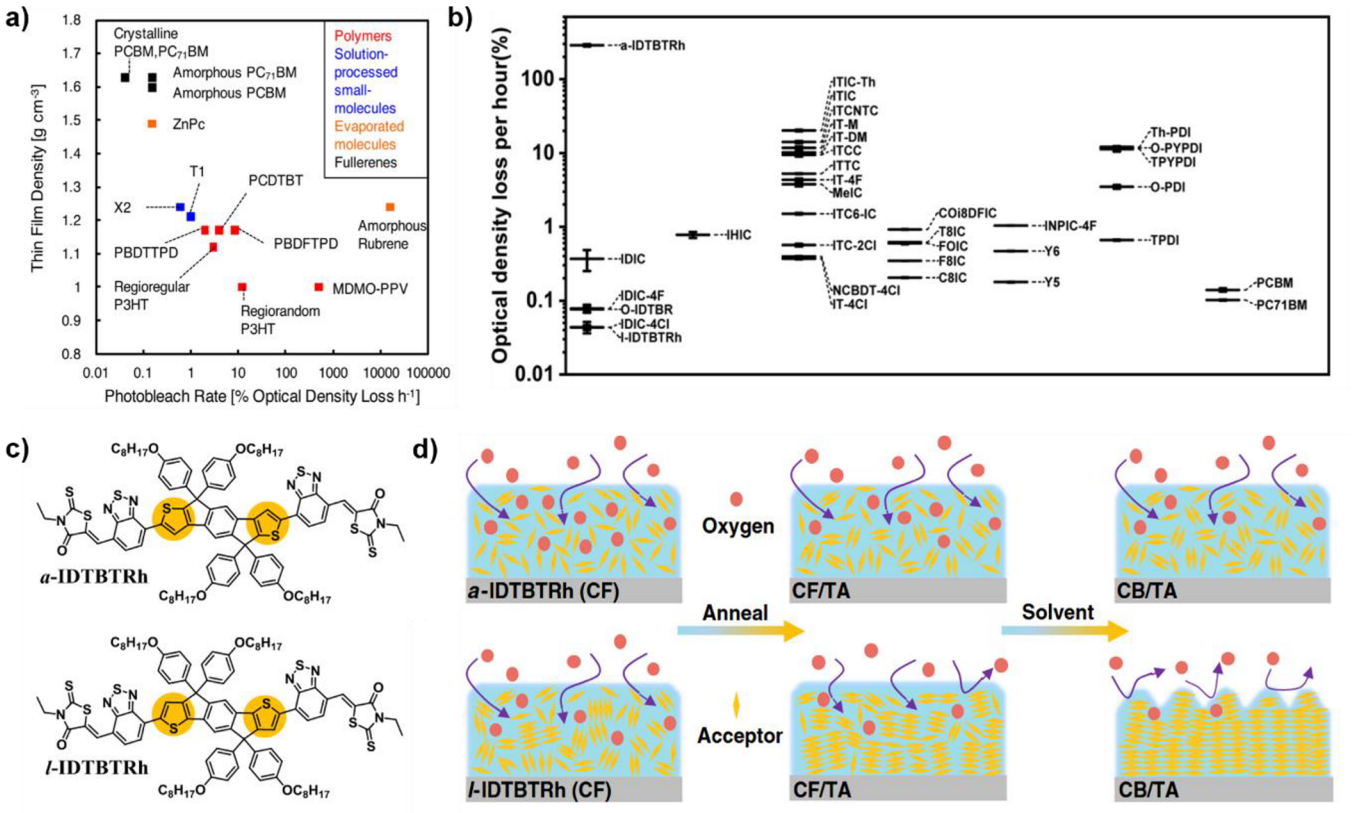

Figure 9. Impact of molecular assembly on photochemical stability of films. a) Thin film density as a function of photobleach rate for solution processed polymers, oligomers and small molecules, and vacuum deposited small molecules. b) Photobleaching rate of acceptor materials including NFAs and fullerene derivatives. c) Chemical structures of *a*-IDTBTRh and *l*-IDTBTRh. d) Illustration of oxygen diffusion behavior into the *a*-IDTBTRh and *l*-IDTBTRh films with and without thermal annealing (TA), which were made by chloroform (CF) or chlorobenzene (CB) solutions. Figure reproduced with permission from ref 176, Copyright 2015 American Chemical Society (a); ref 177, Copyright 2019 Royal Society of Chemistry (b); ref 178, Copyright 2021 John Wiley and Sons (c, d).

photochemically robust materials and film morphology is desired for stable device fabrication and their long-term usage. Manceau and Krebs et al. reported a systematic study on the relationship between the chemical structure of the π-conjugated polymers and their photochemical stability under illumination in air by comparing the total amount of absorbed photons with aging time over a certain range of wavelengths.[173] The authors observed that side chains play a key role in photodegradation and their cleavage largely improves stability even with the same backbone, implying the impact of molecular assembly and morphology on photochemical stability. In addition, aromatic polycyclic units, which can induce linearity and planarity of the backbone, were found to exhibit good photochemical stability.[174] For P3HT with low regioregularity, photo-oxidation is greatly enhanced, probably due to changes in the photophysics, i.e., an increase in the triplet yield as the morphological order of the film decreases.[175] Likewise, an inverse correlation between film density and photobleaching rate was reported for a wide range of conjugated materials ranging from solution processed polymers, oligomers and small molecules, and vacuum deposited small molecules (Figure 9a).[176] In the photobleaching process in air, the concentration of environmental oxygen accelerates the photodegradation. Thus, the penetration of oxygen in the film should be suppressed and minimized for enhancing photochemical stability via morphology control, i.e. crystallinity. Notably, most of NFAs shows poor photochemical stability compared to fullerene derivatives, which results from highly photoactive nature of NFAs[177] (Figure 9b). Thus, fine-tuning of the molecular structure is necessary to effectively improve the photo-oxidation stability of NFAs. There is a good example to show the effect of molecular conformation and crystallinity on photo-oxidation behavior. According to the literature, a subtle change in the central core unit of NFA induced a significant change in molecular conformation, i.e. planarity, resulting in stronger $\pi-\pi$ stacking and higher crystallinity (Figure 9c, d).[110,177] As a result, the difference in film crystallinity between two isomers resulted in a significant difference in photobleaching rate under illumination in air by nearly 4 orders of magnitude,[178] clearly showing the impact of molecular conformation and crystallinity on photo-oxidation. Therefore, for the highest photochemical stability, materials with high planarity, which can form dense and crystalline morphology, should be designed.

1.3.2. Morphological Stability. In blend films, although optimal bulk heterojunction morphology is achieved under various processing conditions, it is inherently metastable and thus interdiffusion or morphological ripening can occur during device operation or storage driven by thermodynamic relaxation due to limited miscibility defined by the Flory–Huggins interaction parameter.[179,180] The kinetics underpinning such morphological ripening is governed by the Gibbs free energy barrier as well as diffusional barrier.[181,182] We refer the readers to an excellent in-depth review on the thermodynamics and kinetics underpinning morphology evolution in OSC blends.[183] Below, we briefly highlight the key aspects of this process. Flory–Huggins interaction parameter χ is described as $\chi = \chi_S +$

https://doi.org/10.1021/acs.chemrev.2c00905
Chem. Rev. 2023, 123, 8395–8487

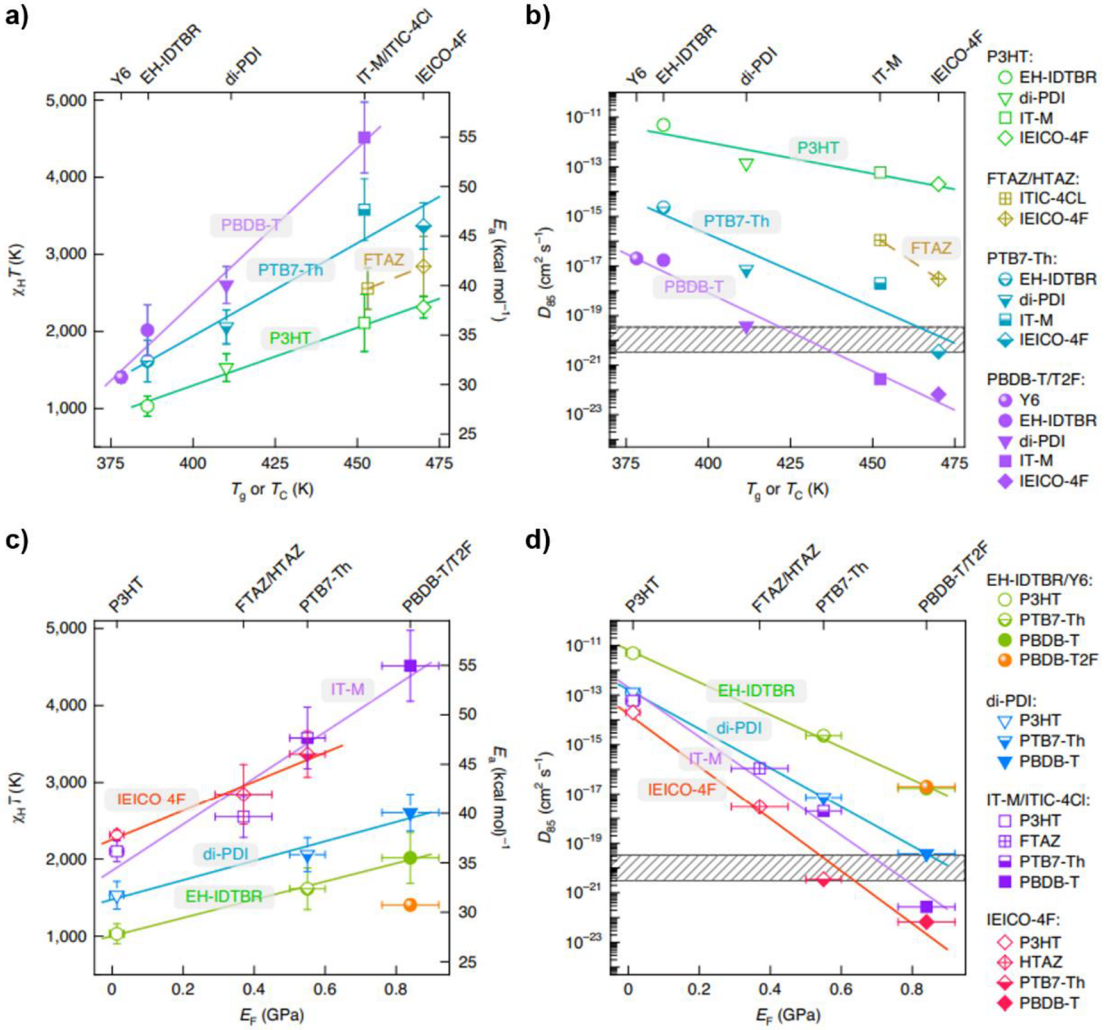

Figure 10. Relationship between parameters, with the χ_H and D_{85} dependence on T_g or T_c of NFAs and E_F of donors. a, b) $\chi_H T$ and D_{85} of donor polymers as a function of T_g of T_c of NFAs. c, d) $\chi_H T$ and D_{85} of NFAs as a function of elastic modulus (E_F) of donor polymers. Figure reproduced with permission from ref 186, Copyright 2021 Springer Nature (a–d).

χ_H, where χ_S = A (entropic component) and $\chi_H = B/T$ (enthalpic component) with A and B as system-dependent constants.[184] Large χ means low miscibility (hypo-miscible) and small χ indicates high miscibility (hyper-miscible). This will be discussed further in Section 4. Most high performing OSC systems are hypo-miscible, suggesting that the optimal BHJ morphology for high efficiency is thermodynamically unstable,[179,180,185] leading to accelerated morphology evolution under thermal stress during device operation. This has been observed especially in the fullerene-based OSC devices, showing poor morphological stability with aging time. To make hypo-miscible systems morphologically stable, it is critical to suppress demixing or crystallization of donor and acceptor by enhancing their kinetic stability. Thermally activated Arrhenius diffusion (D) can be described as

$$D(T) = D_0 \exp\left(-\frac{E_a}{k_B T}\right) \tag{9}$$

where E_a is the activation energy for diffusion, and D_0 is the intrinsic diffusion coefficient at infinite temperature or zero E_a. According to the expression, to suppress the diffusion of photoactive materials, a large E_a is desired for enhancing morphological stability. As shown in Figure 10, Ghasemi and Ade et al. revealed that E_a scales with χ_H and that χ_H is correlated with mechanical and thermal properties of photoactive materials, i.e. the elastic modulus (E_F) and the glass transition or crystallization temperature (T_g or T_c) by using representative polymer donors and NFAs.[186] According to their finding, $\chi_H T$ scales linearly with the T_g of the NFAs within a given polymer, and with the E_F of the polymer within a given NFA, whereas D scales exponentially with the T_g of the NFAs within a given polymer, and with the E_F of the polymer within a given NFA. More importantly, the relationship between D_{85} and T_g (or T_c) of NFAs or E_F of polymer donors is consistent with photostability of OSC devices. This suggests that highly hypo-miscible photoactive materials with high χ_H exhibit high E_a and low D and thus lead to long-term stable morphology by suppressing interdiffusion and self-aggregation. However, the processing window for achieving optimal morphology could be narrow because of hypo-miscibility. In order to design stable OSCs, many questions still remain as for how molecular conformation, aggregate structure and assembly pathways determine morphological stability.

https://doi.org/10.1021/acs.chemrev.2c00905
Chem. Rev. 2023, 123, 8395–8487

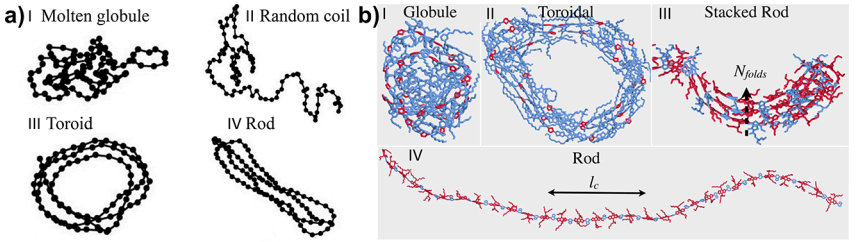

Figure 11. Typical conformations of single-strand polymers. a) Conformations of a 100-segment homopolymer generated by Monte Carlo simulations: I, molten globule; II, random coil; III, toroid; IV, rod. b) Conformations observed in 30mer trajectories in molecular dynamic simulations: I, globule; II, toroid; III, stacked rod; IV, rod. Figure reproduced with permission from ref 190, Copyright 2000 Springer Nature (a); ref 191, Copyright 2015 American Chemical Society (b).

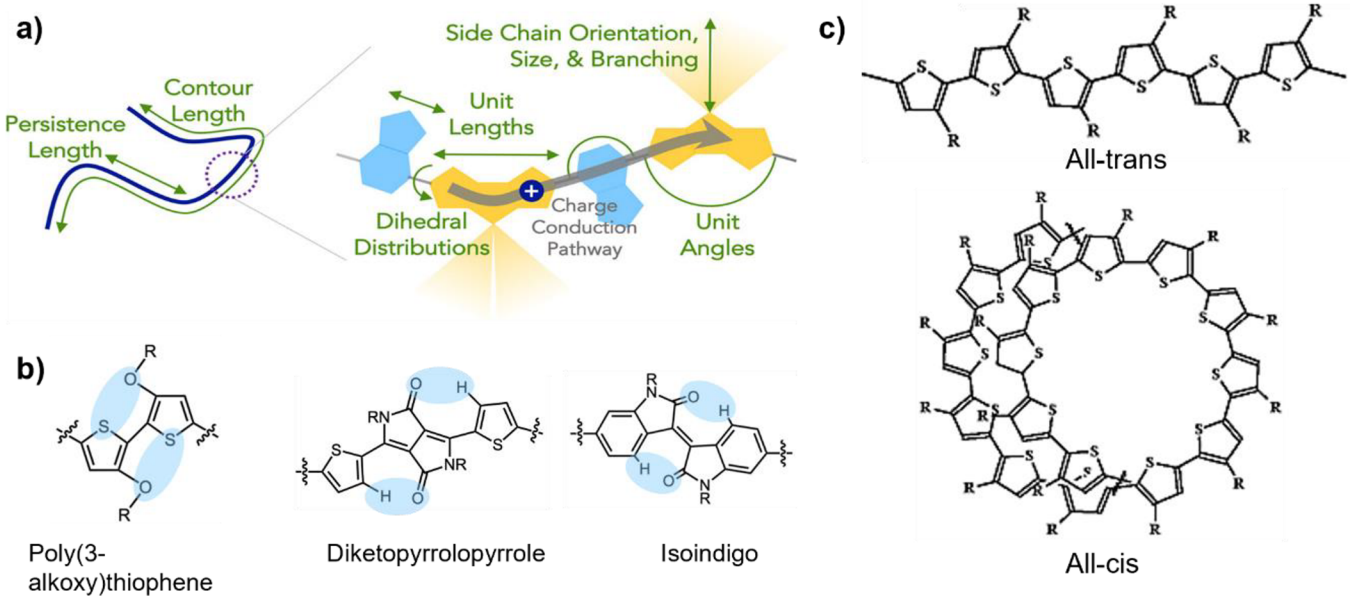

Figure 12. a) Various backbone and side chain attributes that define the persistence length (l_p) of conjugated polymers. b) Noncovalent conformational lock (highlighted with colors) in polythiophene, DPP, and IID units. c) Linear and curved backbone conformation for all-trans and all-cis polymer thiophene, respectively. Figure reproduced with permission from ref 51, Copyright 2022 American Chemical Society (a); ref 200, Copyright 2003 American Chemical Society (c).

2. ASSEMBLY OF POLYMERS

The optoelectronic performance of neat, conjugated polymers sensitively depends on their multiscale morphology, which encompasses molecular-scale intramolecular orientation and intermolecular ordering, mesoscale domain size, orientation, and connectivity, and macroscale alignment and crystallinity. Such a complex hierarchical morphology in the solid-state is largely determined by their assembly pathway from the solution-state. In this section, we will start with our discussion on polymer conformation which serves as the molecular basis underlying the structure−property relationship. Specifically, we summarize several parameters significantly affecting the chain planarity, linearity, and thus the overall rigidity. We will then discuss various strategies that have been developed to control polymer assembly in ink solution, namely, to tune the state of primary aggregate and secondary aggregate structures in the ink solution. We will further show how solution-state assembly sensitively dictates the film morphology including alignment, crystallinity, and molecular orientation. Lastly, we review the structure−property relationships focusing on light absorption, charge transport, and exciton diffusion properties of neat, conjugated polymers.

2.1. Conformation of Conjugated Polymers

Polymer conformation refers to the spatial structure of a polymer determined by the relative locations of its constitutive monomers.[187] Polymers' conformational degree of freedom is rooted in the isomerism that results from the rotation around the single bonds along the backbone.[187,188] Practically, the conformation that a polymer chain adopts depends sensitively on three aspects: the inherent flexibility of the chain, interactions (either attractive or repulsive) between monomers along the chain, and interactions with surroundings (e.g., other chains or solvent molecules).[189] Polymer conformation is the molecular basis underpinning the structure−property relationships and thus has been the core of polymer science.[187] Various experimental analyses and theoretical models have been developed for describing conformations of polymeric chains in solutions, melts, and glasses.[189] "Essentially all physical properties of polymers are manifestations of the underlying polymer conformations or significantly impacted by the conformation properties"[187]—this statement is particularly accurate for conjugated polymers as their optoelectronic properties (e.g., light absorption and charge transport) are sensitively dictated by chain conformation. In this section, we

https://doi.org/10.1021/acs.chemrev.2c00905
Chem. Rev. 2023, 123, 8395−8487

focus our discussion on various parameters that can impact the chain conformation of conjugated polymers.

The conformations available to a polymer chain depend sensitively on the chain rigidity quantified by its persistence length (l_p). The l_p is mathematically defined as the characteristic length scale for the exponential decay of the backbone tangent−tangent correlation functions.[187] In general, for a polymer chain, the relative magnitude of l_p to the contour length l_c determines its statistical conformational classes: When l_p is much smaller than l_c, the polymer chain adopts a flexible coil conformation; When l_p is much larger than l_c, the chain behaves like a rigid rod; Intermediately, when l_p is comparable to the l_c, the chain is more appropriately described by a wormlike chain model. For conjugated polymers, due to the presence of attractive $\pi-\pi$ interactions between segments within a chain, other distinct conformational classes have also been identified. For example, using coarse-grained simulations, Hu and Barbara et al. have suggested four distinct conformational classes of a conjugated polymer−random coil, globule, toroid, and rod (Figure 11a).[190] Later, Jackson and Ratner et al. have established an atomistic link between these conformational classes and molecular structures of single-strand polymers using high-level quantum-chemical calculations.[191] They find that polymers with linear conjugated backbones tend to adopt the ordered conformational classes of rod, stacked rod, and toroid, whereas those with nonlinear backbones are prone to disordered globule state (Figure 11b). Besides, chain planarity is also conducive to an ordered conformation. As we shall discuss, linearity and planarity are also two primary contributors to overall chain rigidity quantified by l_p and are intimately related to the optoelectronic properties of conjugated polymers.

2.1.1. Conformation Dependence on Backbone, Side Chain, and Solvent. How can we tune the conformation of conjugated polymers? The current body of literature has suggested that backbone (dihedral distribution, unit angle, and unit length) and side chain (size, branching, and orientation) design (Figure 12a), and solvent selection are the key factors to be considered.

2.1.1.1. Backbone Attributes. The primary contributions to the backbone stiffness include the planarity and linearity of the monomer units along the backbone. The coplanarity usually results from a high torsional barrier with minima near 0° or 180° in the torsional potential energy curve. For example, the high stiffness of IDTBT polymer is largely attributed to a steep torsional potential with an exceptionally small torsion angle minima of 5°,[49,51,192] resulting in the highest reported l_p so far over 100 nm in solution.[51] In contrast, typical second and third generation conjugated polymers (i.e., alkylated homopolymers and alkylated donor−acceptor copolymers, respectively) only show respectively a persistence length of ∼2 to 10 nm and ∼10 to 10s of nanometers,[51,53,193] usually owing to nonplanar dihedral minima with relatively flat torsional potentials. For example, the torsional potential of IDTBT has been compared to that of PBTTT and naphthalenediimide-bithiophene-based polymer P(NDI2OD-T2) which are two typical second and third generation conjugated polymers, respectively.[192] The PBTTT shows a deviation from planarity by ∼40° at the thienothiophene/thiophene linkage, whereas the backbone of P(NDI2OD-T2) is twisted due to a 45° dihedral between donor and acceptor units with a high energy cost of ∼3 kcal/mol for planarization. Both two polymers show relatively low yet typical persistence length of 9.0 nm for PBTTT,[194] and 5.1 nm for P(NDI2OD-T2).[195] This highlights the importance of the number and the rigidity of the torsion-susceptible single-bond linkages in defining conjugated polymer conformation. A common strategy to construct highly planar structures is based on the concept of noncovalent conformational lock, which involves intramolecular nonbonding interactions including (non)traditional hydrogen bonds, sulfur bonds etc.[196] For instance, in poly(3-alkoxythiophene), the sulfur atom can have though-space S···O interaction with the oxygen atom in the adjacent ring, which provide an energy barrier to rotation and thus promote chain planarity;[50] in DPP-2T the oxygen atom forms (nontraditional) hydrogen bonding (O···H−C) with the hydrogen atoms on thiophene rings to have conformational locks;[196] similar O···H−C locking is also featured in the isoindigo (IID) unit (Figure 12b). Other strategies involve replacing the carbon single-bond with double-bond linkages (as the energy required for rotation around a double bond can be 1 order of magnitude higher than that for a single bond[195,197]) or synthesizing conjugated ladder polymers with fully π-conjugated backbones. We refer the readers to several recent reviews on those strategies for conformational control of conjugated polymers.[196,198,199]

In addition to planarity, the linearity of the backbone determined mainly by the unit deflection angle also affects the persistence length. For instance, thiophene and other five-membered rings lead to a deflection angle around 15° whereas six-membered rings like phenylene tend to maintain the linearity owing to 0° deflection.[53,201] As a result, the typical reported persistence length of poly(3-alkyltihophenes) (P3AT) is around ∼1 to 4 nm,[52,53] whereas poly(*p*-phenylene) (PPP) with a single bond angle of 0° exhibits a much higher persistence up to 28 nm,[202−204] even with nontrivial backbone torsion present.[52] In other words, the loss of chain persistence in polythiophene is caused not only by the deviation from coplanarity due to backbone torsion but also by the presence of *cis* conformation which curves the backbone.[52] Even without any torsion between monomers, P3HT with all-*cis* conformation can have a significantly curved backbone, whereas all-*trans* conformation retains the linearity of the chain (Figure 12c).[200] This also applies to thiophene-containing modern donor−acceptor (D−A) polymers such as DPP-TT-T of which trans conformation is desired to obtain high stiffness.[79] Wang and Pei et al. have systematically tuned the linearity of BDOPV/thiophene copolymer by controlling the number of thiophene on each repeating unit.[205] Due to a consistent deflection caused by thiophene unit along the backbone, the BDOPV-T with only one thiophene adopts a wavy backbone conformation as revealed by quantum calculation and molecular dynamic simulation. BDOPV-2T shows a linear backbone as the 2 thiophenes can adopt an anticonformation and thus cancel the deflection. This is further supported by the small-angle neutron scattering (SANS), which indicates BDOPV-2T forms 1D worm-like structures in solution, whereas BDOPV-T only adopts random coil structures. Subsequently the authors show that BDOPV-2T exhibits a higher electron mobility in transistors because of a linear backbone conformation. Similarly, Wang and Bazan et al. have tuned the linearity of polymer backbone by arranging the position of fluorine substitution to vary the F···H interactions.[206] Rieger and Mullen et al. have shown that the backbone linearity of benzodithiophene(BDT)/thiophene copolymers can be modified by incorporating different BDT isomers with different deflection angles.[207] Both studies have demonstrated that the linearity has far-reaching effects on the electronic performance of the polymers.

https://doi.org/10.1021/acs.chemrev.2c00905
Chem. Rev. 2023, 123, 8395−8487

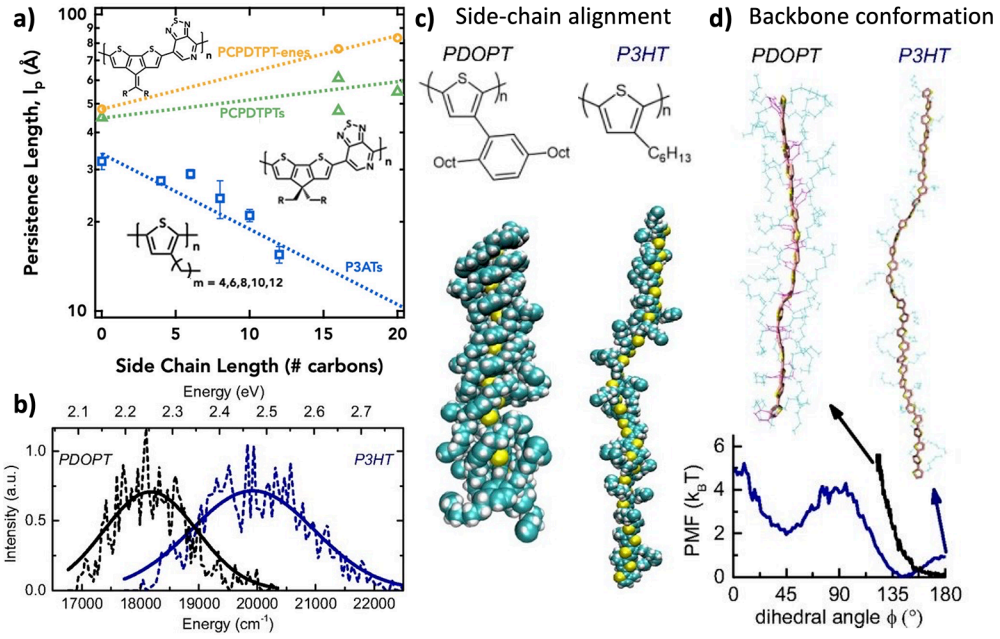

Figure 13. Side chain effect on chain conformation. a) Impact of side chain length and orientation on l_p in various polymeric systems. Symbols represent data obtained from SANS measurement whereas lines represent wormlike chain model fitting. b) Dashed lines denote calculated absorption spectra from thermal ensembles of PDOPT (black) and P3HT (blue). Solid lines denote Gaussian fits to the calculated spectra. c) Snapshots showing the side chain alignment of the two polythiophenes. d) (Top) Snapshots from trajectories of PDOPT16 and P3HT30 chains highlighting the backbone conformation. (Bottom) Corresponding PMF as a function of the dihedral angle φ (blue,P3HT; black, PDOPT). Figure reproduced with permission from ref 51, Copyright 2022 American Chemical Society (a); ref 216, Copyright 2018 National Academy of Sciences (b–d).

2.1.1.2. Side Chain Attributes. Flexible side chains are attached onto the backbone to improve the solubility in organic solvents by providing conformational entropy, thus penalizing backbone π interactions. However, their role goes far beyond solubility and critically impacts the intrachain conformation and interchain packing,[51−53,208] liquid crystalline (LC) phase formation,[16,209] thin film crystallinity, morphology and optoelectronic properties.[210,211] Here, we discuss how the molecular attributes of side chains, including length, orientation, and branching point, affect backbone conformation including both coplanarity and persistence length.

The effects of side chain length and bulkiness have been systematically investigated in polythiophene systems. McCulloch and Segalman et al. have measured the l_p of regioregular polythiophenes with varied side chain length by means of solution SANS measurements.[51,52] They found a trend of decreasing l_p with increasing side chain length. For example, the l_p decreases from 2.9 nm for P3HT with hexyl side chains to 1.6 nm for P3DDT with dodecyl side chains (Figure 13a). They propose that a decrease in persistence length for longer side chain is due to an increase in *cis* conformation, which can curve the backbone as discussed above. The *cis* conformation splays the long side chain apart and increases the side chain accessible volume, representing a lower-energy conformation in P3DDT.[52] In P3HT, however, the *cis* conformation is a higher-energy conformation compared to *trans* conformation because it provides more steric hindrances for shorter side chains which are closer together in the *cis* conformation. Interestingly, the backbone torsion seems to be unaffected by the side chain length, which is evidenced by the similar ultraviolet−visible UV−vis absorption maxima wavelength. In other words, the persistence length is mainly affected by the linearity, but not the dihedral torsion in this scenario.[52] Moser and McCulloch et al. have found a similar trend in their recent work on ethylene glycol (EG)-functionalized polythiophenes, where a decrease of l_p from 6.1 to 3.9 nm is found when the number of EG units on the side chain increases from 3 to 4.[212] Besides, side chain bulkiness influences the backbone planarity via sterically induced twisting, which serves as an effective way for tailoring the optoelectronic property. A seminal work by Andersson and Inganas et al. demonstrates the feasibility of tuning optical bandgap of polythiophene by changing the substituent bulkiness on the backbone.[213] Bulky side chains increase the degree of twisting between adjacent thiophene rings and lead to shorter conjugation length along the backbone, resulting in larger optical band gaps compared to the less bulky substituents. By systematically tuning the side chain-bulkiness, the optical gap of polythiophenes can be varied by nearly 1 eV with the resulting luminescence covering the whole visible spectrum. Imposing backbone torsion via side chain steric hindrance has served as an effective strategy for researchers to study the effect of backbone twisting on the optoelectronic properties.[214,215]

Notably, the effect of side chain length and bulkiness on the polymer backbone conformation observed in polythiophenes may not hold true for other polymeric systems or under certain circumstances. For example, a series of side chain engineered cyclopentadithiophene/pyridalthiadiazole copolymers (PCPDTPT) shows an opposite trend, where l_p increases with side chain length.[51] When functionalized with 2-hexyldecyl (HD) side chains, PCPDTPT-HD and PCPDTPT-ene-HD have l_p of 4.73 and 8.34 nm, respectively. However, l_p increases to 5.49 and 8.34 nm accordingly when HD side chains are replaced by longer 2-octyldodecyl (ODD) ones (Figure 13a). Besides, comparison of l_p among 4 polymers indicates the side chain orientation with respect to backbone may also play an important role. For PCPDTPT-HD and PCPDTPT-ODD, the side chains are orthogonal to the backbone, whereas for the other two polymers (PCPDTPT-ene-HD and PCPDTPT-ene-

https://doi.org/10.1021/acs.chemrev.2c00905
Chem. Rev. 2023, 123, 8395−8487

ODD) the side chains are parallel (Figure 13a). However, the underlying mechanism in this series remains unclear. With respect to planarity, Raithel and Hildner et al. demonstrate that, contrary to the common notion, bulky side chains can drive the backbone of polythiophenes to adopt a planar conformation.[216] The authors have found that as compared to P3HT with relatively short hexyl substituents, a poly(3-(2,5-dioctylphenyl)-thiophene) (PDOPT) polymer with bulkier 2,5-dioctylphenylene side chains possesses a more planar backbone conformation. This is evidenced experimentally by a significant red shift (>2000 cm^{-1}) in the single-chain PL spectra of two polymers, which is furthered supported computationally by quantum-classical atomistic simulations where PDOPT adopts a more planar backbone conformation with torsion minima at 180° with a red-shift in the calculated absorption, and an enhanced conjugation, compared to P3HT (Figure 13b–d). The authors ascribe this unusual observation to a unique T-shaped arrangement of the bulky side chains on PDOPT—the side chain phenyl rings are rotated ∼90° out of the backbone plane (Figure 13c). This perpendicular orientation between thiophene and phenyl units is stabilized by the contacts of *n*-octyl chains attached to the phenyl rings which in turn enforces backbone planarity. Such a side chain-induced planarization is absent from the case of P3HT, where side chains are free from any identifiable packing motif and backbone conformation is rather disordered with torsion minima at 145° (Figure 13d).

Meanwhile, in cases where branched side chains are incorporated, the location of the branch point relative to the backbone has been proven as a critical parameter regulating the chain conformation. It is suggested that branched alkyl side chains, compared to the chemically equivalent linear ones, can hinder the side chain interdigitation and enhance the solubility of conjugated polymers.[211,217,218] Hong and Chen et al. measure the l_ps of P3HT with hexyl side chains and poly(3-(40-methylpentyl)thiophene) (P3(4MP)T) with an isomeric methylpentyl side chains by means of solution SANS.[219] A 1–2 nm decrease of l_p at various temperatures was observed when the branch point was introduced in P3(4MP)T. They ascribe the decrease in l_p to the potential steric interactions of branched side chains, which promote the backbone twisting. In the work by Danielsen and Segalman et al.,[51] the authors systematically change the side chain branch point of IDTBT and reveal a trend of increasing l_p as the butyloctyl branch movied farther from the backbone. Specifically, the l_p measured by solution SANS is 6.70 nm when the branch is one carbon away from the backbone, and gradually increases to 29.1 nm when 11 carbons away. The fitting of the SANS data using the flexible cylinder model indicates the effective radii of the chains are also increasing, which is consistent with the trend of l_p. The authors argue that the l_p should increase to the fourth power of the radius of the chain if treated as an elastic cylinder and confirm this scaling using the measured l_p and fitted radii. Ning and Yi et al. have found a similar dependence in their atomistic simulation study of a difluorinated benzothiadiazole/thiophene copolymer (PffBT4T).[220] The branch point is systematically moved away from the backbone when 1-octylnonyl (1OD), 2-octyldodecyl (2OD), and 3-octyltridecyl (3OD) side chains are attached. The simulated backbone conformations indicate the average l_p follow the trend: 1ON < 2OD < 3OT. In other words, the backbone becomes stiffer as the branch point moves away from the backbone. The authors further demonstrated that the backbone conformation also affects the interchain packing. In particular, 3OT side chain-based polymer shows the strongest temperature-resilient aggregates which preserve at elevated temperature of 400 K, whereas 2OD forms aggregates at room temperature which readily dissolve at 400 K. On the other hand, 1ON cannot aggregate even at room temperature due to its highly twisted main-chain conformation impeding interchain $\pi-\pi$ stacking. The aforementioned trend is consistent with several studies where closer $\pi-\pi$ stacking distance, enhanced (opto)electronic properties in OFETs and OSCs are obtained as the branch point moves away from the backbone.[221−228]

2.1.1.3. Other Molecular Attributes. Besides molecular engineering of backbone and side chains, modulation of other molecular attributes, including regioregularity, chemical defects, molecular weight, and monomer unit length, have also been shown to affect both the persistence length and backbone planarity of conjugated polymers. McCulloch and Segalman et al. have found that the regioregularity of P3HT can significantly affect the persistence length.[52] The l_p decreases from 2.9 nm for highly regioregular (rr-) P3HT to around 1.0 nm for regiorandom (rra-) P3HT. The authors claim that the increased portion of head-to-head arrangement in rra-P3HT can introduce a large steric hindrance between side chains and result in a "kink" causing backbone torsion. This is evidenced by a significant blue shift (∼26 nm) of UV−vis absorption maxima. This is consistent with the MD simulation by Adachi and Barbara et al. where they show that the rr-P3HT 30-mer folds into a highly ordered conformation, whereas the rra-P3HT backbone is twisted and is unable to form such ordered structures.[229] Hu and Vanden Bout showed that this unfavored steric effect caused by head-to-head arrangement in rra-P3HT can be relieved by spacing out the side chains along the backbone.[230] They synthesized rra-poly(3-hexyl-2,5-thienylene vinylene) (P3HTV) with a vinyl unit inserted between each adjacent thiophene ring to obtain a spaced-out side chain distribution. Analysis based on single-molecule fluorescence excitation polarization spectroscopy and MD simulations unveil a highly ordered single-chain conformation in rra-P3HTV regardless of the regiorandom disorder, whereas rra-P3HT exhibits a broad variation of conformations due to sterics imparted by head-to-head arrangement. The lowering of regioregularity typically results in a decrease in film crystallinity, hole mobility, and device performance.[231,232] Similarly, certain types of chemical defects can also act as kinks along the polymer chain and thus render a disordered conformation. Bounos and Barbara et al. have developed a defect inclusion strategy to control the chain conformation of poly(2-methoxy-5-(2′-ethylhexyloxy)-1,4-phenylenevinylene) (MEH-PPV).[233] Three types of defects are introduced onto the polymer backbone with controlled defect concentration: linear para-terphenyl defects, bent ortho-terphenyl defects, and saturated biphenylethane defects. By combining single-molecule polarization absorption measurements and MD simulations, they reveal that incorporation of linear defects that preserve the backbone linearity leads to a highly elongated, anisotropic single-molecule conformation, whereas highly bent defects kink the backbone and result in a disordered, isotropic conformation. Saturated defects, on the other hand, render rotational freedom of the backbone and yield a defect-concentration-dependent conformation. At low defect concentrations, the anisotropic conformation is still prevalent, whereas at high concentrations, a wide range of conformations appear with the inclusion of both a rod-like, anisotropically folded conformation, and a more disordered, isotropic conformation. Besides, molecular weight directly defines the contour length and thus largely determines the conformational classes of a chain with fixed l_p. Previous

https://doi.org/10.1021/acs.chemrev.2c00905
Chem. Rev. 2023, 123, 8395−8487

reports have suggested a rod- to coil-like conformational change once the molecular weight surpasses a threshold value.[234,235] Meanwhile, molecular weight can potentially affect the l_p. Using a combination of a gel permeation chromatograph (GPC), a static light scattering (SLS) unit, and a viscometer, Nagai and Huang et al. have measured l_p of P3HT with varied molecular weight and found that it increases from 2.1 to 2.9 nm over a molecular weight range of 20 to 60 kg/mol.[236] Moreover, increasing the monomer unit lengths is another strategy to enhance the polymer rigidity. This often involves extension of the fused aromatic rings and thus equivalently reduces the number of torsion-susceptible single-bond linkages. For example, the IDT- and CPDT-incorporated conjugated polymers usually exhibit exceptionally high l_p over 50 nm.[51]

2.1.1.4. Solvent Effect. Beyond the molecular design of polymers, solvents are ubiquitous in the assembly of conjugated polymers and naturally serve as another degree of freedom to tune the polymer conformation. "The better the solvent the greater the "swelling" of the molecule. Conversely, the poorer the solvent the smaller the molecule"—the typical conformational evolution of a single flexible polymer chain as solvent quality varies was well captured in this laconic description by Flory in 1953.[188] With decreasing solvent quality, an isolated polymer chain in dilute limit will undergo the coil-to-globule transition from the swollen coil in a good solvent to the ideal coil in a θ condition, and further to a collapsed coil in a poor solvent.[187,237] Therefore, if extrapolated to conjugated polymers, one would expect conjugated polymers to adopt a disordered globule conformation when lowering solvent quality. However, the conformational behaviors of conjugated polymers can be far more sophisticated mainly for two reasons. (i) They readily aggregate even in solvents considered "good" in Flory–Huggins theory and/or at dilute conditions far below the overlapping concentration (c*), meaning aggregation-induced planarization rather than single-chain collapse can take place as solvent becomes poorer. (ii) Introducing solubilizing side chains requires the partitioning of polymer–solvent interaction into two parts (i.e., backbone-solvent and side chain-solvent interactions), making the main-chain conformation less predictable under certain circumstances. Wang and Koynov et al. have employed fluorescence correlation spectroscopy (FCS) to study the aggregation behavior of MEH-PPV in dilute conditions.[238] The FCS is a single-molecule spectroscopy technique which can determine the diffusion coefficient and the hydrodynamic radius (R_H) of fluorescent species at very low concentrations down to picomolar range. This enables them to extract single-chain $R_{H,SC}$ at concentrations below ~1 nM. Further increasing concentrations above 1 nM give rise to aggregation, as evidenced by the deviation of R_H from $R_{H,SC}$ for single chains. Interestingly, this aggregation concentration is several orders of magnitude lower than the so-called overlapping concentration c*, which is calculated to be ~100 μM for those MEH-PPV polymers. In contrast, for conventional flexible polymers, the c* separates the dilute and semidilute solution regimes presented by de Gennes,[239] meaning polymers are isolated single chains when $c < c^*$ and start to overlap at $c = c^*$. Besides, the solvents studied in this work are chloroform, toluene, and 1,2-dichlorobenzene (DCB) which are commonly considered as "good solvents" for conjugated polymers. As another example, Boehm and Huang et al. have used a coarse-grained simulation model to argue that multiple-chain aggregation occurs more rapidly than single-chain folding/collapse for semiflexible conjugated polymers.[240] The relative rates of these two processes have also been found to depend on the stiffness of the chain, with more flexible chains undergoing more rapid folding. Taken together, these works clearly demonstrate that, unlike traditional polymers, conjugated polymer can readily aggregate even at very dilute concentrations far below c* in common organic solvents due to strong $\pi-\pi$ interactions. This is in consistency with our recent work on understanding the solution-state conformation and aggregate structure of isoindigo-bithiophene-based D–A polymer (PII-2T) using small-angle X-ray scattering (SAXS).[241] We calculate the c* to be ~10–20 mg/mL based on a worm-like chain model with computed the l_p. However, analysis of SAXS profiles at various concentrations indicates that aggregation occurs even at a concentration of 1 mg/mL which is 1 order of magnitude lower than c*. Although chain collapse into globule driven by poor solvent environment can be observed for conjugated polymers in very dilute solutions[242] or in single-chain simulation,[243,244] in most scenarios relevant to film printing, as we shall discuss in section 2.2, a poor solvent environment (mostly for backbone) will instead promote extended conformation due to aggregation-induced chain planarization. On the other hand, the side chain-solvent interactions, which have been frequently overlooked when examining the solvent effect, can also affect the backbone conformation. For instance, when dissolved in a solvent (e.g., 1-chlronaphthalene and 1-bromonaphthalene) poor enough for alkyl side chains, side chain packing/ordering can occur to reduce unfavored solvophobic interactions with solvent molecules.[16,245–247] This can further induce backbone planarization, leading to ordered conformation in the solution.

2.1.2. Characterization of Chain Conformation in Solution. UV–vis absorption spectroscopy has been used as a workhorse technique to qualitatively characterize the conformation of conjugated polymers. The backbone planarity is usually inferred by the absorption peak shape and location. For example, when fully dissolved in a good solvent such as DCB or chloroform, homopolymer P3HT adopts a relatively coiled conformation and shows a featureless absorption band centering at *ca.* 450 nm associated with the $\pi-\pi^*$ intraband transition.[14,248–251] However, when solution aggregates are developed by either adding poor solvent (e.g., acetone, acetonitrile) or solution aging, a new absorption band appears with a clear vibronic progression having a 0–0 transition at *ca.* 610 nm and 0–1 transition at ca. 570 nm (or sometimes even a 0–3 transition at ca. 515 nm), owing to intermolecular packing among aggregated, planarized chains.[14,248–251] Modern D–A copolymers (e.g., PII-2T,[16] P(NDI2OD-T2),[252] and PffBT4T-2DT[253]) usually show a prominent low-energy band which is near-IR, followed upstream in energy by a high-energy UV–vis band with lower intensity. Those two bands are usually separated by an energy larger than 1 eV and, according to Spano and co-workers, both bands show very efficient mixing of the charge-transfer states (derived from the stable D^+A^- excitations) and Frenkel-like exciton states (derived from D* and A* states).[253] Interestingly, the high-energy peak always shows featureless characteristics whereas the low-energy one can exhibit pronounced vibronic progression when polymers adopt a planar conformation which usually results from an aggregation-induced planarization. For example, when dissolved in a good solvent[17,252] or heated to a high temperature,[16,253] the D–A polymer solution usually gives rise to a featureless, blue-shifted low-energy absorption peak, indicating a coiled chain conformation in either dissolved[17,252] or amorphously aggregated state.[73] However, lowering the solvent quality or decreasing the

https://doi.org/10.1021/acs.chemrev.2c00905
Chem. Rev. 2023, 123, 8395–8487

solution temperature can result in redshift of the peak, and the concomitant emergence of well-structured vibronic features separated by an energy of quinoidal-aromatic stretching mode (0.149−0.186 eV).[253] The presence of vibronic structures and spectral redshifts in aggregated solution absorption often resembles that of resultant films, which is indicative of aggregation-induced backbone planarization.[12,191]

To quantify the stiffness of the polymer chain in solution, experimental techniques including SANS, SAXS, and light scattering have been utilized to extract the l_p. The exceptionally small wavelength (0.01 to 3 nm) of probing radiation and small detecting angles in SANS/SAXS render a sufficient scattering vector (q) range (typically $\sim 10^{-3}$ to $\sim 10^{-1}$ Å) to characterize a wealth of structural information in the useful range of 1 nm to near micrometer scale. For conjugated polymer solutions, the obtained SANS/SAXS scattering profiles can be fitted to several models, such as Debye and Des Cloizeaux model, to obtain R_g, which can subsequently be used to extract l_p with a known molecular weight.[52,53] However, there are several technical challenges associated with these two techniques, which hampers the prevalence of using SAXS or SANS to probe the solution-state structures of conjugated polymers. First, interpretation of SAXS/SANS scattering profiles is nontrivial due to the complex assembly behaviors of conjugated polymers in solutions, which may involve various hierarchical structures encompassing dissolved chains, primary and even secondary aggregated structures, and the possible structure factor effects. A thorough fundamental understanding of various fitting models, and in most cases, additional real-space information provided by imaging techniques are required to accurately fit the scattering data, and thus to generate a clear molecular picture of solution-state structures. Furthermore, the scattering contrast for SAXS is rooted in the electron density fluctuation, and sometimes polymers and common organic solvents may have a similar element composition, which leads to a poor scattering contrast. Also, when halogenated solvents are needed to dissolve polymers, their high X-ray absorption tendency further reduces the quality of the scattering signal.[19] Moreover, X-ray radiation used in SAXS measurements typically has a high energy (>10 keV), which may cause beam damage to conjugated polymers. Our group has mitigated the beam damage by flowing the solution in a capillary during the measurement.[241] On the other hand, SANS measurements benefit from the isotopic scattering contrast between hydrogenated polymer and deuterated solvent (or vice versa) and the low possibility of radiation damage as neutron beams typically have very low energy compared to X-rays. For example, the energy for 1 Å neutron beam is only 80 meV whereas it is 12.4 keV for X-rays. The SANS measurements, however, can take lengthy experimental time ranging from tens of minutes to tens of hours to obtain high-quality data with sufficient signal-to-noise ratio, which is due to the low neutron flux currently available at synchrotron facilities.[254] This makes SANS measurements challenging for certain solution samples where aggregation is sensitive to solution aging. Laser light scattering experiments, where scattering contrasts depend on the refractive index difference between the scatterer and its environment,[255] can also be utilized to extract the persistence length in some cases. This methodology involves obtaining Zimm plot from a series of measurements at varying angles and concentrations, then R_g can be obtained upon data extrapolation to zero concentration and zero detecting angle.[256,257] Subsequently, the l_p is extracted from R_g using Kratky−Porod model which treats polymer chain as a Gaussian distribution of equivalent Kuhn segments.[256,257] Importantly, this requires that polymers are fully dissolved in solution, and aggregation may impede obtaining accurate l_p for individual chains.[258]

2.2. Primary Solution-State Aggregates

As discussed above, conjugated polymers facilely aggregate in ink solutions, particularly at concentrations relevant to solution processing (∼1−10 mg/mL). It has been shown that, compared to well-dissolved ones, solution-aggregated polymers often exhibit significantly improved device performance.[12,13] Various strategies, including molecular engineering of backbone and side chains,[205,259−268] solvent engineering,[16,18,19,87,245,252,266,269−271] solution temperature modulation,[272−281] and special solution treatment (e.g., UV irradiation,[250] ultrasonication,[270] and solution aging[250,251,258,282,283]), have been utilized to induce and/or enhance degree of aggregation in ink solution. However, several studies have observed the opposite where (certain types of) aggregation is detrimental to solid-state morphology and electronic properties[16,19,87,271,284] which hints that not only the extent but also the detailed structures of solution aggregation matters. Indeed, aggregate structures can exhibit a wide range of diversity owing to the presence of various intramolecular and intermolecular interactions.[16,19,62,285] For example, in order to understand the mechanisms driving polymer aggregation, it is necessary to consider the partition of polymer−solvent interaction, as both $\pi-\pi$ interactions between polymer backbones and dispersion forces among alkyl side chains can play a role.[16,285] Therefore, precisely describing aggregate structures requires a thorough investigation of the complex interactions involved. In this section, we first review strategies commonly utilized to induce aggregation in solution, followed by a discussion of methods to tune aggregation structures. Finally, we summarize various types of aggregate structures reported in the literature and discuss their aggregation mechanisms. It is worth noting that the solution-state assembly process usually couples with the complex solution processing environment with rapid kinetics. We focus our discussion on the steady-state structures and refer readers to our recent perspective for the fundamentals of solution-state crystallization/assembly and coating/printing processes.[286]

2.2.1. Inducing Primary Aggregation in Solution.

Similar to modifying the conformation of conjugated polymers, molecular engineering of the backbone and side chain serves as an effective strategy to induce solution-state aggregation. For instance, Gross and Ludwigs et al. have shown the regioregularity of P(NDI2OD-T2) significantly affects its aggregation tendency in solution.[262] Systematically tuning the ratios of 2,6- and 2,7-linked naphthalenediimide monomers during synthesis results in 4 polymers with varied degree of regioregularity: regioregular (RR)(100:0), regioirregular (RI) (70:30), RI(47:53), RI(24:76). With increasing content of 2,7-linkage (i.e., decreasing regioregularity), they observe a reduced aggregation tendency in solution, evidenced by the strong blue-shifts of the low-energy UV−vis absorption maxima. They further obtain a positive correlation between the degree of solution-state aggregation and charge carrier mobilities of the resultant films: mobility in RR film is one magnitude higher compared to RI films. Although without detailed explanation, this regioregularity-dependent aggregation tendency may relate to the linearity of two naphthalenediimide isomers: 2,6-linked monomer preserve the backbone linearity promoting backbone stacking whereas 2−7 linkage causes backbone deflection discouraging aggregation. Wang and Pei et al. have also

https://doi.org/10.1021/acs.chemrev.2c00905
Chem. Rev. 2023, 123, 8395−8487

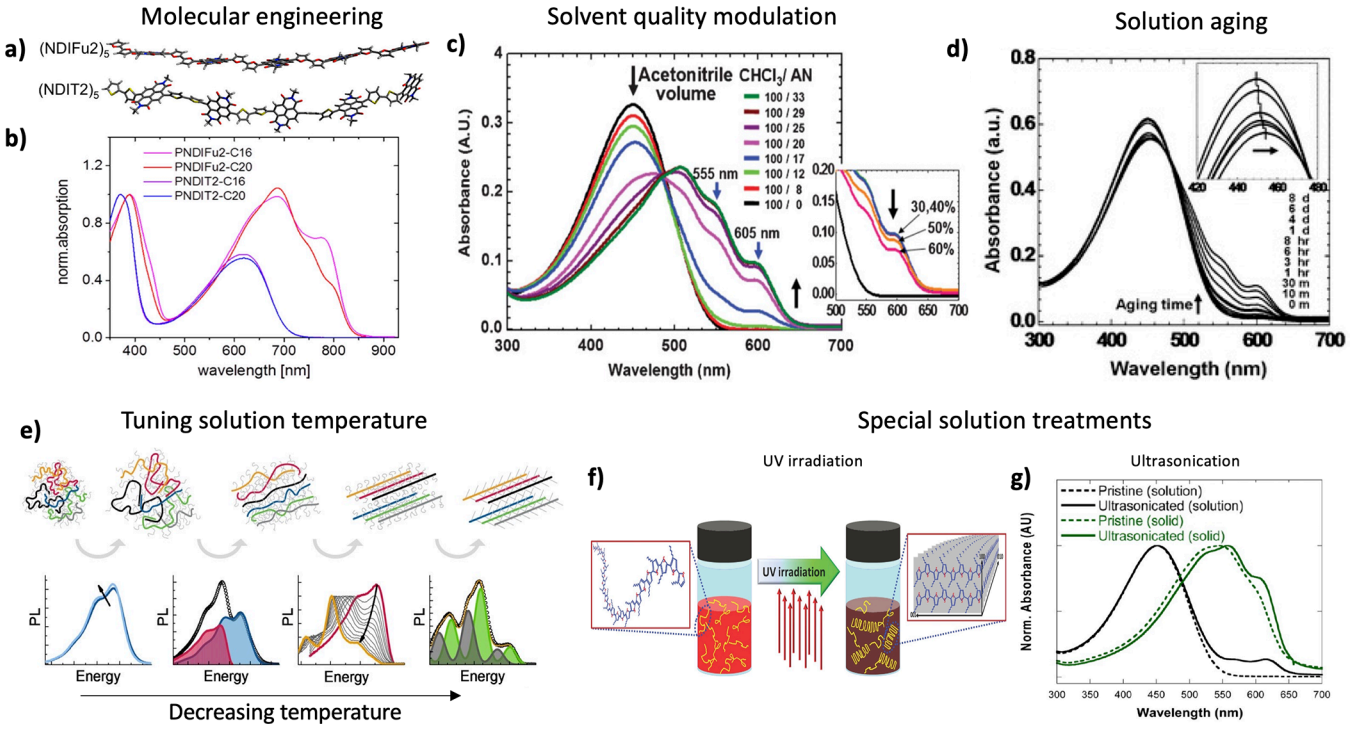

Figure 14. Summary of various methods used to induce solution aggregation. a) DFT optimized ground state structures for model pentamers $(NDIFu2)_5$ and $(NDIT2)_5$. b) Solution UV−vis absorption spectra of PNDIFu2 and PNDIT2 polymers in 1-chloronapthalene. c) UV−vis absorption spectra of P3HT chloroform/acetonitrile solutions with varied solvent mixing ratio. d) UV−vis absorption spectra of P3HT solutions with various aging time. e) Summary of changes that occur in morphology and optical spectra (absorption and photoluminescence) upon cooling a P3HT solution. f) Schematic illustration of UV irradiation induced aggregation from a molecular dissolved P3HT solution. g) Normalized solution and resultant film UV−vis absorption spectra for pristine and ultrasonicated P3HT/chloroform solutions. Figure reproduced with permission from ref 263, Copyright 2017 American Chemical Society (a, b); ref 14, Copyright 2009 John Wiley and sons (c); ref 282, Copyright 2011 Royal Society of Chemistry (d); ref 273, Copyright 2017 American Chemical Society (e); ref 56, Copyright 2014 John Wiley and sons (f); ref 292, Copyright 2013 American Chemical Society (g).

examined the effect of backbone linearity of BDOPV-based polymers.[205] They have concluded that a linear backbone leads to stronger interchain interactions forming 1-D worm-like aggregates, which further results in highly ordered solid-state morphology with high electron mobility. Besides linearity, the planarity of the backbone can also promote aggregate formation by encouraging interchain $\pi-\pi$ stacking. As discussed earlier, the noncovalent interaction between heteroatoms is commonly used to planarize the backbone. Hu and Yan have examined the effect of S···F locking interactions on the aggregation behavior of an isoindigo/quaterthiophene-based polymer PID-T4.[287] Upon fluorination of donor thiophene units, the PID-ffT4 shows a stronger aggregation tendency in solution evidenced by the emergence of an additional solution absorption peak and a higher resemblance between solution and solid absorption compared to that of PID-T4. The fluorination-induced aggregation has been confirmed theoretically by Wang and Bréda.[288] By employing thermodynamic analyses and computational tools, they extracted the Flory−Huggins interaction parameters χ for a series of PBT4T polymers that featured varying numbers and positions of fluorine atoms. The χ parameters increase as the degree of fluorination increases and have a pronounced impact on the solid-state morphological characteristics. Matsidik and Sommer et al. have significantly planarized the PNDI2T backbone by replacing the bithiophene with bifuran (Fu2) units (Figure 14a).[263] As shown in Figure 14b, when dissolved in 1-chloronapthalene, the newly synthesized PNDIFu2 polymer exhibits well-structured vibronic absorption peak due to aggregation, whereas PNDI2T shows a featureless, blue-shifted peak from the well-dissolved single chain.[252] The authors ascribe the backbone planarization by furan to reduced steric hindrance between the imide oxygen and the furan ring compared to thiophene. Furthermore, as discussed above, molecular attributes of side chains including length, bulkiness, and branching point, can affect the aggregation by changing the backbone conformation. Chen and Frechet have examined the effect of linear (n-hexadecyl − C16) vs branched (2-butyloctyl − BO) side chains on the solution aggregation of DPP-based polymer PDPP3F and PDPP2FT.[15] Analyses of solution NMR, variable-temperature UV−vis-NIR, and dynamic light scattering (DLS) spectroscopies reveal that polymers with linear side chains have a stronger aggregation tendency in solution. As a result, the C16-polymers also outperform the BO-substituted analogs in OFETs, featured by a higher hole mobility. This is further supported by the fact that BO polymers show enhanced ordering and mobility upon nonsolvent addition to induce more aggregation in ink solution. As another example discussed earlier, the PffBT4T backbone becomes more twisted as the side chain branching point moving closer to the backbone, which leads to a decrease in solution aggregation tendency.[220]

Dissolving polymer in a poor solvent or adding a poor solvent into the ink solution is another common strategy to induce solution-state aggregation. The solvent dependence aggregation behavior of P(NDI2OD-T2) has been systematically studied by Steyrleuthner and Neher et al. by means of UV−vis and PL

https://doi.org/10.1021/acs.chemrev.2c00905
Chem. Rev. 2023, 123, 8395−8487

spectroscopy.[252] The spectra vary significantly depending on the solvent quality: in a good solvent such as 1-chloronapthalene, the low-energy absorption peak centered at 620 nm is broad and featureless, owing to the fully dissolved polymer chains; in relatively poor solvent like toluene, the peak red shifts to 710 nm with the emergence of an additional shoulder peak around 800 nm, indicating the formation of aggregates. This is consistent with a computational study by Caddeo and Mattoni et al., which demonstrated a lower Flory−Huggins parameter χ is obtained in 1-chloronaphthalene than in toluene.[289] Nahid and McNeill et al. have investigated the effect of solution aggregation on the microstructure and OFET performance of P(NDI2OD-T2).[17] They have observed enhanced ordering using atomic force microscope (AFM) and higher OFET mobility in films printed from poor solvents like toluene compared to those from good solvents. Solution SAXS measurements reveal the formation of large, rod-like aggregates in toluene with R_g up to 300 nm; in contrast, good solvents like chlorobenzene yield much smaller aggregates with R_g ranging from 10 to 15 nm. The authors claim that the large aggregates in toluene promote chain ordering during solution deposition, resulting in a high degree ordering further leading to high OFET performance. This trend is also observed in the work by Luzio and Caironi et al. where devices fabricated from a poorer solvent exhibit higher charge carrier mobility compared to those from good solvent. Addition of nonsolvent to induce ordered aggregates in solution is commonly used to improve the ordering of resultant P3HT films and their performance in OFETs and OSCs (refs 14, 55, 248, 249, 269, 270, 290, and 291). For instance, Park and Cho et al. have shown that adding nonsolvent acetonitrile into P3HT/chloroform solution can induce an ordered aggregate structure from molecularly dissolved solution, evidenced by the emergence of additional red-shifted absorption band (Figure 14c) and increased R_H from DLS.[14] The aggregated state maximizes the favorable $\pi-\pi$ stacking interactions to reduce polymer-nonsolvent interactions, which improves the solid-state ordering and enhances the field-effect mobility.

Several works have shown solution aging serves as an effective strategy to induce aggregation in solution, revealing the time-dependent aggregation behavior of conjugated polymers.[250,251,258,282,283] For instance, Park and Cho et al. have found that, when dissolved in a marginal solvent (i.e., a solvent of intermediate quality for a given polymer), ordered P3HT aggregates can develop as the aging time increases.[282] This is supported by time-dependent UV−vis absorption spectra where red-shifted absorption maximum ($\lambda \sim 450$ nm) and additional bands at lower energies ($\lambda = 555$ and 605 nm) are observed (Figure 14d). Analyses of AFM images of films from solutions with varied aging time reveal the formation of rod-like structures from aged solutions, which promotes molecular ordering and boosts OFET mobility.

An alternative way to tune the extent of aggregation is by solution temperature. Using temperature-dependent optical spectroscopy, Panzer and Kohler et al. have investigated the solution aggregates formation of several conjugated polymers as temperature decreases.[273] As shown in Figure 14e, deconvolution and analysis of optical spectrum unveiled a shared aggregation pathway during solution cooling: swelling of random coils due to backbone planarization and formation of disordered aggregate through order−disorder transition, followed by backbone planarization giving rise to planarized aggregates, and finally crystallized aggregates develop at the lowest temperature due to side chain crystallization. Oh and Jeong et al. have developed a solution cooling-and-heating strategy to induce nanocrystal seeds in P3HT solutions.[274] They have found cooling of P3HT solution to −20 °C leads to formation of fiber aggregates due to the decreased solubility, which is evidenced by the emergence of additional absorption peaks. Interestingly, heating to room temperature does not fully dissolve the nanofibrils in certain solvents (e.g., m- and *p*-xylene) due to an aggregation temperature hysteresis. As a result, the remaining aggregates serve as seeds for the growth of long nanofibrils during film coating, which improves the crystallinity of resultant films and gives rise to higher solar conversion efficiencies.

Special solution treatments such as UV irradiation and ultrasonication can be coupled with poor solvent addition or solution aging to facilitate ordered aggregate formation in solution. An elegant work by Reichmanis and co-workers have demonstrated that low-dose UV-irradiation induces P3HT aggregation into nanofibrillar structures in solution (Figure 14f).[56] This is because UV-irradiation triggers a shift in the overall balance from aromatic- to quinoidal-like resonance structure, which gives rise to a higher degree of backbone planarity and thus facilitates $\pi-\pi$ stacking necessary for fiber aggregates formation. This further improves molecular ordering in the film with concomitant enhancement in OFET mobility. However, the UV-irradiation-induced aggregation becomes saturated after ∼8 min irradiation time, which hinders further improvement of thin-film properties. Therefore, in their later study, solution aging is combined with UV-irradiation to further encourage solution aggregate formation.[250] Aggregated chains are bonded together via $\pi-\pi$ interactions to form nanofibers in solution, leading to reduced tortuosity and entanglement during coating. Consequently, the alignment of polymer chains is greatly improved with increased extent of aggregation, which can be precisely controlled by solution aging time prior to film fabrication. Similarly, they have found the solution ultrasonication treatment can also induce aggregation (Figure 14g)[292] and have also investigated the synergistic effect of nonsolvent addition and ultrasonication on the nucleation and growth for P3HT rod-like aggregates in solution:[270] solution ultrasonication largely contributes to the nucleation sites formation whereas nonsolvent addition renders optimal solution conditions for nanorods growth. AFM images revealed that the rod-like structures are preserved into the thin film and their lengths are well-controlled by the amount of nonsolvent added and ultrasonication time. On average, thin films composed of nanorod structures developed in solution exhibit a 4-fold increase in hole mobility compared to untreated counterparts.

2.2.2. Understanding the Detailed Solution-State Aggregate Structures. Although a vast amount of literature has shown a positive correlation between the extent of solution aggregation and solid-state morphology and electronic properties, several recent studies have instead suggested the opposite. For example, Nahid and McNeill et al. have found that the saturation mobility is lower for P(NDI2OD-T2) OFETs fabricated from aggregated high-molecular-weight polymer solutions in DCB compared to those from molecularly dissolved solutions containing low-molecular-weight polymer.[284] AFM and resonant soft X-ray scattering (RSoXS) measurements reveal a decreased solid-state orientational correlation length with increasing molecular weight. The authors hypothesize that the aggregates in intermediate solvents such as DCB suppress liquid crystalline-like long-range orientational ordering. In contrast, non-aggregated chains can adopt a fully extended

https://doi.org/10.1021/acs.chemrev.2c00905
Chem. Rev. 2023, 123, 8395−8487

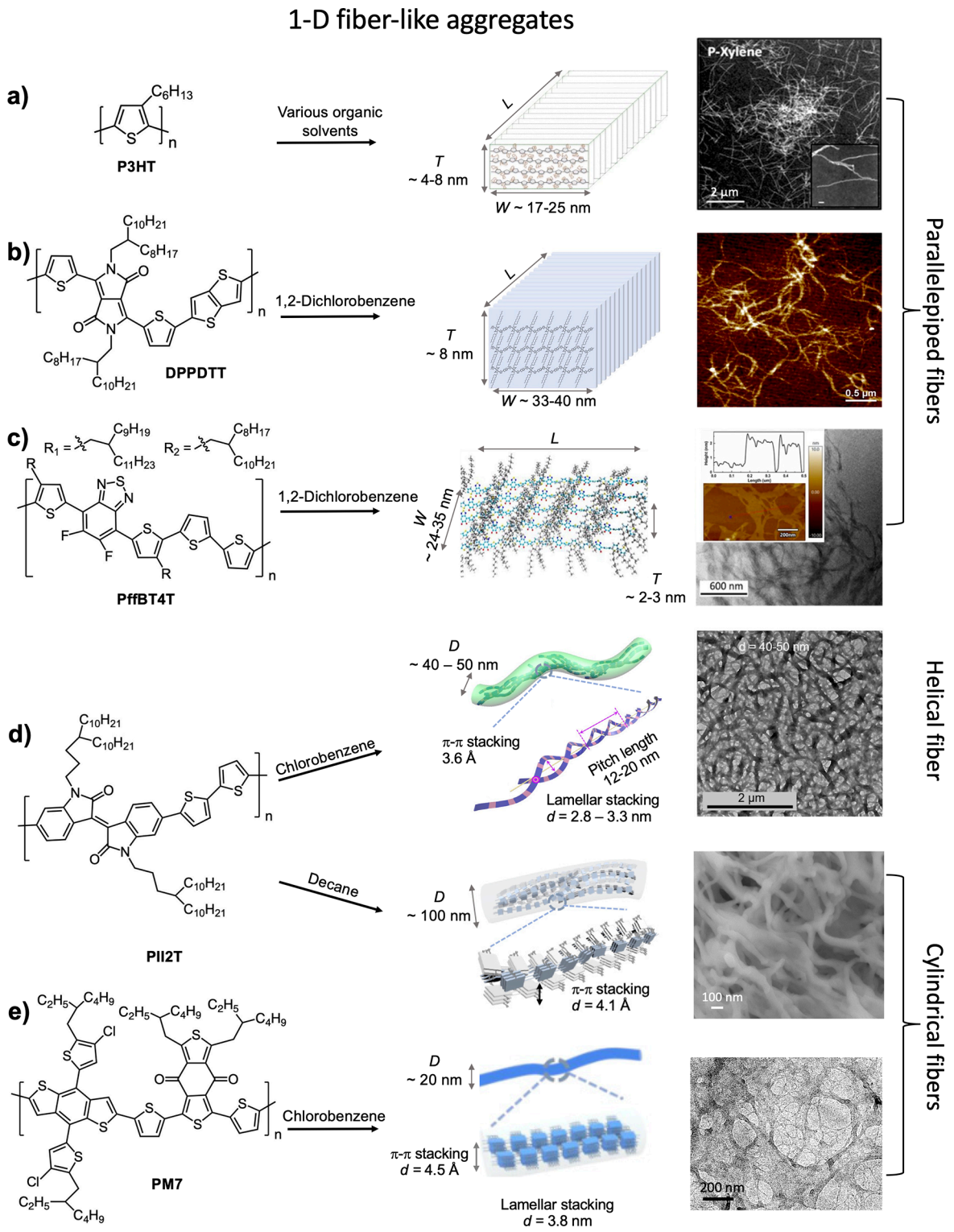

Figure 15. Summary of 1-D fiber aggregate structures of conjugated polymers. Chemical structures, schematic representations, and imaging (AFM, TEM, or SEM) of several conjugated polymers with distinct aggregate structures. a) P3HT parallelepiped fibers and scanning TEM (STEM) images of samples coated from dilute *p*-xylene solutions. b) DPPDTT parallelepiped fibers and AFM images of films spin coated from dilute DCB solutions. c) PffBT4T parallelepiped fibers and TEM and AFM (inset) images of PffBT4T-C8C12 films drop-cast from dilute solutions in DCB. d) PII2T helical fibers in chlorobenzene with TEM images and cylindrical fibers in decane with SEM images of freeze-dried samples. e) PM7 cylindrical fibers and TEM images of samples freeze-dried from chlorobenzene solutions. Figure reproduced with permission from ref 249, Copyright 2013 Royal Society of Chemistry (a-schematic); ref 297, Copyright 2011 American Chemical Society (a-STEM image); ref 258, Copyright 2020 American Chemical Society (b); ref 300, Copyright 2022 American Chemical Society (c); ref 295, Copyright 2022 Springer Nature (d-top); ref 16, Copyright 2022 John Wiley and sons (d-bottom); ref 301, Copyright 2023 American Chemical Society (e).

https://doi.org/10.1021/acs.chemrev.2c00905
Chem. Rev. 2023, 123, 8395−8487

conformation during spin coating, giving rise to enhanced long-range order in the film. As another example, Yao and Pei et al. have shown that the fluorinated-BDOPV polymer films deposited from less-aggregated, high-temperature solutions exhibit less structural disorders and higher electron mobilities (by up to 2 orders of magnitude) in OFETs compared to those from highly aggregated solutions at low temperature.[281] The authors claim that this is due to disordered packing within the aggregates which can be inherited into the film at low temperature, resulting in structural disorder in the solid-state. However, high temperature can partially break these disordered aggregates and enable polymer chains to pack into ordered structures with thermally assisted molecular motions, which further leads to higher crystallinity and lower lattice disorder in films. Moreover, our recent work on PII2T has suggested the amorphous solution aggregates, compared with semicrystalline ones, counterintuitively lead to significantly improved alignment and reduced paracrystalline disorder in solid-state.[16] The underlying mechanism will be discussed in detail later.

The aforementioned controversy around the effect of solution aggregation hints at the importance of the exact nature of polymer aggregate structures in the solution-state. Indeed, several groups have obtained fine-tuned polymer aggregate structures and have found that certain types of aggregates are more favorable than the others. Using a combination of MD simulations, UV−vis, and PL spectroscopy, Li and Janssen et al. have identified two semicrystalline solution aggregates (β_1 and β_2) of an DPP based conjugated polymer when changing the solvent quality.[87] Compared to β_1, the β_2 aggregates are featured by the appearance of an additional absorption peak at longer wavelengths and a reduced $\pi-\pi$ stacking distance. Both phases can be inherited into thin films upon spin coating and β_2 gives rise to a higher mobility in OFETs and an enhanced *EQE* in OSCs compared to β_1, which is ascribed to the closer backbone stacking. Similarly, by tuning the solvent quality, Zheng and Pei et al. have revealed that BDOPV-2T forms 1D semirigid and 2D lamellar aggregate structures when dissolved in a good DCB and a poor toluene solvent, respectively, whereas an intermediate state between those two structures is found in the mixture of toluene and DCB.[19] Notably, upon film deposition, the intermediate-state aggregates render a higher OFET mobility compared to the other two types of aggregates. The authors attribute this result to the favorable tie chains present in the intermediate states, providing enough domain connectivity necessary for efficient charge transport. In contrast, a lack of tie chains between 1D semirigid aggregates and the presence of large grain boundaries among 2D aggregates result in lower OFET mobilities. Moreover, Xi and Pozzo et al. have found the polarity of nonsolvent added to DPPDTT/chloroform solution can also result in different types of aggregation−adding polar nonsolvent such as methanol induces formation of 1-D nanoribbon aggregates whereas nonpolar solvent like *n*-hexane promotes the formation of aggregates with irregular and amorphous shape.[271] An enhancement of OFET mobility resulting from polar nonsolvent addition is observed.

Except for solvent quality, the solvent selectivity toward backbone versus side chain can also be leveraged to tune aggregate structures in solution. Bridges and Segalman et al. have shown that the ordered aggregates of a cyclopentadithiophene-*alt*-thiadiazolopyridine-based polymer CDTPT can form in a side-chain-selective solvent like hexane.[209] The increased length and branching of side chains renders enough solubility in hexane and amphiphilicity for those ordered aggregates developing into lyotropic liquid crystalline phase at high solution concentrations. In contrast, mutual solvents like chlorobenzene and toluene only give rise to disordered aggregates which are not capable of forming LC phase even at elevated concentrations. As a result, polymers traversing the LC phase develop a higher crystallinity compared to those from isotropic phase, which further leads to an increase in OFET mobility. By modulating solvent selectivity and temperature, our recent work has systematically tuned the aggregate structures of PII2T into side-chain-associated amorphous aggregates in a backbone-selective solvent, 1-chloronapthalene, semicrystalline helical fiber aggregates in a mutual-selective solvent DCB with both side chain and backbone stacking, and backbone-stacked agglomerates in a side-chain-selective solvent decane.[16] Surprisingly, we have found that, compared to semicrystalline aggregates, the amorphous aggregates in 1-chloronapthalene lead to a higher degree of alignment and reduced paracrystalline disorder in solution printed films, giving rise to enhanced OFET mobility. The mechanism underpinning this counterintuitive result involves the ability of amorphous aggregates to crystallize into aligned films under the influence of directional convective mass transport induced by capillary flow during printing.[293] In contrast, DCB and decane give rise to chiral LC- and agglomerates-mediated assembly pathways and further lead to twined and isotropic film morphology, respectively. This work highlights the importance of investigating the evolution of solution aggregates in various assembly pathways, which we shall discuss in detail in section 2.3.

In Figure 15, we summarize possible solution primary aggregate structures categorized based on their dimensionality. One-dimensional (1-D) aggregates is the most ubiquitous type owing to the inherent 1-D geometric characteristic of polymer chains. We note the several terminologies for 1-D solution aggregates, including (nano)fibers,[16,19,62,241,294−298] (nano)-ribbons,[258] (nano)rods,[249,270] (nano)whiskers,[299] parallele-piped fibers[271,297] or rods[249] etc., are often used across references. We group these aggregates and unify the terminology as "1-D fiber-like aggregates"; this group can be further partitioned into parallelepiped fibers (i.e., ribbons) (Figure 15a−c) and cylindrical fibers (Figure 15d,e) based on the shape of the fiber cross-section. P3HT has been shown to readily form 1-D fiber aggregates in solution, which can be triggered by poor solvent addition,[14,55,248,249,269,270,291] solution aging,[250,251,282] solution temperature,[273,274] ultrasonication,[270,292] UV irradiation,[56,250] etc. Pozzo and co-workers have investigated the primary P3HT 1-D fiber aggregate structures using SANS and ultrasmall-angle neutron scattering (USANS) in various aromatic solvents.[297,298] The scattering signal from 1-D fiber aggregates in *p*-xylene, toluene, and benzene solutions is best fitted with a parallelepiped form factor, revealing a (near-)rectangular fiber cross section 21−25 nm in width and 5−6 nm in thickness. Later Keum and Hensley et al. have used the same model for P3HT aggregates in chloroform/hexane mixtures.[249] Interestingly, they obtain a similar cross-sectional size of 22.2 × 5.2 nm^2, despite the difference in solvent environment, concentration and molecular weight. The authors also claim that the 22.2 nm width is close to the backbone length (26.4 nm) of fully extended P3HT in their work, also the 5.2 nm thickness is about triple of the lateral width of P3HT monomer (1.8 nm) with fully extended hexyl side chains. Therefore, they propose an internal packing structure of the aggregates where the orthorhombic fiber long axis is parallel to the direction of backbone $\pi-\pi$ stacking (Figure 15a). The authors also argue

https://doi.org/10.1021/acs.chemrev.2c00905
Chem. Rev. 2023, 123, 8395−8487

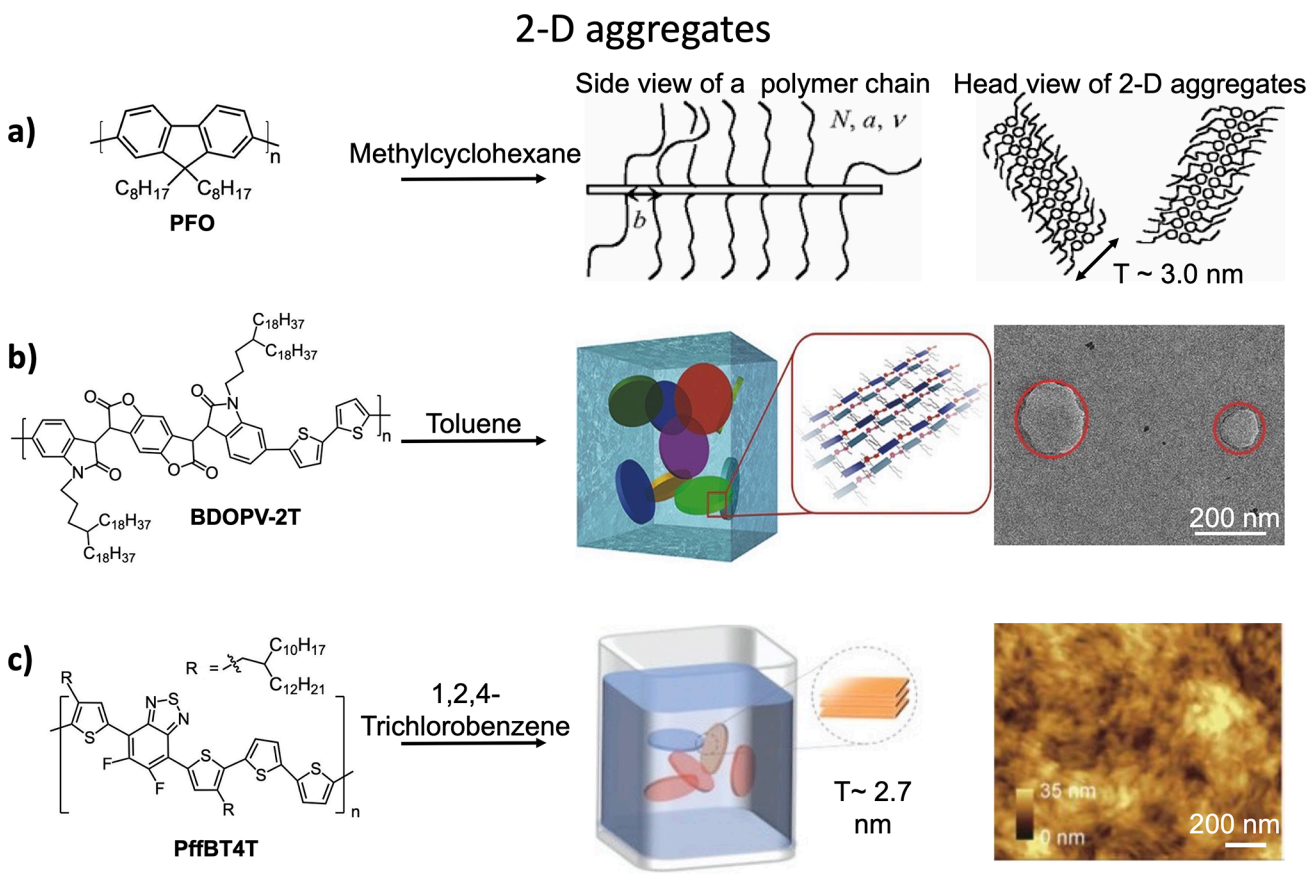

Figure 16. Summary of suggested 2-D aggregate structures of conjugated polymers. a) PFO 2-D aggregates and its schematic representations. b) BDOPV-2T 2-D aggregates and its schematic representations with TEM images on freeze-dried samples. c) PffBT4T 2-D aggregates and its schematic representations with AFM images on films spin coated from TCB solutions. Figure reproduced with permission from ref 304, Copyright 2008 American Physical Society (a); ref 19, Copyright 2017 John Wiley and Sons (b); ref 62, Copyright 2022 John Wiley and Sons (c).

that although backbones are π-stacked in an ordered fashion, the side chains are presumably in a disordered state since hexane is a good solvent for the side chains. A similar orthorhombic fiber structure has been proposed for 1-D aggregates of DPPDTT in DCB by Liu and Wang et al.[258] (Figure 15b), a cross section 33−40 nm in width and 8 nm in thickness is obtained by fitting the SANS data using a parallelepiped form factor. In this case, the polymer backbone direction is also proposed to be perpendicular to the fiber growth direction. Xi and Pozzo have also used the parallelepiped model for the same DPPDTT polymer in chloroform/methanol mixed solvents.[271] The side chain ordering along lamellar direction, however, remains unclear for DPPDTT aggregates, as a high-q structure factor peak (usually attributed to lamellar stacking[241,246]) is absent in the scattering profiles. The parallelepiped fibers long axis can also be parallel to the polymer backbone direction as demonstrated in the case of PffBT4T which is high-performance polymer used in both OFETs and OSCs.[62,300] Using a combination of AFM, TEM, and DLS techniques, Cao and Gu et al. have shown that, when dissolved in DCB, PffBT4T polymers readily aggregate into 1-D primary structures with an anisotropic cross section of 2−3 nm in thickness and 24 or 35 nm in width depending on the side chain length (Figure 15c).[300] Using solution SANS technique, Deng and Li et al. have also revealed the PffBT4T 1-D fiber-like aggregates formed in CF solution, although detailed internal packing structure is not provided.[62] Conjugated polymers can also form cylindrical fiber aggregates with roughly circular cross sections. Our investigation on PII-2T fiber aggregates (Figure 15d) reveals an isotropic cross-sectional shape, evidenced by a similar magnitude between fiber width and thickness measured by AFM on samples freeze-dried from solution.[241] A semiflexible cylinder model is therefore used to fit the solution SAXS profiles.[16,241,295] The fiber diameter is around tens of nanometers depending on the molecular weight and solvent selection.[16,241,295] In contrast to molecular packing within P3HT or DPPDTT fiber aggregates, the $\pi-\pi$ stacking of PII2T is, on average, perpendicular to the long axis of the fiber aggregates (Figure 15d). In other words, the fiber growth direction is along the polymer chain. We further elucidate that backbones adopt a helical conformation and stack in a staggered fashion, which is responsible for the emergence of chirality at high concentrations (discussed in detail later). Besides, lamellar stacking among side chains is also present within the fiber aggregates, validated by a structure factor peak at $q \approx 0.25$ Å in SAXS profiles.[241,295] Those helical 1-D aggregates are found in solvents mutually dissolving polymer backbone and side chains, such as chlorobenzene, DCB and chloroform.[16,241,295] As discussed earlier, when dissolved in a side-chain-selective solvent decane, PII-2T forms another type of 1-D fiber aggregates ($D \approx 100$ nm) where polymers are strongly aggregated only through backbone $\pi-\pi$ stacking. The lack of lamellar ordering is evidenced by the absence of SAXS structure factor peak and is resultant from the solvent affinity toward side chains. Using a similar set of characterization techniques, we have recently revealed that an OSC donor polymer PM7 aggregates into 1-D fiber aggregates when dissolved in

https://doi.org/10.1021/acs.chemrev.2c00905
Chem. Rev. 2023, 123, 8395−8487

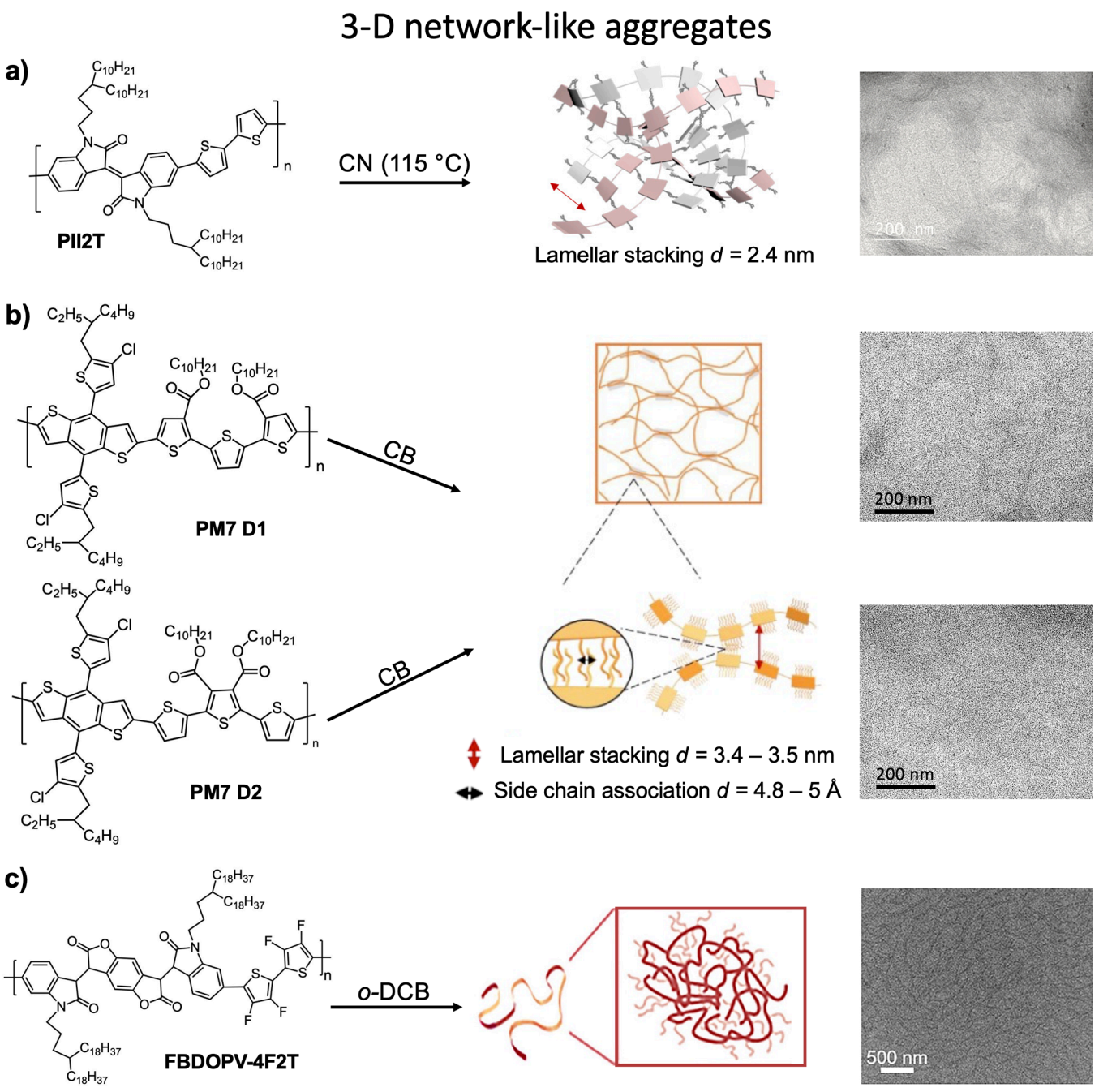

Figure 17. Summary of 3-D network-like aggregates of conjugated polymers. Chemical structures, schematic representations, and TEM images on freeze-dried samples of a) PII2T, b) PM7 D1 and D2, and c) FBDOPV-4F2T. Figure reproduced with permission from ref 16, Copyright 2022 John Wiley and Sons (a); ref 301, Copyright 2023 American Chemical Society (b); ref 259, Copyright 2021 John Wiley and Sons (c).

chlorobenzene solution (Figure 15e).[301] The fiber diameter is around 20 nm as revealed by AFM imaging and fitting of solution SAXS profiles using a semiflexible cylinder model. Polymers within the fiber aggregates are packed through both backbone $\pi-\pi$ stacking along the short axis (corresponding to d_π = 3.65 Å) and ordered lamellar stacking along the long axis (d_{lamellar} = 3.8 nm) obtained from solution wide-angle X-ray scattering (WAXS) and SAXS profiles, respectively. 1-D fiber aggregates have also been discovered in other polymer systems, including PBTTT,[296] P(NDI2OD-T2),[302] BDOPV-2T,[19] DPP-based polymer PDPP-TVT[245] and PDPP4T-HD,[87,268] although without determined internal structures and defined cross-sectional shape.

Besides the ubiquitous 1-D fiber-like aggregates, several studies have suggested the possibility of forming 2-D aggregates in solution.[19,62,303,304] Knaapila and Monkman et al. have demonstrated that polyfluorene-based conjugated polymers aggregate into 2-D structures in solution.[303,304] For example, when dissolved in methylcyclohexane, a poly[9,9-dioctyl-fluorene-2,7-diyl] (PFO) polymer can form 2-D nanosheets, which is inferred from a Porod exponent of 2 in solution SANS profile.[303] The nanosheets have a thickness around 3 nm which corresponds to the thickness of 2−3 polymer chains (Figure 16a). As mentioned earlier, Zheng and Pei et al. have also found BDOPV-2T polymer chains aggregate into 2-D lamella-like structures in toluene solution, mainly supported by a SANS

https://doi.org/10.1021/acs.chemrev.2c00905
Chem. Rev. 2023, 123, 8395−8487

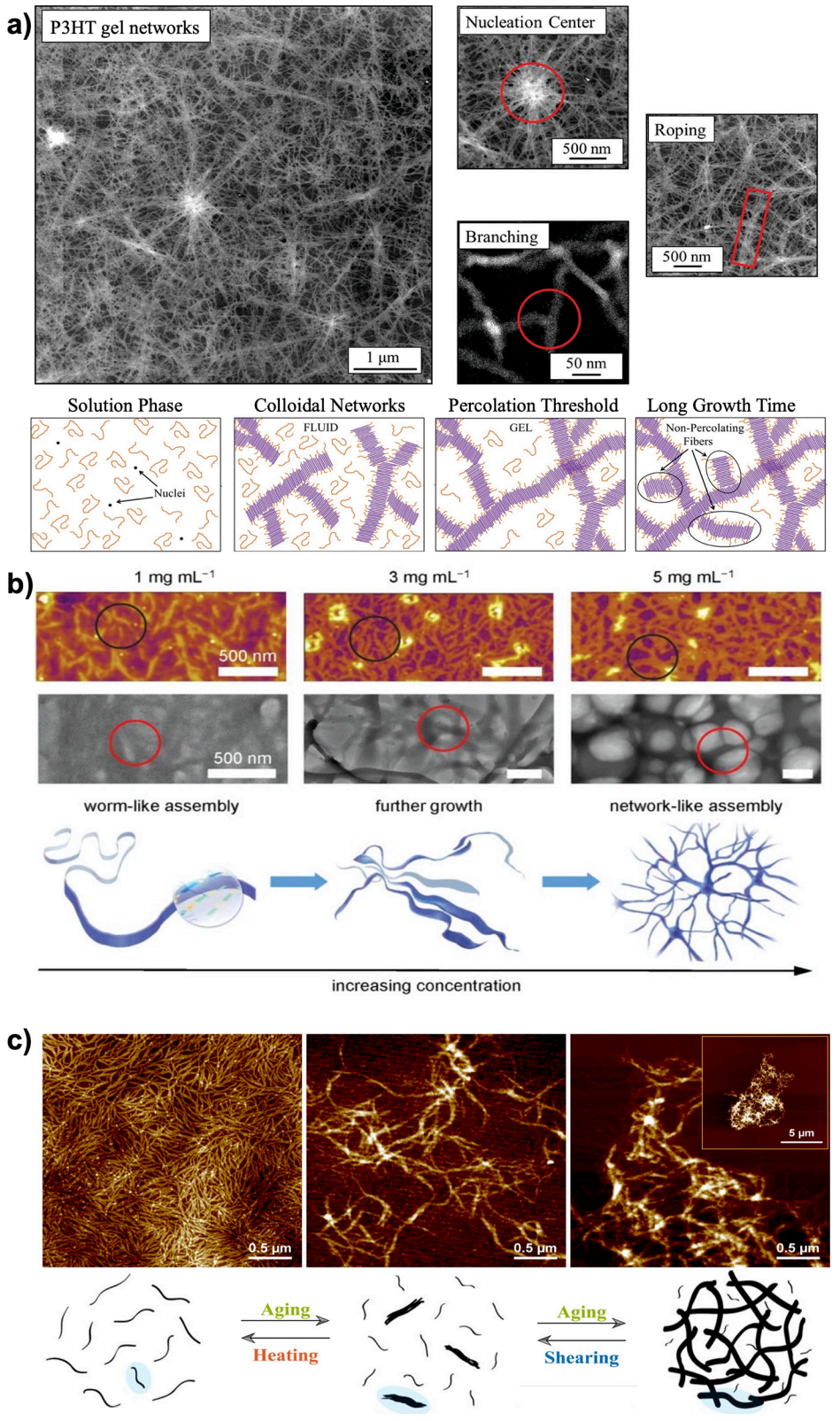

Figure 18. Formation of secondary network-like structures of conjugated polymers. a) STEM images (top) of P3HT gel networks with features including nucleation centers, fibrillar roping and branching. Schematic (bottom) of gelation mechanism for P3HT in aromatic solvents. b) AFM height images (top), TEM images (middle) of F_4BDOPV-2T assemblies obtained by freeze-drying from chloroform solutions with concentrations of 1, 3, and 5 mg/mL. Schematic (bottom) of development of network-mediated assembly with concentration. c) AFM height images (top) of solid-state films by spin coating DPPDTT/DCB solution (0.05 mg/mL) after aging at 25 °C for 2, 30, and 53 h. Schematic illustration (bottom) of the solution-state assembly. Figure reproduced with permission from ref 306, Copyright 2012 American Chemical Society (a); ref 309, Copyright 2019 John Wiley and Sons (b); ref 258, Copyright 2020 American Chemical Society (c).

https://doi.org/10.1021/acs.chemrev.2c00905
Chem. Rev. 2023, 123, 8395−8487

Porod exponent of 2.22 (indicating a dimensionality close to 2) and plate-like objects observed in TEM imaging of freeze-dried samples (Figure 16b).[19] The authors propose that polymer chains within the aggregates adopt a coiled conformation and interact with each other through $\pi-\pi$ stacking. Recently, Deng and Li et al. have also proposed a similar 2-D lamellar structure for PffBT4T-2DT in 1,2,4-trichlorobenzene (TCB) solution, based on a Porod exponent close to 2 (2.56 at 25 °C and 2.10 at 50 °C) found in SANS profiles.[62] The 2-D layer has a thickness around 2.7 nm obtained from SANS fitting (Figure 16c). It is worth noting that none of those studies give a detailed internal packing structures within those 2-D aggregates. Besides, a Porod exponent between 2 and 3 can also be ascribed to the fractal dimension of isotropic network-like aggregates instead of a 2-D sheets. For example, Yi and Hua have suggested that PBTTT forms isotropic aggregates in chlorobenzene solution and gives rise to a Porod exponent of 2.23 and 2.43 at 0.9 and 1.2 mg/mL, respectively.[294] Further, SANS fitting is proceeded based on the assumption that only one population is present in the solution, which omits the possibility that scattering contribution may come from more than one species (e.g., dissolved chain and primary aggregates). In that case, deconvolution may be needed to reveal the true Porod decay exponent.

3-D isotropic network-like aggregates composed of randomly oriented polymer chains is another type of primary solution aggregates. As mentioned earlier, our recent work has shown that PII2T can form 3-D network-like aggregates when dissolved in backbone-selective solvent 1-chloronapthalene at high temperature (115 °C), revealed by TEM imaging (Figure 17a) and SAXS fitting that returns a power law with an exponent of 3.1 at low q.[16] Meanwhile, a blue-shifted, featureless low-energy absorption peak centered at ca. 640 nm indicates that the backbone adopts a coiled conformation. Further, a lamellar stacking structure factor peak present at high q in the SAXS profile suggests that those coiled backbones are linked by side chain association (Figure 17a); the absence of a π-stacking peak in electron diffraction proves that coiled backbones are free from ordered stacking. We have also found two donor polymers used in OSCs (PM7 D1 and D2) form network-like primary aggregates in chlorobenzene (Figure 17b).[301] The formation of network-like structures is revealed by AFM phase imaging of the freeze-dried samples and is further supported by a Porod region with slopes between −2 and −3. Electron diffraction and SAXS measurements reveal that both alkyl chain stacking (d_{alkyl} = 4.8−5 Å) and lamellar ($d_{lamellar}$ = 3.4−3.5 nm) stacking are present within the network-like aggregates. Wang and Pei et al. have proposed that the FBDOPV-4F2T polymer in DCB forms network-like aggregates composed of coiled polymer chains (Figure 17c).[259] This is inferred from the Porod exponent of 2.07 in SANS which is ascribed to the fractal dimension of the network and is further demonstrated by imaging the freeze-dried samples. The SANS data are then fitted with a combined model involving a semiflexible cylinder form factor plus a fractal model. Besides these network-like aggregates in which the primary building units are single polymer chains, network-like aggregates can also be composed of primarily aggregated 1-D fibers, which we term as secondary aggregate structures which will be discussed in detail in Section 2.3.

2.2.3. Characterization of Primary Solution-State Aggregate Structures. Structural characterization of solution aggregates often relies on both reciprocal-space scattering and real-space imaging. SANS/SAXS can be used to extract structural parameters of solution aggregates once a proper fitting model is applied. For example, semiflexible cylinder or parallelepiped model is often used to fit 1-D fiber aggregates,[16,241,249,258,271,297−299] and sometimes another semiflexible cylinder model is needed to account for scattering contribution from dissolved polymer chains mainly at high-q region.[16,241,297,298] Parameters such as radius (or width and thickness), persistence length, contour length of the dispersed polymer chains and fiber aggregates can be extracted if captured within the accessible q range. However, the typical lowest q accessible in SANS/SAXS measurement is around 3×10^{-3} Å, which makes it challenging to characterize large-length-scale features. For examples, the fiber length is usually out of the q range and not captured during SANS/SAXS fitting,[241,249,258] and the Guinier knee corresponding to the semiflexible cylinder radius moves below 0.003 Å if the radius is larger than 60 nm.[241] USANS/ultrasmall angle X-ray scattering (USAXS) or SLS techniques can serve as complementary tools to extend the q-range. For examples, Pozzo group has extended the lowest accessible q to 4×10^{-5} Å using USANS and Hua group has extended it to 8×10^{-4} Å with SLS.[294,297] Complementary to reciprocal-space scattering, real-space imaging on freeze-dried samples can provide direct visualization of aggregated structures.[16,19,241] The freeze-drying process often involves solution freezing in either liquid propane-ethane mixture or liquid nitrogen and subsequent sublimation of solvent under vacuum, which may result in further aggregation of the polymer during the process.[19] Therefore, in situ microscopy technique such as liquid-phase TEM can be further explored to better visualize the solution-state structures.[305]

2.3. Secondary Solution-State Structures

The aforementioned studies have surmised the important role of solution aggregates in improving optoelectronic performance, and some of them have provided detailed structural information on distinct aggregates. However, the structural evolution of primary solution aggregates during evaporative solution processing has been frequently overlooked. It is usually the secondary aggregates, rather than the primary ones, that directly template the microstructures in final thin films by defining the assembly pathways. In this section, we review several works that investigate the secondary aggregate structures that emerge during solution assembly.

2.3.1. Secondary Networks. One of the commonly observed secondary structures is the network-like assembly of 1-D fiber-like primary aggregates.[258,298,306−309] P3HT is known to form gels where primary fibers split and branch to form interconnected networks.[298,306−308] Pozzo group has systematically studied the gelation mechanism of P3HT solutions using a combination of (U)SANS, sTEM, rheology, and conductivity measurements.[298,306] As shown in Figure 18a, upon cooling of a concentrated P3HT solution, the dissolved polymer chains first aggregate into primary fiber aggregates from nucleation sites. The dispersed 1-D fiber further grows with time and then reaches the percolation threshold to form gels. Longer growth time allows further development with the newly emerged fibers which may contribute differently to the developing gel properties such as elasticity and conductivity. They have also demonstrated that the nanoscale fiber structure is relatively constant and insensitive to solvent or concentration. For example, the fiber has cross-sectional thickness (i.e., height) of *ca.* 5−6 nm with width of ca. 21−25 nm, which is stable in various organic solvents over a 5−50 mg/mL concentration range. They have proposed that as the cross-sectional dimension

https://doi.org/10.1021/acs.chemrev.2c00905
Chem. Rev. 2023, 123, 8395−8487

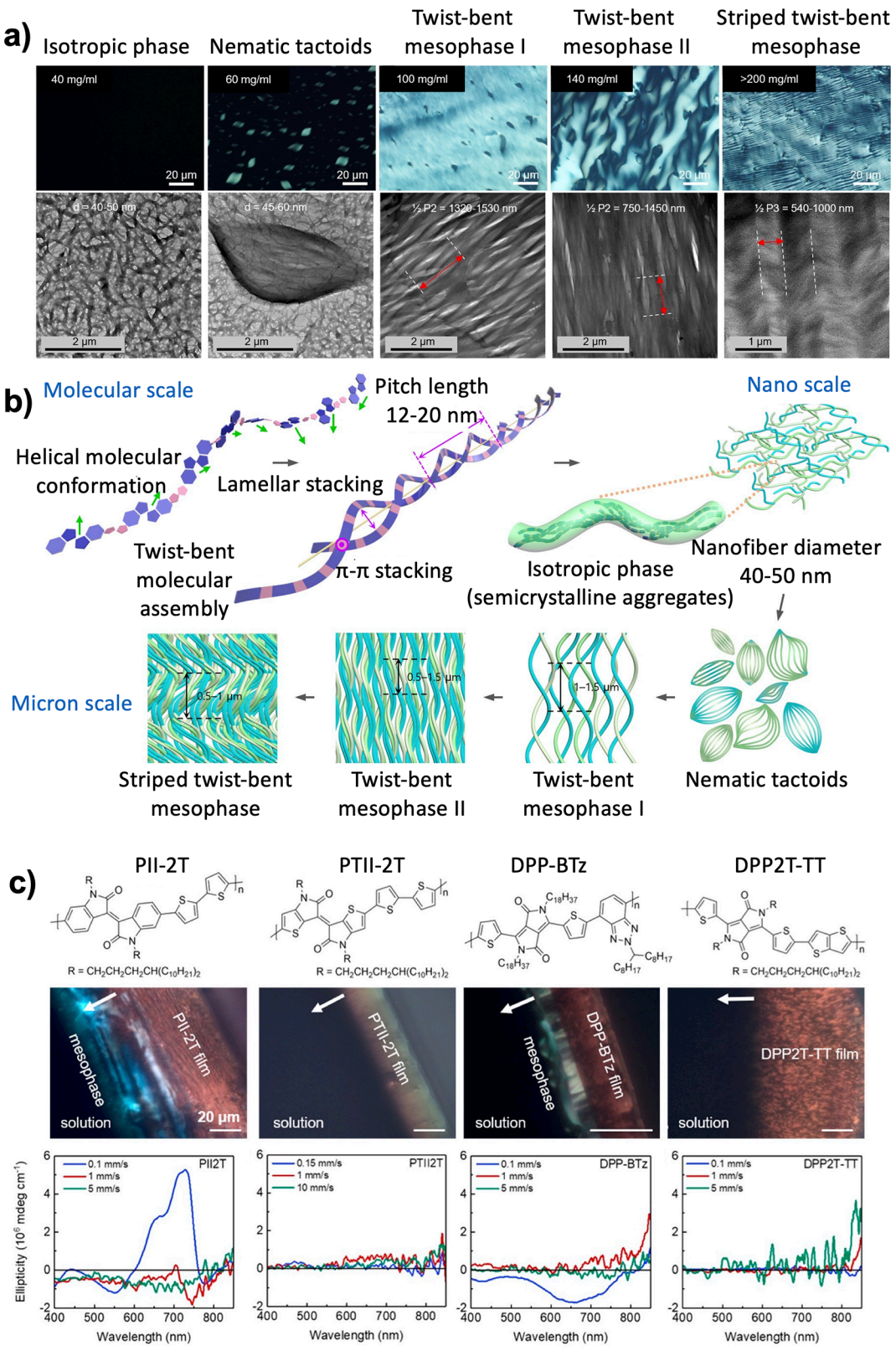

Figure 19. Chiral twist-bent mesophase-mediated assembly of PII-2T and its control by molecular engineering, printing flow, and solvent selectivity. a) CPOM (top) and TEM (images) of PII-2T solutions at various concentrations. The half-pitch length of the helical fibers is marked with red arrows. b) Schematic illustration of proposed chiral emergence in multistep hierarchical assembly of achiral conjugated polymers. c) Molecular structures of two pairs of twisted polymers (PII-2T and DPP-BTz) and the planar counterparts (PTII-2T and DPP2T-TT) (top). CPOM images of the solution- to solid-state transition of four polymers in a receding meniscus driven by solvent evaporation (middle). CD spectra of polymer films coated from different printing regimes (bottom). Figure reproduced with permission from ref 295, Copyright 2022 Springer Nature (a, b); ref 83, Copyright 2019 American Association for the Advancement of Science (c).

https://doi.org/10.1021/acs.chemrev.2c00905
Chem. Rev. 2023, 123, 8395−8487

is always smaller than the maximum exciton diffusion length (~20 nm), most excitons generated within the gel fibers would effectively dissociate into electrons and holes and be effectively conducted to the corresponding electrodes. This optimal size for exciton diffusion, together with the high specific surface area and ample void space for backfilling with small molecule n-type semiconductors, makes P3HT networks promising for application like OSCs. Yao, Lei, and Pei et al. have investigated the multiscale assembly process of F4BDOPV-2T and achieved wafer-scale fabrication by taking advantage of the secondary network aggregates.[309] As shown in Figure 18b, the polymer first aggregates into 1-D worm-like structures through $\pi-\pi$ interaction driven by using a poor solvent. These primary aggregate structures grow with concentration and eventually form a network-like secondary structure during evaporative assembly. This is evidenced by solution SANS along with TEM imaging on samples freeze-dried at various concentrations. This fiber network-mediated assembly pathway allows fabrication of large-area monolayer films of n-type F4BDOPV-2T with interconnected fibers which provides significantly high electron mobilities up to 1.88 $cm^2 V^{-1} s^{-1}$. The DPPDTT parallelepiped fibers mentioned earlier also tend to interconnect and form micrometer-sized secondary networks with solution aging (Figure 18c). With further aging or increasing concentration, the networks attain percolation and become nonflowing gels. This gelation process can be reversed by shearing or solution heating. It should be noted that these secondary structures are induced by cooling, aging, or concentrating the dilute ink solutions. In some cases, polymers readily aggregate into fiber networks even at low concentration without any solution treatments. For example, PII2T agglomerates in decane can be understood as secondary networks composed of randomly oriented 1-D fibers, which exist in very dilute conditions down to 0.1 mg/mL.[16] As another example, PBTTT in toluene has been suggested to form secondary network aggregates composed of primary 1-D rod-like aggregated species (~10 nm in length; aspect ratio ~2), which can happen at concentrations below 1 mg/mL.[294]

2.3.2. Lyotropic Liquid Crystalline Phases. Another commonly observed solution-state secondary structure for conjugated polymers is LC mesophases. LC represents mesomorphic states of matter, where molecules maintain both the fluidity of liquid and the crystallinity of solids. LCs can be classified into two main categories: thermotropic and lyotropic LCs. Thermotropic LC mesophases appear within a certain temperature range, whereas the phase behaviors of lyotropic LCs are governed by both temperature and concentration of molecules in a solvent. The stiffness of semiflexible conjugated polymers renders a tendency toward thermotropic ordering when heated above the mesophase transition temperature. The early discovery of thermotropic LC phases of conjugated polymers starts in the 1990s, focusing mainly on the second generation conjugated polymers including PPVs,[310] polyfluorenes,[311−314] and poly(1,4-phenylene-2,5-thiophenes).[315] These early studies, however, mainly aim to investigate the mesophase structure−photophysical properties.[311−314] The exerted influence of LC mesophases on thin-film microstructures and charge-transport properties remains unclear until Sirringhaus and coworkers publish their pioneer work in 2000.[316] By annealing the film of fluorene/bithiophene copolymer F8T2 in the LC phase on a rubbed substrate, they obtain a high degree of uniaxial alignment of the polymer chains along the rubbing direction, which further enhances the charge carrier mobility in transistor devices. Since then, designing and annealing thermotropic liquid crystalline conjugated polymers serves as a common practice to improve structural order and enhance charge carrier mobility.[316−321] Theoretical investigations have also been conducted to examine the ordering of chains within LC mesophases.[322−324] It is typically observed that the organized assembly and high crystallinity can be facilitated in the LC phase and retained during the subsequent crystallization upon cooling to room temperature.[320] Formation of lyotropic LC phases, on the other hand, is facilitated by both the stiffness and amphiphilicity (imparted by chemical dissimilarity of the backbone and the side chain[209]) of the conjugated polymers when dissolved in an appropriate organic solvent. It has been suggested that the formation of lyotropic mesophases requires a balanced $\pi-\pi$ interaction among the backbones and van der Waals forces among the side chains.[209,217,286] A wide range of conjugated polymers have been shown to exhibit lyotropic ordering in solution, spanning from first generation conjugated polymer polydiacetylene,[325] to later second generation polymers including polyfluorene,[304] PPV,[326,327] PPP,[203] P3AT,[328−330] and poly(*p*-phenyleneethylene) (PPE),[326,331,332] and to modern third generation D−A polymers such as PII2T,[16,83,295] P(NDI2OD-T2),[302,333] CDTPT,[209,226] cyclopentadithiophene-benzothiadiazole-based copolymer (CDTBTZ-C16),[334] and DPP/benzotriazole-based polymer DPP-BTz.[335] More importantly, lyotropic LCs are of direct relevance to evaporative assembly wherein polymers traverse the entire concentration regime necessary for mesophase formation. Given the sensitivity of LC phase to the external field such as shear flow and its role in lowering free energy barrier to crystallization, it is promising to obtain long-range order and high crystallinity from lyotropic LCs.[217,302,326,336,337] Indeed, several recent works have suggested that a lyotropic LC mediated assembly pathway can significantly improve in-plane alignment,[217,286,302,336] enhance the film crystallinity and boost the device performance of thin films.[208,209,226] We refer readers to our recent reviews on understanding and controlling lyotropic LC-mediated assembly pathways and their influence on solid-state morphology and electronic properties.[293]

While the critical role of LC phase on molecular orientation, alignment, and crystallization has been demonstrated, there is a lack of detailed structural characterization in those LC phases, which hinders a fundamental understanding of the LC-mediated assembly pathway and its tunability. Our group has recently discovered a lyotropic, chiral twist-bent nematic (N_{tb}) phase from an achiral conjugated polymer PII2T with relatively torsional backbone conformation.[295] Combining in situ and ex-situ optical and electron microscopy, X-ray scattering techniques, together with molecular dynamic simulations, we reveal that this N_{tb} phase features a hierarchical helical structure which is developed through a multistep assembly pathway (Figure 19a,b). Wavy helical polymer chains first aggregate into helical nanofibers in a staggered fashion, constituting the isotropic phase at relatively low concentrations (<50 mg/mL). Further increasing concentration triggers the emergence of an LC phase as spindle-like nematic tactoids surrounded by an isotropic phase. At ~ 100 mg/mL, those tactoids tend to merge into a coherent mesophase domain of aligned, twisted fibers exhibiting a half-pitch length of 1.3−1.5 μm at micron scales, which concomitantly shows emergence of chirality. At ~140 mg/mL, those fibers become thicker, and their packing gets denser, giving rise to a reduced half-pitch length of 0.7−1.4 μm. Increasing concentration further to 200 mg/mL results in a

https://doi.org/10.1021/acs.chemrev.2c00905
Chem. Rev. 2023, 123, 8395−8487

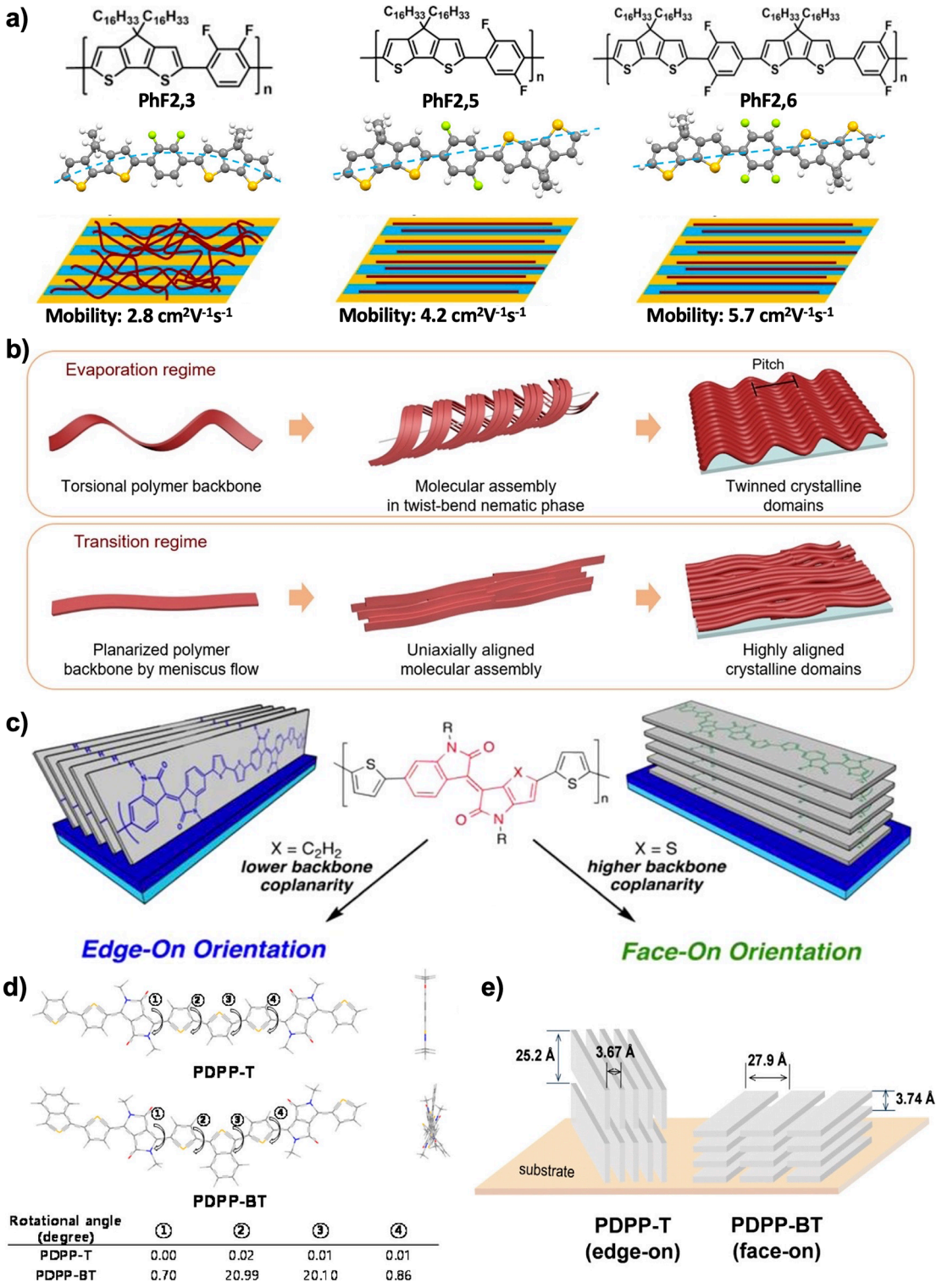

Figure 20. Impact of chain conformation on film alignment and molecular orientation. a) Chemical structures (top), molecular structures determined by single crystal X-ray diffraction on small molecule analogues (middle), and schematic representation of chain alignment and highest OFET mobility for PhF2,3, PhF2,5, and PhF2,6 polymers. b) Schematic illustration of the inferred flow-controlled chain planarity of PII2T and resultant assembly and crystalline domain alignment. c) Schematic illustration for the effect of chain planarity on molecular orientation for isoindigo-based polymers. d) Optimized molecular configuration for PDPP-T and PDPP-BT. e) Schematic representation of crystalline packing structures of PDD-T and PDPP-BT revealed by 2D GIWAXS. Figure reproduced with permission from ref 206, Copyright 2017 American Chemical Society (a); ref 83, Copyright 2019 American Association for the Advancement of Science (b); ref 343, Copyright 2013 American Chemical Society (c); ref 346, Copyright 2017 American Chemical Society (d, e).

zigzag twinned morphology with a domain width of 0.5−1 μm. In addition to the helicity at micron scales, we further demonstrate the existence of molecular and nano scale helicity using MD simulations and high-resolution transmission electron

https://doi.org/10.1021/acs.chemrev.2c00905
Chem. Rev. 2023, 123, 8395−8487

microscopy, respectively. With detailed structural characterizations on this chiral LC-mediated assembly pathway with hierarchical helical structures, we further explore its tunability by printing flow, molecular engineering, and solvent environment.[16,83] When printed in the evaporation regime in meniscus-guided solution coating, the N_{tb} phase is readily observed through in situ cross polarized optical microscopy (CPOM) imaging of the receding meniscus (Figure 19c), and the developed twisted polymer/nanofibers can be inherited into resultant thin films, giving rise to relatively lower conjugation length and degree of alignment. However, increasing strain rates in the transition regime stretches out the twisted chains and thus eliminates the N_{tb} phase, resulting in highly planar chain conformation and enhanced in-plane and out-of-plane alignment. Due to backbone planarization, a maximum 4-fold increase in the hole mobility is achieved compared to films printed in the evaporation regime mediated by the N_{tb} phase. Besides printing flow, the removal of N_{tb} phase can also be realized through molecular engineering to promote backbone planarity. As shown in Figure 19c, by comparing two pairs of twisted D−A conjugated polymers (PII-2T and DPP-BTz) and their planar counterparts (thieno-isoindigo-bithiophene-based polymer, PTII-2T, and diketopyrrolopyrrole-thienothiophene-based polymer, DPP2T-TT), we found the twisted backbone conformation is conducive to forming N_{tb} phase whereas planar conformation eliminates the mesophase, evidenced by the absence of LC phase in meniscus preceding the dried film for planar PTII-2T and DPP2T-TT. Further, the emergence of the lyotropic N_{tb} phase is sensitive to the solvent selectivity: the N_{tb} phase of PII-2T only forms in solvents (e.g., DCB, chlorobenzene, toluene) mutually dissolving backbone and side chains but is absent in solvents selective to either backbone (1-chloronapthalene) or side chains (decane).[16] We elucidate that the constituting nanofibers in LC phase only form in mutual solvents where a balanced backbone vs side chain interaction prevails. In contrast, the side chain selective solvents give rise to solution agglomerates with strongly packed chains through $\pi-\pi$ interactions, which is incapable of being disentangled or aligned under printing flow; backbone selective solvent leads to amorphous network aggregates linked by side chain association, which renders a direct crystallization pathway whereby growth of π-stacked crystals can be guided by the solution-coating process. As a result, distinct film morphologies are obtained by modulating the assembly pathway via solvent selectivity.

2.3.3. Characterization of Secondary Solution-State Structures. The reciprocal-space scattering and real-space imaging techniques for primary solution aggregates are still valid to probe the nanoscale structures within those secondary assembly. Besides, the secondary structures can be micrometers in size, which offers an opportunity to visualize through optical microscope. For example, CPOM serves as a powerful tool to investigate LC phases-mediated assembly pathways. The emergence of lyotropic LC phase can be readily observed under CPOM once the concentration surpasses a threshold value. Besides, LC phase may exhibit distinct textures under CPOM, such as the Schlieren textures from nematic phase[209] and stripe texture of N_{tb} phase,[295] which is informative to phase evolution driven by concentration increase during evaporative film printing. Besides, imaging (SEM, TEM, and AFM) on freeze-dried samples can provide nanoscale structural insights in the LC phases, such as the organization of fibril building blocks and resultant pitch in N_{tb} phase.[295] Circular dichroism (CD) spectroscopy is routinely used to test possible chiral assembly of conjugated polymer in solution and their chiroptical properties.[338] Moreover, various state-of-the-art in situ measurements have been developed for deciphering assembly pathways of organic electronics and organic photovoltaics. We refer the readers to the comprehensive review article by Richter, DeLongchamp, and Amassian.[339]

2.4. Impact of Conformation, Primary, and Secondary Aggregate Structures on Film Morphology

This section focuses on understanding of how film morphology depends on polymer solution-state conformation, primary aggregates, and secondary aggregate structures in solution. Specifically, we focus our discussion on the degree of alignment, crystallinity, and molecular orientation in the solid-state of direct relevance to charge and exciton transport in horizontal and vertical devices such as transistors and solar cells. Recent advances have showcased strong correlations between solution-state structures and film morphology, which highlights the importance of understanding and controlling the solution-state structures mentioned above.

2.4.1. Role of Molecular Conformation. It has been suggested that a planar and linear polymer backbone conformation is conducive to improving the solid-state chain alignment. For example, Wang and Bazan have reported a significant impact of backbone linearity of clopentadithiophene-difluorophenylene copolymers on their self-assembly and chain alignment on nanogrooved (NG) substrates (Figure 20a).[206] Chain linearity is tuned by the different placement of fluorine atoms on the phenylene structural units, resulting in different arrangements of F···H noncovalent interactions in model compounds PhF2,3, PhF2,5, and PhF2,6. As revealed by single crystal X-ray diffraction from small molecule analogues, for the PhF2,3 molecule, the F···H interactions between the DFPh core and the CDT units render a pseudo cis conformation where the methyl groups of two CDT units point toward the same direction; for the PhF2,5 molecule, the F···H interactions cause the methyl groups of the two CDT units to point in opposite directions (pseudo trans); for the PhF2,6 molecule, the two CDT units are also in a pseudo trans conformation. The difference in cis vs trans conformation observed in small molecules can be further extrapolated to polymers as demonstrated by DFT calculations. Therefore, a more linear backbone is expected for PhF2,5 and PhF2,6, relative to PhF2,3. Intriguingly, the GIWAXS measurements on films deposited on NG substrates reveal that two linear polymers adopt a significantly higher degree of alignment than the curved polymer. The high degree of alignment in PhF2,5- and PhF2,6 films further give rise to enhanced OFET mobility up to 4.2 and 5.7 $cm^2 V^{-1} s^{-1}$, respectively, which are significantly higher than that of PhF2,3 (2.8 $cm^2 V^{-1} s^{-1}$) showing inferior degree of alignment. Except for linearity, our work on flow-induced chain planarization of PII2T has demonstrated that chain planarity is also crucially important for obtaining highly aligned thin-film morphology (Figure 20b).[83] As mentioned earlier, the N_{tb} phase assembled by helical polymer chains is readily inherited into thin films printed in the evaporation regime, resulting in poor alignment with twinned domains aligned parallel to the printing direction. Grazing incident X-ray diffraction (GIXD) measurements reveal a dichroic ratio (R_{GIXD}) of ~0.64 for films printed in the evaporation regime. However, the increased strain rate in the transition regime induces chain planarization, which further improves the fibril alignment along the chain direction evidenced by high R_{GIXD} reaching 11.4. Chen and Han et al.

https://doi.org/10.1021/acs.chemrev.2c00905
Chem. Rev. 2023, 123, 8395−8487

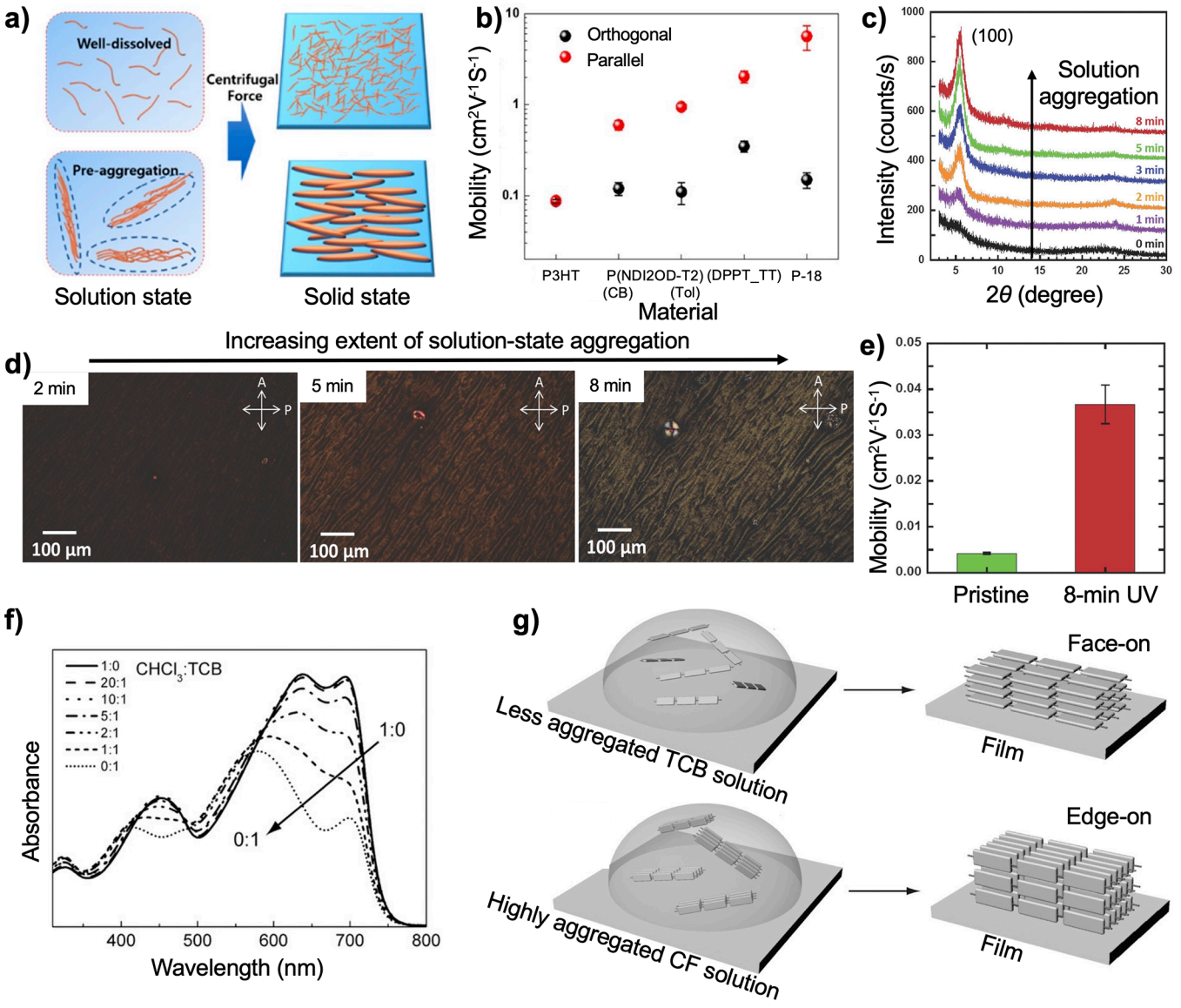

Figure 21. Effect of extent of aggregation on film alignment, crystallinity, and molecular orientation. a) Schematic illustration of well-dissolved and aggregated polymer in solution and solid-state. b) OFET mobility of various polymers when alignment direction is parallel (red) and perpendicular (black) to the transistor channel. c) Grazing incidence X-ray diffraction profiles of P3HT films obtained from the UV irradiated solutions. d) CPOM images of P3HT films spin coated on glass from P3HT/chloroform solutions UV irradiated for various times. e) OFET mobilities of P3HT pristine and UV-irradiated films. f) Evolution of absorption spectra of difluoroben-zothiadiazole-based polymer solution in mixed solvents of chloroform and TCB. g) Schematic illustration of the polymer molecular orientation that is modulated by aggregation in solution. Figure reproduced with permission from ref 12, Copyright 2015 American Chemical Society (a, b); ref 56, Copyright 2014 John Wiley and Sons (c–e); ref 18, Copyright 2016 John Wiley Sons (f, g).

have reported that the macroscopic alignment of IID-based conjugated polymers can be improved by planar conformation.[340] Among three model compounds with varied donor moieties including thieno-[3,2-*b*]thiophene (IID-TT), bithiophene (IIDDT), and benzodithiophene (IID-BDT), IID-TT shows the most coplanar conformation as evidenced by the theoretical calculations and the most red-shifted absorption onset in both solution- and solid-state. The IID-TT films obtained through solvent vapor enhanced drop-casting exhibit the highest degree of alignment evidenced by optical dichroic ratio of 2.08 higher than that of IIDDT (1.07) and IID-BDT (1.33).

The relationship between chain conformation and degree of crystallinity currently remains an open question for conjugated polymers. On one hand, it is intuitive that increasing the chain rigidity can potentially improve the intra- and intermolecular ordering and thus contribute to a high degree of crystallinity. For example, the highly crystalline PBTTT polymer with higher rigidity (l_p = 9 nm[53]) imparted by the fused thienothiophene unit shows a higher degree of crystallinity than the moderately crystalline parent polymer P3HT with a lower rigidity ($l_p \approx 3$ nm when regioregular[52]).[36] On the other hand, modern D–A polymers tend to be less crystalline than P3HT/PBTTT, despite the fact that they are typically featured by fused-ring, rigid building blocks and thus have more rigid conformation than thiophene-based polymers. For example, the IDTBT polymer is nearly amorphous regardless of its exceptionally high rigidity with l_p = 131 nm.[51] One plausible explanation is that a certain degree of conformational freedom is required to assist the chain

https://doi.org/10.1021/acs.chemrev.2c00905
Chem. Rev. 2023, 123, 8395–8487

segments in packing into crystallites and thus achieving high crystallinity.[51]

Currently, there is a controversy regarding the dependence of out-of-plane molecular orientation (i.e., face-on vs edge-on) within crystallites on molecular conformation: some works have demonstrated that a planar, linear conformation facilitates development of face-on molecular orientation,[341−343] whereas others have suggested the opposite.[344−346] For example, Chen and Fréchet et al. have observed an increased preference for edge-on orientation with improving chain planarity for IID-based conjugated polymers (Figure 20c).[343] The chain planarity is systematically improved by substituting thiophenes for phenyl rings within the IID unit, which is supported by DFT calculations and UV−vis absorption spectroscopy. GIXD measurements on spin coated films reveal that planar polymers favor face-on orientation whereas polymers with a twisted, helical backbone display a preference for edge-on packing. The authors argue that a face-on packing is energetically favored for a planar conformation due to the maximization of van der Waals interactions between the rigid π-conjugated backbone and substrate surface. The cofacial $\pi-\pi$ interchain interactions subsequently guide other chains to adopt a similar orientation during crystallization, eventually producing films comprising face-on oriented crystallites. In contrast, the twisted backbone precludes strong polymer−substrate interactions and thus experiences negligible energy benefit for adopting a face-on orientation. Therefore, the solution-state aggregates created by intermolecular $\pi-\pi$ and/or lamellar interactions may play a role in governing the molecular packing and giving rise to a preferentially edge-on orientation. Similarly, Lee and Yang have found an increase in face-on crystallite population with enhancing the chain planarity in D−A polymers containing thieno-benzo-isoindigo (TBIG) and IID acceptor units and a bithiophene donor.[341] The ratios of TBIG and IID units have been systematically tuned to vary the chain planarity, resulting in 4 polymers (PTBIG-100, PTBIG-75, PTBIG-50, and PTBIG-25). Using a combination of DFT calculations, UV−vis absorption spectroscopy, and GIXD measurements, the authors have revealed that an increase in TBIG unit fraction leads to improved chain planarity and stronger preference for edge-on orientation in spin coated films. Lee and Cho et al. have also found a planar, linear 9-bis(2-ethylhexyloxy)naphtho[1,2-b:5,6-b′]dithiophene (NDT)-based polymer PNDT adopts a preferentially face-on orientation, whereas its twisted, curved counterpart PBDT has a tendency to adopt an edge-on orientation.[342] There exist, however, several studies that contradict the observation that planar chain favors face-on orientation. For instance, Jeon and Kim et al. have found PDPP-T having a planar chain conformation exhibits an edge-on molecular orientation in spin coated films whereas its twisted counterpart PDPP-BT adopts a face-on assembly (Figure 20d,e).[346] This is consistent with conformation-molecular orientation relationship reported in two other works.[344,345] Based on the concentration-dependent solution-state absorption spectroscopy, the authors propose that the planar PDPP-T polymer readily aggregates as concentration increases during evaporative assembly, leading to edge-on orientation guided by solution aggregation; the lack of aggregation of PDPP-BT chains in solution is responsible for a preferential face-on orientation. This works has suggested that molecular conformation is not the sole factor that governs the molecular orientation. The solution-state primary aggregates or even secondary structures may exert significant influence on the packing orientation, which we shall discuss in detail below.

2.4.2. Role of Primary Solution-State Aggregates. Recent studies have reported that films fabricated from aggregated ink solutions often exhibit higher degree of alignment than those from dissolved solutions.[12,13,15,72] For instance, Kim and Noh et al. have printed several chemically diverse polymers using off-center spinning process and found that solution aggregation is a prerequisite for obtaining highly aligned film (Figure 21a).[12] Using a combination of AFM, GIXD, polarized UV−vis absorption, and polarized-charge modulation microscopy, they have concluded that the strong alignment of polymer chains occurs at the top film surface rather than in the bulk, which is critical to OFET devices. As shown in Figure 21b, the highly aligned feature gives rise to high charge transport anisotropy in films of solution-aggregated polymers such as P(NDI2OD-T2) and DPPT-TT. In contrast, P3HT films from molecularly dissolved chlorobenzene solution barely show any transport anisotropy due to poorly aligned morphology. Chu and Reichmanis et al. have demonstrated the macroscopic alignment of P3HT films can be significantly enhanced by aging-induced aggregation in corresponding ink solutions.[250] This is attributed to the reasoning that fiber aggregates significantly reduce tortuosity and entanglement effect of long polymer chains during blade coating process. Luzio and co-workers have also found, when cast from aggregated solution in toluene or mesitylene, P(NDI2OD-T2) films exhibit highly aligned, hundreds-of-micrometers-wide region with remarkable molecular orientational order.[13,333] Using bar coating, they have obtained a high degree of alignment in both bulk and top surface of the film, which is quantified by dichroic ratio of 7.7 and 4.8 obtained from bulk-sensitive GIWAXS and surface-sensitive NEXAFS measurements, respectively.[13] This further leads to significant charge transport anisotropy that electronic transport is more favorable along the fibril axis parallel to the bar-coating direction. Conversely, films fabricated from solutions in DCB, which is a less-aggregating solvent for P(NDI2OD-T2), barely show any alignment and transport anisotropy. The authors thus conclude that the existence of solution aggregates is necessary to obtain a high degree of alignment in printed films.

It has also been noted that solution-state aggregation is conducive to enhancing the resultant film crystallinity.[14,15,56−58,269] Reichmanis group has found that inducing solution-state aggregation of P3HT can dramatically increases the corresponding film crystallinity and further boosts the charge transport characteristics.[55−57] For instance, as shown in Figure 21c, a gradual increase in the intensity of (100) lamellar stacking peak in the film is observed with increasing the UV irradiation time of the precursor solutions.[56] This is ascribed to an increase of size and/or number of crystallites due to enhanced solution-state aggregation. Besides, with increased UV irradiation time, the film birefringence under CPOM progressively enhances (Figure 21d), which is another indicator of increased molecular ordering and/or crystallinity. As a result, the OFET mobility increases concomitantly in films fabricated from aggregated solutions (Figure 21e). Reichmanis group has also enhanced the film crystallinity by poor solvent addition and ultrasonic irradiation of P3HT solution, which is also modulated through the control of solution-state aggregation.[55,57] Similarly, Chen and Fréchet et al. have also demonstrated the importance of solution aggregation on enhancing the film crystallinity in a DPP-based polymer system.[15] They have synthesized two types

https://doi.org/10.1021/acs.chemrev.2c00905
Chem. Rev. 2023, 123, 8395−8487

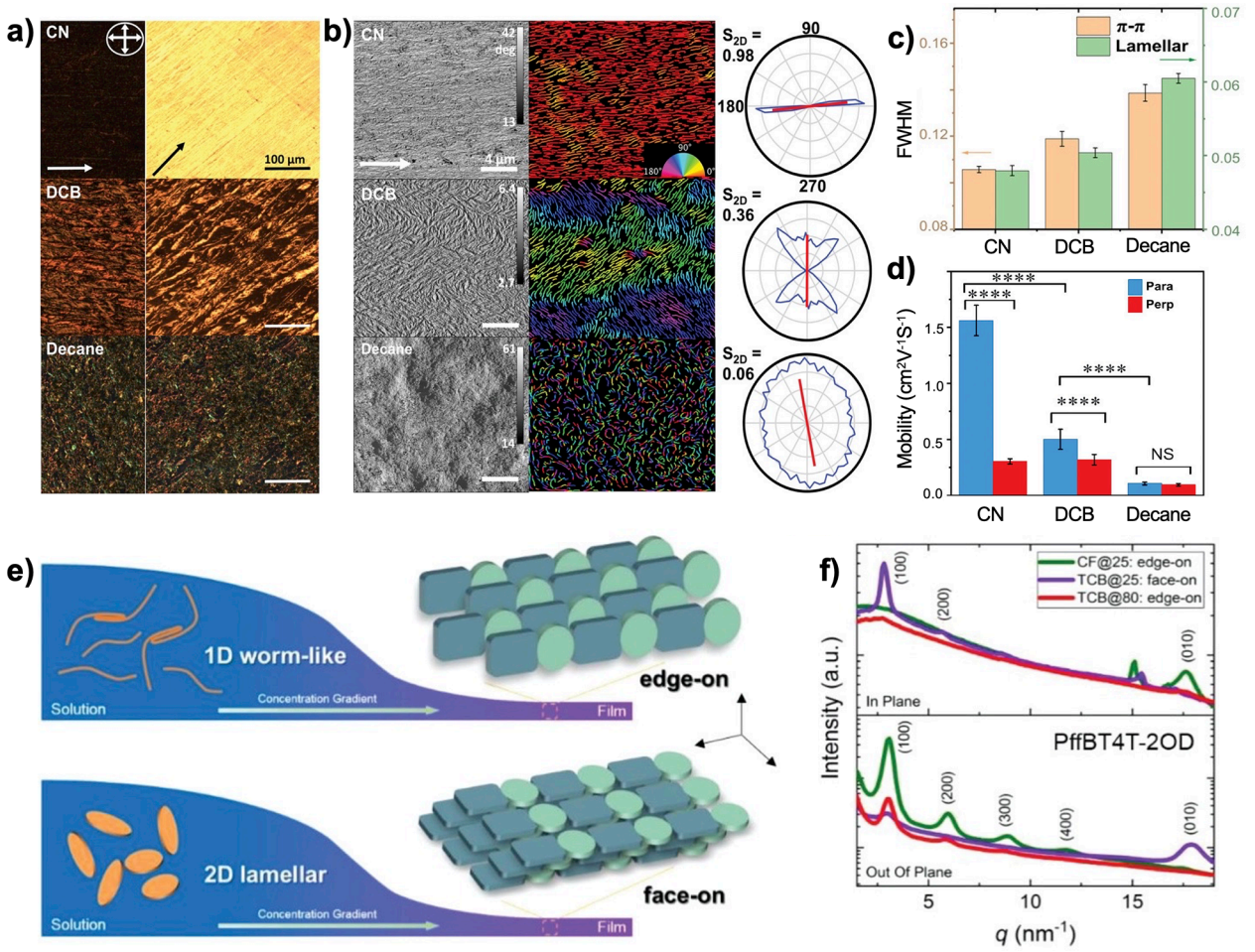

Figure 22. Effect of distinct aggregate structures on film alignment, crystallinity, and molecular orientation. a) CPOM images of PII-2T films oriented at 0° and 45° relative to the polarizer/analyzer with arrows indicating the film coating direction. b) AFM phase images (left), orientation mapping analysis (middle), and pole figures of the fiber orientation distribution with S_{2D} values (right) for films printed using the three solvents. The arrows indicate the coating direction. c) fwhm of $\pi-\pi$ stacking (010) and lamellar stacking (200) peak from GIXD. The error bars are from the peak fitting. d) Hole mobility in OFET devices measured at $\varphi = 0°$ and $\varphi = 90°$. e) Schematic illustration of the determinant role of solution-state supramolecular assembly in the molecular orientation of conjugated polymer films. f) 1D GIWAXS in-plane and out-of-plane profiles of PffBT4T-2OD thin films. Figure reproduced with permission from ref 16, Copyright 2022 John Wiley and Sons (a-d); ref 62, Copyright 2022 John Wiley and Sons (e, f).

of DPP-based polymer backbone: PDPP3F with 3 furan units and PDPP2FT with 2 furan and 1 thiophene units within each repeating unit, substituted with either linear *n*-hexadecyl (C16) or branched 2-butyloctyl (BO) side chains. Based on solution NMR, UV−vis absorption, and DLS measurements, among 4 polymers, the PDPP3F−C16 shows the strongest tendency to aggregate in solution due to a relatively linear backbone and ineffective linear solubilizing side chains. GIXD measurement reveals that PDPP3F−C16 spin coated films show the highest correlation length (L_c = 3.9 nm) extracted from the full width at half-maximum (fwhm) and the closest $\pi-\pi$ stacking distance (d = 3.52 Å), which correlates well with the strong tendency to aggregate in solution. In contrast, other 3 less aggregated polymers show L_c ranging from 1.1 and 2.2 nm, and d between 3.68 to 3.85 Å. Besides, the authors also demonstrate that enhancing solution aggregation by poor solvent addition can enhance the film crystallinity of PDPP3F−C16 and PDD3F-BO polymers. Therefore, those results suggest that solution-state aggregation of conjugated polymers is conducive to high film crystallinity.

In addition to film alignment and crystallinity, solution-state aggregation has a significant impact on the molecular orientation.[15,17,18,62,67,71] A notable work done by Li, Müllen, and Pisula et al. has shown that the molecular orientation of difluorobenzothiadiazole (FBT)-based polymers can be tuned by controlling their solution aggregation.[18] When dissolved in chloroform, the polymers aggregate into 1-D fiber-like structures as evidenced by AFM imaging on drop-cast samples. However, progressively adding TCB, which serves as a better solvent for the polymers, decreases the extent of aggregation as suggested by blue-shifting and decreasing in intensity of the lowest-energy absorption band (Figure 21f). Importantly, the molecular orientation in drop-cast films is tuned from edge- to face-on when using pure chloroform to pure TCB solvent (Figure 21g). The authors speculate that the change in the molecular orientation is associated with different extents of aggregation which affect the relative polymer−polymer and polymer−substrate surface interactions. Namely, (relatively) isolated polymer chains in TCB tend to "lie flat" to maximize their interactions with the substrate. Conversely, the intermolecular $\pi-\pi$ interaction between aggregated chains in chloroform is strong enough to compensate for the energy barrier required for chains to "stand up" on the substrate. This work highlights that an edge-on orientation is more favorable when ink solution is

https://doi.org/10.1021/acs.chemrev.2c00905
Chem. Rev. 2023, 123, 8395−8487

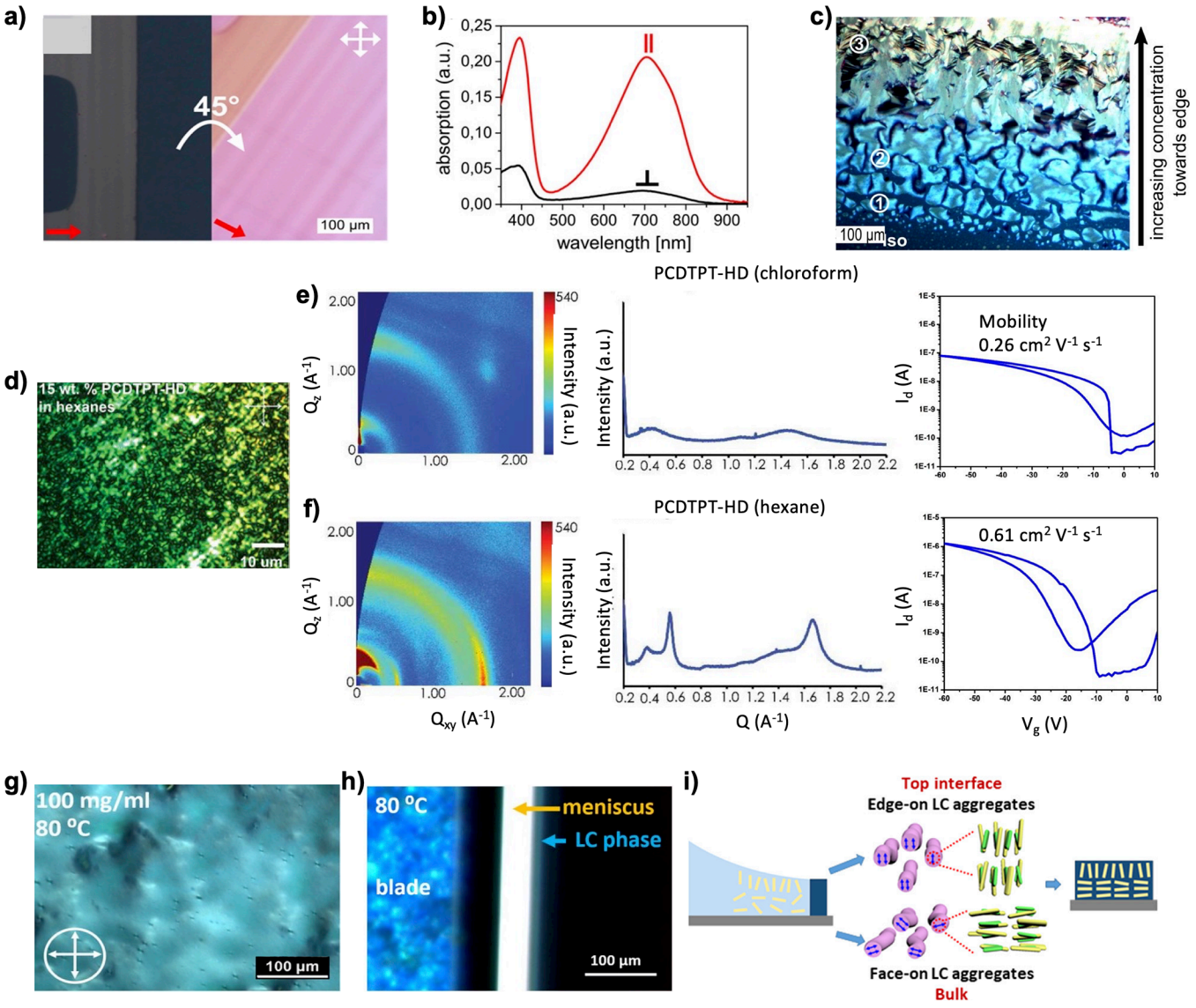

Figure 23. Effect of lyotropic mesophase on film alignment, crystallinity, and molecular orientation. a) CPOM images of a film coated on a transistor substrate. The red arrows indicate the printing direction. b) Polarized optical absorption spectra parallel (red) and perpendicular (black) to coating direction. c) CPOM image of a 20 mg/mL P(NDI2OD-T2) solution in chlorobenzene sandwiched between two glass slides. Solution evaporation from the sample edge gives rise to a concentration gradient. d) CPOM image of concentrated PCDTPT-HD solution in hexane indicating emergence of lyotropic LC mesophase. 2D-GIWAXS data (left), in-plane line cuts (middle), and OFET transfer cuves (right) for PCDTPT-HD film cast from e) chloroform and f) hexane solutions. g) CPOM image of a lyotropic LC mesophase in a concentrated (100 mg/mL) DPP-BTz solution. h) In situ CPOM image of the receding meniscus during solution coating of 10 mg/mL DPP-BTz in chlorobenzene solution. (i) Schematics of lyotropic LC-mediated assembly of DPP-BTz with distinct out-of-plane orientation at the top vs in the bulk film. Figure reproduced with permission from ref 302, Copyright 2018 American Chemical Society (a–c); ref 209, Copyright 2016 American Chemical Society (d–f); ref 335, Copyright 2020 American Chemical Society (g–i).

highly aggregated. Similarly, in the work mentioned previously by Chen and Fréchet et al., the highly aggregated PDFF3F–C16 polymer adopts an edge-on orientation whereas more soluble PDPP2FT-C16 polymer adopts a mixed orientation in spin coated films;[15] the former system shows a high $R_{in/out}$ (defined as the ratio of in-plane to out-of-plane $\pi-\pi$ scattering intensities in the GIXD pattern) between 11.94 and 15.87 whereas the $R_{in/out}$ for the later system ranges from 1.51 to 2.31. Additionally, they have found that promoting the solution aggregation of PDPP3F-BO by poor solvent (methanol) addition leads to a greater preference for edge-on orientation. The ratio $R_{in/out}$ is found to increase from 1.9 to 4.2 when methanol fraction in solution increases from 10% to 30%. Nahid and McNeill et al. have also shown that decreasing the solvent quality leads to a higher degree of edge-on orientation of P(NDI2OD-T2) at the air/film interface: as revealed by NEXAFS measurements, the average backbone tilt angles with respect to the substrate increase from ∼60° for good solvents (xylene:1-chloronaphthalene mixture and DCB) to ∼62°–63° for solvents with intermediate quality (chlorobenzene and chloroform), and eventually to ∼67° for poor solvents (toluene and xylene).[17] Wang and Han et al. have found that P(NDI2OD-T2) films spin coated from chloroform solution show a mixed orientation, whereas the edge-on content progressively increases from 38% to 54% upon adding 4 vol % ethylene glycol (considered as a poor solvent) into the solution.[67] Taken together, these works suggest that enhancing

https://doi.org/10.1021/acs.chemrev.2c00905
Chem. Rev. 2023, 123, 8395–8487

the extent of solution-state aggregation is conducive to forming or increasing the extent of edge-on orientation in the corresponding films. However, this rule of thumb may not be universal and may not translate to other polymeric systems. For instance, Li and Han et al. have found a negative correlation between the extent of solution aggregation of PCDTPT-ODD and the edge-on content in the resultant drop-cast films.[71] When the polymer is cast from solution in chloroform which is the least aggregating solvent among the selected ones, the highest edge-on content (∼75%) is obtained in the film, whereas the lowest film edge-on content (∼55%) is obtained when the film is cast from in isooctane solution where the polymer shows the highest aggregation tendency. Based on the in situ GIWAXS measurement during film formation, they have proposed that the face-on and edge-on crystalline regions are produced from ordered aggregates and disordered polymer chains in solution, respectively. Besides, in addition to the extent of aggregation, different internal structures of the solution aggregate may give rise to distinct molecular orientation, which will be discussed below.

As discussed earlier, not all aggregates are conducive to improving the film morphology,[281,284] and distinct aggregate structures may largely modulate the film alignment, crystallinity, and molecular orientation.[16,19,62] For example, our group has found that the PII-2T amorphous aggregates in hot 1-chloronaphthalene solution (backbone selective solvent) give rise to an exceptionally high degree of alignment in films prepared by meniscus guided coating (Figure 22a,b). In contrast, the semicrystalline agglomerates in decane (side chain selective solvent) are incapable of being disentangled or aligned, resulting in almost isotropic films.[16] The semicrystalline 1-D fiber aggregates in DCB (mutual solvent) develop into twinned domains as a result of an N_{tb} mesophase mediated assembly, leading to biaxial alignment in coated films. Besides in-plane alignment, the paracrystalline disorder goes from the lowest to the highest from 1-chloronaphthalene, DCB, to decane coated films, which is estimated from the fwhm of GIXD peaks (Figure 22c). Owing to the high degree of alignment and reduced paracrystalline order, the 1-chloronaphthalene films show the highest mobility in OFET devices (Figure 22d). Zheng and Pei et al. have also investigated the effect of BDOPV-2T aggregate structures on the resultant film crystallinity by extracting the coherence length (L_c) from GIXD patterns.[19] The results indicate that 1-D fiber-like (in DCB) and 2-D lamella-like (in toluene) structures lead to a L_c of 13.5 and 12.1 nm, respectively. Mixing DCB and toluene solutions gives rise to larger 1-D aggregates representing a transitional structure between 1-D and 2-D with an increased L_c of 15.1 nm. Deng and Li et al. have reported that the paracrystallinity disorder is reduced from 15.71% to 11.69% when PffBT4T films are spin coated from 2-D lamellar aggregates in TCB compared to those from 1-D fiber aggregates in CF.[62] Besides, they have also found 1-D aggregates facilitate edge-on packing in films whereas 2-D aggregates are conducive to face-on packing (Figure 22e,f).

2.4.3. Role of Secondary Solution-State Structures. Recent studies have suggested that a lyotropic LC mediated assembly pathway can significantly improve in-plane alignment, enhance film crystallinity, and boost device performance of thin films. Trefz and Ludwigs et al. have achieved high degree in-plane alignment in bladed coated P(NDI2OD-2T) film with high optical dichroic ratio (Figure 23a,b), reaching up to 18, along with a concomitant charge transport anisotropy of up to 14.[302] As shown in Figure 23c, the lyotropic characteristics of the polymer are directly observable under CPOM in a concentrated solution sample. The authors also demonstrate the film morphology tunability by increasing the oriented domain size upon solvent vapor annealing, which is presumably mediated by the lyotropic LC phase. Schott and Sirringhaus et al. also have fabricated highly aligned films of liquid crystalline DPP-BTz using soft blade solution shearing.[336] Optimal temperature and printing speed enable a high structural anisotropy in films printed from chlorobenzene solution, evidenced by an optical dichroic ratio up to 14 and charge transport anisotropy larger than 10. Kim and co-workers have proposed a molecular design rule for achieving lyotropic mesophase of thiophene-phenylene-based polymers with direct alignment capability in meniscus-guided coating.[217] When the design rule is satisfied, the polymer traverses a lyotropic LC-mediated assembly pathway and shows an exceptionally high emission dichroic ratio of 16.67 in the resultant film, which further leads to more than 3 orders of magnitude faster anisotropic hole mobility along the chain alignment direction than the orthogonal direction. In contrast, polymers with design requirements unfulfilled barely show any alignment in coated films due to the incapability of forming lyotropic LCs. The development of high degree of in-plane alignment induced by lyotropic LC during meniscus-guided coating of CDTPT is investigated by Wu and Richter et al. using in situ UV−vis absorption spectroscopy.[334] A significant increase in the film absorption anisotropy is only detectable 50 s after the meniscus passage, corresponding to a volume fraction of polymer larger than 0.5 in the drying meniscus. The authors propose that the bulk alignment is mediated by lyotropic LC phase and appears at high concentration driven by solvent evaporation. Persson and DeLongchamp et al. have drawn a similar conclusion that bulk alignment of P(NDI2OD-T2) film can be established through lyotropic LC phase and occurs very late in the meniscus drying process,[347] evidenced by in situ GIWAXS and UV−vis reflectance data.

Besides in-plane alignment, Segalman and co-workers have demonstrated that lyotropic LC-mediated assembly also gives rise to high crystallinity and charge-carrier mobility in the solid-state.[209] They have found that PCDTPT polymer with 2-hexyldecyl (HD) side chains forms lyotropic LC consisting of ordered aggregates in a selective solvent hexane (Figure 23d), whereas mesophase is absent when aggregates dissolve in a good mutual solvent such as chloroform. GIWAXS reveals increased crystallinity and larger crystallites in films cast from lyotropic hexane solutions to those from isotropic chloroform solutions (Figure 23e, f). As a result, charge-carrier mobility is enhanced when the assembly is mediated by LC mesophase (Figure 23e, f).

Moreover, the out-of-plane molecular orientation distribution can also be directed by lyotropic LC mesophase as demonstrated in one of our recent works.[335] Using CPOM, a lyotropic LC phase of DPP-BTz in chlorobenzene is readily observed in concentrated solution and at the meniscus front during solution coating (Figure 23g, h), and its molecular and mesoscale structural attributes are characterized using SAXS and in situ GIWAXS. A preferred face-on orientation is revealed in the bulk of the liquid crystalline layer whereas an edge-on orientation prevails at the top air−liquid interface in the meniscus (Figure 23i). We elucidate that side chains tend to stick out of the top interface to minimize the surface energy, leading to a predominantly edge-on orientation. In contrast, the molecules in the bulk liquid layer may adopt a twisted backbone conformation and a chiral helical assembly, leading to an overall

https://doi.org/10.1021/acs.chemrev.2c00905
Chem. Rev. 2023, 123, 8395−8487

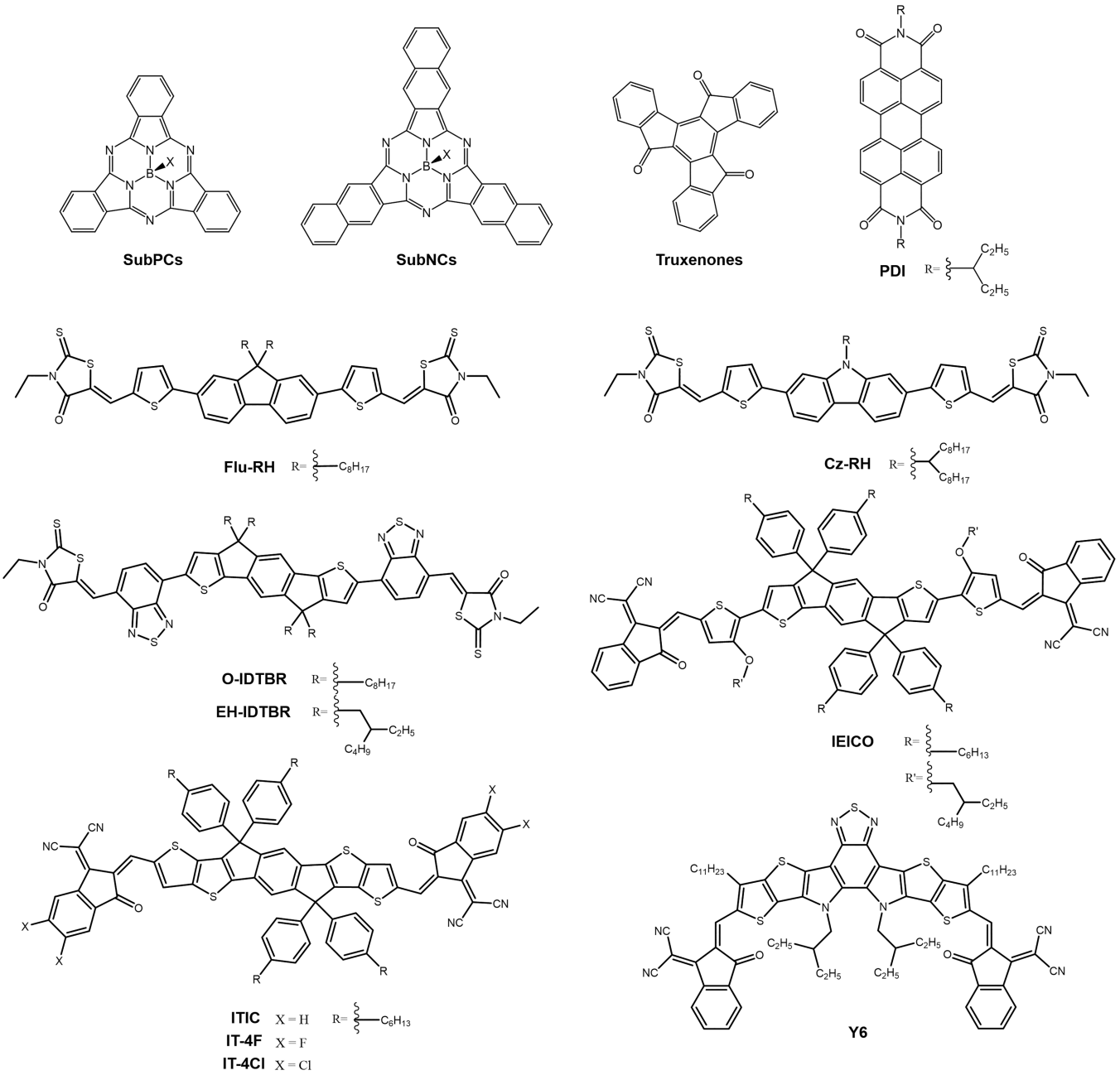

Figure 24. Representative examples of main classes of small molecule NFAs.

broad yet preferentially face-on orientation. This unique molecular orientation distribution developed in the mesophase is subsequently transferred into the thin films upon drying, which showcases an effective strategy to control the out-of-plane orientation in a mesophase-mediated assembly pathway.

Unlike lyotropic LCs with intrinsic orientational ordering and fluidity that can guide long-range orientational order during film processing, the secondary solution network-like assembly usually represents an isotropic and disordered state where primary aggregated fibers are randomly oriented and interconnected.[258,298,306−309] Although it has been suggested that special gel network processing (involving heating to molten state and subsequent mechanical shear) can produce highly aligned polymer films, it is usually observed that these network-like structures are readily inherited into the solid-state, resulting in poorly aligned films.[16,258,309,348] Besides, although the constituting primary fibers are suggested to improve the film crystallinity as discussed above, it is unclear how their secondary network-like assembly can have additional contribution to the crystallinity. It also remains an open question how these network-like structures can affect the molecular orientation in the final solid-state. Nevertheless, the secondary networks structures that are preserved into the solid-state films are found to show enhanced electronic properties.[306,349,350] For example, Malik and Nandi et al. have found that, when compared to films cast from dilute solutions without gelation, P3HT films slowly dried from concentrated solutions containing gels exhibit ∼10- and ∼50-fold increase in conductivity in undoped and doped state, respectively.[349,350] Newbloom and Pozzo et al. have also shown the conductivity of P3HT gel networks (up to 7 μS/m) prepared from aged, high-concentration solution is significantly higher than those reported for films from solution without

https://doi.org/10.1021/acs.chemrev.2c00905
Chem. Rev. 2023, 123, 8395−8487

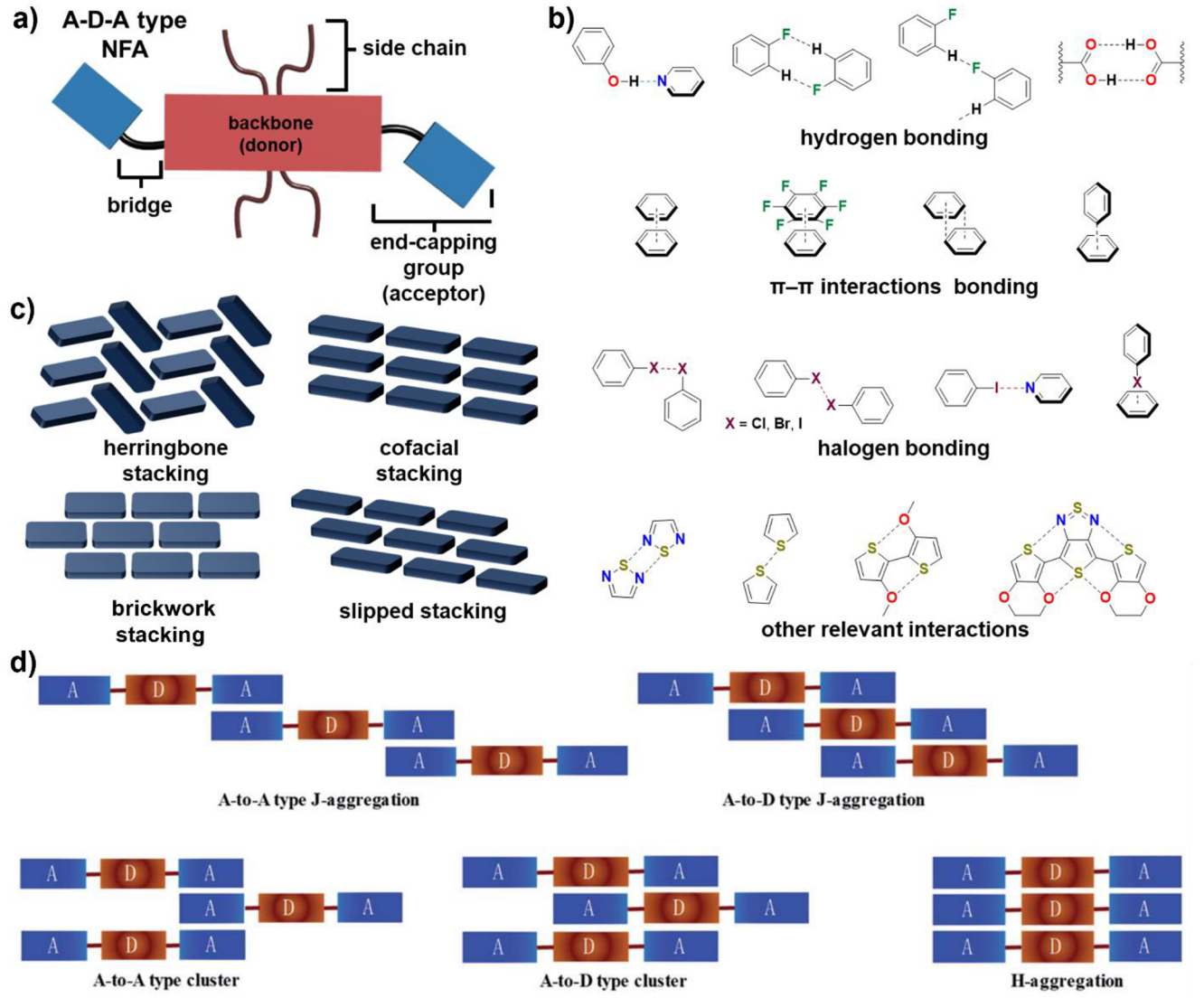

Figure 25. a) Schematic of a typical A−D−A NFA molecular structure. b) Supramolecular synthons of common interactions observed in crystalline structures. c) Typical molecular packing modes in single crystals. d) Molecular stacking formed in NFAs, reproduced with permission from ref 435, Copyright 2020 Royal Society of Chemistry.

gelation process (0.678 μS/m).[306] They have also demonstrated the conductivity can be enhanced by increasing the branching within the networks and the significant percolation enables effective charge transport over large distances (with samples as thick as 2 mm). As mentioned earlier, through a fiber network-mediated assembly pathway in dip-coating, Yao and Pei et al. have fabricated wafer-scaled transistors showing high electron mobilities up to 1.88 $cm^2 V^{-1} s^{-1}$, which is comparable or even better than that of spin coated films but with almost 1 order of magnitude smaller contact resistances.[309]

It has also been demonstrated that the formation of secondary gel networks can have a significant impact on the device performance of OSCs.[351−358] For example, an early work by Huang and Chang et al. has shown that aging-induced P3HT gelation in concentrated xylene solution can improve the *PCE* of P3HT:PCBM based OSCs, reaching 3.78% after optimizing the gelation time.[351] The authors propose that solution gelation alters the morphology of the photoactive layer, leading to nanoscale phase separated structures of P3HT:PCBM which can increase the maximum electrical output due to the increased efficiency of charge separation, charge transport, and/or photon absorption. In a more recent work by He and Lee et al., the P3HT gel networks prepared by rapid solution cooling are shown to have nanosized pores using cryogen-based SEM.[353] The porous network structures provide a continuous pathway for charge transport and large interfacial area with PCBM phase. As a result, the presence of those networks in the OSC photoactive layers leads to an enhanced *PCE* of 3.9% compared to that of reference cells (2.7%). Similarly, Li and Song et al. have obtained a *PCE* of 2.35% in P3HT:PCBM BHJs fabricated from solution containing gels, which is 5.6 times higher that of devices from solutions without gelation.[355]

3. ASSEMBLY OF NFA

In this section, we will focus on the assembly of conjugated organic small molecules, in particular NFAs, relevant to OSCs. Since their introduction, NFAs, have played the key-role in overcoming the drawbacks from their fullerene-based counterparts such as their thermal and photochemical instabilities, limited tunability of electron affinities, limited absorption in the UV−visible region of the solar spectrum, and time-consuming purification.[359,360] NFAs are also remarkable absorbers due to

https://doi.org/10.1021/acs.chemrev.2c00905
Chem. Rev. 2023, 123, 8395−8487

the highly tunable physicochemical properties and absorption that expands to the near-infrared (NIR) region of the electromagnetic spectrum (780 to 2500 nm).[361,362] The quest for effective property modulation of OSCs has motivated the progressive synthetic design of NFAs with distinct classes of molecular architectures.[360] In a broad sense, some of the most common small molecule NFAs can be classified as subphthalocyanines (SubPCs), subnaphthalocyanines (SubNCs),[363] truxenones,[364] perylene diimides (PDIs),[365] fluorene- and carbazole-based acceptors,[366] indacenodithiophene- (IDT), indacenodithienothiophene- (IDTT), and benzodithiophene (BDT)-based acceptors (Figure 24).[367]

Within the rich diversity of molecular architectures of NFAs, the specific molecular interactions and solution processing conditions have the capacity to influence the assembly pathways and improve device performance.[368,369] As noted elsewhere, one of the key aspects of evolution of OSCs is understanding and exploiting the self-assembly pathways of neat components and BHJ blends.[31] Compared to the complex assembly pathways of conjugated polymers forming primary and secondary aggregates in solution as discussed in Section 2, small molecules, particularly NFAs, do not exhibit as complex concentration-driven pathways during evaporative solution processing. Instead, direct crystallization and amorphous-to-crystalline transition have been reported.[370] The fundamentals of such pathways will be presented in Section 4.1.1. Most research studies report that the molecular assembly of NFAs mainly affect the crystal packing structures in the solid-state. Therefore, in this section, we will mainly focus on the crystal packing and polymorphism of NFAs in the solid-state which is largely determined by the molecular features of NFAs and various forms of intermolecular interactions. Relevant fundamentals of polymorphisms of organic electronic crystals were covered in our prior review.[40] Due to the rapid progression and evolution of NFA materials, our discussion will focus on assembly and crystal engineering aspects of several main classes of NFAs. Discussions of individual classes have been reviewed extensively in previous publications.[30,359,371−373]

3.1. Structural Features and Assembly Control of Neat NFAs

This section focuses on the current understanding of correlations of structural features with morphology and crystal packing of common NFAs. Morphology, as the link that connects molecular structure with device performance, is of fundamental importance for the development of more efficient OSCs.[374] A comprehensive review by Gu, Liu, Zang et al. focuses on key parameters such as material interaction and crystallization. Here, special emphasis will be given to high-efficiency acceptor−donor−acceptor (A−D−A), where the D unit can be extended to more complex DA′D cores (e.g., A−DA′D−A) NFAs, which are the frontline of OSC development due to being closer to the threshold of practical application (Figure 25a).[375]

In the context of molecular architecture, A−D−A NFAs are considered push−pull structures constructed by connecting an electron-rich core (D) with an electron deficient end-group (A).[376,377] A−D−A NFAs are typically decorated with side chains that allow for a high degree of structural tunability and solubility processability and miscibility (Figure 25a).[151,359] This section will provide an overview of current strategies to control molecular assembly of NFAs and the structural underpinnings for relevant properties. Specifically, we will focus on the crystallographic landscape of NFAs, which is intrinsically related to the molecular architecture and processing. In the discussion, aspects of crystal engineering[378,379] of OSCs and their impact on OSC morphologies will be covered.

3.1.1. Crystallographic Landscape of NFAs. Molecules in crystals are held together by a combination of attractive and repulsive forces induced by surrounding molecules through weak, noncovalent (i.e., supramolecular) interactions.[380] The crystal packing principle aims to maximize density, minimize free volume and packing energy. To gain a better understanding of the molecular interactions and supramolecular architectures and synthons[381] of NFAs, a variety of X-ray diffraction techniques (e.g., single-crystal X-ray diffraction (SCXRD), powder X-ray diffraction (PXRD), two-dimensional WAXS (2D-WAXS), GIXD have been employed on pristine NFA systems. In particular, SCXRD facilitated by synchrotron radiation beamlines have resulted particularly useful in obtaining unambiguous structural data from NFAs single crystals,[382] which tend to grow smaller compared to analogous organic molecules making data collection harder on conventional X-ray diffractometers.[151] Methods to successfully grow high quality single crystals of OSCs include slow evaporation,[382] slow precipitation of the mother liquor by cooling,[383] antisolvent vapor diffusion,[384] liquid−liquid interfacial precipitation.[385,386] Combined crystallographic characterization approaches have provided holistic understanding of the molecular assembly and morphologies in monolayers and thin films.[11,387] Crystallographic databases (e.g., Crystallography Open Database,[388] The Cambridge Crystallographic Data Centre[389,390]) provide a unique resource to deposit, and share obtained data sets to the scientific community, particularly with the rapid advancement of data science approaches to predict and generate improved chemical systems for OSCs.[391]

3.1.1.1. Supramolecular Synthons and Interactions. As discussed in the previous section, judicious manipulation and modification of intermolecular interactions in NFAs can have a profound impact on the crystal packing motifs of OSC materials.[378] The ability to control crystal packing relies on noncovalent, intermolecular interactions (i.e., supramolecular), as well as known supramolecular synthons (i.e., structural units within supramolecular architectures or molecular crystals that can be formed/assembled by known or conceivable synthetic operations using intermolecular interactions),[378,381] which is the basis of the field of crystal engineering. The molecular packing of various small molecule NFAs and optoelectronic materials[378] has been extensively reviewed, providing useful design elements and guidance for the design of future OSCs. In this section, we will discuss various strategies to control the assembly, crystal packing and molecular arrangements in the solid-state of various representative systems, as well as components of the supramolecular toolbox of intermolecular interactions (Table 1 and Figure 25b,c).

3.1.1.1.1. *π−π Interactions.* Broadly speaking, π−π interactions encompass the contacts between the π-orbitals of a molecular system.[378,392] Pioneering work by Hunter and Sanders outlined the geometrical requirements for π−π interactions and geometries, which can be broadly categorized in face-to-face, edge-to-face, and offset π-stacking modes.[393] The model takes in consideration a combination of electrostatic, induction, dispersion and repulsion energies, where the major contributor being typically electrostatic and van der Waals components. The ideal fixed separation of two π-atoms is typically in the order of ∼3.4 Å. Since the most widely available electronic molecules are highly conjugated, π−π interactions can

https://doi.org/10.1021/acs.chemrev.2c00905
Chem. Rev. 2023, 123, 8395−8487

Table 1. Representative Supramolecular Interactions and Energies Used in the Design of OSCs[a]

Supramolecular Interaction	Energy (kcal mol^{-1})	Examples
$\pi-\pi$ interactions	2−10	phenyl···phenyl, graphite
Hydrogen bond (weak)	<12	C−H···O, O−H···π, C−H···π
Hydrogen bond (moderate)	16−60	DNA, acids, alcohols
Hydrogen bond (very strong)	60−120	O−H···O$^-$, F−H···F$^-$
Halogen bond	1−42	N···Br, N···I, S···I, I···I
van der Waals	0.25−2	CH_3···CH_3, CH_3···phenyl

[a]Adapted with permission from refs 434 and 378, Copyright 2007 John Wiley and Sons and 2019 Elsevier.

be a powerful tool to dictate the overall packing and resulting properties in NFAs. Specifically, $\pi-\pi$ interactions have been identified to provide one of the most significant charge transport channels:[394] stronger $\pi-\pi$ stacking and shorter displacement would lead to more effective charge transfer and higher device performance.[394,395] π stacking modulation has also been related to enhanced mechanical properties,[396] thin film morphology and stabilities.[397,398] In addition to the most common modes of $\pi-\pi$ interactions, structurally related variations (e.g., cation−π,[399] anion−π,[400] hydrogen bond−π[401]) derived from π contacts have also been described and exploited in crystal engineering. Further, radical-based π−stacking (i.e., pancake bonding)[402−404] has also been used toward chemical design of novel OSC architectures.[50] Current strategies to influence the π−stacking in organic electronics include the incorporation of processing additives,[405] substrate selection,[406] chemical modification,[407] and cocrystallization.[408,409]

3.1.1.1.2. *Hydrogen Bonding*. Widely considered as the "master-key" interaction in crystal engineering because of its potential to design multifunctional materials,[410] a hydrogen bond, according to IUPAC, encompasses the attractive interaction between a hydrogen atom from a molecule or a molecular fragment X−H in which X is more electronegative than H, and an atom or a group of atoms in the same of a different molecule, in which there is evidence of bond formation.[411] In the context of organic electronics and OSCs, hydrogen bonding, while less common, has been demonstrated to serve as a long-range hole transport channel,[412] and to be able to control processability,[413] morphology[414,415] and solar cell efficiency.[413,416] Hydrogen bonds have also been utilized to enforce $\pi-\pi$ interactions in aromatic molecules through molecular templates,[417−419] and to act synergistically with π-stacking to improved organic photovoltaic efficiency.[420,421]

3.1.1.1.3. *Halogen Bonding*. Halogen bonding is another type of highly directional, electrostatically driven supramolecular interaction that involves an electronically depleted outer lobe in a half-filled p-type orbital (i.e., σ-hole) in a halogen atom.[422] According to the IUPAC definition, a halogen bond occurs when there is evidence of a net attractive interaction between an electrophilic region associated with a halogen atom and a nucleophilic region of another chemical entity.[423] Depending on the geometry, halogen bonds can be classified as type I (symmetrical interactions where $\theta_1 = \theta_2$) and type II (bent interactions where $\theta_1 \approx 180°$ and $\theta_2 \approx 90°$). Also, depending on the interacting molecular motifs, halogen bonds can range from 10 kJ/mol for weak interactions (e.g., N···Cl contacts) to 150 kJ/mol for strong interactions (e.g., I_2···I^- adduct).[424] While the incorporation of halogens into the molecular structure of OSC materials has been primarily motivated by the electron-withdrawing nature of halogens (i.e., increased absorption of IR light), it has been evidenced that halogen bonding can also improve morphology and packing efficiency such as in the case of Y3, ITIC, IT-4Cl,[425−428] and the stability and *PCE* of a Y6-based OSC.[429]

3.1.1.1.4. *Other Relevant Short Contacts for OSC Design*. In the design of functional OSCs, weak supramolecular interactions (e.g., chalcogen bonding, van der Waals, weak hydrogen bonding) have been used to provide conformational locking and achieve planarity/twisting in the molecular structure of NFAs.[174,430−432] For instance, it has been revealed by microcrystal electron diffraction that in electron-rich NFAs (e.g., β-ITIC-Th) sulfur atoms play an important supporting role in the formation of S···S and S···H short intermolecular contacts between the thienothiophene rings of IDTT backbones and the pendant thiophenes, resulting in the most distorted NFA backbone reported to date.[433]

Based on the above interactions, specifically, A−D−A type NFAs show various molecular packing behavior depending on the intermolecular coupling between donor and acceptor moieties, affecting the dimensionality of molecular assembly. A-to-A type J-aggregation (chain-like) and A-to-A type clusters can be observed in ITIC derivatives, while A-to-D type clusters can be formed in N3 molecular aggregates.[435,436] Thus, research groups have established design elements and strategies to modulate and control the confinement, extended packing, and crystallization of NFAs. The strategies can be broadly categorized as 1) core engineering, 2) end-capping group engineering, 3) side chain engineering, and 4) halogenation and single-atom substitution (Figure 25).

3.1.2. Backbone Engineering. In order to maximize $\pi-\pi$ interactions (i.e., considered as the primarily driving force for self-assembly) and reduce system energy,[437] NFAs are typically designed with fused aromatic rings as backbones.[361] As shown in Figure 26a, the type of extended packing and electronic properties can be significantly influenced by the length of the backbone and conjugation as demonstrated by crystal structures of ITIC (backbone length: 27.6 Å), 4TIC (25.1 Å) and 6TIC (28.7 Å). Specifically, ITIC molecules pack in a "2D brickwork" architecture through "end-to-end" $\pi-\pi$ stacking, generating 2D transport pathways (Figure 25c). The 2D brickwork layers assemble into lamella structure via van der Waals interactions between adjacent side chains. 4TIC, having a shorter backbone, organizes into a tight 3D web structure via the end group $\pi-\pi$ stacking with X-assemblies as the basic geometry. 6TIC shows different organization hierarchies including a zigzag assembly, hydrogen bonding 2D assembly, 2D layers and a 3D structure facilitated by additional $\pi-\pi$ stacking. For these cases, 4TIC and 6TIC exhibit 3D transport channels.[438] Similarly, substitution of benzene ring for a naphthalene ring in the backbone resulted in NDIC, which showed an increased *PCE* in blends, and broader optical band gap compared to IDIC. Both IDIC and NDIC have a planar conformation (i.e., enhanced $\pi-\pi$ stacking and charge transport) as demonstrated by DFT calculations and crystal structures.[439] High backbone planarity has also been linked with an increase of OSC efficiencies; in addition to covalent bonding, noncovalent interactions introduced by heteroatoms such as O, S, N, or unsaturated bonds (i.e., ring-locking strategy)[440] have the potential to "lock" the backbone planarity. One example is the use of chalcogen bonding (e.g., O···S or S···Se) to improve the planarity, fine-tuning of their optical energy gap, and the

https://doi.org/10.1021/acs.chemrev.2c00905
Chem. Rev. 2023, 123, 8395−8487

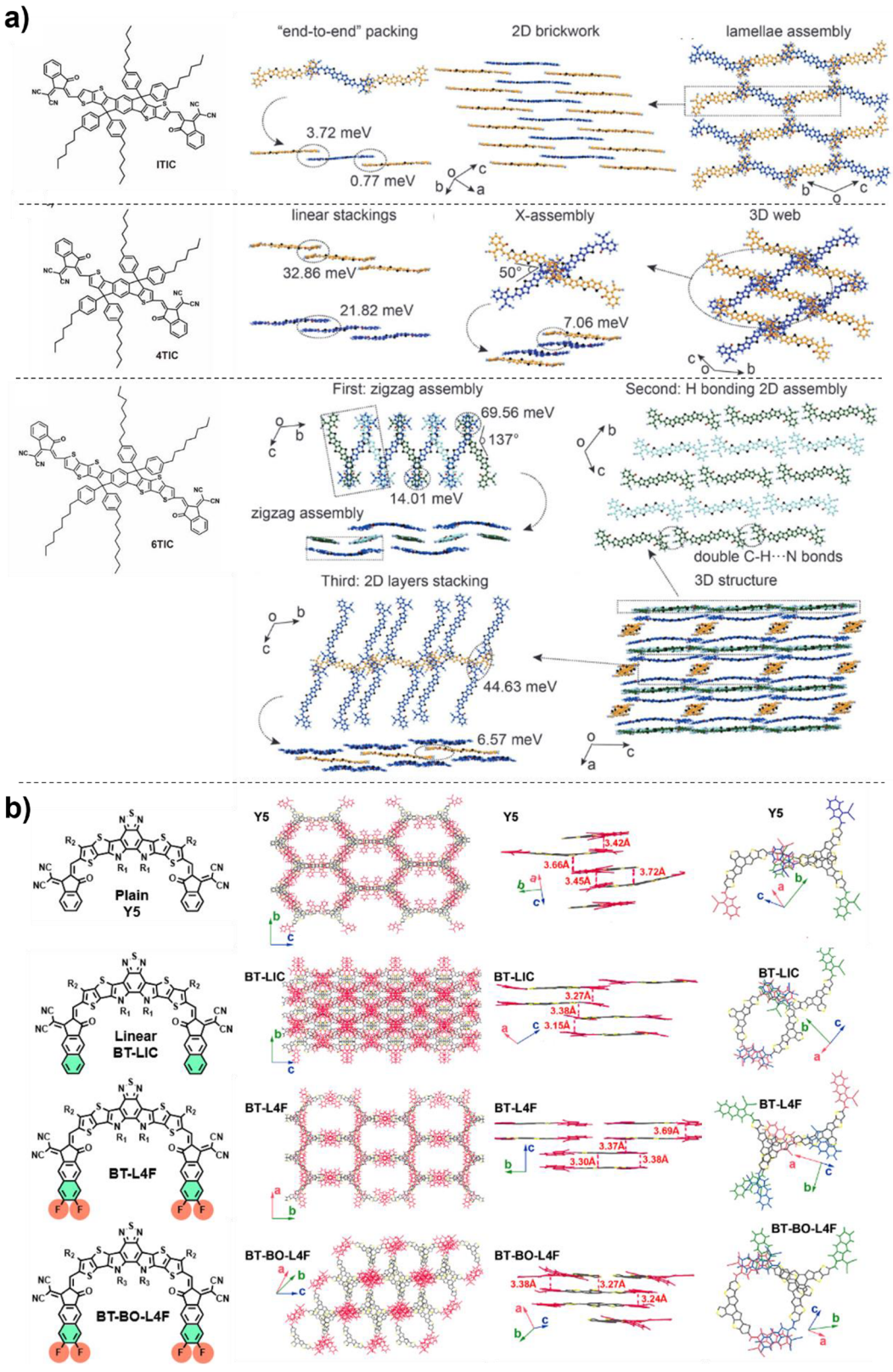

Figure 26. a) Chemical structures and single crystal structures of ITIC, 4TIC, and 6TIC. b) Molecular structures of acceptors (Y5, BT-LIC, BT-L4F, and BT-BO-L4F) and their single crystal packing with $\pi-\pi$ interlayer distance and intermolecular stacking pattern. Figure reproduced with permission from ref 438, Copyright 2022 John Wiley and Sons (a); ref 447, Copyright 2021 American Chemical Society (b).

HOMO and LUMO levels in IDTO-T-4F, IDTO-Se-4F, and IDTO-TT-4F.[441] An alternative strategy to improve OSC performance is the addition of bulky functional groups (i.e., 2,4,6-tri-isopropylphenyl) to a nonfused aromatic core, enhancing the conformational stability of the planar core structure, in a similar way to the use of noncovalent conformational lockers,[432] and in generating a 3D interpenetrated network that facilitates electron transport.[442]

https://doi.org/10.1021/acs.chemrev.2c00905
Chem. Rev. 2023, 123, 8395−8487

3.1.3. End-Capping Group Engineering. The selection of an appropriate electron-withdrawing end group in NFAs is one of the most effective and easily accessible strategies to obtain high-performance OSCs.[443,444] The choice of the end group is directly related to the optoelectronic properties and photovoltaic performance of acceptor molecules.[359] Specifically, the energy offsets of the LUMO and HOMO between donors and acceptors can facilitate charge transfer, as electron-withdrawing groups (e.g., carbonyl, cyano) can downshift LUMO levels.[361] A comprehensive review comprising typical end group moieties used in NFAs (e.g., derivatives of rhodanine, cyanide groups, 2-(3-oxo-2,3-dihydroinden-1-ylidene) (IC), diketopyrrolopyrrole (DPP), and malononitrile) describes the individual features of the molecular motifs and the overall effect on NFAs.[445] In terms of molecular packing of NFAs, modulation and decoration of end groups provide a platform for increasing supramolecular interactions (e.g., end-group $\pi-\pi$ stacking, F···S, F···H, S···S), which result in improved light harvest capabilities and better morphologies of NFAs in blended films (i.e., donor and acceptor phases with high crystallinity have appropriate sizes for charge generation and transport).[446,447] For instance, it has been shown that π-extension[446] and halogenation[448] strategies in end groups can synergistically promote face-to-face (cofacial) π-stacking, system crystallinity, reduce internal reorganization energies, and improve *PCEs*.[112,449] A related strategy, isomeric substitution, (i.e., changing substitution site and connecting position) can modulate the intermolecular packing and aggregation of NFAs and morphologies of blends.[450] Li and Mark et al. reported the impact of end group functionalization (π-extension and fluorination) in A−DAD−A type NFAs, Y5, BT-LIC, BT-L4F, and BT-BO-L4F (Figure 26b). The linear π-extension and fluorination lead to red-shift of optical absorption with broader bandwidth, and lower the reorganization energies, facilitating the fast exciton dissociation. In particular, the extended end groups by the π-extension were observed to enhance intermolecular electronic coupling owing to their enlarged π-overlap and to have preferential face-on orientation. Although BT-L4F exhibited the largest intermolecular coupling, its high coupling feature resulted in reduced solubility and miscibility in the blend system, which can be improved by elongating alkyl side chain (BT-BO-L4F). The effect of side chain and halogenation will be discussed further in the next sections.

3.1.4. Side Chain Engineering. Side chain engineering is an important strategy to improve the solubility and aggregation properties of conjugated polymers in OSCs.[451] Similarly, for small-molecule NFAs, the influence of side chains has shown a profound effect on the molecular packing of highly conjugates systems.[398] For instance, DFT calculations of NDI derivatives with alkyl side chains of varying lengths demonstrated that the introduction of longer chains does not significantly affect the energy levels of molecular orbitals but has a significant impact on the molecular packing efficiency. NDIs in slipped stacks (Figure 25c) with longer side chain show decreased mobilities (i.e., displacement of $\pi-\pi$ stacking along the short axis). Systems with a herringbone packing (Figure 25c) show an opposite trend (i.e., charge mobility increases with alkyl side chain) due to more efficient overlap of π orbitals).[398] A similar effect in the long-range structural ordering has been observed for IDTT derivatives, in which side chains with increased length (i.e., increased van der Waals contacts) reduce the end-group $\pi-\pi$ stacking of TIC motifs, whereas shorter side chains promote $\pi-$ stacking.[151] Generally, extended side chains have also shown increased solubility (i.e., better microphase separation) and processability for device fabrication.[452] Recent studies show the installation of branched alkyl and alkoxy chains to NFAs results in an increase in interdigitation of the supramolecular architecture, facilitating isotropic charge transfer and achieving higher mobilities and improved morphologies.[362,384,453−455] Similarly, the addition of electron-rich units to side chains (e.g., thienylhexyl group) have also shown an increase in the *n*-type mobility of ITIC-based systems.[384]

3.1.5. Halogenation and Single-Atom Substitution. It has been noted that fluorination of organic semiconductors and NFAs results in (1) down-shifting HOMO and LUMO levels, (2) increased supramolecular interactions (e.g., F···H, S···F, π···F) that modulate packing, crystallinity, and improve charge transport,[28,456] (3) absorption properties of neat NFAs based on the position of fluorine atoms.[408,445,449] A systematic study demonstrated that fluorine incorporation in a series of benzodifurandione-based oligo(p-phenylenevinylene) (BDOPV) resulted in significant changes in electron mobilities and supramolecular architectures of the n-type organic molecule.[395] When larger halogens are incorporated in the NFA architecture (e.g., Cl, Br), stronger halogen bonding capacity arises from the increased σ-hole, which leads to more effective down-shifting the energy levels compared to fluorination.[422,427,457] For instance, the precise positioning of chlorine atoms at the IC end groups in an IDTT backbone was able to increase the planarity, level of interpenetration (i.e., 3D interpenetrated network) of the extended structures, and provide stronger $\pi-\pi$ interactions, ultimately providing better *PCE* due to the more ideal isotropic transmission properties of the 3D network.[458,459] The single atom substitution strategy in the backbone with large heteroatoms has also been linked to an increase in planarity and charge carrier mobilities. For instance, a Y6-based derivative with a selenium atom instead of the central sulfur in the acceptor moiety showed a more efficient exciton dissociation, better charge transportation and lower extent of charge recombination.[460]

3.1.6. Polymorphism in NFAs. The increasing structural diversification of NFAs has been accompanied by the realization of structural polymorphism (i.e., the ability of a compound to crystallize in more than one crystal structure).[40,461,462] McCrone's statement "*[. . .] the number of forms known for that compound is proportional to the time and money spent in research on that compound.*"[463] particularly holds true for NFAs, which is an emerging powerhouse of OSCs. The proper understanding and control of polymorphism in NFAs can pave the way for unparalleled and unique opportunities for the proper tunability and diversification of OSC materials. Indeed, one should consider not only the many combinations resulting from hundreds of donors and acceptors (small molecule or polymer), but also with the type of polymorph or arrangement of the neat NFA system and its influence in the blend.[29,95,464−467] However, due to the nature of BHJ device fabrication, characterization of most NFAs and blends has been mainly carried out and studied on thin films,[438] generating challenges in identifying the presence of polymorphs (i.e., films have been observed to confine transient metastable polymorphs at room temperature).[468,469] In addition, poor capacity of NFAs to crystallize as single crystals have limited the dependability of SCXRD for structural characterization and study of structure−property relationships. Although several reviews and reports have highlighted the unique properties and opportunities of crystalline NFAs (e.g., crystal packing),[22,23] there remains a need to provide a clear and concise analysis dedicated to poly-

https://doi.org/10.1021/acs.chemrev.2c00905
Chem. Rev. 2023, 123, 8395−8487

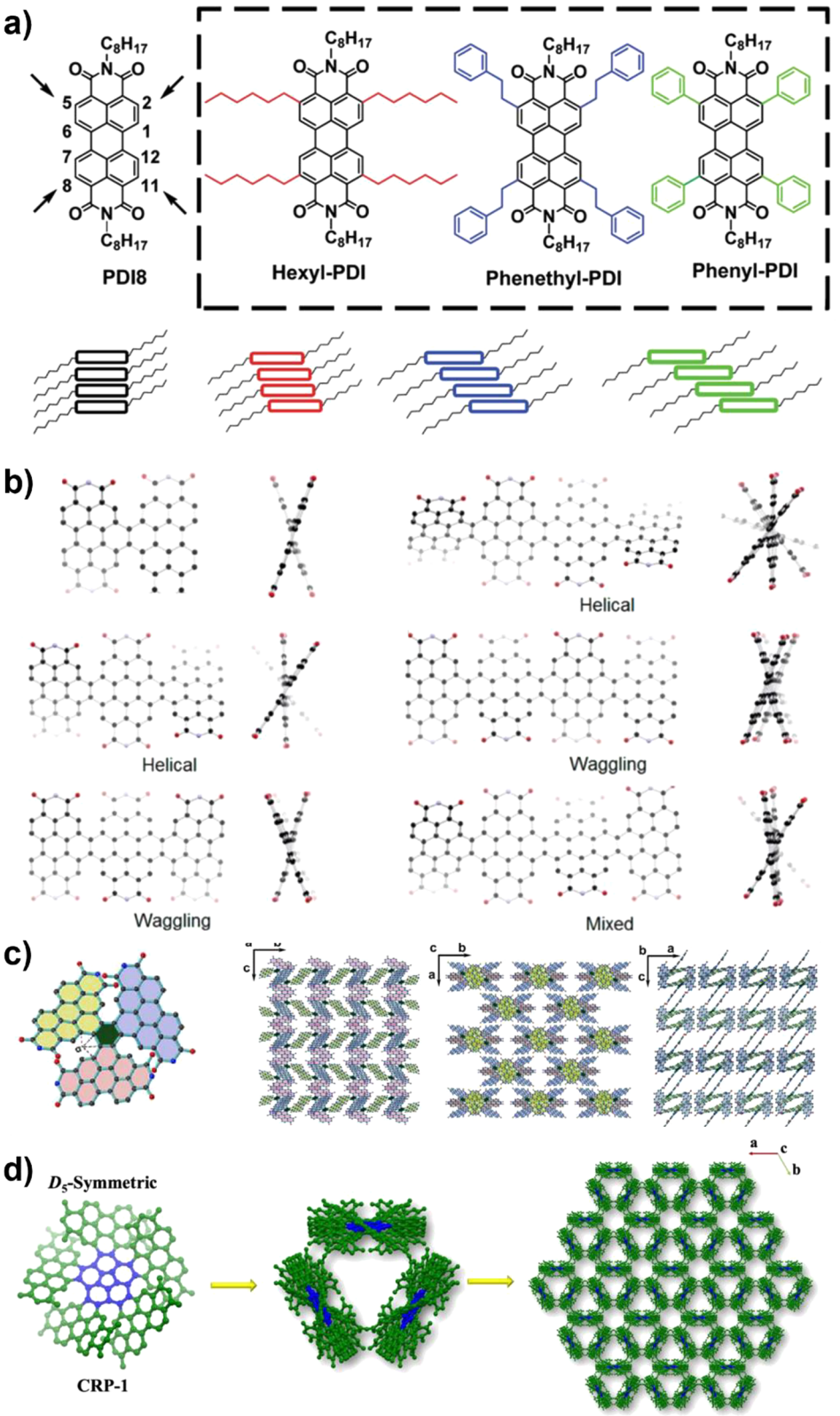

Figure 27. a) Chemical structures of PDI acceptors and their possible molecular packing structures. The headland positions of PDI (C_2, C_5, C_8, and C_{11}) are denoted by arrows in the PDI8. b) Molecular conformation of PDI dimer, trimer and tetramer from DFT models. c) Molecular structure of triperylene hexaimides (TPH) and the slipped 3D stacking mode of TPH. d) Molecular structure and crystal assembly of isomeric PDI-fused corannulene acceptor, corannurylene pentapetalae (CRP). Figure reproduced with permission from refs 477, 480, and 482, Copyright 2014 American Chemical Society (a); ref 481, Copyright 2014 American Chemical Society (b); ref 483, Copyright 2016 American Chemical Society (c); ref 483, Copyright 2021 Chinese Chemical Society (d).

https://doi.org/10.1021/acs.chemrev.2c00905
Chem. Rev. 2023, 123, 8395−8487

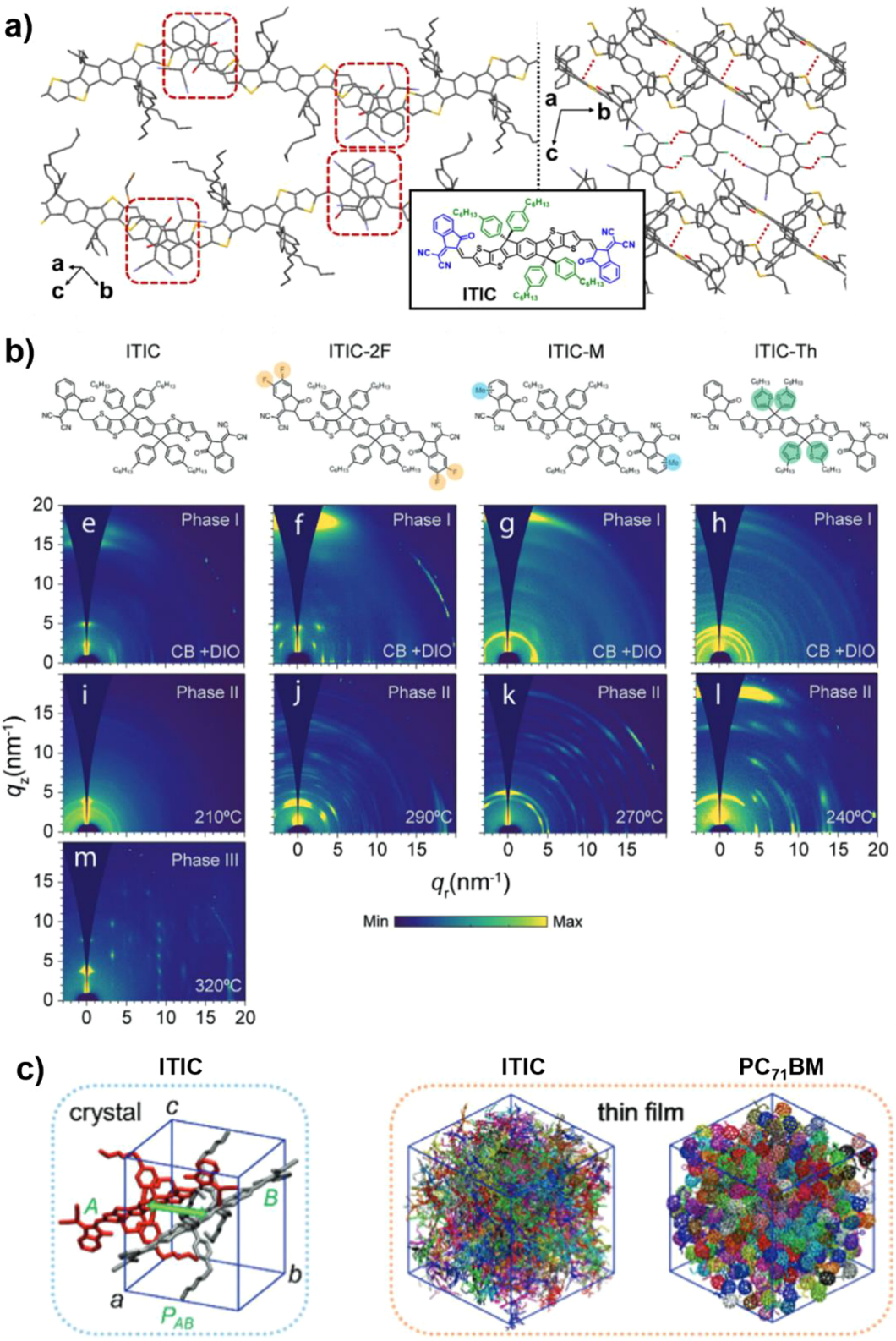

Figure 28. a) Crystal structures of polymorphs 1 and 2 of ITIC indicating end group−end group $\pi-\pi$ interactions with boxes and S$\cdots\pi$ and H-bonding interactions with dotted lines. b) Molecular structures of ITIC and its derivatives and corresponding 2D GIWAXS patterns of the different polymorphs observed at low- and high-temperature. c) Chemical structures of ITIC and $PC_{71}BM$ (top), unit cell of ITIC (polymorph 2) and simulated molecular packing morphologies of thin films of ITIC and $PC_{71}BM$ (bottom). Figure reproduced with permission from ref 386 and 470, Copyright 2019 John Wiley and Sons (a); ref 471, Copyright 2021 John Wiley and Sons (b); ref 436, Copyright 2017 Royal Society of Chemistry (c).

morphism and its opportunities for the advancement of OSCs. Polymorphs in NFAs have been primarily observed for main series of A−D−A and A−DA′D−A type systems,[95,466,467,470,471] which will be discussed in the following sections.

https://doi.org/10.1021/acs.chemrev.2c00905
Chem. Rev. 2023, 123, 8395−8487

3.2. Structure−Property Relationships in Major NFA Series

In this section, we will summarize some of the topical literature reports of representative NFA series showcasing the molecular evolution from original development to current high-performing architectures. Structure and property design that have led to state-of-the-art OSCs will also be discussed. Selected examples of small molecule NFAs will provide a comprehensive insight with connections to morphology, electron mobility and exciton behavior. Correlation of structural packing with property development will provide a molecular snapshot of design elements that have paved the way for efficient OSCs.

3.2.1. PDI Series. The design for PDI systems comprises an electron-withdrawing imide group, which provides a high electron affinity, and a central rylene framework of linked naphthalene units that facilitate high electron mobility and tunability by chemical modification.[472] Most of the typical PDI molecules involve A−D−A configuration and range from monomers to more sophisticated oligomers (e.g., trimer, tetramer) (Figure 27).[472−475] Monomeric PDIs show a higher propensity to aggregate due to the strong intermolecular $\pi-\pi$ stacking, leading to the formation of micrometer-sized domains. Although the increased $\pi-\pi$ stacking facilitates charge transport, too large crystalline domains by strong self-aggregation prevent efficient exciton dissociation in the blend film.[476] Early generations of PDI-based NFAs involved the use of a monomer with the capacity to molecular diversification and functionalization at the *ortho*, *bay*, and/or imide positions (Figure 27a).[472,477] By introducing substitutions at the headland positions, the PDI molecules has been shown to organize in slip-stacked structure, which is more like J-aggregate and inhibits formation of excimer, a short-lived dimeric molecule. Felter and Grozema et al. investigated the relation between molecular packing, exciton diffusion and charge transport behavior using two monomeric PDIs with different alkyl chains.[478] Octyl-imide substituted PDI (PDI-octyl) forms large crystalline aggregates, whereas the bulky branched chains in hexylheptyl-imide substituted PDI (PDI-hexhep) reduces intermolecular $\pi-\pi$ stacking between PDI cores, which is generally introduced for improving solubility. PDI-octyl showed higher charge carrier mobility (0.32 $cm^2\ V^{-1}\ s^{-1}$) as well as longer exciton diffusion length (60 nm) than those of PDI-hexhep (0.02 $cm^2\ V^{-1}\ s^{-1}$ and 20 nm), implying the importance of solid-state packing on charge transport and exciton diffusion.

Multi-PDI arrays with π−core extended and twisted structures can form various 3D molecular architectures that facilitate isotropic charge transport and suppress detrimental self-aggregation. As shown in Figure 27b, fusion of PDIs by ethylene bridges induces the steric congestion at the fusion point, creating helical structure and inducing an intense long wavelength transition.[479,480] More recently, star-shaped acceptors based on PDIs have combined the advantages of NFAs (e.g., strong light absorption, tunable energy levels, solubility, morphological stability) while maintaining fullerene-based acceptor properties (high electron mobility and isotropic charge-transport properties). Additional advantages include the intramolecular charge transfer, wide absorption range, inhibition of excessive aggregation, and improved exciton dissociation due to the 3D molecular geometry (i.e., reduced energy gap, E_g) (Figure 27c,d).[481−483] Recently, combining a PDI with IDT and 2FIC units in both sides resulted in the formation of an A−DA′D−A architecture with strong absorption, delocalized frontier orbitals, suitable energy levels and favorable face-on packing, which are helpful for exciton generation and dissociation.[484]

3.2.2. ITIC Series and A−D−A type Acceptors. Among fused-ring electron acceptors (FREAs), ITIC have stood out due to remarkable performance in the past five years. Initially developed by Zhan et al. in 2015,[361] the design of ITIC marked the first wave of NFAs based on the A−D−A configuration and became a model compound for further structural modifications and film morphology optimization studies.[361] ITIC is a push−pull molecule composed of a bulky seven-ring fused core (indacenodithieno[3,2-*b*]thiophene), end-capped with 2-(3-oxo-2,3-dihydroinden-1-ylidene)malononitrile groups, and with four 4-hexylphenyl groups as side chains. The strategy for the design of ITIC followed the observations of calamitic shaped small molecule acceptors, which are characterized by a discrete separation of electron rich and poor sections, allowing a high degree of modularity.[371,377] A benefit derived from the A−D−A structure is that the strong intrachain charge transfer between the donor and acceptor moieties yields narrow bandgaps (∼1.6−1.2 eV), excellent extinction coefficients ($>10^5\ cm^{-1}$), and nearly double absorbance as the PDI-based NFAs. The rigid backbone of IDT enhances the crystallinity in neat and blended films, leading to high electron mobilities ($\sim10^{-4}-10^{-3}\ cm^2\ V^{-1}\ s^{-1}$).[29,485,486] Due to the intense research endeavor, the presence of polymorphs in single crystals and different phases on thin films has been observed.[386,470] ITIC is known to crystallize in at least two packing arrangements depending on the growing conditions. A face-to-face slipped stacking and edge-to-face packings can be obtained from CH_2Br_2/*n*-heptane and CH_2Cl_2/petroleum ether, respectively (Figure 28a).[408,436] The observation suggests there may be more than one energy minimum packing arrangement in the energy landscapes of small molecule NFAs.[386] The differences in molecular packing show a direct correlation to the electronic properties by orders of magnitude. On the one hand, edge-to-face packing, typically driven by S···π interactions between the cores of two acceptor molecules and H-bonding interactions (Ar−H···N≡C and Ar−H···O=C) between the end groups, exhibit only transport of charge along a 1D path, limiting charge transport dimensionality and charge mobility. On the other hand, face-to-face stacking, stacked columns, or interleaved bricks of π-stacked molecules provide greater charge transport directionality and overall carrier mobility.[386,408,436] It was also observed that the ITIC derivatives showed superior exciton diffusion length over 20 nm to other NFAs and, in particular, IT-4F exhibited the longest exciton diffusion length of 45 nm among the ITIC derivatives,[135] which also surpasses those of most of donor polymers.

In thin films, pioneering work on polymorphism of NFAs by the Martin group showed the presence of at least two crystalline forms (i.e., low- and high-temperature polymorphs), which were found in ITIC and its derivatives ITIC-M, ITIC-2F, and ITIC-Th (Figure 28b).[470] The work demonstrated that the metastable low-temperature polymorphs show continuous 1D-chain or multidimensional mesh-like structures with poor structural order along the $\pi-\pi$ stacking direction. The high-temperature phase (ITIC has two phases) reveals a highly ordered structure. Surprisingly, low-temperature polymorphs exhibited better charge transport properties, device performance and stronger light absorption compared to high-temperature polymorphs. The low-temperature motifs have been also found in similar high-performing NFAs.[277,384,386,459,470] In addition to electronic properties, a separate study determined the relative stability of polymorphs of ITIC and ITIC-4F in thermally annealed films by

https://doi.org/10.1021/acs.chemrev.2c00905
Chem. Rev. 2023, 123, 8395−8487

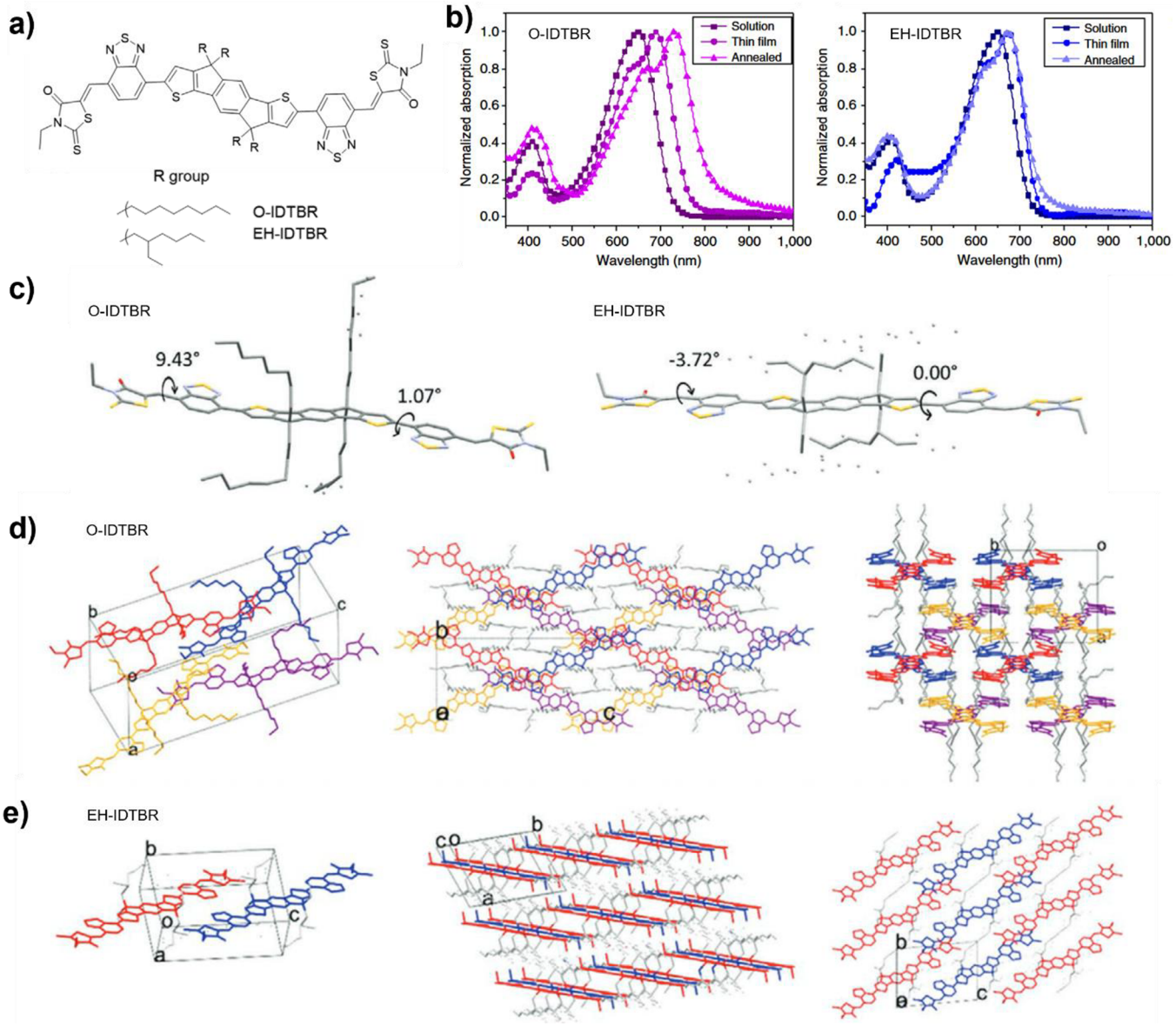

Figure 29. a) Chemical structure of IDTBRs. b) Normalized absorption spectra of solutions and films of O-IDTBR and EH-IDTBR. c) Molecular conformation of O-IDTBR and EH-IDTBR. d, e) Unit cells and crystal structures of O-IDTBR and EH-IDTBR. Figure reproduced with permission from ref 384, Copyright 2019 John Wiley and Sons (a, c, d, and e); ref 491, Copyright 2016 Springer Nature (b).

photoluminescence and Raman spectroscopy. It was revealed that for ITIC, the high temperature phases (II and III) show the highest stability while ITIC-4F shows the opposite trend, exhibiting less crystallinity at higher temperatures,[487] which may indicate a trade-off between performance and stability. Differences and similarities between crystal structures and films in the ITIC system have been explored by the Yi group by a combination of SCXRD, MD simulations, and mobility calculations, demonstrating that the thin film possesses higher electron mobility than those of the single crystals due to a 3D molecular packing by local $\pi-\pi$ stacking interaction between the terminal IC groups, thus generating an isotropic electron transport (Figure 28c).[436,466] The significant effect of terminal groups on the crystal structure and film properties in NFAs[436,465] has motivated the generation of ITIC derivatives and structurally related A−D−A type acceptors through organic synthesis.[151,379,384,386,433,435,458] For instance, as discussed in Section 3.1.2, the design of structurally related 4TIC and 6TIC systems, which differ on the backbone length and degree of conjugation adopt overall 3D crystal structures (Figure 29a).[438] For the case of 4TIC, linear stackings and X-assemblies of molecules generate a 3D web architecture, while 6TIC arranges into a interlayered zigzag assembly that results in a 3D structure.

Single crystal polymorphism was also reported for the IDIC system as three forms (i.e., α, β, and γ phases). The polymorphism in IDIC system exhibited the potential for efficient modulation of the exciton binding energies. Namely, the systems exhibited significantly different E_b in the solid-state change by ≤50% as demonstrated by molecular modeling. On the one hand, it was observed that the lower crystal density and dimensionality of the γ-phase increased E_b (>0.3 eV). Interestingly, higher dimensionality of the α-phase resulted in a decrease in E_b (0.21−26 eV). The results underline the importance of polymorph engineering in the context of NFA acceptors to effectively modulate electronic-related properties.[95]

https://doi.org/10.1021/acs.chemrev.2c00905
Chem. Rev. 2023, 123, 8395−8487

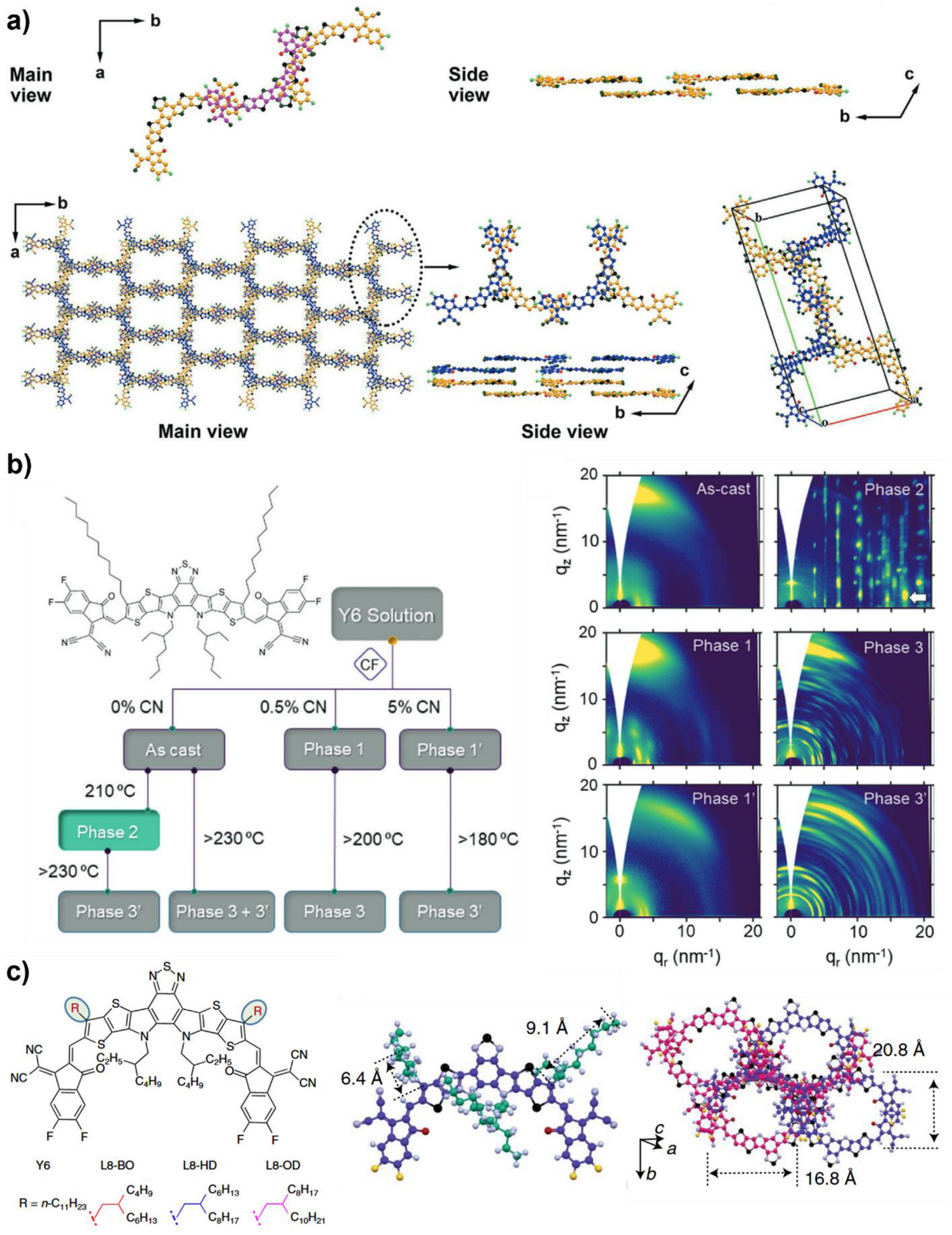

Figure 30. a) Crystal structure of Y6 showing different views and unit cell. b) Chemical structure of Y6 and processing routes toward different polymorphs in thin films. c) Chemical structure of branched derivatives of Y6 (including L8-BO), crystal packing of L8-BO molecules. Figure reproduced with permission from refs 464 and 471, Copyright 2020 John Wiley and Sons (a); ref 472, Copyright 2022 John Wiley and Sons (b); ref 454, Copyright 2021 Springer Nature (c).

It is relevant to note that the presence of solvent (i.e., crystal solvate) has been observed to sustain the packing of single crystals of ITIC and related NFAs, particularly for systems with high solvent−solute interactions (i.e., high solubility) or for systems with frustrated molecular packing.[467,488] Additional discussion on the presence of polymorphism and solvent

https://doi.org/10.1021/acs.chemrev.2c00905
Chem. Rev. 2023, 123, 8395−8487

inclusion in NFAs can be found in the meta-analysis of Morse et al. and the review by Lai and He.[379,467]

3.2.3. IDTBR Series. The IDT core unit in IDTBR has advantage of planarizing the molecular structure due to the increased quinoidal character of phenyl-thienyl bond and the reduced steric twisting from adjacent α−C-H bonds on the coupled phenyl rings.[489,490] This planar feature induces significant red-shift of absorption as well as increase of crystallinity, which is favorable for charge separation and transport. There are two representative NFAs with the IDT core unit, O-IDTBR with linear *n*-octyl alkyl chains and EH-IDTBR with branched 2-ethylhexyl chains (Figure 29a). The small change in side chains induces different conformation and crystal structures, resulting in a considerable change in optoelectronic and thermal properties such as absorption, charge carrier mobility, and crystallization temperature[384,491] (Figure 29b, c). The unit cells and motifs of O-IDTBR and EH-IDTBR are displayed in Figure 29d, e. For O-IDTBR, interdigitated columnar packing motif was observed, where the terminal electron accepting units (rhodanine and benzothiadiazole unit) stack in columns (Figure 29d). These columns result in a 3D network, possibly giving excellent and isotropic charge transport. On the other hand, for EH-IDTBR, 1D slipped stack packing motif was observed (Figure 29e). Since each molecule has only two nearest neighbors with which it can form π−π stacking, an electron transfer integral (17 meV), indicating electron coupling and charge transfer between molecules, is much lower than that of O-IDTBR (50 meV).[384] From OFET devices, low saturation mobility of 0.05 $cm^2 V^{-1} s^{-1}$ was obtained for EH-IDTBR, while O-IDTBR exhibited much higher saturation mobility of 0.12 $cm^2 V^{-1} s^{-1}$, which is attributed to the changes in intermolecular packing by side chains. Exciton lifetimes of O-IDTBR and EH-IDTBR were also obtained via time-resolved PL decay measurement, exhibiting 561.5 and 898.3 ps, respectively, much longer than that of ITIC (305.3 ps). It is worthy to note that a long singlet exciton lifetime was found to be a key parameter to maintain an efficient device operation at negligible HOMO offset.[492] Thus, this result confirms a potential of IDTBRs as good acceptors for efficient exciton dissociation. According to the other literature, EH-IDTBR showed a exciton diffusion length (15 nm) which is comparable to those of donor polymers.[135] Interestingly, the exciton diffusion length of EH-IDTBR is shorter than that of ITIC (25 nm) even with its longer exciton lifetime, which is caused by relatively low exciton coupling parameters possibly due to 1D slipped stack packing.

3.2.4. Y Series and A−DA′D−A type Acceptors. Molecular engineering inspired by the high efficiency using NFAs with a 3D network packing led to the development of the Y series of NFAs. "Y" has been used to name A−DA′D−A type acceptors with the key feature of containing an electron-deficient (A′) segment into the middle of the central D conjugated building blocks to form a fused DA′D backbone.[493] In fact, the first A−DA′D−A type acceptor (BZIC) combined a thiophene unit (D) with a benzotriazole unit (A′) to form a coplanar interfused DA′D. The backbone of BZIC is decorated with ICT acceptors and has sp^2-N instead of sp^3-C of ITIC to promote increase π electron delocalization and charge transfer.[328,329,392,393] After realizing solubility and film morphology with blended polymers were a limiting factor for Y1−Y3 as seen by AFM micrographs, chemical optimization of Y compounds evolved to include a benzothiadiazole (BT) to promote additional intermolecular S···S and S···π interactions in Y6.[267,329,392,394,371] SCXRD revealed that banana-shaped Y6 overlaps with two adjacent molecules through the IC end group staking to form a twisted 1D transport channel. The other set of Y6 molecules form another 1D channel, which arranges into a 2D network with the first set. Y6 further interacts with efficient face-to-face π-core interactions with a pathway built from closely packed indanones to generate a 3D network (Figure 30a).[464,494] The crystal packing proved to exist in neat and blended films with PBDB-T-2F according to GIWAXS measurements and molecular dynamics simulations.[495] The singlet exciton lifetime of Y6 was found to be 1016 ps, leading to efficient exciton splitting in the blend film even with small HOMO offset.[492] In addition, it was observed that Y6 has a long exciton diffusion length of ∼40 nm,[21,135] which is much longer than those of high-performing donor polymers.

In a similar fashion to ITIC, Y6 has also exhibited a rich polymorphism of at least five crystal phases, in addition to an oriented glassy microstructure, which paves the way for additional processing routes toward more efficient systems using additives or thermal annealing (Figure 30b). In the study, an annealed phase exhibited electron mobilities as high as 2.4 $cm^2/(V\ s)$,[471,496] surpassing even single crystal thin-film transistors.[497]

Several NFA molecules inspired by Y6 have been designed via modifications on alkyl chains, halogenation, single atom substitution, and backbone.[374] For instance, the addition of branched chains to the beta position of the thiophene units on a Y6 core led to major improvements in molecular packing and blend morphologies. Specifically, single crystals of branched system L8-BO exhibit three π−π packing motifs, which can provide more charge-hopping channels (vs two packing motifs of Y6). It is suggested that a relatively strong electronic coupling enables L8-BO with high electron mobility in thin films. Compared to Y6, the L8-BO neat thin film features a π−π stacking peak and has a better structural order. In addition, AFM morphology revealed the films to be relatively more homogeneous than other examples, indicating a good morphological stability.[454]

4. ASSEMBLY OF POLYMERS AND NFA IN THE BLEND

In previous sections, we have discussed the assembly pathways of conjugated polymers and NFAs induced by various forms of intermolecular interactions and their impact on the neat film morphology and optoelectronic properties. In this section, we will shift our focus to blend systems relevant to OSCs. The photoactive layer of most high performing OSCs consists of an interpenetrating network of phase-separated donor and acceptor materials or BHJ morphology which substantially influences the device performance of OSCs.[498−501] Compared to a bilayer architecture where the donor and acceptor materials are sequentially deposited in a layer-by-layer fashion, the BHJ structure enables larger donor−acceptor interfacial area which enhances charge generation and device performance of OSCs.[23,24,502] Since BHJ morphology is a blend of donor and acceptor materials, it is not only influenced by the molecular assembly of donor and acceptor molecules, but also by their miscibility, relative crystallization behaviors, and nonequilibrium conditions such as the drying kinetics.[280,502−507] As a result, all of these factors need to be considered for establishing the relationship between the molecular assembly pathways and the BHJ morphology.

To better understand how molecular assembly affects BHJ morphology, it is necessary to examine the crystallization and

https://doi.org/10.1021/acs.chemrev.2c00905
Chem. Rev. 2023, 123, 8395−8487

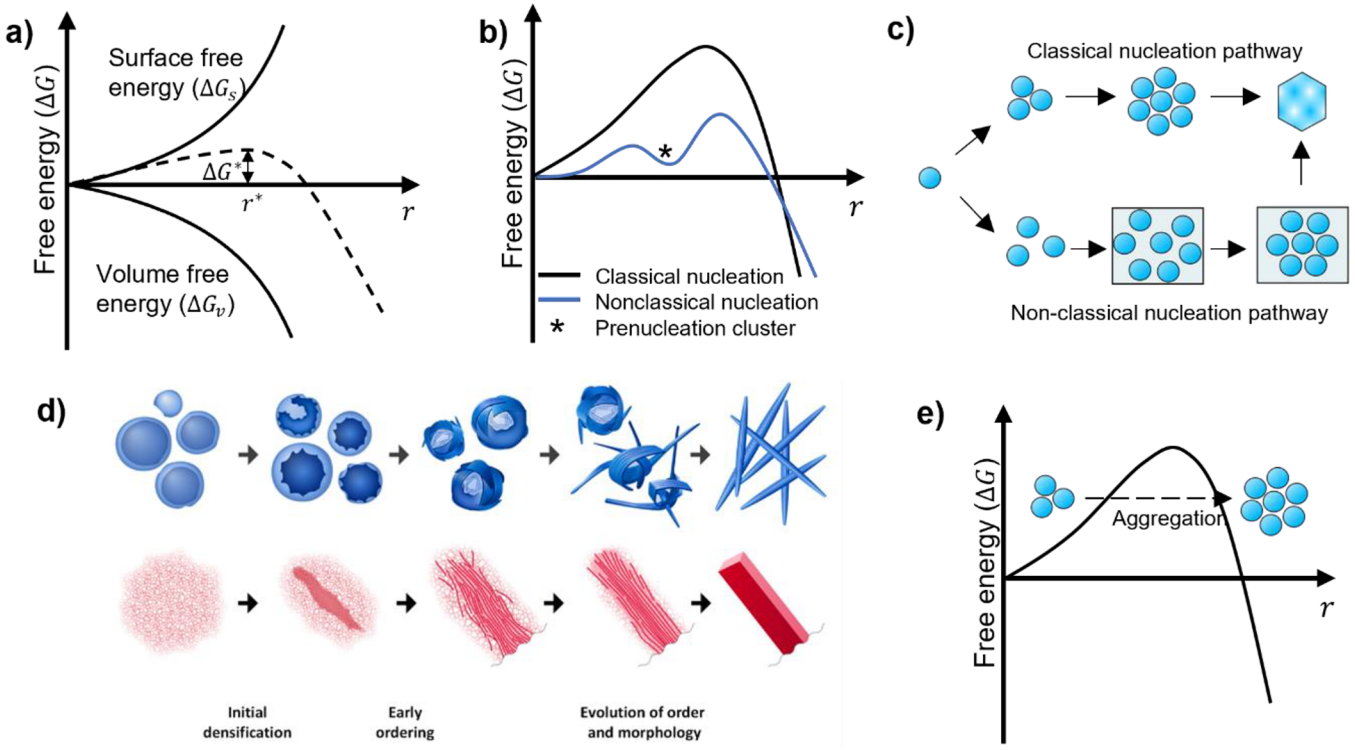

Figure 31. a) The Gibbs free energy diagram for nucleation. b) The free energy landscape comparison for classical nucleation and nonclassical nucleation theories and c) their corresponding schematic illustrations. d) Illustration of molecular assembly process in two types of PDI derivatives in solution. e) Crystallization pathway where the nucleation barrier is bypassed via aggregation of the subcritical nuclei. Figure adapted with permission from ref 370, Copyright 2018 American Chemical Society (d); ref 510, Copyright 2016 Springer Nature (e).

phase separation processes that occur during evaporative solution processing. Crystallization is induced by solvent evaporation during film deposition and is closely tied to the molecular assembly processes discussed in Sections 2 and 3. Meanwhile, the phase separation process is unique to blend systems and determines the microphase-separated structure responsible for efficient charge generation in OSCs. This section aims to demonstrate how phase separation and crystallization pathways, along with film drying conditions, impact the blend film morphology and device properties of OSCs. We will first introduce the fundamentals of solvent evaporation-induced phase transitions, focusing on crystallization and phase separation processes of donor and acceptor materials, and explain how these processes determine blend film morphology. We will then provide specific examples of OSCs emphasizing the importance of molecular assembly, crystallization, and phase separation processes on the morphology and device properties of OSCs. We will also include some examples of how processing conditions can affect these processes. For further reading on similar topics, we recommend referring to previous outstanding reviews.[34,35,183,339] Compared to prior reviews, we will give special emphasis on the molecular assembly of polymer/NFA blends.

4.1. Fundamentals of Crystallization and Phase Separation Processes and Their Impact on the Blend Film Morphology

Since the microstructure of the BHJ-based OSCs plays an essential role in the device performance, it is necessary to understand how it forms and what factors contribute to the formation of BHJ morphology for efficient charge generation and transport. OSCs are typically fabricated using various solution processing techniques such as spin coating, blade coating, and slot-die coating, which involve the use of a blend solution comprising donor and acceptor materials. Thus, the thermodynamics and kinetics of crystallization and phase separation processes during film deposition are the primary factors affecting the BHJ morphology. In this section, we will focus on the fundamentals of these processes and their impact on the blend morphology of OSCs.

4.1.1. Fundamentals of Crystallization. In Sections 2 and 3, we discussed how various molecular assembly pathways can impact the solution-state properties, neat film morphology and optoelectronic properties of conjugated polymers and small molecules. For conjugated polymers, the self-assembly process can lead to various types of aggregated structures in the solution-state which ultimately govern the film morphology, whereas for small molecules, molecular assembly largely impacts the crystal packing structures in the solid-state. Complementary to the molecular views presented in Sections 2 and 3, in this section, we present a thermodynamic and kinetic view of the process of solution crystallization, summarizing both classical and non-classical nucleation theories and illustrate how molecular assembly processes can be involved.

For both conjugated polymers and small molecules, crystallization is induced either by undercooling from the melt or supersaturation from solution. In the case of OSCs, crystallization of conjugated organic molecules occurs via supersaturation upon solvent removal. The simplest theory to describe the crystallization process is the classical nucleation theory which is developed by Gibbs at the end of the 19th century.[508] Although this theory may not apply to conjugated organic molecules, it provides a basic understanding of the nucleation and growth process. According to this theory, the first step of crystallization is the formation of a stable nucleus of

https://doi.org/10.1021/acs.chemrev.2c00905
Chem. Rev. 2023, 123, 8395−8487

critical size which acts as the center of crystallization.[509] Once a stable nuclei is formed, repeat units start to add to the nucleus to form a crystal until there is no remaining crystallizable material or solvent is removed completely. Therefore, the most critical step of crystallization is the nucleation process. However, the formation of a nucleus is thermodynamically unfavorable with a positive free energy change (ΔG) which is equal to the sum of the free energy change of phase transformation (or volume free energy) and the free energy change for the formation of a surface (or surface free energy) as illustrated in Figure 31a. When solubility is exceeded, the volume free energy change is always negative and acts as the driving force for crystallization because the solid-state is more stable than the liquid state; however, the surface free energy change is always positive because forming a surface requires free energy. Quantitatively, the Gibbs free energy change for a spherical nucleus as a function of the radius of the nucleus can be expressed as shown below where the first term corresponds to the volume free energy change whereas the second term represents the surface free energy change:

$$\Delta G = -\frac{4\pi}{3} r^3 \Delta G_v + 4\pi r^2 \gamma \tag{10}$$

where ΔG_v is the bulk free energy change and γ is the interfacial free energy between the nucleus and the surroundings. Based on the equation above, competition between the bulk free energy and the surface free energy terms, therefore, determine the critical nucleus size, r^*, below which the nucleus is unstable and easily dissolve back into the solution:

$$r^* = \frac{2\gamma}{\Delta G_v} \tag{11}$$

Although the formation of a nuclei is determined by thermodynamic factors discussed above, nucleation kinetics is also an important consideration since fast drying during film deposition could kinetically hinder the nucleation process. According to the classical nucleation theory, the steady-state rate of nucleation per unit of volume and time can be generally expressed in terms of Arrhenius equation as shown below:

$$Nucleation rate \propto A^* \exp\left(-\frac{\Delta G}{kT}\right) \tag{12}$$

where k is the Boltzmann constant, and A is a pre-exponential factor that is related to the molecular kinetics of the nucleation process.[511] This equation can be further modified by the Gibbs–Thomson relationship to obtain the rate of nucleation caused by supersaturation which is relevant to solution crystallization:[512]

$$Nucleation rate \propto A^* \exp\left(-\frac{B}{\ln^2 S}\right) \tag{13}$$

where B is a constant related to the nucleation thermodynamics and S is the supersaturation parameter defined as the ratio of the solution concentration and the saturation concentration at a given temperature. This equation implies that increasing supersaturation increases the rate of nucleation in solution. It is important to note that these rate equations apply under the isothermal condition in a closed system where an enclosed solution is quench cooled to surpass the solubility limit and kept at constant temperature and supersaturation level for nucleation to take place. During an evaporative crystallization process relevant to organic electronic solution deposition, mass, momentum and heat transfer closely couple with the crystallization process to determine the spatial and temporal evolution of supersaturation level and nucleation rate. We refer the readers to recent numerical simulation work to describe the process.[513]

Compared to small molecules, the nucleation and growth of polymers are much more complex due to the ability of a single polymer chain to be incorporated into multiple nuclei and the large conformation change (and thus entropic penalty) required for a polymer chain to be incorporated into a nucleus or crystal. As a result, polymers often form far less perfect crystals featuring paracrystalline disorder and coexistence of crystalline with amorphous domains. Depending on the rigidity and molecular weight of the polymer chain, as well as the solidification rate determined by the processing conditions, polymers can either form chain-folded or chain-extended crystallites.[35] For instance, flexible polymers such as P3HT often undergo chain-folding to form 1D nanowhiskers and 2D nanoribbons upon crystallization with the width direction along the backbone and the length direction along the $\pi-\pi$ stacking direction.[514] However, more rigid donor–acceptor conjugated polymers are harder to fold during crystallization, resulting in chain-extended crystallites with the length direction along the backbone and the width direction along the $\pi-\pi$ stacking direction, which is in stark contrast to the chain-folded crystallites.[515] Considering these characteristics, semicrystalline conjugated polymers have been modeled by the fringed-micelle model, which describes their solid-state as bundle-like crystalline polymers with chain-extended structures embedded in an amorphous polymer matrix.[516] One of the most commonly used models to describe the crystal growth kinetics of conjugated polymers is the Hoffman–Lauritzen theory,[517] which is based on a secondary nucleation theory to describe the lamellar growth of chain-folded crystallites. However, for more rigid donor–acceptor conjugated polymers, there is no widely accepted theory to describe the crystallization process due to the complex assembly pathways induced by various intermolecular interactions as discussed in Section 2. For a more extended discussion on characteristics of conjugated polymer crystallization, we refer the readers to our recent review.[293]

Although the above classical nucleation theories are useful in understanding the crystallization process of some materials, they may not directly apply to conjugated polymers and small molecules. The reason is that the assembly pathways of these materials can be highly complex, and crystallization can be a multistep process rather than a simple one-step monomer-by-monomer addition process implied by the classical nucleation theory. As discussed in Sections 2 and 3, conjugated organic molecules, particularly conjugated polymers, can form aggregates of various structures even in dilute solutions, which can then form secondary structures before crystallization. This pathway is nonclassical in that the free-energy landscape of crystallization is rather complicated, with one or more local minimum corresponding to the formation of intermediate structures such as primary and secondary aggregates.[510,518]

One of the most widely known nonclassical nucleation mechanism is a two-step nucleation with one local minimum (Figure 31b) which indicates formation of metastable prenucleation clusters or primary aggregates.[509,519] The formation of such prenucleation aggregates can reduce the energy barrier for nucleation so that nucleation happens at supersaturation levels lower than estimated by the classical nucleation theory.[510] An example of such a two-step process is amorphous-to-crystalline transition, in which molecules first form amorphous aggregates in solution before forming the

https://doi.org/10.1021/acs.chemrev.2c00905
Chem. Rev. 2023, 123, 8395–8487

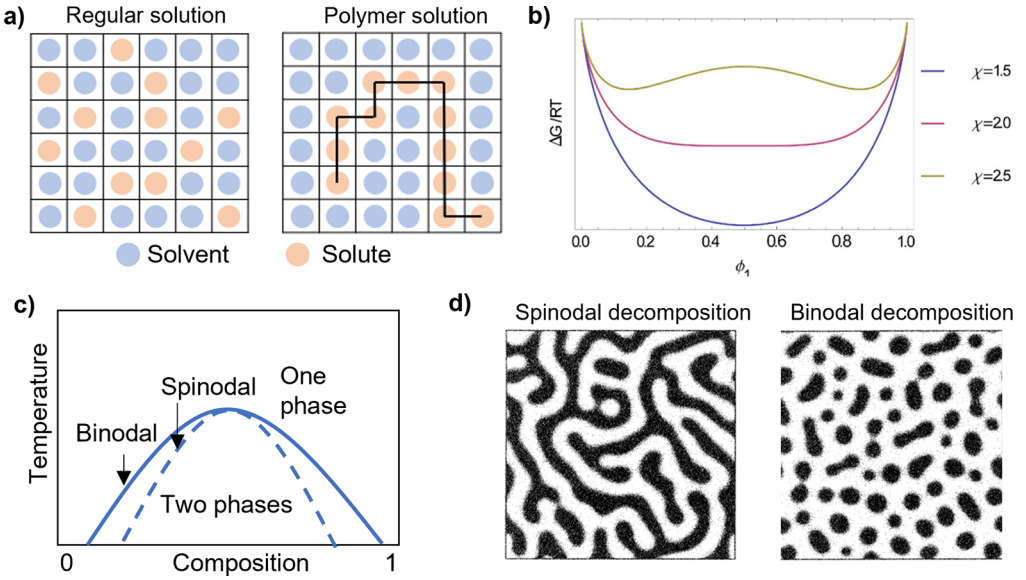

Figure 32. a) Schematic representation of the lattice model which shows regular solution (left) and polymer solution (right). b) The Gibbs free energy diagram as a function of the solute composition at three different χ values. c) Binary phase diagram which displays UCST behavior. d) Simulated morphology for spinodal and binodal phase separation. Figure reproduced with permission from ref 339, Copyright 2017 American Chemical Society (b); ref 529, Copyright 1998 IOP Publishing (d).

crystalline nuclei.[520,521] Figure 31c illustrates this two-step nucleation process in comparison with direct crystallization (classical nucleation) where nucleation happens via monomer-to-monomer addition to form a critical nucleus which further grows to give the final crystallite. Two-step nucleation has been observed in many systems including inorganic nanoparticles,[522] proteins,[523] and colloidal particles.[524] It has also been reported that conjugated small molecules can crystallize via the amorphous-to-crystalline transition.[370,525] In particular, Tsarfati et al. has shown the crystallization mechanism of two derivatives of perylene diimide molecules (PDIs) in solution via direct imaging using cryo-TEM.[370] The authors found that one type of PDI first forms spherical aggregates which then lead to fibrous crystals as illustrated in Figure 31d (top) upon dissolving the PDI molecules in water/tetrahydrofuran mixture. Interestingly, they observed that the other type of PDI first forms an initial diffuse amorphous phase which densifies to form needle-like crystals as illustrated in Figure 31d (bottom). Although these two processes are mediated by two distinct structures of amorphous phases, crystallization in both cases occurs by (1) initial densification resulting in amorphous precursors which then lead to (2) early ordering and (3) concurrent evolution of order and morphology. Compared to direct crystallization where molecules need to overcome a high free energy barrier of nucleation, amorphous-to-crystalline transition requires a much lower free energy barrier and thus occurs more rapidly.[510] This could also be one of the reasons why aggregated polymer ink solutions often lead to improved crystallinity as compared to nonaggregated solutions.[14,15] In particular for conjugated polymers, 3D amorphous network-like aggregates that we discussed in Section 2.2.2 could be crystallizing via the amorphous-to-crystalline transition during solution processing; however, the crystallization pathway of these primary aggregates is unknown and requires further investigation.

Other than having one local minimum in the free energy landscape (two-step nucleation), two or more local minima may occur corresponding to formation of more than one intermediate structures such as secondary or even tertiary aggregates.[518] For conjugated polymers, we have previously discussed that secondary aggregates such as fiber network or LC phases can be formed during evaporative solution processing, typically following formation of primary aggregates. The formation mechanism of these secondary aggregate structures and their crystallization mechanism is not fully understood; it could involve, for instance, self-assembly of polymer nanofibers into orientationally ordered LC phases followed by thin film crystallization, all driven by solvent evaporation and concentration increase.[295] For conjugated small molecules, such a complex concentration-driven assembly pathway is rarely reported since small molecules typically have lower molecular weight and weaker intermolecular interactions in the solution-state. Nevertheless, some perylene diimide based molecules have shown lyotropic LC phases in solution, indicating that their assembly pathways can be as complex as conjugated polymers.[526]

Although the nuclei or intermediate structures are thermodynamically unstable, it is possible for them to be kinetically stabilized via aggregation.[510,527] This occurs when the collision rate of molecules is faster than the dissolution rate, or when the molecules tend to readily aggregate via strong intermolecular interactions. In such cases, two or more subcritical nuclei ($r < r^*$) can combine to form postcritical nuclei ($r > r^*$), which is past the critical free energy barrier as shown in Figure 31e.[510] Once the aggregates with sizes above the critical radius are formed, they become stable and do not dissolve back into the solution, even at low supersaturation. For instance, the semicrystalline 1D fiber-like aggregates of conjugated polymers discussed in Section 2 may be stabilized by the strong intermolecular interactions even if they are not thermodynamically stable. In many cases, metastable structures can be stabilized by kinetic factors, thus making it complicated to understand the exact crystallization mechanism of conjugated organic molecules undergoing molecular assembly processes.

Furthermore, solvent drying kinetics is also important for crystallization as it sets the duration for phase transition as well as the temporal profile of concentration. Let us take the two-step

https://doi.org/10.1021/acs.chemrev.2c00905
Chem. Rev. 2023, 123, 8395−8487

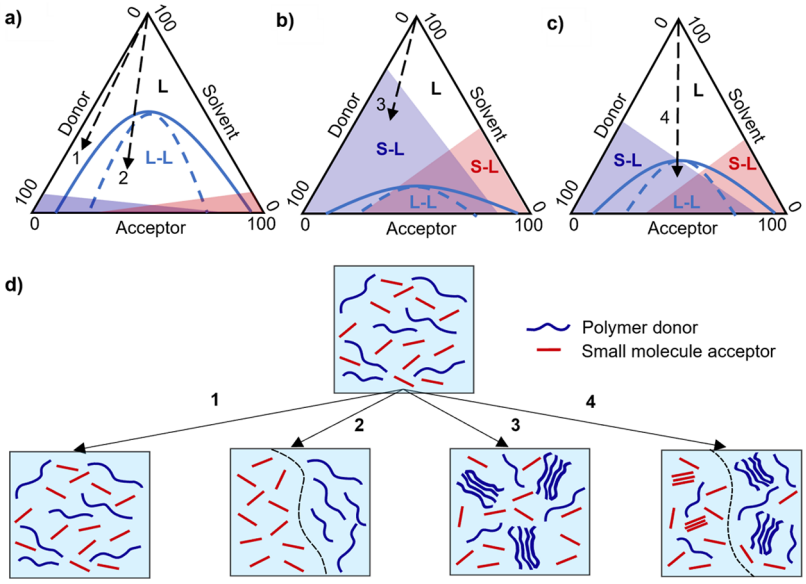

Figure 33. Ternary phase diagram composed of donor, acceptor, and solvent for a) a system with good solubility and low miscibility and b) a system with poor solubility and high miscibility, c) a system with partial miscibility and medium solubility. The dashed arrows indicate the phase separation pathways upon solvent removal and the colored region indicates the solubility limit for the donor and acceptor materials inside which S−L phase transition can occur upon crystallization of the components. d) Schematics of phase separation pathways corresponding to the dashed arrows from the ternary phase diagrams. The blue background represents solvent.

amorphous-to-crystalline transition of conjugated organic molecules for instance. Although this transition has a lower free energy barrier than direct crystallization, nucleation can still be kinetically hindered due to fast solvent removal, resulting in poorly crystalline or amorphous thin films. The same principle can be applied to systems that exhibit multistep assembly processes such as liquid crystalline mediated pathways. Any step during this multistep assembly process can be kinetically hindered, resulting in thin films that are either governed by the LC phase or the aggregated phase prior to the formation of LC phase. In addition to drying kinetics, crystallization of conjugated organic molecules during solution processing is also sensitive to many other parameters such as temperature, solution printing speed or regime, substrate chemistry, and confinement which have been extensively reviewed in other works.[293,528]

4.1.2. Fundamentals of Phase Separation. The phase separation behavior between the donor and acceptor materials is largely determined by their relative miscibility which can be explained using the Flory−Huggins theory, derived from a lattice-based model. Figure 32a represents how solvent and solute molecules are arranged on a lattice for regular solutions such as a solution of small molecules in comparison with polymer solution. The main distinction between a regular solution and a polymer solution is the number of possible rearrangements of the solute and solvent molecules on the lattice site, which determines the entropy of mixing. A polymer solution has a lower entropy of mixing than regular solution because polymer molecules have fewer rearrangements on the lattice as compared to small molecules. In addition to the entropy of mixing, solvent and solute molecules form attractive or repulsive interactions, resulting in the enthalpy of mixing. Combining these two terms, the Gibbs free energy of mixing per unit volume for a solution with single solute component can be derived as shown below:

$$\frac{G}{RT} = \phi_1 \ln \phi_1 + \frac{\phi_2}{N} \ln \phi_2 + \phi_1 \phi_2 \chi \tag{14}$$

where ϕ_1 and ϕ_2 are the volume fractions of the solvent and the solute respectively, χ is the Flory−Huggins interaction parameter between the solvent and the solute which is dependent on temperature, and N is the degree of polymerization for a polymer solute. If the solute is a small molecule instead of a polymer, N is equal to 1. The first two terms in this equation are related to the entropy of mixing, which, as previously stated, arises from the number of different arrangements of the solvent and solute components on a lattice and thus always acts to promote mixing. The entropy term for a polymer is less than that of a small molecule since the N factor is much larger than 1. The last term in the equation above represents the enthalpy change during mixing, which can either oppose mixing, promote mixing, or form ideal mixtures. Whether this enthalpic term is favorable for mixing is primarily determined by the Flory−Huggins interaction parameter, χ. A negative value for χ indicates that there is a net attraction between species, increasing the miscibility of the components, whereas a positive value indicates that there is a net repulsion, which can lead to phase separation of the components.[189] Furthermore, based on this equation, the Gibbs free energy as a function of the solute composition at different χ values can be graphed shown in Figure 32b.[339] Depending on the value of the interaction parameter, the diagram exhibits either one or two minima, implying the likelihood of phase separation in solution. At equilibrium, the chemical potential of each species $\left(\frac{\partial \Delta G}{\partial \phi_i}\right)$ should be equal in each phase. For systems that exhibit one minimum, the minimum is the only condition which satisfies this requirement; therefore, no phase separation takes place. However, for systems that exhibit two minima, phase separation can occur depending on the initial condition. For starting

https://doi.org/10.1021/acs.chemrev.2c00905
Chem. Rev. 2023, 123, 8395−8487

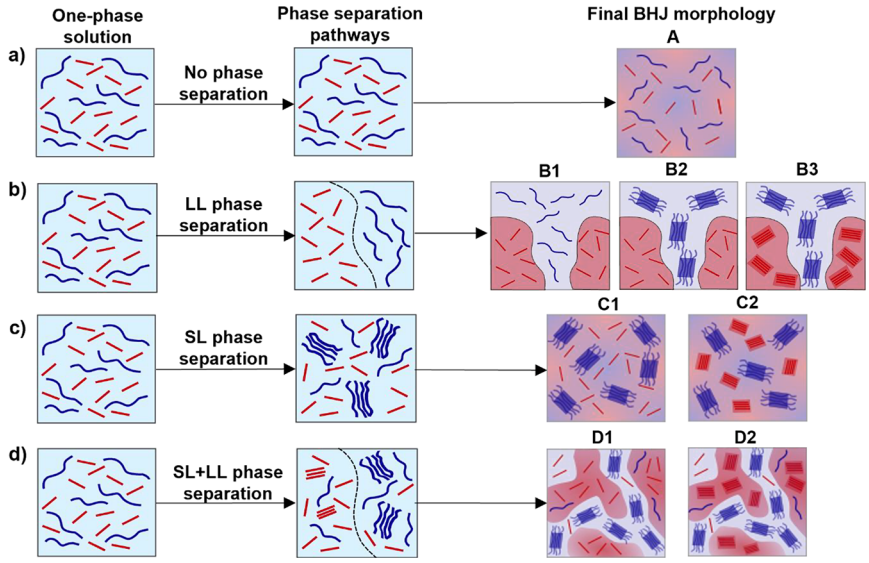

Figure 34. Schematic representation of various phase separation and crystallization pathways and their corresponding BHJ morphologies where mesh-colored regions indicate mixed phases, whereas solid colors indicate pure phases. One-phase solution undergoing a) no phase separation, b) L−L phase separation, c) S−L phase separation, d) S−L and L−L phase separation.

positions above the inflection points $\left(\frac{\partial^2 \Delta G}{\partial^2 \phi_i} > 0\right)$ phase separation will occur spontaneously.

Since the interaction parameter χ is dependent on temperature, the Gibbs free energy diagram can be converted to the commonly used binary phase diagram of temperature versus composition as shown in Figure 32c, which displays a solution with an upper critical solution temperature (UCST) feature. In other words, the phase diagram exhibits a maximum point or the critical temperature, above which the solution exists as a homogeneous phase at all concentrations. It is also possible for a solution to exhibit a lower critical solution temperature (LCST) feature depending on the relationship between temperature and the interaction parameter χ. However, regardless of whether the solution exhibits UCST or LCST the phase diagram represents three regions divided by the binodal and spinodal curves. The binodal curve separates the homogeneous (one phase) phase from the phase-separated (two-phase) region while the spinodal curve separates the stable and unstable regions within the two-phase region. If the initial solution composition falls within the spinodal curve, the solution becomes unstable and leads to spontaneous phase separation of solvent-rich and solute-rich phases, a process known as spinodal decomposition. Within this unstable region, small fluctuations in concentration drive large-scale liquid−liquid (L−L) phase separation as displayed in Figure 32d (left). On the other hand, if the initial solution composition lies within the metastable regime or in between the spinodal and binodal curves, small concentration fluctuations are not enough to drive phase separation into the binodal. Instead, L−L phase separation occurs by the nucleation and growth mechanism, resulting in droplet like phase-separated structures shown in Figure 32d (right).[529]

In OSCs, the situation becomes more complicated since the solution is a mixture of three components which are solvent (S), donor (D), and acceptor (A). In this case, the Flory−Huggins equation includes additional terms in both its entropic and enthalpic contributions to reflect these three components in the system as shown:[34,530]

$$\frac{G}{RT} = \phi_s \ln(\phi_s) + \left(\frac{\phi_D}{N_D}\right)\ln(\phi_D) + \left(\frac{\phi_A}{N_A}\right)\ln(\phi_A) + \chi_{SD}\phi_S\phi_A + \chi_{SA}\phi_S\phi_A + \chi_{DA}\phi_D\phi_A \quad (15)$$

Like the binary phase diagram, a ternary phase diagram (Figure 33a) of solvent, donor, and acceptor mixture can be constructed from the equation above. Different from the binary phase diagram which represents phase separation as a function of temperature, in the ternary phase diagram, phase separation is induced by solvent removal as indicated by the dashed arrows in Figure 33a. The dashed arrows represent two phase separation pathways of the blend solution upon solvent removal which are (1) no phase separation, (2) L−L phase separation which can be either due to nucleation and growth or spinodal decomposition. In addition to L−L phase separation, solvent removal can lead to solute molecules to aggregate or crystallize upon reaching their solubility limit as indicated by the dashed arrow (3) in Figure 33b. This type of phase separation is often referred to as solid−liquid (S−L) phase separation or crystallization which can occur after the components reach their solubility limits and when the components are highly miscible. If the components reach the two-phase region and their solubility limits at the same time as shown in Figure 33c, it is also possible for both S−L phase separation and L−L phase separation to take place at the same time or sequentially. In this case, the relative kinetics of these two processes will dictate which phase separation process will dominate. For instance, if crystallization is rapid, the donor and acceptor materials crystallize first after reaching their solubility limit, thereby possibly delaying significant L−L demixing. On the other hand, if the crystallization of the components is kinetically hindered even after reaching their solubility limit, L−L phase separation will dominate the phase separation process followed by crystallization of the components. Figure 33d displays these four phase separation pathways where (1) no phase separation, (2) L−L phase separation, (3) S−L phase separation, and (4) the combination of S−L and L−L phase separation. In fullerene-based OSCs, L−L phase separation is commonly reported due to the tendency of fullerenes to vitrify during solidification, resulting in domains that lack long-range

https://doi.org/10.1021/acs.chemrev.2c00905
Chem. Rev. 2023, 123, 8395−8487

order in the solid-state.[35] Meanwhile, S−L phase separation is commonly observed in nonfullerene based OSCs due to the likelihood of nonfullerene acceptors to crystallize during film deposition and their improved miscibility with the donor polymers compared to fullerenes. We will later discuss how each of these phase separation pathways combined with the crystallization behavior of the components and drying kinetics can impact the blend morphology of OSCs in Section 4.1.3.

4.1.3. Effect of Phase Separation and Crystallization Pathways on the Blend Film Morphology. During solution processing, both crystallization and phase separation processes described earlier play an important role in determining the blend film morphology. These processes are largely influenced by thermodynamic and kinetic factors such as miscibility, solubility, crystallization rate as well as film drying kinetics. In this section, we will summarize how these factors could impact phase separation and crystallization pathways and determine the final film morphology. First, let us consider the thermodynamic factors that affect phase separation and crystallization processes, which are determined by the miscibility and crystallization tendency of the donor and acceptor materials. In the simplest case, if the donor and acceptor materials are miscible and both are noncrystallizable, no phase separation takes place and the resulting BHJ morphology will exhibit an intimately mixed amorphous domains of donor and acceptor materials as shown in Figure 34a. On the other hand, if the materials are immiscible or poorly miscible, L−L phase separation will likely dominate the phase separation process, and the components will then crystallize within their respective domains upon reaching their saturation limits.[531,532] Studies have shown that if phase separation is dominated by L−L demixing, the final blend film leads to large donor and acceptor domains due to their strong repulsive interactions or poor miscibility.[530,533] The BHJ films that are formed via L−L demixing (spinodal decomposition or nucleation and growth mechanisms) often lead to domains that are at least an order of magnitude higher than the exciton diffusion length, which significantly reduces the probability of charge separation.[534] This type of large scale L−L demixing has been observed in polymer:fullerene systems in which fullerene molecules form large droplet-like amorphous domains.[535−537] Shown in Figure 34b is the illustration of L−L phase separation process followed by crystallization of the components leading to three possible blend film morphologies depending on the crystallization tendency of the components. If both components are noncrystallizable or amorphous, the final BHJ morphology forms large-scale phase-separated amorphous domains (B1). If only one of the components is crystallizable, crystallization will take place in the phase rich in the crystallizable component, leading to a mixture of large crystalline and amorphous domains (B2). On the other hand, when both components are crystallizable, crystallization can take place sequentially in their respective domains after L−L phase separation, forming large crystalline domains (B3). Besides forming large domain sizes, each domain is overly pure and forms sharp interfaces due to the poor miscibility of the components.[538]

When the donor and acceptor materials are highly miscible and one or both components are crystallizable, crystallization (S−L phase separation) can occur preceding L−L phase separation (Figure 34c). Depending on the crystallization behavior of the donor and acceptor materials, two possible scenarios can happen. If one of the components is noncrystallizable or amorphous, it can be excluded from the crystalline region of the other component to the mixed region as shown in C1.[539,540] This process is driven by entropy since molecules can move freely outside the closely packed region. However, if this process is diffusion limited, the amorphous component will accumulate in the crystalline region, thereby lowering the rate of crystallization of the other material.[541] On the other hand, if two crystallizable materials are present but have different crystallization rates, then the material with higher crystallization rate will crystallize first followed by the other component, leading to sequential crystallization. The slow crystallizing component, therefore, can either crystallize in a confined environment such as the interlamellar regions or is excluded out of the crystallized regions to form separate crystalline regions. If diffusion is rapid and crystallization is slow, segregated crystallization occurs, but if diffusion is slow and crystallization is rapid, crystallization occurs in the interlamellar region of the other component.[531,542,543] C2 from Figure 34c illustrates the blend film morphology for the rapid diffusion case where the two components form segregated crystalline domains surrounded by intermixed regions. In partially miscible polymer:fullerene OSCs, Kohn and Hüttner et al. observed a displacement of PCBM molecules into the interlamellar region of P3HT, leading to 10 nm-wide lamellar domains.[544] Interestingly, these authors reported that the crystallinity of P3HT is not affected by the displacement of PCBM into P3HT, but instead crystallization of PCBM is hindered by the miscibility of PCBM and P3HT which explains why PCBM typically leads to amorphous domains in polymer:fullerene OSCs causing the donor polymer crystallization to determine the blend film morphology.[545]

In partially miscible systems with at least one crystallizable component, S−L phase separation can also couple and concur with L−L phase separation as shown in Figure 34d. In this case, rather than thermodynamics, kinetics of these two processes determines the final morphology. If S−L phase separation is kinetically favored, the components would crystallize first, thereby changing the composition of the remaining liquid phase to higher solvent content which could delay L−L phase separation.[34] Eventually this delayed L−L phase separation would result in smaller phase-separated domains as compared to large-scale phase-separated morphology of immiscible/poorly miscible system as previously discussed. D1 and D2 from Figure 34d show the hypothetical blend film morphologies corresponding to this type of phase separation pathway depending on whether one or both components are crystallizable. Besides forming small domain sizes, due to the partial miscibility of the components, this type of morphology could also contain mixed domains and rougher interface as compared to the morphology caused by L−L phase separation.[538] If, on the other hand, crystallization is kinetically hindered, the film morphology will likely lead to large phase-separated domains shown in Figure 34a. Therefore, inducing S−L phase separation by depleting the solutes via aggregation or crystallization delays large-scale L−L demixing and yields smaller donor and acceptor domains which are favorable for charge generation.[34] Due to this reason, poor solvent additives have been successfully utilized to decrease the domain sizes of large droplet-like domains of polymer:fullerene based OSCs to facilitate early solution aggregation.[537,546,547]

Although thermodynamic parameters determine the equilibrium state morphologies, kinetics of these processes relative to the solvent drying time eventually sets the extent of phase separation and crystallization processes. For instance, when solvent dries too fast, there is not sufficient time for either crystallization or phase separation to occur, leading to an

https://doi.org/10.1021/acs.chemrev.2c00905
Chem. Rev. 2023, 123, 8395−8487

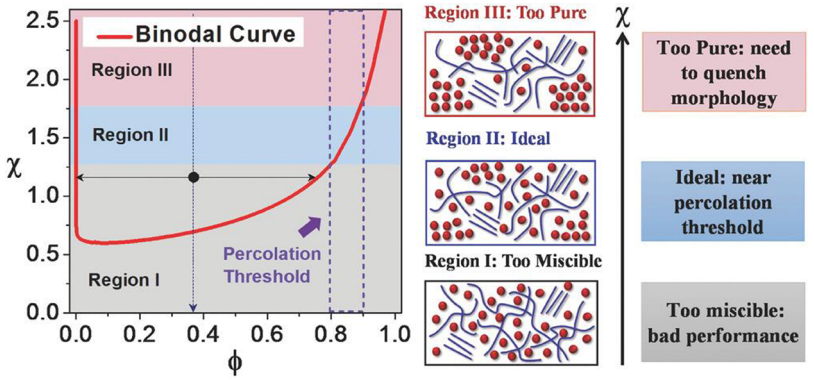

Figure 35. Schematic illustration of three regimes in the $\chi-\phi$ diagram. The three regimes represent cases when χ values are high, medium, and low and the percolation threshold is indicated by the purple dashed lines. Figure adapted with permission from ref 185, Copyright 2018 John Wiley and Sons.

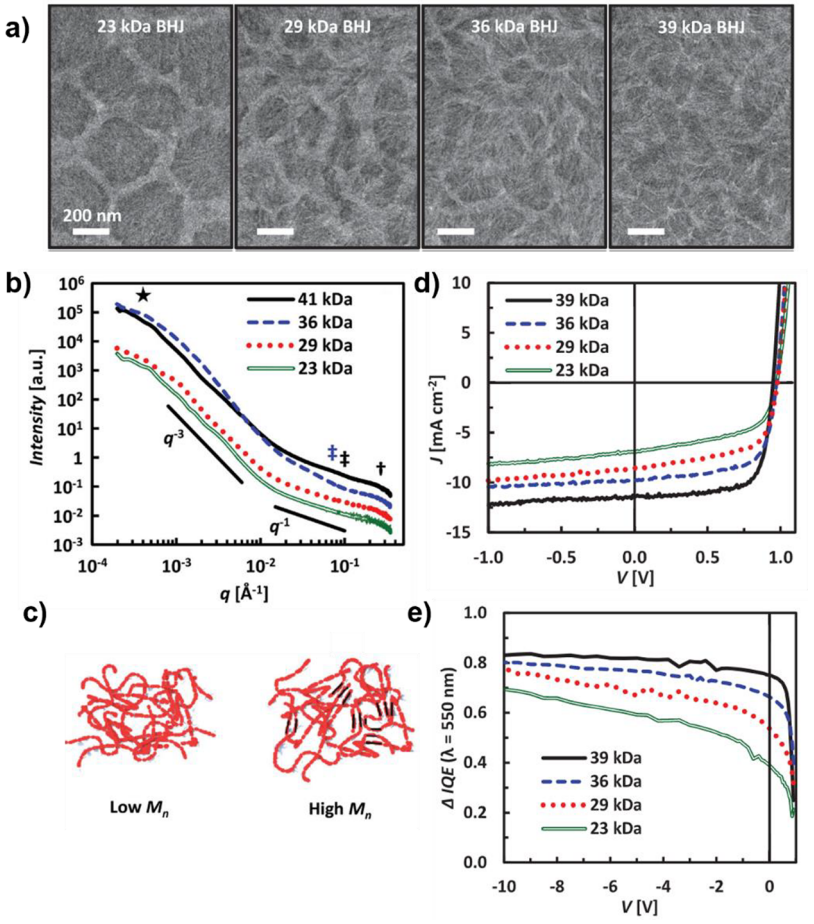

Figure 36. a) TEM images of PBDTTPD:PCBM[70] blend films processed in chlorobenzene with different molecular weights as indicated. b) Combined USAXS and SAXS measurement intensity versus the scattering vector, q, for PBDTTPD dissolved in chlorobenzene solution. The intermediate Guinier knee region is indicated by black and blue daggers for the 36 and 41 kDa solutions. c) Illustration of polymer aggregation in low M_n and high M_n solutions. d) Current density versus voltage characteristics for PBDTTPD:PCBM[70] based solar cells processed from chlorobenzene. e) The differential internal quantum efficiency versus applied bias voltage. Reproduced with permission from ref 537, Copyright 2014 John Wiley and Sons (a–e).

intermixed morphology similar to the case of highly miscible amorphous components (A from Figure 34a). However, different from A, such a morphology is kinetically trapped; therefore, upon thermal annealing, the blend morphology will reach its thermodynamic equilibrium state as determined by the miscibility and crystallizability of the components. For a system dominated by L–L phase separation, both experimental and simulation results have shown that increasing the drying time increases the phase-separated domain sizes, which could be detrimental to charge generation.[548] On the other hand, S–L phase separation dominated systems, increasing the drying time will likely enhance the crystallization of the components by allowing for sufficient time for crystallization, but this could also lead to large crystalline domains that are unfavorable for charge generation. For a system where both S–L and L–L phase separation occur, studies have shown that increasing the solvent

https://doi.org/10.1021/acs.chemrev.2c00905
Chem. Rev. 2023, 123, 8395–8487

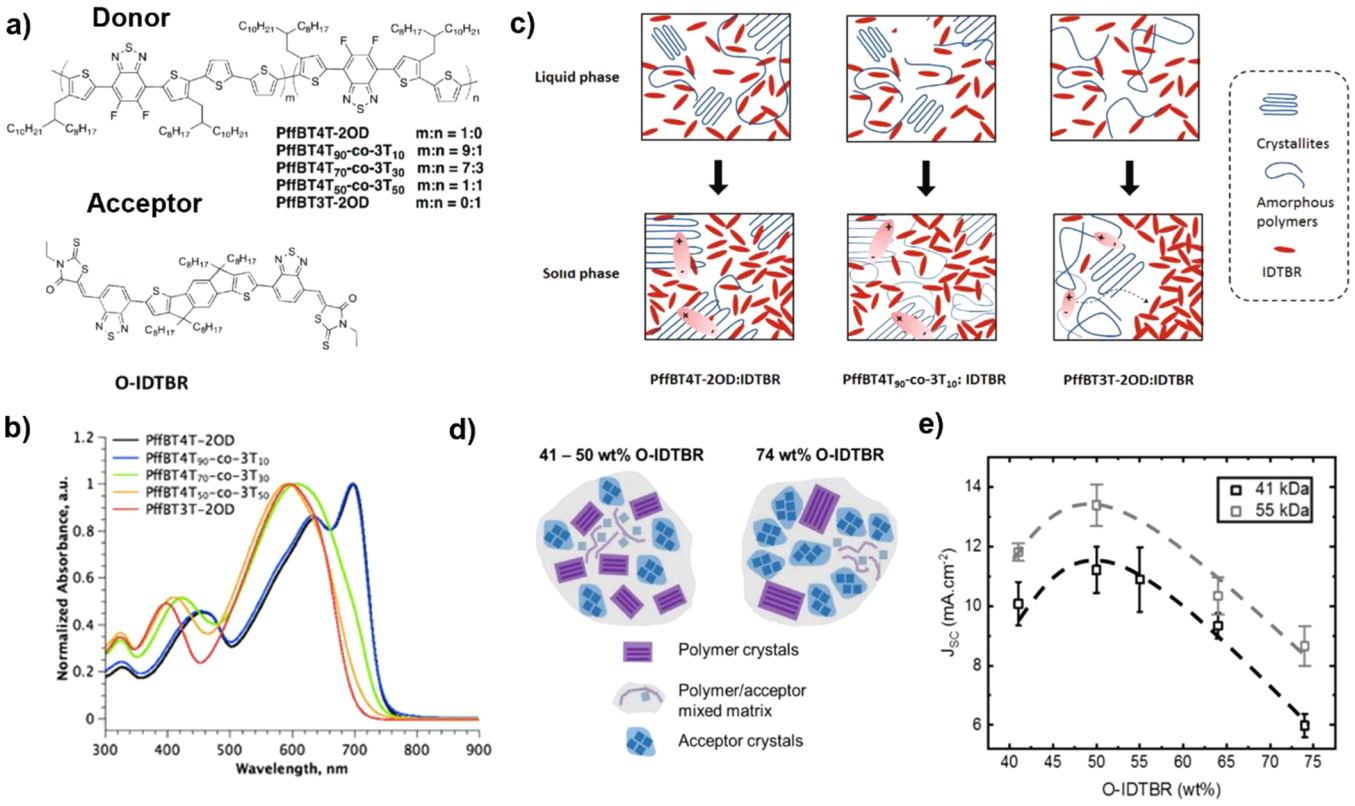

Figure 37. a) Chemical structures of the polymer donors and acceptor molecule, O-IDTBR. b) Solution UV−vis spectroscopy of the donor polymers illustrating the extent of aggregation in the solution. c) Illustration of the phase separation pathways and the resulting blend film morphologies. d) Schematic representation of PffBT4T-2OD:O-IDTBR blend films with different acceptor contents. e) J_{SC} versus O-IDTBR content. Figure adapted from ref 506, Copyright 2020 John Wiley and Sons (a, c); ref 554, Copyright 2018 American Chemical Society (b); ref 555, Copyright 2020 John Wiley and Sons (d, e).

drying time could be effective for enhancing the crystallization and delaying L−L demixing, thereby yielding small phase-separated domains in the blend film.[533]

In addition to the domain sizes and crystallinity of the blend film, domain purity and composition of the mixed phase region is critical for the device performance of OSCs and largely depend on the miscibility of the donor and acceptor materials.[185,186,549] In particular, the best performance can be achieved when composition of the mixed region is near the percolation threshold.[185,507] However, in a system with high miscibility of donor and acceptor materials with impure domains, the composition of the mixed region cannot reach the percolation threshold and thus leads to high charge recombination and low FF.[507] Region I from Figure 35 demonstrates a system with high miscibility (low interaction parameter, χ) where the maximum achievable purity as indicated by the binodal composition is below the percolation threshold. Similarly, the system with poor miscibility (region III) exhibits an overly pure mixed phase which is also prone to significant device performance loss. In this case, the morphology needs to be kinetically quenched (e.g., rapid drying) near the percolation threshold for efficient charge transport. On the other hand, such a kinetically trapped morphology is thermodynamically unstable and prone to over purification that can lead to significant loss of device performance or burn-in degradation.[180] Recently, however, Ghasemi and Ade et al. showed that the stability of hypo-miscible (high χ) systems depend on the activation energy of diffusion of the acceptor to the polymer donor phase.[186] Therefore, even though hypo-miscible systems are thermodynamically unstable, they can be kinetically stabilized if NFAs exhibit high activation energy of diffusion. Nevertheless, the best device performance and stability can be obtained when the miscibility lies within region II in Figure 35 where the equilibrium composition of the mixed phase is close to the percolation threshold.

4.2. Impact of Assembly Processes and Processing Conditions on BHJ Morphology and Device Properties

In Section 4.1, we discussed the fundamental principles of crystallization and phase separation processes and how they can affect the blend film morphology of OSCs. In this section, we will delve deeper into these concepts and provide relevant examples from the existing literature on OSCs. We will focus on how the molecular assembly of donor and acceptor molecules in blend systems is closely related to phase separation processes, and how their relative crystallization behavior and miscibility can influence the blend morphology and device performance of OSCs. Additionally, we will explore how processing conditions can impact phase transition. By analyzing these various factors, we can gain a comprehensive understanding of how they collectively impact the morphology and device properties of OSCs.

4.2.1. Impact of Donor Polymer Assembly. In polymer:-fullerene based OSCs, large droplet-like domains are typically observed, leading to large scale L−L phase separation.[530,535,537] However, donor polymer aggregation in solution can influence the blend film morphology by changing the phase separation pathway from L−L demixing to S−L phase separation.[530,533]

https://doi.org/10.1021/acs.chemrev.2c00905
Chem. Rev. 2023, 123, 8395−8487

For instance, Bartelt and McGehee et al. investigated the effect of molecular weight of the donor polymer on BHJ morphology and device properties of PBDTTPD:PCBM[70] system.[537] Shown in Figure 36a is the TEM images of the blend films of PBDTTPD:PCBM[70] system cast from varying molecular weight (M_n) of the PBDTTPD polymer. With increasing M_n of the donor polymer, the blend film morphology changes from forming large fullerene-rich domains to small fibrillar network-like domains, which resulted in a substantial enhancement in the *PCE* (Figure 36d). Investigating the solution-state aggregation of the polymer at different M_n using a combined USAXS and SAXS measurement, the authors found that high M_n polymer solutions exhibit Guinier knees in the intermediate scattering region marked by the double daggers in Figure 36b which are attributed to the formation of small, ordered aggregates. Low M_n polymer solutions, on the other hand, do not show these bumps in the intermediate q regime, implying that these polymers only lead to agglomerates of single polymer chains (Figure 36c). This result indicates that the polymer with high M_n has a stronger tendency to self-assemble in solution, and the resulting ordered aggregates act as seed sites to initiate polymer aggregation during film deposition and facilitate the formation of polymer fibrils. Further investigating the cause of the poor performance in the low M_n polymer system, the authors discovered that low molecular weight devices suffer from significant amounts of geminate recombination as evidenced by the differential (internal quantum efficiency) *IQE*, Δ*IQE*, which varies significantly with respect to the bias voltage (Figure 36e).[550−553] This increased recombination loss is attributable to the extensive phase separation of low M_n blend films which leads to overly pure domains. The formation of overly pure domains is detrimental to the device performance of OSCs as it indicates that the concentration of PCBM[70] in the mixed regime is below the percolation threshold.[537] Similarly, Qian and Hou et al. showed that the primary solution-state aggregation is beneficial for forming proper domain sizes in the blend film although it has little Influence on the molecular orientation and crystallinity of the blend.[505] Compared to the previous case, these authors modified the extent of solution-state aggregation by thermally treating the solution at 90 °C and cooling back to 30 °C before spin coating, which reduced the solution-state aggregation. When the thermally treated solution was used to fabricate polymer:fullerene based OSCs, the device performance was reduced from 6.67% to 4.72%, clearly indicating the importance of primary solution-state aggregation of polymers on the device performance of polymer:fullerene based OSCs.

In polymer:NFA systems, L−L phase separation can also occur if the donor and acceptor materials exhibit poor miscibility. In this case, donor polymer aggregation can affect the phase separation pathways, which in turn dictate the morphology and device performance of OSCs. For instance, Yi and So et al. demonstrated that donor polymer aggregation ensures proper domain sizes and purity in the blend film by inducing early S−L phase separation and preventing L−L phase separation.[506] Shown in Figure 37a is the molecular structures of the donor polymers and the small molecular acceptor, O-IDTBR used in this work. The authors infer that PffBT4T-2OD and PffBT4T$_{90}$-co-3T$_{10}$ polymers exhibit strong aggregation tendency as compared to PffBT3T-2OD revealed by their red-shifted UV−vis spectra exhibiting fine vibronic features (Figure 37b).[554] Due to its weak aggregation tendency in solution, PffBT3T-2OD:IDTBR system undergoes L−L demixing, forming highly purified domains that limit exciton dissociation and charge transport similar to the polymer:fullerene systems as previously discussed. On the other hand, the strongly aggregating polymers undergo fast aggregation prior to L−L phase separation, thereby forming smaller donor−acceptor domains which lead to stronger PL quenching and more efficient exciton dissociation (Figure 37c). The authors also find that the strongly aggregating polymers showed good miscibility with the NFA, leading to well-mixed domains which promote both charge generation and transport. Similarly, using the strongly aggregating donor polymer (PffBT4T-2OD) and the same acceptor molecule, IDTBR, Hamid and McCulloch et al. found that L−L phase separation can occur in this system when the acceptor content in the blend solution is increased (Figure 37d). At low acceptor content, polymer aggregation dominates phase separation, whereas at high acceptor content, L−L demixing dominates the microstructure formation, resulting in highly pure isolated large domains which substantially decreased the J_{SC} (Figure 37e).[555]

L−L phase separation, however, is not commonly observed in polymer:NFA systems since donor polymers exhibit higher miscibility with NFAs than with fullerenes due to their structural similarity[556] and matching surface energies.[557,558] This suggests that in polymer:NFA systems, S−L phase separation or crystallization of the donor and acceptor materials likely dominate the blend film morphology; therefore, the final morphology will strongly depend on the assembly of neat materials including their aggregation and crystallization behavior. Prior studies suggest that excessive aggregation and crystallization of donor polymers is detrimental to the device performance of polymer:NFAs as they can lead to large domains that limit charge generation.[559−561] A notable work done by Li and Yan et al., therefore, has proposed that donor polymers with reduced crystallinity match better with NFAs.[560] By simply changing the position of the fluorine substitution group of highly crystalline PTFB-P polymer, these authors synthesized donor polymer, PTFB-O, with reduced crystallinity which enhanced the device performance from 7.85% to 10.13% when blended with a small molecule acceptor, ITIC. This improved device performance was mainly attributed to forming smaller domain sizes which led to more efficient PL quenching and an improved J_{SC}. Meanwhile, in polymer:fullerene based OSCs, PTFB-O showed a much lower *PCE* of 6.53%. Similarly, several studies have achieved proper domain sizes in polymer:NFA systems by reducing the crystallinity and aggregation property of the donor polymers via molecular design.[562−564] For instance, Yan and co-workers synthesized two donor polymers (PfBTAZ and PfBTAZS) which have nearly identical chemical structures with the only difference being the regiochemistry of the alkyl chains.[564] Although the crystallinity of the two polymers is nearly identical based on their neat film GIWAXS, the domain sizes almost doubled in the PfBTAZ:O-IDTBR system. Using neat film characterization of PfBTAZ with AFM imaging, the authors suggest that this polymer tends to aggregate into large polymer fibers ranging from 100 to 200 nm whereas PfBTAZS shows much smaller surface features (30−50 nm) suggesting that the strong aggregation property of this polymer is responsible for the large domains observed in the blend film.

To avoid forming large domains in the blend, Yan and co-workers suggest that using donor polymers with temperature-dependent aggregation (TDA) property can give highly crystalline and yet reasonably small polymer domains in both polymer:fullerene and polymer:NFA systems.[275] Polymers with TDA property can be fully disaggregated at high temperatures;

https://doi.org/10.1021/acs.chemrev.2c00905
Chem. Rev. 2023, 123, 8395−8487

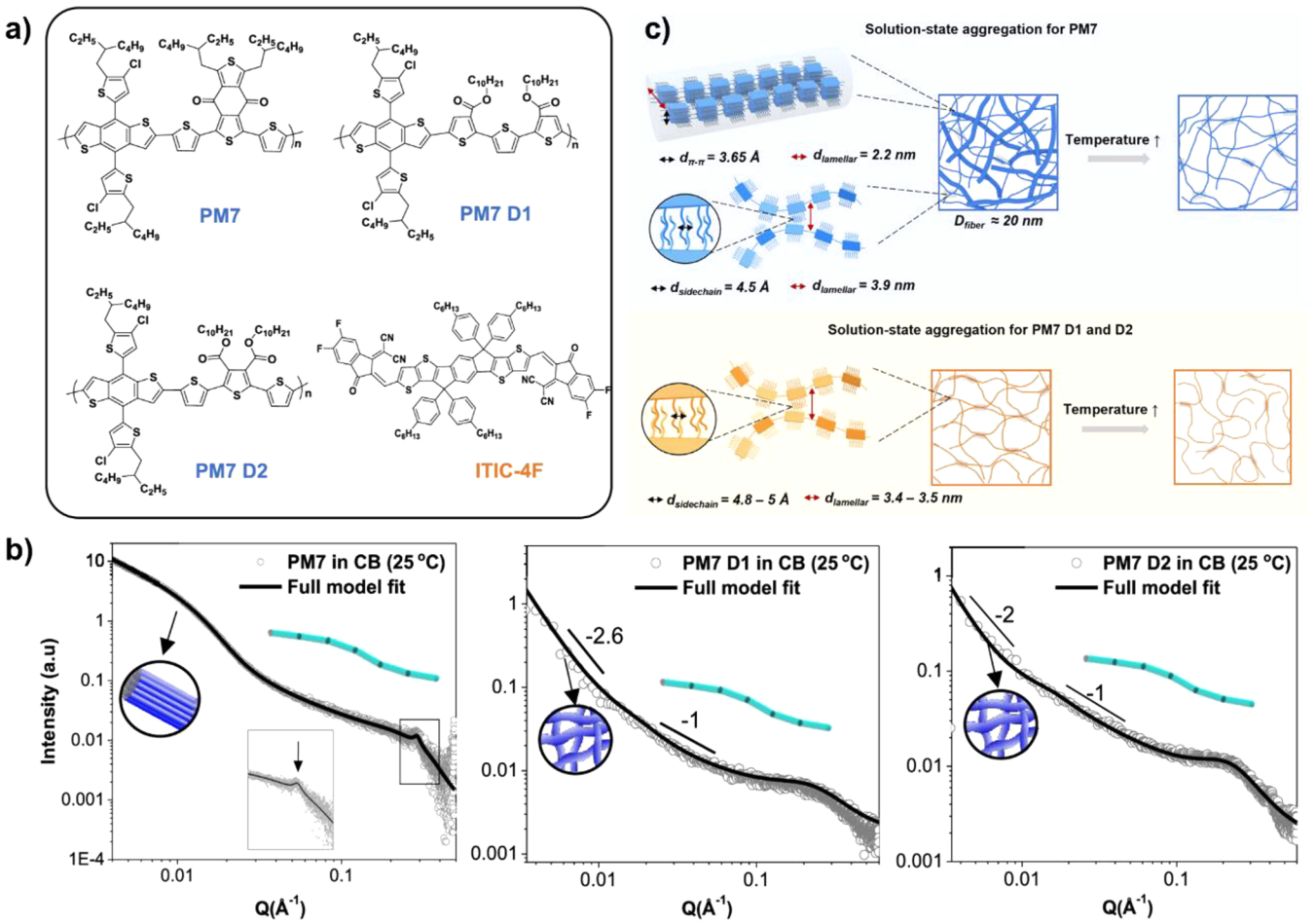

Figure 38. a) PM7, PM7 D1, and PM7 D2 molecular structures. b) SAXS profiles for PM7, PM7 D1, and PM7 D2 solutions. c) Schematics showing the aggregate structures of PM7 as a comparison with PM7 D1 and D2 polymers. Figure adapted with permission from ref 301, Copyright 2023 American Chemical Society (a, b, and c).

however, upon cooling at room temperature during film deposition they can form highly crystalline but reasonably small domains in the blend film which are beneficial for efficient charge generation and transport.[275,280,565] TDA property of donor polymers is often inferred from the temperature-dependent UV−vis spectroscopy in which a drastic blueshift occurs in accordance with the disappearance of the vibronic fine features with increasing temperature, indicating disaggregated solution.[32,566] Although TDA approach has been utilized in many polymer:fullerene[280,504,505] and polymer:nonfullerene[275,565−567] systems to achieve highly crystalline phases with proper domain sizes, several reports suggest that it may not be appropriate for controlling the morphology in all-polymer based OSCs.[568−570] Furthermore, research studies also show that when using donor polymers with TDA property, careful tuning of processing parameters, particularly processing temperature, is often required for the optimal morphology and device performance, making it challenging to control the morphology.[339,571] To overcome this issue, Seo and Kim et al. has synthesized PBDB-Bz donor polymer by replacing the thienyl side chains of PBDB-T with side chains with extended 2D conjugation which led to strong aggregation behavior in solution independent of the solution temperature as compared to PBDB-T which exhibits TDA property.[572] When blended with P(NDI2OD-T2) polymer acceptor, PBDB-Bz:P(NDI2OD-T2) not only exhibited higher device performance than PBDB-T:P(NDI2OD-T2) but also showed processing temperature-insensitive performance. The authors suggest that this processing temperature-insensitive behavior of PBDB-Bz based devices is likely due to the interpenetrating network of the donor polymer which persists even at high temperatures; however, the detailed nature of the solution-state aggregate structure of this polymer has not been reported.

In most blend systems used for OSCs, the donor polymer solution-state aggregation, particularly the structure of the primary aggregates, is not well-characterized and is often inferred from the neat films, which are not representative of the solution state. However, in our recent work, we show that BDT-based donor polymers can aggregate into distinct structures in solution dictated by the polymer backbone conformation. The solution-state structures of the polymer aggregates were unveiled by SAXS and freeze-dried imaging, which largely modulate the blend morphology and device properties in NFA based OSCs.[301] This work highlights the importance of probing the precise structure of solution-state aggregates, not just the extent of aggregation. As shown in Figure 38a, we synthesized three donor polymers (PM7, PM7 D1, and PM7 D2) where PM7 D1 and D2 polymers are made more conformationally flexible than PM7 by cracking open the ketone ring on the acceptor unit of PM7. Driven by both $\pi-\pi$ and lamellar stacking, the more rigid PM7 forms semicrystalline fiber-like aggregates with ∼20 nm diameter as determined by

https://doi.org/10.1021/acs.chemrev.2c00905
Chem. Rev. 2023, 123, 8395−8487

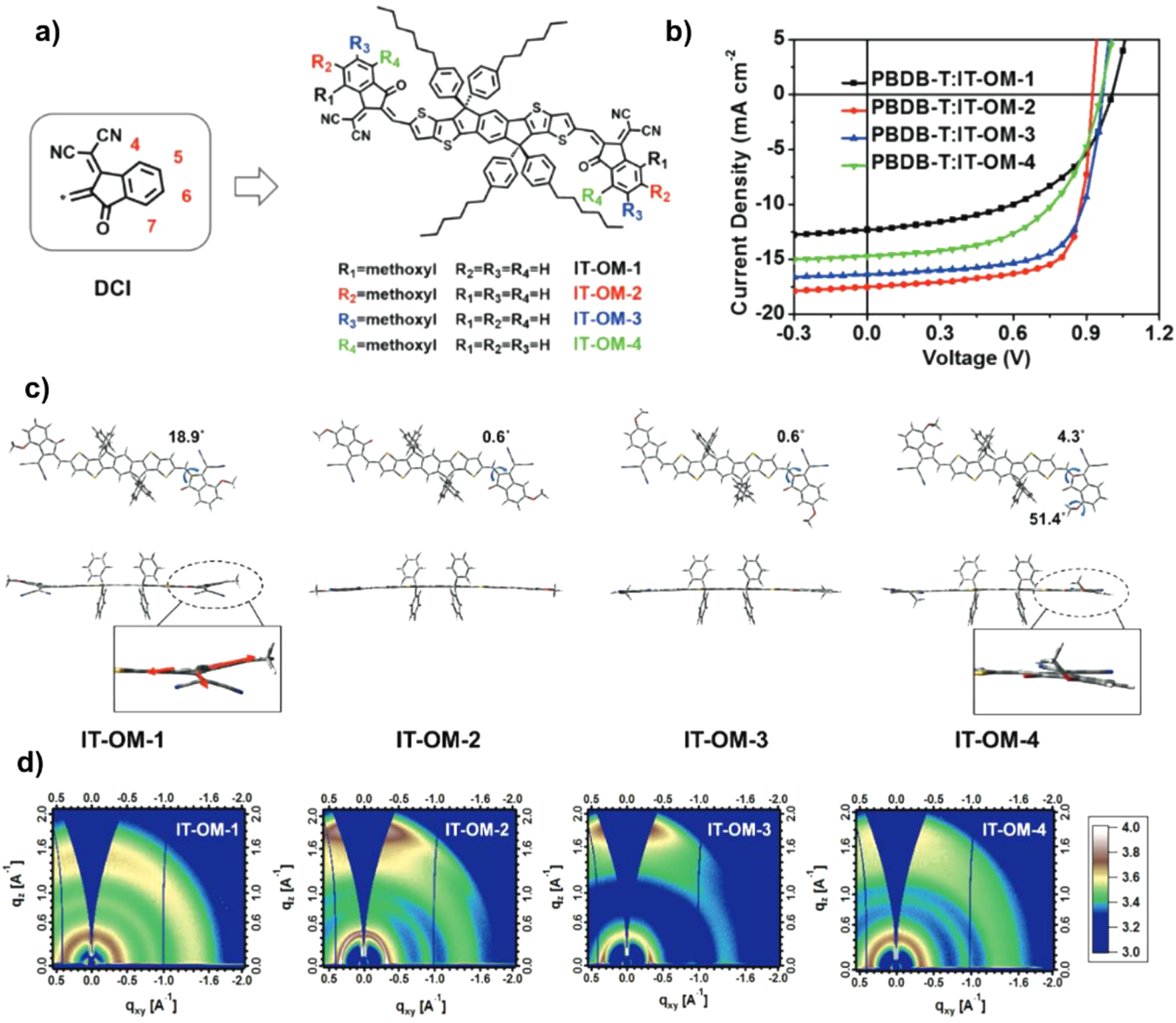

Figure 39. a) Chemical structures of the terminal group, DCI, and the four NFAs (IT-OM-1, IT-OM-2, IT-OM-3, and IT-OM-4) where methoxyl group is substituted on different sites of the DCI unit. b) Current density versus voltage relationship of OSCs using the four NFAs blended with PBDB-T polymer. c) Face view (top) and side view (bottom) images of the optimized molecule structures via DFT calculations at the B3LYP/6-31G(d, p) level. d) 2D GIWAXS patterns of the neat acceptor films. Figure reproduced with permission from ref 573, Copyright 2017 John Wiley and Sons (a–d).

solution SAXS and freeze-dried AFM and TEM imaging. On the other hand, the more flexible PM7 D1 and D2 formed polymer network-like aggregates. Using SAXS, we determined that these network aggregates are composed of well-solvated polymer chains exhibiting Porod slopes between −2 and −3 in the low Q region, indicating a fractal or a network-like structure (Figure 38b). These two types of aggregate structures showed distinct temperature dependence: the PM7 fiber aggregates dissolve and lose their crystalline order at high temperatures, leaving the polymer network-like aggregates behind in the solution state; in contrast, the network aggregates of PM7 D1 and D2 remain stable independent of the solution temperature as depicted in Figure 38c. We further demonstrated that these network aggregates, regardless of the polymer system, led to blend films with smaller domains, stronger $\pi-\pi$ stacking, more face-on preferred molecular orientations, and higher *PCEs* as compared to the fiber aggregates and showed stronger processing temperature-resiliency. As described in Section 2, donor polymers used in OSCs may form other types of primary solution-state aggregates; however, the detailed nature of these aggregates and their assembly pathways are rarely reported, making it challenging to establish a clear understanding of how the precise structure of donor polymer aggregates impacts the blend morphology and device properties.

4.2.2. Impact of NFA Assembly. In Section 3, we discussed how molecular design approaches are used to tune the crystallinity and molecular packing of A−D−A or A−DAD−A based NFAs. In blend systems consisting of polymer:NFA, molecular assembly of NFAs also influences the crystallinity and molecular packing in the blend film and has a drastic impact on the device performance of OSCs. In particular, end-capping group engineering is one of the most commonly used approaches to tune the crystallinity and molecular packing of the NFAs in the blend. A notable work by Li and Hou et al.

https://doi.org/10.1021/acs.chemrev.2c00905
Chem. Rev. 2023, 123, 8395−8487

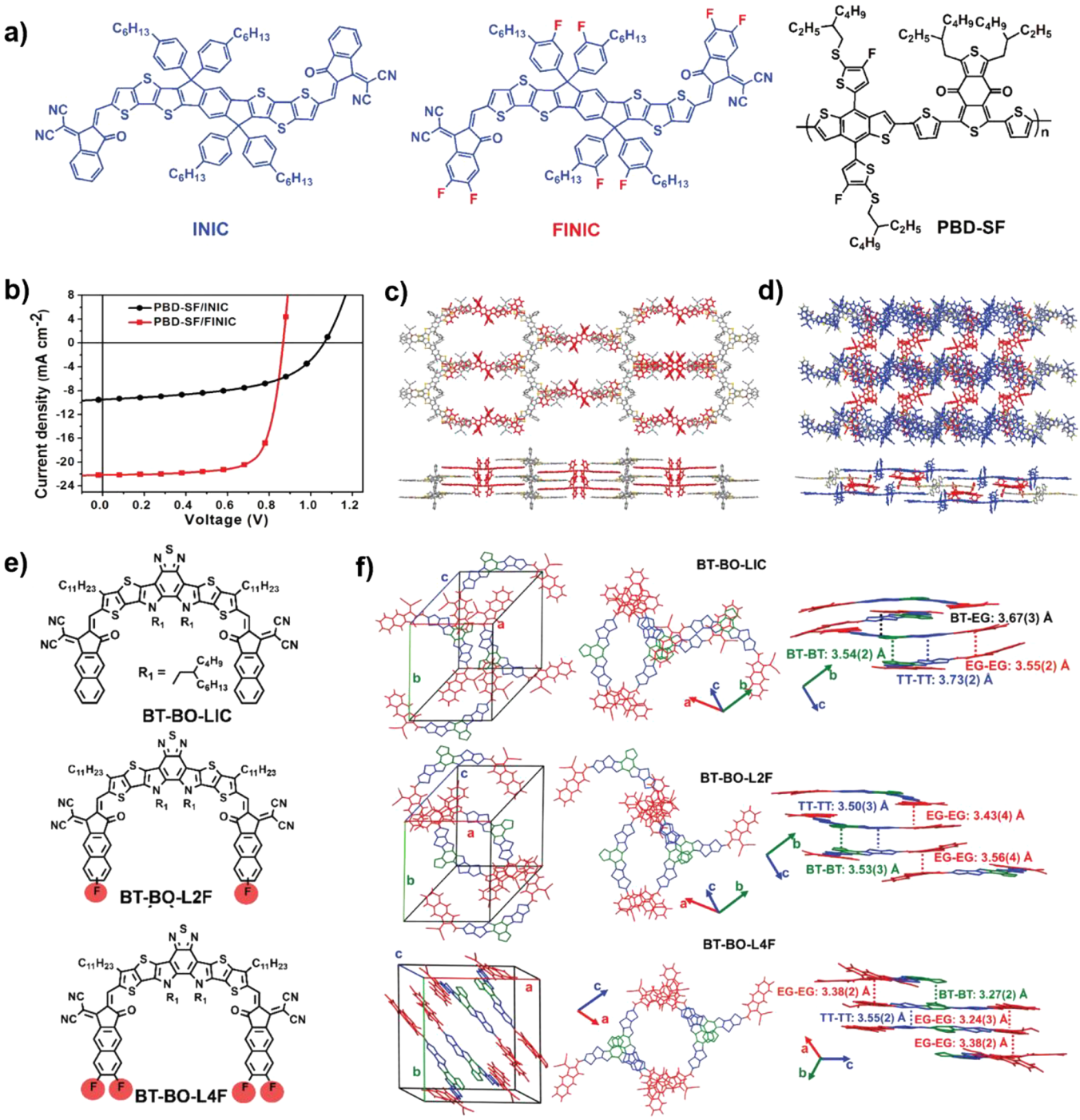

Figure 40. a) Chemical structures of INIC, FINIC, and PBD-SF molecules. b) Current density and voltage relationship comparison of PBD-SF:INIC and PBD-SF:FINIC devices. c) INIC stacking modes along π plane (top) and perpendicular to the π plane (bottom). Two different conformations of INIC are represented as red and gray in the figure. d) FINIC stacking modes along π plane (top) and perpendicular to the π plane (bottom). Three different conformations of FINIC are color coded as red, gray, and blue. e) Molecular structures of BT-BO-LIC, BT-BO-L2F, and BT-BO-L4F. f) Left: Unit cells of the three NFAs. Middle: Visualization of the stacking directions. Right: Stacking modes of the three NFAs showing the $\pi-\pi$ stacking distances. The colors represent different components of the NFA: red - the end groups, blue - thieno[3,2-*b*]thiophenepyrrole unit of the core, green - thiadiazole unit of the core. Figure adapted with permission from ref 576, Copyright 2020 John Wiley and Sons (a–d); ref 577, Copyright 2021 John Wiley and Sons (e, f).

showed that the substitution position of electron-withdrawing functional group on the end group of IT-OM acceptor impacts its molecular packing in both neat and blend films.[573] Shown in Figure 39a is the molecular structures of four IT-OM acceptors where the methoxy group is substituted on different positions of the dicyanovinylindan-1-one (DCI) terminal group, leading to IT-OM-1, IT-OM-2, IT-OM-3, and IT-OM-4, respectively. When these acceptor molecules are blended with PBDB-T donor polymer, PBDB-T:IT-OM-2 shows the highest device performance (Figure 39b). By investigating the molecular geometry of these acceptor molecules with density functional theory (DFT) calculations, the authors determined that IT-OM-

https://doi.org/10.1021/acs.chemrev.2c00905
Chem. Rev. 2023, 123, 8395–8487

2 and IT-OM-3 acceptor have excellent planarity whereas for IT-OM-1 and IT-OM-4, the DCI terminal groups are distorted from planarity due to the steric hindrance of the methoxy unit with its adjacent groups (Figure 39c). This terminal group distortion dramatically increases the $\pi-\pi$ stacking distance as observed from the neat film GIWAXS patterns (Figure 39d) where IT-OM-1 exhibits the largest $\pi-\pi$ stacking distance of 4.24 Å, whereas IT-OM-2 is the shortest around 3.44 Å. IT-OM-2 also exhibits the largest coherence length as compared to the other acceptor molecules indicating its strong crystalline order which leads to high electron mobility. In addition to changing the position of substitution on the end group, the substituents can also be varied to modulate molecular stacking. In particular, fluorine substitution is commonly used to lower the LUMO level, extend the absorption range, and enhance intermolecular interactions by forming noncovalent F···S and F···H interactions.[28,29] Notably, Dai and Zhan et al. synthesized INIC3, an A−D−A type acceptor molecule, with two fluorine substitutions on each terminal group which enhanced the device performance drastically from 7.7% to 11.5% owing to its downshifted LUMO level, red-shifted absorption spectrum, and enhanced crystallinity in the blend film.[574]

Besides crystallinity, the crystal packing of NFAs, particularly 3D packing motifs, in the blend film is crucial for efficient charge transport and is largely influenced by modifying the terminal groups, side chains, and the fused ring core.[151,453,575,576] By fluorinating both end groups and side chains of INIC with 8 fluorine atoms, Dai and Zhan et al. developed a fullerene-free acceptor, FINIC, which led to a substantial enhancement in the device performance from 5.1% to 14.0% when using PBD-SF as the donor polymer (Figure 40a, b).[576] Interestingly, the resulting blend film not only exhibited closer $\pi-\pi$ stacking but the crystal structure changed to a 3D network formed through C−H···O hydrogen bonding, F···S interactions and $\pi-\pi$ stacking for FINIC; in contrast, INIC forms a "honeycomb" motif solely through $\pi-\pi$ stacking (Figure 40c, d). Due to its strong intermolecular interaction and favorable packing geometry which enables multiple charge transport channels, FINIC leads to an order of magnitude higher electron mobility and a more balanced hole and electron mobility in the blend film as compared to INIC, thus yielding reduced charge recombination and higher *FF*. Furthermore, despite its enhanced crystallinity and more ordered packing in the blend film, the domain size of PBD-SF:FINIC blend film remains small and comparable to that of PBD-SF:INIC. By varying the degree of fluorination of the terminal groups in A−DAD−A type acceptor, BT-BO-LIC, as shown in Figure 40e, Zhang and Marks et al. also demonstrated how molecular packing of this NFA can be manipulated.[577] Shown in Figure 40f is the crystallographic packing structures of nonfluorinated BT-BO-LIC, difluorinated BT-BO-L2F, and tetrafluorinated BT-BO-L4F, indicating that fluorination of the terminal group promotes intermolecular interaction via forming more end-group-to-end-group (EG-EG) stacking and decreasing the $\pi-\pi$ stacking distance. Due to the close packing structure with multiple end-group charge transport pathways, the device performance of PM6:BT-BO-LIC drastically increased from 9% to 16.8%.[577] Similarly, Lai and He et al. investigated changing the substitution position of the electron-withdrawing group on the terminal unit of an A−D−A type acceptor ITIC.[458] The authors synthesized two types of ITIC-2Cl, namely ITIC-2Cl-δ and ITIC-2Cl-γ, by varying the position of the chlorine groups on the terminal units. Compared to the linear stacked crystalline structure of ITIC-2Cl-δ, ITIC-2Cl-γ exhibits closely packed 3D interpenetrating network structure, which is responsible for its efficient charge transport, reduced bimolecular recombination, and enhanced device performance from 11.51% to 13.03%. Besides end-group engineering, modifying the alkyl side chains by increasing the length or introducing branched alkyl side chains has shown effective in manipulating the packing structure of NFAs to enhance the charge transport in polymer:NFA systems.[151,454]

Although crystallinity and crystal packing of NFAs are critical for efficient charge transport in polymer:NFA based systems, excessive aggregation or crystallization of NFAs can cause oversized domains, which are detrimental for charge generation in OSCs. This suggests that the assembly of NFAs has a substantial influence on the domain sizes of the blend films. In particular, PDIs, one of the early nonfullerene systems used for OSCs, are well-known for their strong self-aggregation properties and molecular stacking tendency, leading to oversized domains in the blend film.[578] Due to their unfavorable phase separation, molecular engineering approaches have been extensively utilized to reduce the backbone planarity and aggregation tendency of PDIs to control their domain sizes in the blend film.[579,580] For example, introducing multiple PDI units to the phenyl core and constructing twisted backbone by linking two PDI units with a π bridge or functionalizing the PDI chromophores have effectively suppressed the crystallization of PDIs in the blend film.[578,581−583] Notably, Zhan and co-workers developed a star shaped PDI (S(TPA-PDI)) with a triphenylamine (TPA) core which showed reduced molecular aggregation and enhanced charge transport owing to its three-dimensional structure.[584] Alkyl side chain engineering, such as increasing the length of the side chain or changing the branching point, is also widely used to improve NFA solubility and prevent excessive NFA aggregation in the blend film.[453,454,585] In particular, Jiang and Yan et al. investigated the effect of the alkyl side chain branching points of the Y6 molecule on the blend film morphology of OSCs and discovered that the third position branched alkyl chains resulted in optimal solubility, improving the device performance from 15.7% to 16.74%.[586] On the other hand, the fourth position branched alkyl side chains on Y6 led to excessive solubility which resulted in large domains, poor domain purity, and edge-on orientation in the blend film, thus yielding slightly decreased performance of 14.31%. Similarly, Dong and Huang et al. showed that the solubility of Y6 in a nonhalogenated solvent, o-xylene, can be enhanced by increasing the length of its alkyl side chains which led to photovoltaic performance enhancement from 11% to 16% when processed from o-xylene with PM6 as the donor polymer.[585]

4.2.3. Impact of Relative Aggregation and Miscibility between Donor Polymers and NFAs. Beyond the molecular assembly of donor polymers and NFAs, relative aggregation and crystallization of these materials ultimately dictate the phase separated structures in polymer:NFA systems.[127,559,561,587,588] When donor polymers exhibit lower aggregation and crystallinity than NFAs, they allow NFAs to control the morphology, resulting in large acceptor domains in the blend film.[464,559,561,589] Meanwhile, when donor polymer aggregation or crystallization is more dominant, the morphology is controlled by the aggregation of the donor polymers. Liu and Zhang et al. thus suggested that using donor polymers with moderate molecular weight (MW) leads to optimal morphology and device performance for PM6:Y6 system, resulting in a *PCE* of 17.1%.[589] When low MW donor polymer was used, the crystallization of the acceptor, Y6, dominated the morphology,

https://doi.org/10.1021/acs.chemrev.2c00905
Chem. Rev. 2023, 123, 8395−8487

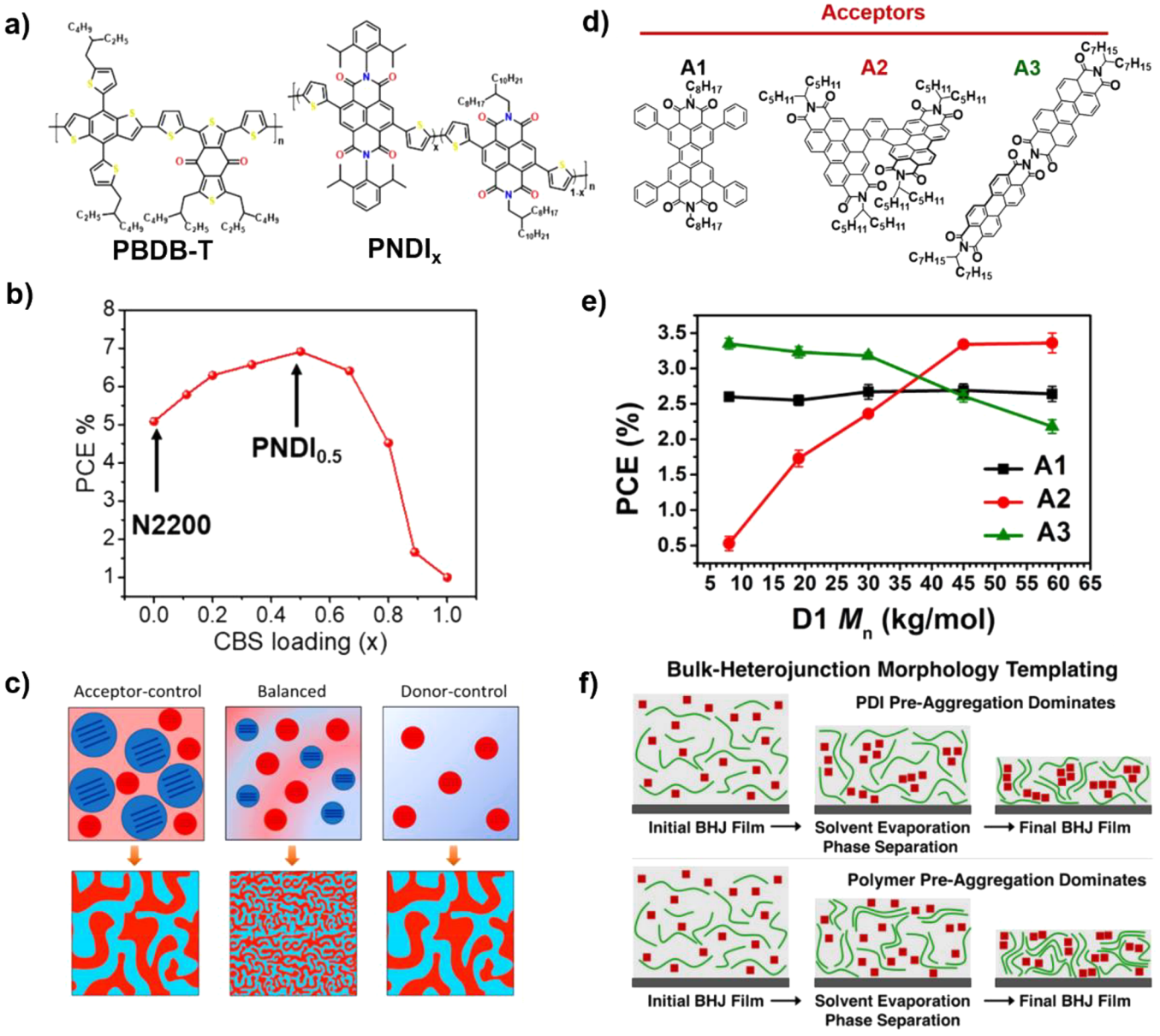

Figure 41. a) Molecular structures of PBDB-T and PNDI with CBS. b) Device performance with respect to CBS loading. c) Illustration of how balanced aggregation of acceptor and donor crystallinity leads to optimal small-scale phase-separated domains. d) Molecular structures of the PDI based NFAs with different crystallinity (A1 > A2 > A3). e) Device performance with respect to the molecular weight of the donor polymer when different acceptor molecules are used. f) Schematics of the acceptor (top) versus donor polymer (bottom) templated morphology. Figure adapted with permission from ref 559, Copyright 2020 American Chemical Society (a–c); ref 561, Copyright 2017 American Chemical Society (d–f).

leading to large and impure domains as evidenced by their RSoXS measurements. On the other hand, when high MW donor polymer was used, excessive aggregation of the donor polymer led to overly pure domains which hampered the charge percolation pathways. By introducing compact bulky side chains (CBS) at various ratios to a PNDI-based acceptor molecule, Wu and Bao et al. also tuned the relative aggregation and crystallization of the donor and acceptor phases in PBDB-T:PNDI based all-polymer solar cells (Figure 41a).[559] The authors found that the optimal performance was achieved when CBS loading ratio to the PNDI molecule was 0.5 (Figure 41b). At this ratio, the donor and acceptor aggregation and crystallization were balanced, which led to the smallest average domains size (~65 nm). In contrast, at low or high CBS loading, the average domain size reached over >300 nm when either the donor or acceptor aggregation dominated (Figure 41c). Eastham and Marks et al. also demonstrated that the morphology of polymer:NFA system can be templated by either the donor or the acceptor molecules.[561] As compared to previous works, these authors tuned the aggregation and crystallization of both donor and acceptor materials. For the acceptor molecules, three PDI based NFAs with varying crystallinity (A1 > A2 > A3) shown in Figure 41d were synthesized, and the aggregation of the donor polymer, PTPD3T, was tuned by changing the molecular weight as previously reported.[590] Shown in Figure 41e is the relationship between device performance with respect to donor polymer molecular weight when using the three NFAs with varying crystallinity. For the highly crystalline acceptor (A1), the device performance is insensitive to the molecular weight of the donor

https://doi.org/10.1021/acs.chemrev.2c00905
Chem. Rev. 2023, 123, 8395−8487

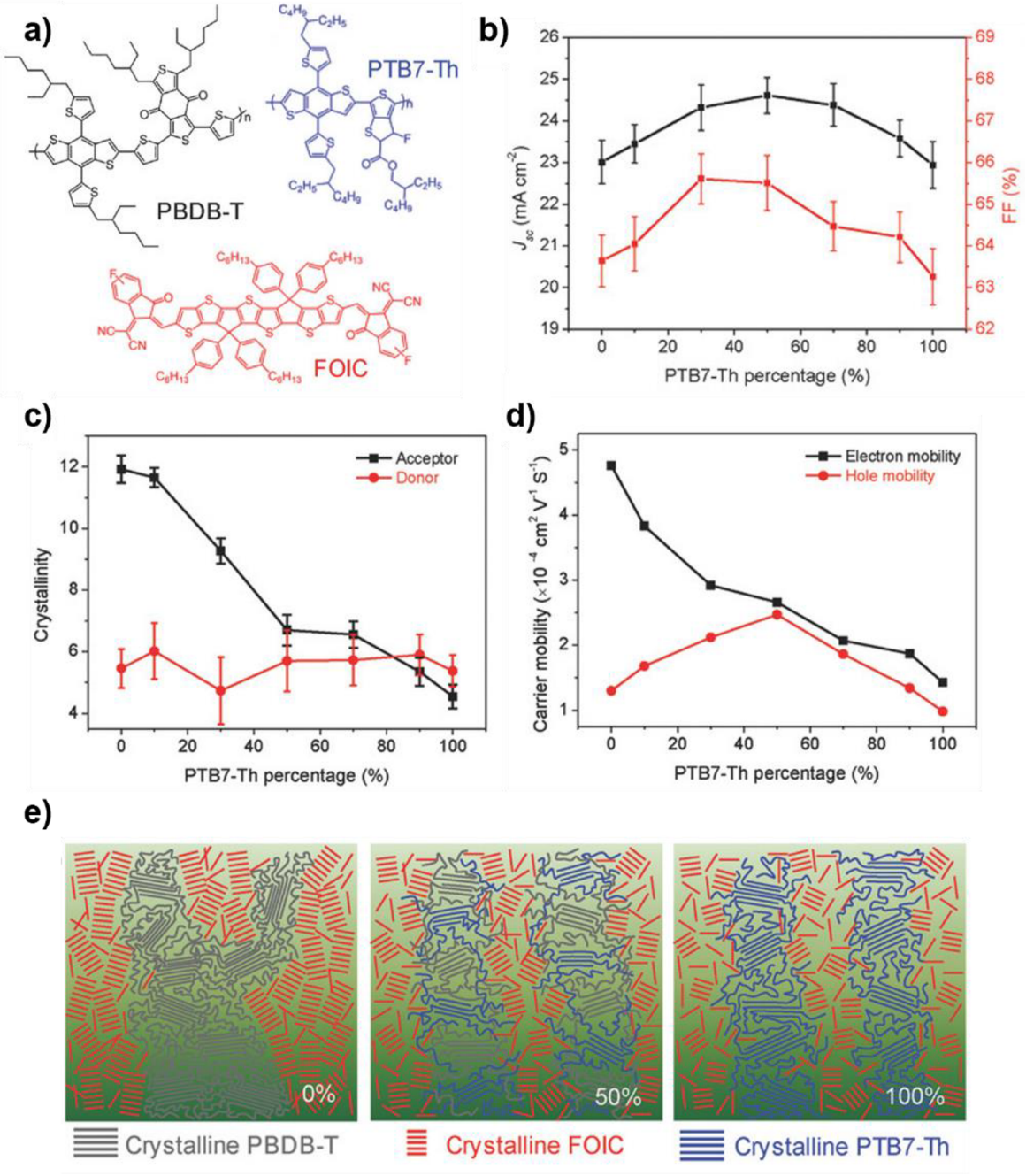

Figure 42. a) Molecular structures of PBDB-T, FOIC, and PTB7-Th. b) J_{SC} and *FF* as a function of PTB7-Th percentage. c) Crystallinity of the donor and acceptor phases as a function of PTB7-Th percentage. d) Electron and hole mobility as a function of PTB7-Th percentage. e) Illustration of the blend morphology at PTB7-Th percentages of 0, 50, and 100%. Figure reproduced with permission from ref 127, Copyright 2018 John Wiley and Sons (a–e).

polymer as the blend film morphology is dictated by the strong aggregation of A1. On the other hand, when a less crystalline acceptor (A2) is used, the morphology is strongly dependent on polymer aggregation and exhibits optimal performance at high molecular weight. This result is attributed to the blend morphology being templated by the donor polymer aggregation at high molecular weight whereas at low molecular weight, the poor aggregation of the donor polymer allows the acceptor to control the morphology. When the acceptor molecule exhibits the lowest crystallinity (A3), the donor polymer aggregation templates the blend morphology and suggests that weaker polymer aggregation is favorable when the acceptor crystallinity is low. These processes are schematically illustrated in Figure 41f where either the aggregation of donor or the acceptor dominates the blend morphology in polymer:NFA systems.

Besides relative aggregation and crystallization of the donor and acceptor materials, their miscibility is extremely important for the BHJ morphology of polymer:NFA systems, particularly the domain purity.[591,592] Although in polymer:NFA systems, the miscibility of donor polymers and NFAs is typically higher than that of polymer and fullerene acceptors,[29,556] which prevents large-scale phase separation, they are more prone to forming intimately mixed domains which lead to severe geminate and nongeminate recombination.[29] Therefore, decreasing the

https://doi.org/10.1021/acs.chemrev.2c00905
Chem. Rev. 2023, 123, 8395–8487

miscibility of NFAs and donor polymers to increase the average domain purity is critical to suppress charge recombination and enhance charge transport provided that percolation is maintained. To improve the phase purity of polymer:NFA systems, molecular engineering of NFAs is an effective strategy to decrease the miscibility between the donor and acceptor molecules. For instance, Ma and Tang et al. synthesized a series of TPIC-X molecules as NFAs with different halogenated end groups to show that halogenation decreases the miscibility of the donor and acceptor materials, resulting in a better phase-separated morphology.[593] Similarly, Hou and co-workers reported that halogenation of IT-M acceptor molecule to obtain IT-4F decreased its miscibility with PBDB-TF donor polymer, which improved the domain purity of the blend film and photovoltaic performance.[594] They also observed that simply replacing the methoxy group substitution on IT-OM acceptors showed a drastically different phase separated morphology[573] which was later correlated to the difference in the miscibility of the acceptor and donor polymers as suggested by Bredas and co-workers.[595] Besides molecular engineering approaches to tune the miscibility of the donor and acceptor molecules, introducing a third component that has lower miscibility with the donor and acceptor components has also been suggested to improve the phase-separated morphology.[558,596]

In addition to domain purity, miscibility can also impact the crystallinity of the donor and acceptor phases in a blend. This suggests that the molecular assembly behavior in blends can deviate from neat systems due to interactions between the donor and acceptor materials. For example, when the strongly crystallizing polymer, PTFB-P, is blended with ITIC acceptor, it loses its crystallinity while it maintains its crystallinity when blended with fullerene acceptors.[560,591] Hu and Yan et al. also showed that the crystallinity of the small molecule acceptor, ITIC-Th, in a blend film changes depending on the choice of donor polymers.[591] When the donor polymer is highly miscible with the NFA, both the crystallinity and the domain purity of the acceptor phase are reduced, resulting in poor *FF*.[29] These findings suggest that decreasing the miscibility of the donor polymers and NFAs can be beneficial for not only improving the domain purity but also maintaining the crystallinity of the blend film. However, decreasing the miscibility too much can be undesirable as it causes overpurity and suppresses percolation pathways as previously discussed in Section 4.2.1.

When either the donor or the acceptor material exhibits excessive aggregation, increasing the miscibility between the two phases or introducing a third component with higher miscibility can be beneficial for balancing the crystallization of the two components.[597,598] For example, Zhang and Ma et al. achieved an optimal performance of 12.02% in PBDB-T:FOIC blend system by adding the third component (PTB7-Th) as the donor polymer at various ratios (Figure 42a, b). By adding PTB7-Th, the crystallinity of the acceptor, FOIC, is gradually reduced due to the high miscibility of PTB7-Th with FOIC (Figure 42c). At the point when their crystallinity is balanced, electron and hole mobilities are equally balanced (Figure 42d), resulting in the optimal J_{SC} and *FF* observed.[127] Figure 42e illustrates how the crystallinity of the donor and acceptor phases change with respect to the percentage of PTB7-Th where the optimal morphology occurs at 50%. Dong and Cao et al. also showed that using P(NDI2OD-T2) acceptor polymer as the third component suppressed excessive aggregation of NFAs in both PM6:ITIC-4F and PM6:Y6, which led to a drastic improvement in their photovoltaic performance.[597] The reduced crystallization of the small molecule acceptors in the blend films was attributed to the P(NDI2OD-T2) polymer being localized inside the acceptor domains due to its high miscibility with the NFAs, thereby confining the growth of the small molecules. Similarly, Chen and co-workers used a star shaped acceptor, TF1, into PM6:Y6 which reduced the excessive aggregation of Y6 in the blend film due to its strong miscibility with Y6, thereby enhancing the device performance from 15.62% to 16.67%.[598] On the other hand, adding a third component which is more readily crystallized as compared to the host materials could enhance the crystallization of the donor and acceptor phases.[21,599] In a notable work done by Zhu and Liu et al., an average *PCE* of 19.3%, one of the highest efficiencies reported so far, was reported when a more crystalline D18 donor polymer was added to PM6:LB8O system.[21] These authors observed that the blend film formed a double fiber network of donor and acceptor phases which was facilitated by the addition of D18. The observation of NFA fibril network crystallization is surprising and encourages further investigation into the molecular assembly of NFAs during solution processing.

4.2.4. Impact of Processing Conditions. The BHJ morphology and device performance of OSCs heavily depend on the processing parameters during the film deposition process. In particular, film drying kinetics, which is influenced by parameters such as the rate of spin coating, processing temperature, and solvent additives, determines the extent of crystallization and phase separation processes. Moreover, processing temperature and solvent additives also affect the solvent quality, which has a significant impact on the aggregation and crystallization behavior of the donor polymers and NFAs. In particular, the blend film morphology of OSCs containing donor polymers with TDA properties strongly depends on the processing temperature. Additionally, the use of cosolvents, typically poor solvent additives, can decrease the solubility of the donor and acceptor molecules, thereby promoting aggregation and crystallization processes. As a result, the impact of processing conditions on the morphology of BHJ based OSCs is challenging to predict since processing parameters can influence not only the drying kinetics but also the aggregation behavior of the donor and acceptor materials. Therefore, this section aims to discuss the complexity of processing parameters and their impact on the phase transition process during film deposition as well as their influence on the blend film morphology and device performance of OSCs.

In polymer:fullerene systems with strong L−L demixing, longer film drying times have been shown to increase the domain size and purity of the blend film.[530,548] For instance, Kouijzer et al. observed large droplet-like domains in PDPP5T:PCBM blend films which coarsened due to Ostwald ripening at longer drying times or slower spin coating rates, leading to poor device performance.[530] On the other hand, in polymer:fullerene systems with higher miscibility, slow drying times can induce aggregation and crystallization of the donor materials in the blend film, leading to S−L phase separation.[600−602] Abdelsamie and Amassian et al. showed that the degree of aggregation of P3HT in P3HT:PCBM system can be enhanced by interrupting spin coating prematurely to extend the drying time.[600] Based on UV−vis measurements of the blend film, they reported a substantial improvement in the fraction of P3HT aggregates in the blend film. Using electron diffraction measurements, they observed increased π-stacking crystallinity of P3HT in the blend film. Schmidt-Hansberg and Schabel et al. also reported that increasing the solvent evaporation time during blade coating of

https://doi.org/10.1021/acs.chemrev.2c00905
Chem. Rev. 2023, 123, 8395−8487

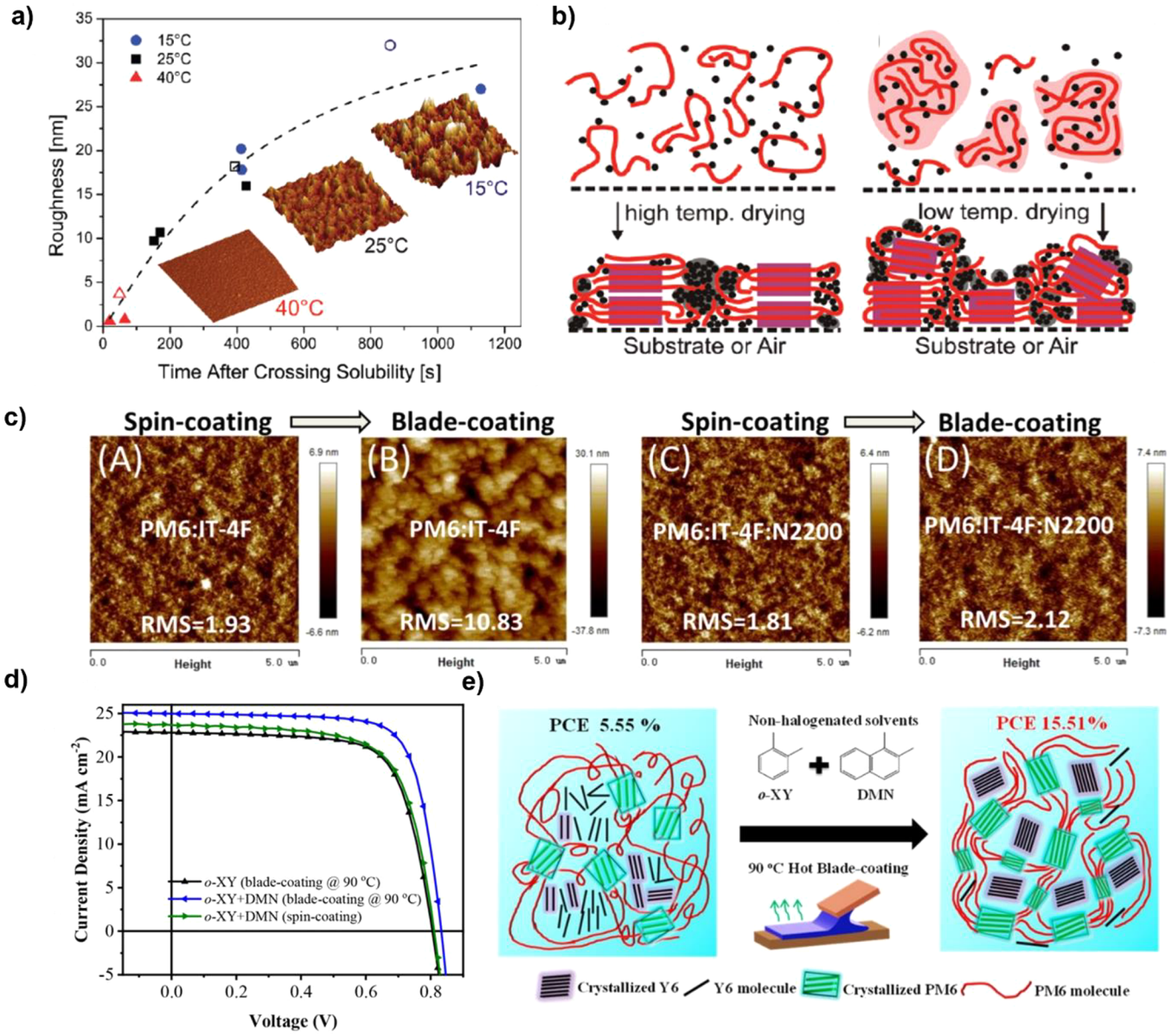

Figure 43. a) Influence of drying time on film roughness for neat P3HT (open symbols) and the blend film (filled symbols) at different drying temperatures. b) Schematic comparison of the blend film formation at high temperature drying (left) and low temperature (right) drying conditions. c) AFM height images for PM6:ITIC-4F comparing spin coated versus blade coated films without and with P(NDI2OD-T2) addition. d) *J*−*V* characterization curves of PM6:Y6 blend under different conditions. e) Schematics of the two different BHJ morphologies obtained at different processing conditions, leading to *PCE*s of 5.55% and 15.51% respectively. Figure adapted with permission from ref 601, Copyright 2011 American Chemical Society (a, b); ref 597, Copyright 2019 John Wiley and Sons (c); ref 603, Copyright 2021 American Chemical Society (d, e).

the same P3HT:PCBM system improves the device performance mainly due to the aggregation of P3HT.[601] These authors tuned the solvent evaporation time using both nitrogen flow and stage temperature to find that the best device performance was achieved when both the stage temperature and nitrogen flow velocity were the lowest. This result was attributed the strong aggregation of P3HT as both blend and neat P3HT films (filled and open symbols respectively in Figure 43a) showed increased film roughness, suggesting that large-scale morphology features were formed mainly due to P3HT aggregation. The UV−vis measurements also indicated a red shift in the P3HT spectra and enhanced vibronic shoulders, suggesting increased conjugation length and interchain interactions at slow drying conditions. The schematics of the film drying process at high and low temperatures are indicated in Figure 43b, where low temperature drying results in strong aggregation of P3HT, indicative of S−L phase separation driven phase transition.

In nonfullerene based OSCs where S−L phase separation or crystallization is typically the dominant pathway, slow drying kinetics can lead to excessive aggregation of NFAs and form large phase-separated domains which deteriorate charge separation.[597,602] For instance, Dong and Cao et al. reported that aggregation of acceptor molecules, Y6 and IT-4F, resulted in lower device performance when blade coating is used as compared to spin coating due to slow drying kinetics.[597] The authors found that spin coated PM6:Y6 shows a *PCE* of 15.8% whereas blade coated devices only exhibit 13.2%. Adding a small amount of P(NDI2OD-T2), however, effectively suppressed the aggregation of NFAs due to its high miscibility with the acceptors, which resulted in a *PCE* of 16.5% for blade coated

https://doi.org/10.1021/acs.chemrev.2c00905
Chem. Rev. 2023, 123, 8395−8487

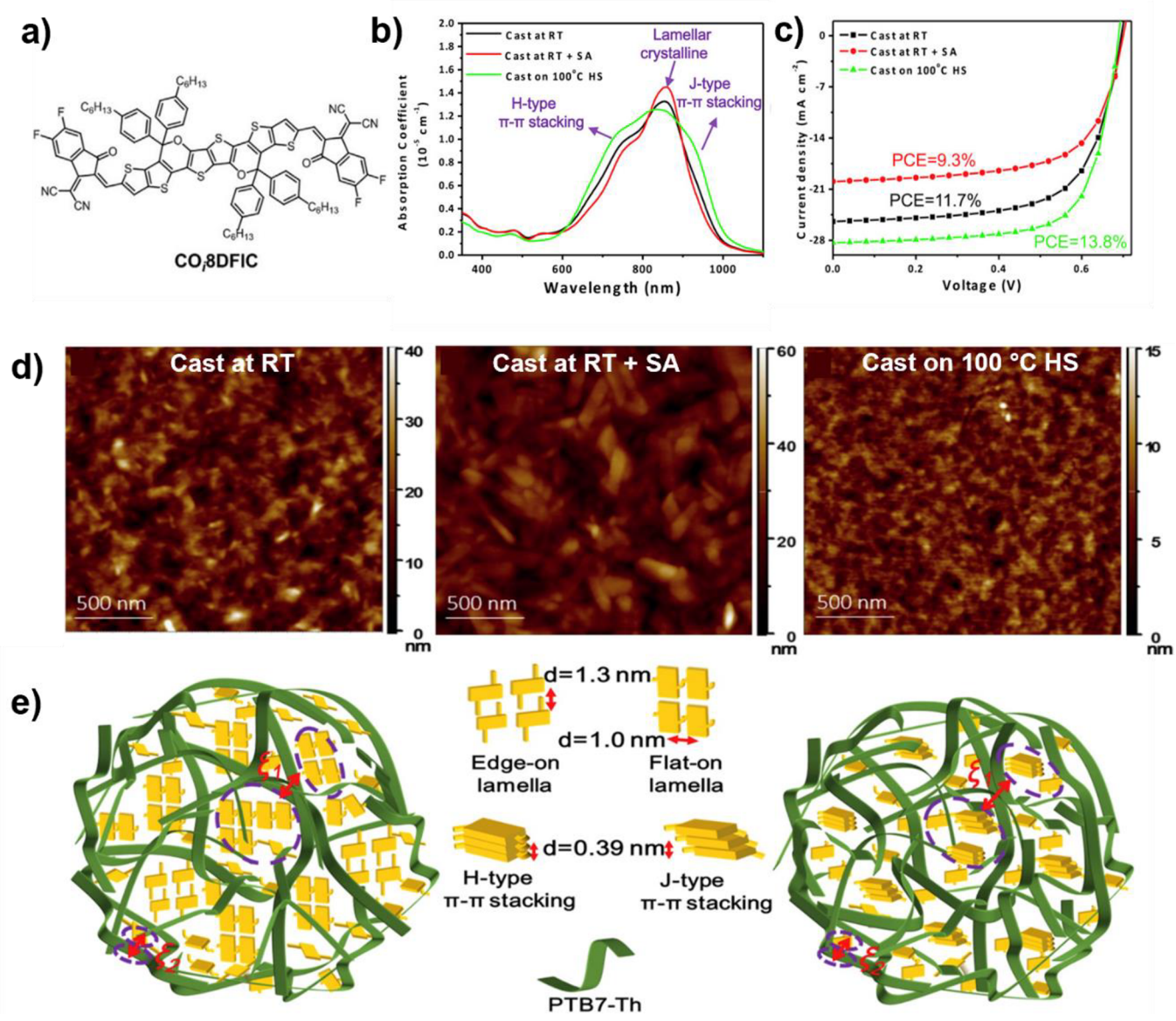

Figure 44. a) Chemical structure of the small molecule acceptor, CO*i*8DFIC. b) Absorption spectra of CO*i*8DFIC films cast at room temperature (RT), at room temperature + solvent annealing (RT + SA), or on 100 °C hot substrate (HS). c) Current density versus voltage curves obtained for PTB7: CO*i*8DFIC under three casting conditions (RT, RT + SA, and 100 °C HS). d) SPM images of the blend films cast from the three drying conditions. e) Illustration of the blend film morphologies obtained from slow drying (left) versus fast drying (right) conditions. Figure reproduced with permission from ref 81, Copyright 2019 Cell Press (a−e).

PM6:Y6:P(NDI2OD-T2). Figure 43c shows the AFM images of the PM6:IT-4F blend films, illustrating how blade coating forms rough films due to the aggregation of IT-4F and how introduction of P(NDI2OD-T2) leads to a smoother film, indicating small-scale phase-separated morphology. Processing the blend films using a high stage temperature to reduce the drying time has also been shown effective in controlling the excessive aggregation of NFAs.[571,597] Li and Wang et al. demonstrated that spin coating PBDB-T:INPIC on a hot stage (100 °C) suppressed the aggregation of small molecule acceptor and formed small phase-separated morphology.[602] On the other hand, spin coating the blend film under solvent vapor led to excessive crystallization of INPIC due to the prolonged drying time. Similarly, using blade coating on a 90 °C substrate with 1,2-dimethylnaphthalene (DMN) as an additive, Li and Xie et al. reported a *PCE* of 15.51% for PM6:Y6 in a nonhalogenated solvent, o-xylene, as compared to 5.55% when processed from 30 °C substrate without DMN as an additive.[603] Meanwhile, when only hot blade coating is used, a *PCE* of 12.98% was achieved, clearly indicating the effect of both the substrate temperature and the additive on the device performance (Figure 43d). The authors suggest that high stage temperature inhibits the aggregation of Y6 by reducing the drying time, thereby leading to small-scale phase separation whereas the role of additives is to induce nucleation of both PM6 and Y6 which promotes close packing of the molecules. Figure 43e illustrates this process where blade coating at low temperature leads to poorly crystalline large-scale phase-separated domains whereas the combination of high temperature coating and DMN additives result in smaller domains that are highly crystalline.

Solvent drying kinetics not only influences the extent of aggregation but also determines the molecular organization and orientation in the blend film.[81,145] In an early work, Lee and Cho et al. demonstrated that the molecular orientation of donor

https://doi.org/10.1021/acs.chemrev.2c00905
Chem. Rev. 2023, 123, 8395−8487

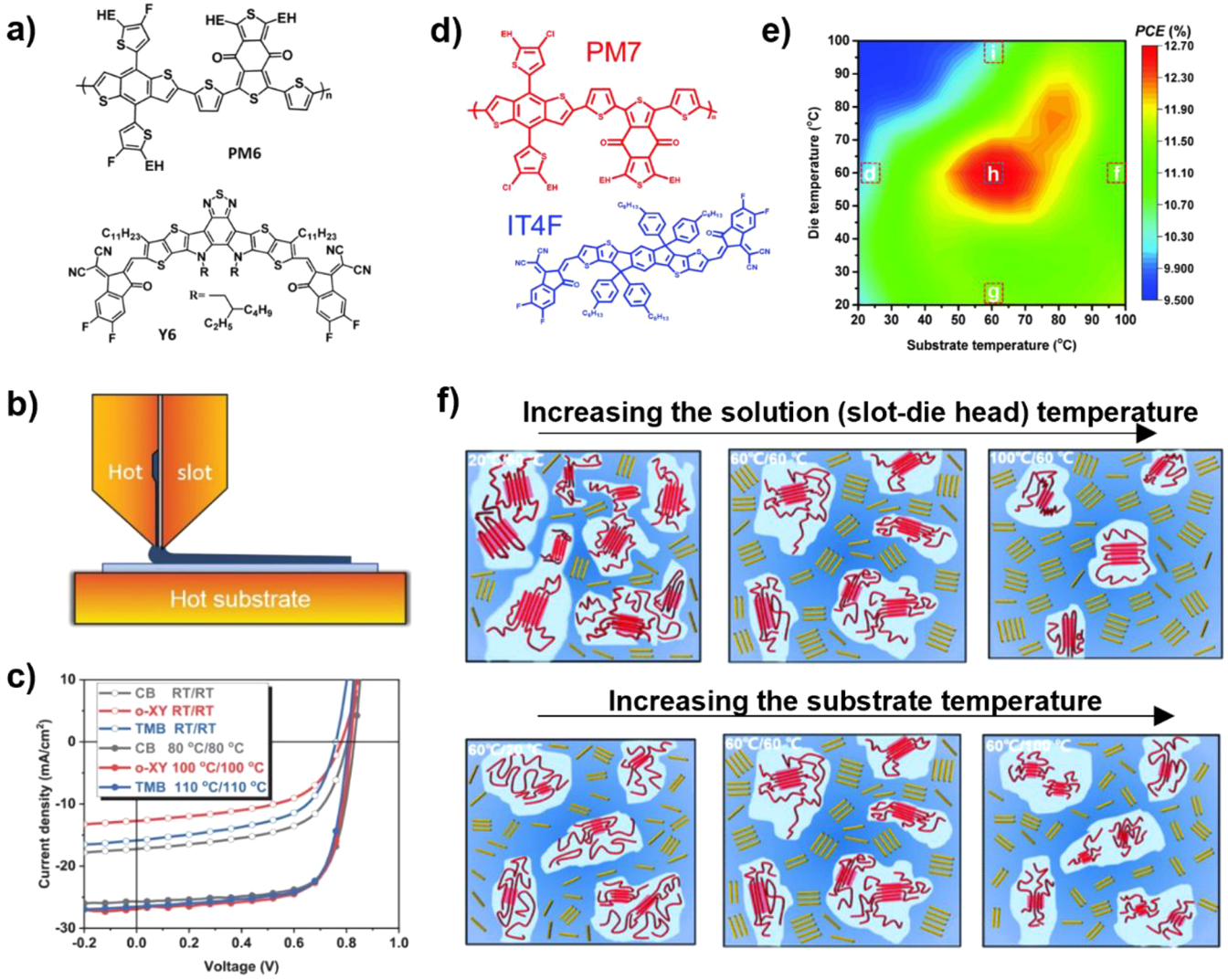

Figure 45. a) Molecular structures of PM6 and Y6. b) Schematics of the hot slot-die coating where both the slot-die head and the substrate temperatures are controlled. c) *J*−*V* characterization curves for PM6:Y6 system processed at different slot-die/substrate temperature conditions. d) Molecular structures of PM7 and ITIC-4F. e) *PCE* of PM7:ITIC-4F based devices fabricated using the slot-die coating method at various die (solution) and substrate temperatures. f) Schematics of the PM7:ITIC-4F microstructure processing from varying the solution temperatures while keeping the substrate temperature constant (top) and varying the substrate temperatures while the solution temperature is maintained. Figure reproduced with permission from ref 571, Copyright 2020 John Wiley and Sons (a, b, and c); ref 588, Copyright 2020 Royal Society of Chemistry (d, e, and f).

polymer P3HT in a bilayer device made of P3HT:PCBM, can be changed from edge-on at slow drying conditions to face-on at fast drying conditions, which increased the photocurrent generation.[145] More recently, Li and Wang et al. demonstrated that both molecular orientation and organization of small molecule acceptor CO*i*8DFIC in a polymer:NFA based BHJ system can be tuned by changing the solvent drying kinetics.[81] The authors tuned the film drying time by using high substrate temperature during spin coating for fast drying or using solvent vapor annealing for slow drying, and room temperature casting for the medium-drying condition. When drying was medium and slow, CO*i*8DFIC formed both edge-on and flat-on lamellar crystals which were determined from optical microscopy imaging and GIWAXS measurements. However, at fast drying, the intensity of the diffraction rings from GIWAXS substantially decreased, and no crystallites were observed from optical microscopy, indicating that fast drying inhibits the aggregation of CO*i*8DFIC into lamellar crystals. Instead, UV−vis absorption spectra of the neat films broadened and exhibited peaks at both short and long wavelengths as shown in Figure 44b, indicative of H- and J-type $\pi-\pi$ stacking, respectively. From GIWAXS measurements, they also observed a strong out-of-plane $\pi-\pi$ stacking peak corresponding to CO*i*8DFIC which suggests predominantly face-on oriented stacking. When OSCs are fabricated by blending with PTB7 donor polymer, the fast-drying condition resulted in the highest performance of 13.4% as compared to the 9% achieved for slow-drying (Figure 44c). This substantial drop in the device performance is attributed to the large-scale phase-separated morphology as evidenced by the scanning probe microscopy (SPM) images in Figure 44d where the slow and medium drying conditions show large CO*i*8DFIC domains indicated by the white regions. Figure 44e shows the schematics of the blend film microstructures showing large domains of flat-on and edge-on lamellar crystallites of CO*i*8DFIC in the slow-drying case and smaller domains of

https://doi.org/10.1021/acs.chemrev.2c00905
Chem. Rev. 2023, 123, 8395−8487

predominantly face-on H- and J-type $\pi-\pi$ stacking of CO*i*8DFIC in the fast-drying condition.

Besides controlling the drying kinetics, processing temperature can also directly impact donor polymer aggregation, particularly when TDA based donor polymers are used.[571] Ro and Yan et al. demonstrated that blade coating of PffBT4T-2OD:PCBM system where the donor polymer is a TDA based donor polymer can produce drastically different morphologies depending on the processing temperatures.[503] In particular, the authors found that processing temperature influences the crystal orientation, phase-segregated structure, and phase purity, whereas the blend film crystallinity remains unchanged.[503] When processed at 90 °C, the blend film exhibited edge-on orientation, whereas when processed at 55 °C, it mainly formed face-on orientation. Furthermore, 90 °C processed film formed hierarchical structures with high domain purity whereas the 55 °C processed film led to one broad phase-separated structure with lower domain purity as evidenced by RSoXS measurements. These drastic morphological differences are attributed to the TDA behavior of the donor polymer which crystallizes differently depending on the processing temperature. At 90 °C, the polymer is well-solvated in solution, so the crystallization likely occurs by nucleation and growth upon reaching supersaturation late in the drying stage at the air interface, leading to edge-on crystals. On the other hand, film formation at 55 °C occurs via preaggregation of the polymer solution which may favor adsorption to the substrate interface, resulting in face-on crystal orientation.

Similarly, in polymer:NFA systems, Ma and co-workers used a hot slot-die coating method in which both the solution (slot-head) and the processing stage temperature are controlled at the same time.[571] The authors achieved nearly the same average device performances of 15.2%, 15.4%, and 15.6% for PM6:Y6 system (Figure 45a) despite using three different solvents (chlorobenzene, trimethylbenzene, and o-xylene). The similar device performances obtained in these three different solvents were achieved by matching their solution-state aggregation and drying kinetics using hot slod-die head and substrate (Figure 45b). On the other hand, processing the blend films from room temperature slot-head and substrate (RT/RT) resulted in poor device performances with significant performance differences among the three solvents due to unmatched solution-state aggregation and drying kinetics (Figure 45c). The inferior performance of devices fabricated at room temperature is attributed to the TDA property of PM6, which exhibits strong preaggregation at room temperature leading to low crystallinity and large phase-separated domains.[604] The Ma group also investigated the effect of solution-state aggregation and drying kinetics by systematically tuning the solution and substrate temperature using the hot slot-die coating method. Using this approach, they achieved an average *PCE* of 13.2% for PM7:ITIC-4F system at 60 °C solution temperature/60 °C substrate temperature (Figure 45d, e).[588] They demonstrated that the main impact of solution temperature is on the phase-separated morphology, whereas substrate temperature mainly impacts the drying kinetics, which determines the extent of nucleation and growth during crystallization. Based on RSoXS measurements, the authors found that the blend films processed from low (20 °C) and high (100 °C) solution temperatures with the same substrate temperature (60 °C) resulted in large domains, whereas the medium temperature led to finer domains as illustrated in Figure 45f (top). This result was attributed to the TDA behavior of the donor polymer which exhibits strong aggregation at low temperatures, whereas at high solution temperatures, the crystallization of ITIC-4F enlarges the domains as the polymer aggregates dissolved. Meanwhile, when the substrate temperature is varied while maintaining the solution temperature at 60 °C, both low (20 °C) and high (100 °C) substrate temperatures led to poor crystallinity, whereas the medium substrate temperature showed the highest crystallinity as illustrated in Figure 45f (bottom). The poor crystallinity of the blend films processed at low and high solution temperatures was attributed to the impact of substrate temperatures on the nucleation and growth of the crystallites. Using differential scanning calorimetry (DSC) measurements, the authors showed that nucleation was limited to low substrate temperatures, whereas at high substrate temperatures, the crystal growth was restrained by rapid solvent evaporation.

Besides tuning the drying kinetics and processing temperatures, using solvent additives and cosolvents are commonly utilized to tune the phase separation and crystallization processes during film deposition.[34] In particular, the effect of solvent additives on the BHJ morphology of polymer:fullerene systems is well investigated in literature.[537,605−607] As previously discussed, these systems can exhibit large-scale droplet-like fullerene domains or "islands" in the blend film as their phase separation is dominated by L−L demixing during solvent removal.[530,533,535] In these systems, introducing a less volatile solvent can change the phase separation pathway by preventing L−L demixing and allowing for sufficient time for crystallization.[530,535,605,608,609] A notable work by Franeker and Janssen et al., showed that using o-DCB as a cosolvent for PDPP5T:PCBM[70] solution in chloroform leads to finely mixed domains as compared to forming micron scale large domains when processed without cosolvents.[535] Using in situ optical techniques, the authors compared the film drying processes in solutions with 5% vs without o-DCB to find that solvent evaporation takes longer in o-DCB added chloroform solutions due to its higher boiling point as compared to the neat solvent. As chloroform evaporates first during the spin coating process, the concentration of o-DCB rises, causing polymer aggregation in the solution before L−L phase separation takes place. Moreover, these authors further showed that the type of cosolvent used can affect the domain size in polymer:fullerene systems.[536] They discovered that the relative polymer solubility in the cosolvents is the most influential factor that determines the width of the fiber network observed in the blend film. When the polymer exhibits poor solubility in a cosolvent, the blend films formed the smallest phase-separated fiber network, whereas in the good cosolvents, the width of the fibers became larger. This finding is attributed to the nucleation and growth mechanism of the free polymers in solution. If the nucleation rate is faster than the growth rate, polymers nucleate more easily than they grow until there is depletion of free polymers. On the other hand, if growth is faster, the nucleated fibers grow until depletion, leading to a large fiber network. The effect of poor cosolvent is, therefore, to decrease the nucleation barrier so that more nucleus of smaller size can be formed, thereby depleting the free polymers from growth into large fibers.

In nonfullerene based solar cells, solvent additives are also commonly used to improve the crystallinity of the donor and acceptor phases;[362,610−612] however, the effect of additives on the morphology of nonfullerene based OSCs can be very different from fullerene based OSCs as NFAs can lead to overcrystallization.[141] Song and Baran et al. showed that the device performance of PTB7-Th:PCBM[70] based OSCs

https://doi.org/10.1021/acs.chemrev.2c00905
Chem. Rev. 2023, 123, 8395−8487

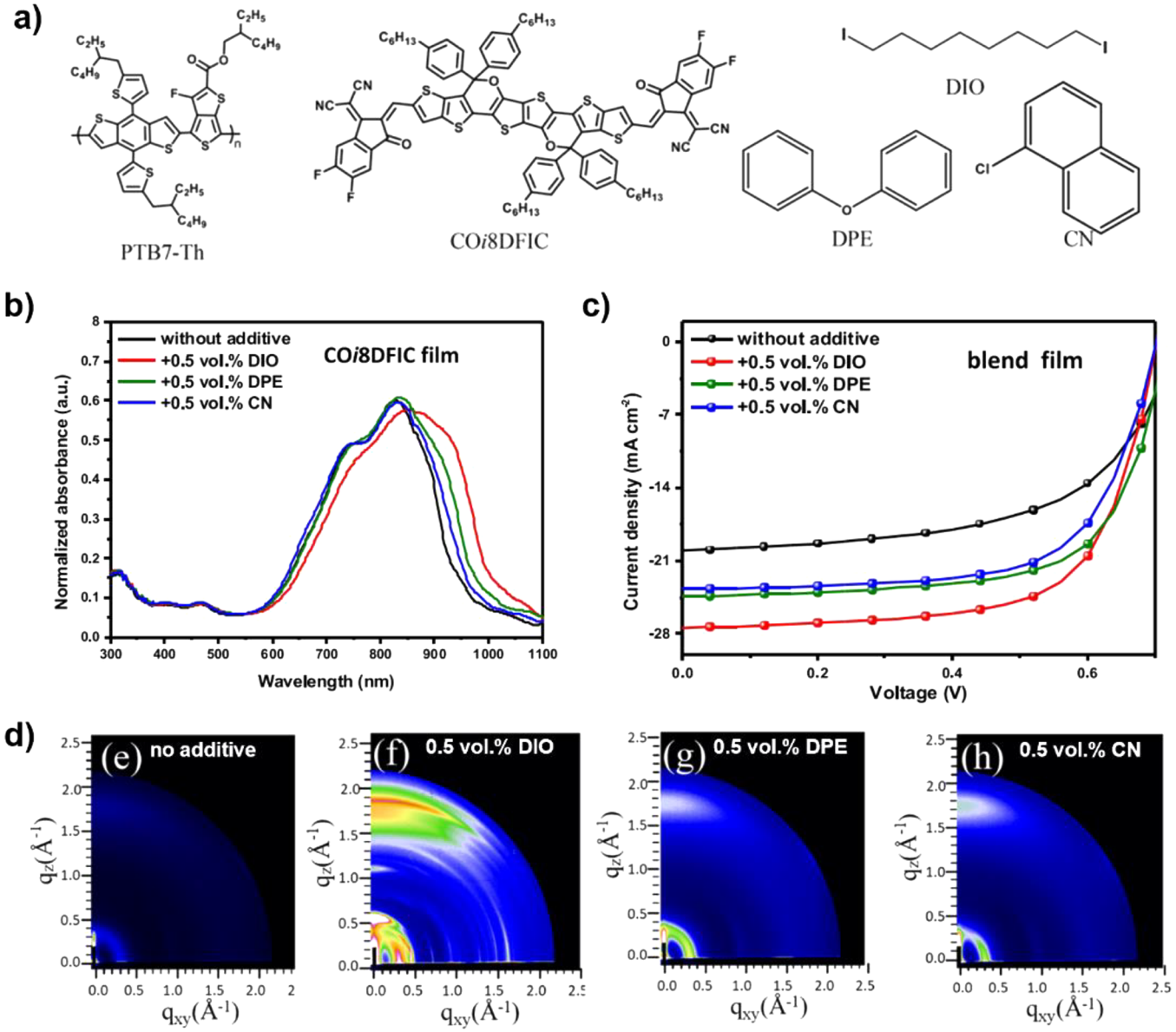

Figure 46. a) Molecular structures of the donor and acceptor molecules and the solvent additives. b) Neat acceptor film UV−vis absorption spectroscopies without and with the three different additives. c) *J*−*V* characterization curves for PTB7-Th:CO*i*8DFIC devices without and with the three different additives. d) 2D GIWAXS profiles of the PTB7-Th:Co*i*8DFIC blend films processed without and with additives. Figure reproduced with permission from ref 617, Copyright 2020 Cell Press (a−d).

significantly improved with 3% 1,8-diiodooctane (DIO) additive whereas the same amount of additive deteriorated the device performance of NFA based PTB7-Th:ITIC OSCs due to the formation of coarse morphology.[141] Similarly, Alqahtani and Collins et al. have recently shown that NFAs can be highly sensitive to additive contents, forming large crystals in the blend film even when the additive is slightly above the optimal concentration.[613] Nevertheless, solvent additives have been successfully utilized in numerous polymer:NFA systems, suggesting its critical role in achieving favorable morphology and device properties.[614,615] Notably, Song and Baran et al. demonstrated that an ultrahigh J_{SC} value of 27.3 mA/cm^2 can be achieved by using 4% 1-chloronaphthalene (CN) additive in PTB7-Th:IEICO-4F system, owing to the increased $\pi-\pi$ coherence length of the acceptor, higher domain purity, and improved face-on/edge-on ratio.[614] However, increasing the CN content to 7% led to a sharp drop in the device performance due to the formation large domains above 60 nm, which may correspond to L−L phase separation caused by the slower drying process.[616] Using donor polymer, PTB7-Th, and small molecule acceptor, CO*i*8DFIC, Zhang and Wang et al. have recently discovered that solvent additives can impact the molecular packing of NFAs.[617] Shown in Figure 46a is the molecular structures of the donor and acceptor molecules as well as the solvent additives, DIO, diphenyl ether (DPE), and CN used to cast the blend films from a chloroform solvent. As previously discussed, this small molecule acceptor can form edge-on/flat-on lamella as well as H- and J-type of $\pi-\pi$ stacking depending on the solvent drying time.[81] In this case, the authors found that using additives enhanced J-type aggregation evidenced from the emergence of the red-shifted absorption peak as shown in Figure 46b. Particularly when using DIO as the additive, the UV−vis spectra indicates a strong J-aggregate character which enhanced the light absorption to longer wavelengths and boosted the *PCE*

https://doi.org/10.1021/acs.chemrev.2c00905
Chem. Rev. 2023, 123, 8395−8487

from 8.5% (without additives) to 12.9% (Figure 46c).[618] Other additives also enhanced the device performance owing to their more pronounced face-on $\pi-\pi$ stacking observed from GIWAXS measurements (Figure 46d). On the other hand, 2D GIWAXS image of the DIO additive case shows a large number of sharp diffraction peaks, indicating its highly crystalline nature. Furthermore, using molecular dynamics simulations, the authors determined that DIO interacts strongly with alkyl side chains of the acceptor molecule, making them flexible to accommodate stacking between the acceptor and donor units of the molecule which leads to the J-type aggregation to form three-dimensional pathways for charge transport.[619]

5. SUMMARY AND OUTLOOK

"The Journey is the Destination" (Dan Eldon). Conjugated molecular systems are living out this quote—it is their journey from the solution to the solid state that defines the thin film morphology and (opto)electronic device properties. As the applications of conjugated molecules are constantly evolving and continuously taken into new exciting domains such as thermoelectrics,[620,621] photocatalysts,[622−624] spintronics,[625−629] their assembly pathway remains crucial to any new emergent property, yet we have just recently begun to understand their remarkably complex journeys. In this review, we focus on molecular assembly pathways of conjugated polymers and NFA materials to shed light on how their assembly processes impact the solid-state morphology and optoelectronic properties. We further discussed how molecular assembly processes in blend systems relevant to OSCs couple with phase separation and crystallization pathways during evaporative solution processing to determine the BHJ morphology and device performance of OSCs.

We began the review with a summary of the multiscale morphology−optoelectronic property relationship. We then shifted our focus to the molecular assembly of conjugated polymers, beginning with polymer conformation, which is determined by the chain linearity and planarity, and overall stiffness quantified by l_p. These properties are dictated by the dihedral distribution, unit angle, and unit length along the backbone and are significantly impacted by the side chain size, branching, and orientation. Our discussion then progressed to the possible primary/secondary aggregate structures in polymer solutions suggested by the current body of literature. Conjugated polymers tend to aggregate in ink solutions forming primary aggregates through backbone and/or lamellar stacking via $\pi-\pi$ and London dispersion interactions, resulting in the formation of distinct aggregate structures, including 1-D fibers, 2-D sheets, and 3-D networks. These primary aggregates then develop into secondary aggregates, including lyotropic liquid crystals (such as nematic and twist-bend nematic mesophases) and polymer/fiber networks during evaporative assembly, which significantly influence the neat film morphology and optoelectronic properties.

Following the discussion of polymer assembly, we further delved into the assembly of NFAs which are widely used in the state-of-the-art OSCs. Compared to fullerene-based acceptors, NFAs offer many advantages, one of which is their ability to assemble or form various crystal packing structures through noncovalent interactions including $\pi-\pi$ stacking, hydrogen bonding, halogen bonding, and other van der Waals interactions. These interactions facilitate electron mobility, exciton diffusion and tunability of optical absorption, making them highly desirable for use in OSCs. However, the molecular assembly pathways of NFAs and intermediate solution structures are rarely reported. It is expected that they either directly crystallize from solution or form amorphous aggregates which then undergo amorphous-to-crystalline transition to form the final crystalline film in the solid-state, but other pathways are possible and remain to be discovered. Due to scarcity of literature on their assembly pathways, we instead focused on the crystal packing and polymorphism of NFAs in the solid-state and their impact on the electron mobility and exciton diffusion, and ultimately the device performance of OSCs.

Finally, we discussed how molecular assembly of conjugated polymers and NFAs can impact the blend morphology and device properties of OSCs. Since OSCs are often fabricated from a blend solution of donor and acceptor materials, we have first emphasized the fundamentals of crystallization and phase separation processes that occur during solution processing. Although crystallization is often described by classical nucleation theories which indicate that crystals are formed by monomer-by-monomer addition, the complex molecular assembly pathways of conjugated polymers and small molecules make the crystallization mechanism diverge from these classical theories. Instead, crystallization of conjugated organic molecules can involve multistep processes forming intermediate structures such as primary and secondary aggregates. In addition to crystallization, blend solutions of donor and acceptor materials undergo phase separation depending on the miscibility between the donor and acceptor materials which ultimately governs the domain sizes and purity of the blend films. The relative crystallization of the donor and acceptor materials is also critical for the microstructures of BHJ morphology. Therefore, compared to neat systems, establishing a clear relationship between molecular assembly and BHJ morphology is extremely complicated and relies on many parameters such as the miscibility, relative crystallization behavior of the donor and acceptor phases, and processing conditions.

Although we have summarized works which have provided invaluable insights into the structural diversity of conjugated polymers in solution, crystal packing of NFAs, and their impact on the blend film morphology of OSCs, we highlight some challenges and future research directions as follows.

5.1. Assembly of Conjugated Polymers

Although many works allude to solution aggregation and lyotropic liquid crystals of conjugated polymers, thus far only a few intermediate solution-state structures and corresponding assembly pathways have been elucidated with structural details. The following questions often remain unclear: What is the backbone conformation in the aggregate? What molecular interactions drive the aggregate formation, such as $\pi-\pi$ stacking, lamella stacking, halogen interactions etc? By what configurations do these packing motifs occur? For instance, $\pi-\pi$ stacking could take place in a staggered fashion rather than the commonly believed cofacial stacking.[295] What is the multiscale morphology of secondary aggregates? What is the ensuing assembly pathway with increasing solution concentration? And how do smaller length scale structural features define larger length scale morphology? Answering these questions requires extensive characterizations of solution state structures which remain challenging. The workhorse tools are solution small-angle X-ray and neutron scattering, electron microscopy imaging and electron diffraction of freeze-dried solutions, temperature and concentration dependent UV−vis spectroscopy, and polarized optical microscopy et al. More advanced character-

https://doi.org/10.1021/acs.chemrev.2c00905
Chem. Rev. 2023, 123, 8395−8487

ization tools such as liquid-phase TEM could serve as a promising candidate for in situ visualization of conjugated polymer assembly pathways at nanometer and even atomic resolution,[630−632] if beam damage can be mitigated. Advanced techniques are desired to visualize single fibers or single molecules in the fully solvated state.

Besides elucidating the structures of aggregates, thermodynamic and kinetic stabilities of intermediate solution state structures are often unknown. It has been famously shown that solution aggregates of P3HT keep on evolving over weeks.[282,633] Little is known of the metastability and temporal evolution of solution aggregates of donor−acceptor conjugated polymers, which is expected to depend on the type of aggregates and their structures. It could be possible that certain aggregate structures, while thermodynamically metastable, are self-limiting and thus kinetically stable.[634] This could have profound implications on stability at the device level.

Further, it is expected that solution aggregation is sensitively dependent on the environment and processing conditions. Solvent is expected to play a crucial role in largely modulating solution state structures. While elegant works have been reported on solvent effect,[16,288] more generalizable principles are desired to prescribe solvents for a conjugated polymer to target a particular type of aggregation behavior. Processing imposes a highly complex environment for the assembly and aggregation to take place. Much remains unclear about how fluid flow (flow types, strain rates), multiphase interfaces (solution−air, solution-substrate, triple phase contact line) and confinement effect (volume confinement, surface confinement) interplay with solution aggregation to redefine their structure and subsequent assembly pathways.

A holy grail is to develop general design principles relating molecular design with solution aggregation and assembly pathways, and ultimately with solid-state properties. A major hurdle to such fundamental studies lies in the lack of precision and throughput in conjugated polymer synthesis beyond P3HT and the often very large batch-to-batch variations.[635]

5.2. Assembly of NFAs

Although many NFAs have been developed and studied for their application to OSC devices, there is still a lack of understanding of their molecular assembly behavior, crystallization mechanism and solid-state packing in both the neat form and in blends. While crystal structures have often been reported, it is in fact challenging to grow large, high-quality crystals of NFAs due to their large molecular sizes and steric effects imposed by side chains and end groups, as well as the nonspecific nature of $\pi-\pi$ and quadrupole interactions and conformational flexibility. Further, the complex interplay between side chains, backbone and end groups and their distinct solvent affinities can give rise to complex phase behavior and polymorphism which are understudied. Given the often-unknown phase behaviors and crystal polymorphism, it remains a question what forms of assemblies NFA actually adopt when blended with the donor polymers, which could be distinct from their bulk crystal packing. Even more challenging to answer is the question of molecular packing and orientations right at the polymer/NFA interface.

Besides solid-state packing, assembly pathways of NFAs from solution to the solid-state are largely overlooked as most studies tend to focus on relating molecular design directly to bulk crystal structures in the solid-state. The rich interplay between side chain, backbone, and end groups as well as the unique shapes of NFA molecules could give rise to rich solution state structures and intermediate phases, which are yet to be uncovered. Advanced in situ characterization techniques mentioned above and established before could be applied to answering these questions.[339] Given the challenges in predicting crystal structures of complex and large conjugated molecules, machine learning approaches could be helpful for establishing NFA structure-assembly relations and predicting how solid-state packing affects optoelectronic properties, which then lay the foundation for developing molecular design rules. Given the increasing importance of processing and manufacturing in translating OSCs to the market, investigating nonequilibrium assembly of NFAs is at least of equal importance to tune the crystal packing and polymorphism in NFAs in a more controlled fashion.

5.3. Assembly of Polymers and NFAs in the Blend

Although researchers have heavily relied on molecular design approaches to improve the device properties of OSCs, increasing number of studies show the impact of solution-state aggregation on the blend film morphology, thus indicating that the molecular assembly processes should not be overlooked. It is relatively well-understood how neat, conjugated polymers and small molecules assemble from the solution- to the solid-state. However, in blends, the complexity of crystallization and phase separation pathways make it difficult to establish a clear relationship between molecular assembly processes and the blend film morphology. For instance, in Chapter 2, we have discussed that conjugated polymers can form various types of primary aggregates in the solution-state such as 3D network, 1D fibers, or 2D lamellar crystalline aggregates. However, the detailed solution-state structures of state-of-the-art donor polymers and their complex assembly pathways remain unknown, let alone their molecular assembly pathways during solution processing. Although some conjugated polymers such as P(NDI2OD-T2) have been reported to undergo liquid-crystalline mediated pathways during solution processing,[302,333] to the best of our knowledge, such a complex assembly pathway has not been reported for any donor polymers used in OSCs.

Due to the lack of understanding of molecular assembly in blends, the morphology control of OSCs thus remains challenging, relying largely on trial-and-error based approaches for molecular design and processing parameter optimization. Furthermore, as the power conversion efficiency of OSCs is nearing competing technologies, overcoming their poor device stability has become a major bottleneck for the successful commercialization of OSCs. Since the morphology of OSCs is often kinetically quenched for optimal device performance at the expense of morphological stability, understanding molecular assembly pathways may offer possibilities to achieving thermodynamically stable blend films with optimal device properties.

5.4. Data Science Driven Approaches

Beyond this bottom-up approach to understanding structure−property relationship in OSCs, researchers are also developing data science-driven approaches to accelerate material discovery and device optimization in organic electronics. High-throughput computation has emerged as a promising strategy for designing and discovering materials in the field of material science, utilizing a computational database of thermodynamic and electronic structure methods.[636] In 2011, Aspuru-Guzik et al. published the Harvard Clean Energy Project (CEP), as a high-throughput in silico screening of OSC-related molecules with

https://doi.org/10.1021/acs.chemrev.2c00905
Chem. Rev. 2023, 123, 8395−8487

the aim of understanding structure−property relationships.[637] Based on 26 different molecular fingerprints extracted from the literature, the CEP database screened up to 1.3 million donor materials and enabled researchers to design donor polymers and organic crystals with high hole mobility.[638,639] There were a few studies that established database for donor polymers and NFAs based on their molecular descriptors and moieties based on literature data and simulated properties.[367,640] Although these studies sped up the molecular design and screening process at first, device fabrication and optimization required a significant amount of human labor time and resources and remained challenging to test computationally suggested molecules rapidly.

To tackle the labor-intensiveness of material discovery and device optimization process, high-throughput experimentation approaches have been developed.[641] With the advantage of solution processing that enables parametric gradients in several processing conditions,[642] researchers could leverage parameters such as thickness,[643,644] precursor solution formulation,[49,645−649] and temperature[650,651] to optimize the device performance. Researchers have also implemented self-driven laboratories based on autonomous robotic experimental platform and combined with machine learning (ML) or artificial intelligence (AI) to further minimize human resources and increase the data yield and reproducibility. In 2020, Berlinguette group has built a modular self-driven laboratory called Ada by automating thin film fabrication and characterization process to optimize the hole mobility of fabricated films.[652] Brabec group incorporated a Bayesian optimization algorithm to automate quaternary OSC device fabrication and photostability testing.[653] They also developed AMANDA Line One(autonomous materials and device application platform), an automated OSC fabrication and characterization platform to optimize *PCE* and photostability of PM6:Y6 blend devices.[654] Just very recently, Xu and collaborators developed Polybot self-driven laboratories that integrates automated synthesis, characterizations, device testing and machine learning to accelerate polymer electronics research.[655]

These autonomous robotic platforms have paved the way for high-throughput generation of consistent, abundant, and high-quality experimental data on molecular and device properties which is crucial for ML-based property prediction. Further integrating automated experiments with AI/ML enables inverse design of materials and processing parameters, making it possible to "close the feedback loop" between material design, processing, and device properties. We believe that these AI based approaches, coupled with insights gained from molecular assembly, would enable rational design of new materials with controlled morphology and device properties, bringing us a step closer to the successful commercialization of organic electronics and photovoltaics.

AUTHOR INFORMATION

Corresponding Author

Ying Diao − *Department of Chemical and Biomolecular Engineering, University of Illinois Urbana−Champaign, Urbana, Illinois 61801, United States; Department of Chemistry, University of Illinois Urbana−Champaign, Urbana, Illinois 61801, United States;* orcid.org/0000-0002-8984-0051; Email: yingdiao@illinois.edu

Authors

Azzaya Khasbaatar − *Department of Chemical and Biomolecular Engineering, University of Illinois Urbana−Champaign, Urbana, Illinois 61801, United States;* orcid.org/0000-0002-4145-3511

Zhuang Xu − *Department of Chemistry, University of Illinois Urbana−Champaign, Urbana, Illinois 61801, United States*

Jong-Hoon Lee − *Department of Chemical and Biomolecular Engineering, University of Illinois Urbana−Champaign, Urbana, Illinois 61801, United States;* orcid.org/0000-0001-9102-0872

Gonzalo Campillo-Alvarado − *Department of Chemistry, Reed College, Portland, Oregon 97202, United States;* orcid.org/0000-0002-1868-8523

Changhyun Hwang − *Department of Chemical and Biomolecular Engineering, University of Illinois Urbana−Champaign, Urbana, Illinois 61801, United States;* orcid.org/0000-0003-1720-7852

Brandon N. Onusaitis − *Department of Chemical and Biomolecular Engineering, University of Illinois Urbana−Champaign, Urbana, Illinois 61801, United States*

Complete contact information is available at: https://pubs.acs.org/10.1021/acs.chemrev.2c00905

Author Contributions

⊥A.K., Z.X., and J.-H.L. contributed equally. CRediT: **Azzaya Khasbaatar** visualization, writing-original draft, writing-review & editing; **Zhuang Xu** visualization, writing-original draft, writing-review & editing; **Jong-Hoon Lee** visualization, writing-original draft, writing-review & editing; **Gonzalo Campillo-Alvarado** writing-original draft; **Changhyun Hwang** writing-original draft, writing-review & editing; **Brandon Onusaitis** writing-original draft; **Ying Diao** conceptualization, funding acquisition, project administration, supervision, writing-review & editing.

Notes

The authors declare no competing financial interest.

Biographies

Azzaya Khasbaatar received her BSE degree in Chemical Engineering from the University of Michigan in 2018, where she worked under the guidance of Prof. Xiaoxia (Nina) Lin as an undergraduate research assistant. She then started her Ph.D. program in Chemical and Biomolecular engineering at the University of Illinois at Urbana−Champaign, where she is currently a graduate student in Prof. Ying Diao's lab. Her research focuses on understanding how solution-state aggregation of donor polymers and their aggregate structures impact the blend film morphology and device properties of organic solar cells.

Zhuang Xu completed his M.S. degree in Polymer Science and Engineering from the University of Akron. Motivated to pursue advanced research, he proceeded to the University of Illinois at Urbana−Champaign for his Ph.D. in Chemistry. He joined the Diao Lab in Fall 2019, and his research focuses on probing the assembly pathway of conjugated polymers from solution to thin films.

Jong-Hoon Lee received his BEng degree in Materials Science and Engineering from Korea University, Republic of Korea, and his Ph.D. in 2018 from Gwangju Institute of Science and Technology (GIST) under the supervision of Prof. Kwanghee Lee. After postdoctoral training at GIST, he worked as a professor in Energy Resources at Huree University of Information Communication Technology, Mongolia, supported by World Friend Korea (WFK) Techno Peace Corp (TPC) program from National Research Foundation (NRF), Republic of Korea. He joined Prof. Diao's group at the University of Illinois at Urbana−Champaign as a phostdoctoral researcher in 2021. His

https://doi.org/10.1021/acs.chemrev.2c00905
Chem. Rev. 2023, 123, 8395−8487

research focuses on developing all-printed organic solar cells for autonomous OSC fabrication and characterization systems and studying fundamentals of chirality emergence in conjugated polymers and their application to organic optoelectronics.

Gonzalo Campillo-Alvarado is an Assistant Professor of Chemistry at Reed College in Portland, OR (USA). His research focuses on designing dynamic crystalline materials with an emphasis on boron for applications of chemical separations, pharmaceutics, and electronics. Before joining Reed, he was an Illinois Distinguished Postdoctoral Research Associate at the University of Illinois at Urbana−Champaign, mentored by Ying Diao. He received his Ph.D. in chemistry from the University of Iowa, and his B.Sc. in biopharmaceutical chemistry from Universidad Veracruzana (Mexico).

Changhyun Hwang received his BE degree in Chemical and Biological engineering from Korea University. He is not pursuing his Ph.D. at UIUC under the supervision of Prof. Ying Diao where he focuses on developing a self-driven lab for closed-loop discovery of organic solar cell materials.

Brandon N. Onusaitis is a first year Ph.D. student in Materials Science and Engineering at Northwestern University. He is advised by Dr. Olvera de la Cruz, and he studies iontronics using molecular dynamics (MD) simulations. He received his bachelor's degree in chemical engineering from the University of Illinois at Urbana−Champaign. During his undergraduate studies, he worked as a researcher in the Dr. Diao lab where he investigated the mechanical and electronic properties of organic crystals.

Ying Diao is an Associate Professor, University Scholar, I. C. Gunsalus Scholar, and Dow Chemical Company Faculty Scholar at University of Illinois at Urbana−Champaign. She received her Ph.D. degree in Chemical Engineering from MIT in 2012. Her doctoral thesis was on understanding heterogeneous nucleation of pharmaceuticals by designing polymeric substrates. In her subsequent postdoctoral training at Stanford University, she pursued research in the thriving field of printed electronics. The Diao group, started in 2015 at Illinois, focuses on understanding assembly of organic functional materials and innovating printing approaches that enable structural control down to the molecular and nanoscale.

ACKNOWLEDGMENTS

A.K. and Y.D. acknowledge support by the Office of Naval Research under grant number N00014-22-1-2202. Z.X. and Y.D. acknowledge support by the NSF CAREER award under Grant No. 18-47828. J.-H.L., C.H., and Y.D. acknowledge support by NSF through the Molecular Maker Lab Institute under Grant No. 20-19897. G.C.-A. acknowledges financial support from The Office for Access and Equity, the DRIVE Committee, and the Illinois Materials Research Center (University of Illinois at Urbana−Champaign) through the DRIVE Distinguished Postdoctoral Fellowship. A.K. is thankful to Frank Zhang for all the help and feedback on managing the references cited in this review.

REFERENCES

(1) Forrest, S. R. *Organic Electronics: Foundations to Applications*; Oxford University Press, 2020; pp 3−30.
(2) Akamatu, H.; Inokuchi, H. On the Electrical Conductivity of Violanthrone, Iso-Violanthrone, and Pyranthrone. *J. Chem. Phys.* **1950**, *18*, 810−811.
(3) Pope, M.; Kallmann, H. P.; Magnante, P. Electroluminescence in Organic Crystals. *J. Chem. Phys.* **1963**, *38*, 2042−2043.
(4) Shirakawa, H.; McDiarmid, A.; Heeger, A. Focus Article: Twenty-Five Years of Conducting Polymers. *Chem. Commun.* **2003**, 1−4.
(5) Chiang, C. K.; Fincher, C. R.; Park, Y. W.; Heeger, A. J.; Shirakawa, H.; Louis, E. J.; Gau, S. C.; MacDiarmid, A. G. Electrical Conductivity in Doped Polyacetylene. *Phys. Rev. Lett.* **1977**, *39*, 1098−1101.
(6) Shirakawa, H.; Louis, E. J.; MacDiarmid, A. G.; Chiang, C. K.; Heeger, A. J. Synthesis of Electrically Conducting Organic Polymers: Halogen Derivatives of Polyacetylene, (Ch) X. *J. Chem. Soc., Chem. Commun.* **1977**, 578.
(7) Tang, C. W.; VanSlyke, S. A. Organic Electroluminescent Diodes. *Appl. Phys. Lett.* **1987**, *51*, 913−915.
(8) Tang, C. W. Two-Layer Organic Photovoltaic Cell. *Appl. Phys. Lett.* **1986**, *48*, 183−185.
(9) Koezuka, H.; Tsumura, A.; Ando, T. Field-Effect Transistor with Polythiophene Thin Film. *Synth. Met.* **1987**, *18*, 699−704.
(10) Hong, G.; Gan, X.; Leonhardt, C.; Zhang, Z.; Seibert, J.; Busch, J. M.; Brase, S. A Brief History of Oleds-Emitter Development and Industry Milestones. *Adv. Mater.* **2021**, *33*, 2005630.
(11) Mas-Torrent, M.; Rovira, C. Role of Molecular Order and Solid-State Structure in Organic Field-Effect Transistors. *Chem. Rev.* **2011**, *111*, 4833−4856.
(12) Kim, N.-K.; Jang, S.-Y.; Pace, G.; Caironi, M.; Park, W.-T.; Khim, D.; Kim, J.; Kim, D.-Y.; Noh, Y.-Y. High-Performance Organic Field-Effect Transistors with Directionally Aligned Conjugated Polymer Film Deposited from Pre-Aggregated Solution. *Chem. Mater.* **2015**, *27*, 8345−8353.
(13) Bucella, S. G.; Luzio, A.; Gann, E.; Thomsen, L.; McNeill, C. R.; Pace, G.; Perinot, A.; Chen, Z.; Facchetti, A.; Caironi, M. Macroscopic and High-Throughput Printing of Aligned Nanostructured Polymer Semiconductors for MHz Large-Area Electronics. *Nat. Commun.* **2015**, *6*, 8394.
(14) Park, Y. D.; Lee, H. S.; Choi, Y. J.; Kwak, D.; Cho, J. H.; Lee, S.; Cho, K. Solubility-Induced Ordered Polythiophene Precursors for High-Performance Organic Thin-Film Transistors. *Adv. Funct. Mater.* **2009**, *19*, 1200−1206.
(15) Chen, M. S.; Lee, O. P.; Niskala, J. R.; Yiu, A. T.; Tassone, C. J.; Schmidt, K.; Beaujuge, P. M.; Onishi, S. S.; Toney, M. F.; Zettl, A.; et al. Enhanced Solid-State Order and Field-Effect Hole Mobility through Control of Nanoscale Polymer Aggregation. *J. Am. Chem. Soc.* **2013**, *135*, 19229−19236.
(16) Xu, Z.; Park, K. S.; Kwok, J. J.; Lin, O.; Patel, B. B.; Kafle, P.; Davies, D. W.; Chen, Q.; Diao, Y. Not All Aggregates Are Made the Same: Distinct Structures of Solution Aggregates Drastically Modulate Assembly Pathways, Morphology, and Electronic Properties of Conjugated Polymers. *Adv. Mater.* **2022**, *34*, 2203055.
(17) Nahid, M. M.; Welford, A.; Gann, E.; Thomsen, L.; Sharma, K. P.; McNeill, C. R. Nature and Extent of Solution Aggregation Determines the Performance of P(Ndi2od-T2) Thin-Film Transistors. *Adv. Electron. Mater.* **2018**, *4*, 1700559.
(18) Li, M.; An, C.; Marszalek, T.; Baumgarten, M.; Yan, H.; Mullen, K.; Pisula, W. Controlling the Surface Organization of Conjugated Donor-Acceptor Polymers by Their Aggregation in Solution. *Adv. Mater.* **2016**, *28*, 9430−9438.
(19) Zheng, Y. Q.; Yao, Z. F.; Lei, T.; Dou, J. H.; Yang, C. Y.; Zou, L.; Meng, X.; Ma, W.; Wang, J. Y.; Pei, J. Unraveling the Solution-State Supramolecular Structures of Donor-Acceptor Polymers and Their Influence on Solid-State Morphology and Charge-Transport Properties. *Adv. Mater.* **2017**, *29*, 1701072.
(20) Cui, Y.; Xu, Y.; Yao, H.; Bi, P.; Hong, L.; Zhang, J.; Zu, Y.; Zhang, T.; Qin, J.; Ren, J.; et al. Single-Junction Organic Photovoltaic Cell with 19% Efficiency. *Adv. Mater.* **2021**, *33*, 2102420.
(21) Zhu, L.; Zhang, M.; Xu, J.; Li, C.; Yan, J.; Zhou, G.; Zhong, W.; Hao, T.; Song, J.; Xue, X.; et al. Single-Junction Organic Solar Cells with over 19% Efficiency Enabled by a Refined Double-Fibril Network Morphology. *Nat. Mater.* **2022**, *21*, 656−663.
(22) Wei, Y.; Chen, Z.; Lu, G.; Yu, N.; Li, C.; Gao, J.; Gu, X.; Hao, X.; Lu, G.; Tang, Z.; et al. Binary Organic Solar Cells Breaking 19% Via Manipulating the Vertical Component Distribution. *Adv. Mater.* **2022**, *34*, 2204718.

https://doi.org/10.1021/acs.chemrev.2c00905
Chem. Rev. 2023, 123, 8395−8487

(23) Halls, J. J. M.; Walsh, C. A.; Greenham, N. C.; Marseglia, E. A.; Friend, R. H.; Moratti, S. C.; Holmes, A. B. Efficient Photodiodes from Interpenetrating Polymer Networks. *Nature* **1995**, *376*, 498−500.
(24) Yu, G.; Gao, J.; Hummelen, J. C.; Wudl, F.; Heeger, A. J. Polymer Photovoltaic Cells: Enhanced Efficiencies Via a Network of Internal Donor-Acceptor Heterojunctions. *Science* **1995**, *270*, 1789−1791.
(25) Sajjad, M. T.; Ruseckas, A.; Samuel, I. D. W. Enhancing Exciton Diffusion Length Provides New Opportunities for Organic Photovoltaics. *Matter* **2020**, *3*, 341−354.
(26) Sariciftci, N. S.; Smilowitz, L.; Heeger, A. J.; Wudl, F. Photoinduced Electron Transfer from a Conducting Polymer to Buckminsterfullerene. *Science* **1992**, *258*, 1474−1476.
(27) Kumari, T.; Lee, S. M.; Kang, S.-H.; Chen, S.; Yang, C. Ternary Solar Cells with a Mixed Face-on and Edge-on Orientation Enable an Unprecedented Efficiency of 12.1%. *Energy Environ. Sci.* **2017**, *10*, 258−265.
(28) Zhao, W.; Li, S.; Yao, H.; Zhang, S.; Zhang, Y.; Yang, B.; Hou, J. Molecular Optimization Enables over 13% Efficiency in Organic Solar Cells. *J. Am. Chem. Soc.* **2017**, *139*, 7148−7151.
(29) Zhang, J.; Tan, H. S.; Guo, X.; Facchetti, A.; Yan, H. Material Insights and Challenges for Non-Fullerene Organic Solar Cells Based on Small Molecular Acceptors. *Nat. Energy* **2018**, *3*, 720−731.
(30) Cheng, P.; Li, G.; Zhan, X.; Yang, Y. Next-Generation Organic Photovoltaics Based on Non-Fullerene Acceptors. *Nat. Photonics* **2018**, *12*, 131−142.
(31) Gurney, R. S.; Lidzey, D. G.; Wang, T. A Review of Non-Fullerene Polymer Solar Cells: From Device Physics to Morphology Control. *Rep. Prog. Phys.* **2019**, *82*, 036601.
(32) Fu, H.; Wang, Z.; Sun, Y. Polymer Donors for High-Performance Non-Fullerene Organic Solar Cells. *Angew. Chem., Int. Ed. Engl.* **2019**, *58*, 4442−4453.
(33) Zhou, H.; Yang, L.; You, W. Rational Design of High Performance Conjugated Polymers for Organic Solar Cells. *Macromolecules* **2012**, *45*, 607−632.
(34) McDowell, C.; Abdelsamie, M.; Toney, M. F.; Bazan, G. C. Solvent Additives: Key Morphology-Directing Agents for Solution-Processed Organic Solar Cells. *Adv. Mater.* **2018**, *30*, 1707114.
(35) Treat, N. D.; Chabinyc, M. L. Phase Separation in Bulk Heterojunctions of Semiconducting Polymers and Fullerenes for Photovoltaics. *Annu. Rev. Phys. Chem.* **2014**, *65*, 59−81.
(36) Gu, K.; Loo, Y. L. The Polymer Physics of Multiscale Charge Transport in Conjugated Systems. *J. Polym. Sci., Part B: Polym. Phys.* **2019**, *57*, 1559−1571.
(37) Fratini, S.; Nikolka, M.; Salleo, A.; Schweicher, G.; Sirringhaus, H. Charge Transport in High-Mobility Conjugated Polymers and Molecular Semiconductors. *Nat. Mater.* **2020**, *19*, 491−502.
(38) Zhenan Bao, J. L. *Organic Field-Effect Transistors*, 1st ed.; CRC Press, 2007; p 30.
(39) Noriega, R.; Rivnay, J.; Vandewal, K.; Koch, F. P.; Stingelin, N.; Smith, P.; Toney, M. F.; Salleo, A. A General Relationship between Disorder, Aggregation and Charge Transport in Conjugated Polymers. *Nat. Mater.* **2013**, *12*, 1038−1044.
(40) Chung, H.; Diao, Y. Polymorphism as an Emerging Design Strategy for High Performance Organic Electronics. *J. Mater. Chem. C* **2016**, *4*, 3915−3933.
(41) Kim, M.; Ryu, S. U.; Park, S. A.; Choi, K.; Kim, T.; Chung, D.; Park, T. Donor-Acceptor-Conjugated Polymer for High-Performance Organic Field-Effect Transistors: A Progress Report. *Adv. Funct. Mater.* **2020**, *30*, 1904545.
(42) Wurfel, U.; Neher, D.; Spies, A.; Albrecht, S. Impact of Charge Transport on Current-Voltage Characteristics and Power-Conversion Efficiency of Organic Solar Cells. *Nat. Commun.* **2015**, *6*, 6951.
(43) Kim, J. M.; Kim, J. J. Charge Transport Layers Manage Mobility and Carrier Density Balance in Light-Emitting Layers Influencing the Operational Stability of Organic Light Emitting Diodes. *Org. Electron.* **2019**, *67*, 43−49.
(44) Lin, G.; Peng, H.; Chen, L.; Nie, H.; Luo, W.; Li, Y.; Chen, S.; Hu, R.; Qin, A.; Zhao, Z.; et al. Improving Electron Mobility of Tetraphenylethene-Based Aiegens to Fabricate Nondoped Organic Light-Emitting Diodes with Remarkably High Luminance and Efficiency. *ACS Appl. Mater. Interfaces* **2016**, *8*, 16799−16808.
(45) Rivnay, J.; Inal, S.; Salleo, A.; Owens, R. M.; Berggren, M.; Malliaras, G. G. Organic Electrochemical Transistors. *Nat. Rev. Mater.* **2018**, *3*, 17086.
(46) Chow, P. C. Y.; Someya, T. Organic Photodetectors for Next-Generation Wearable Electronics. *Adv. Mater.* **2020**, *32*, 1902045.
(47) Prins, P.; Grozema, F. C.; Schins, J. M.; Patil, S.; Scherf, U.; Siebbeles, L. D. High Intrachain Hole Mobility on Molecular Wires of Ladder-Type Poly(P-Phenylenes). *Phys. Rev. Lett.* **2006**, *96*, 146601.
(48) Rivnay, J.; Noriega, R.; Northrup, J. E.; Kline, R. J.; Toney, M. F.; Salleo, A. Structural Origin of Gap States in Semicrystalline Polymers and the Implications for Charge Transport. *Phys. Rev. B* **2011**, *83*, 121306.
(49) Venkateshvaran, D.; Nikolka, M.; Sadhanala, A.; Lemaur, V.; Zelazny, M.; Kepa, M.; Hurhangee, M.; Kronemeijer, A. J.; Pecunia, V.; Nasrallah, I.; et al. Approaching Disorder-Free Transport in High-Mobility Conjugated Polymers. *Nature* **2014**, *515*, 384−388.
(50) Bronstein, H.; Nielsen, C. B.; Schroeder, B. C.; McCulloch, I. The Role of Chemical Design in the Performance of Organic Semiconductors. *Nat. Rev. Chem.* **2020**, *4*, 66−77.
(51) Danielsen, S. P. O.; Bridges, C. R.; Segalman, R. A. Chain Stiffness of Donor-Acceptor Conjugated Polymers in Solution. *Macromolecules* **2022**, *55*, 437−449.
(52) McCulloch, B.; Ho, V.; Hoarfrost, M.; Stanley, C.; Do, C.; Heller, W. T.; Segalman, R. A. Polymer Chain Shape of Poly(3-Alkylthiophenes) in Solution Using Small-Angle Neutron Scattering. *Macromolecules* **2013**, *46*, 1899−1907.
(53) Kuei, B.; Gomez, E. D. Chain Conformations and Phase Behavior of Conjugated Polymers. *Soft Matter* **2017**, *13*, 49−67.
(54) Zhang, X.; Bronstein, H.; Kronemeijer, A. J.; Smith, J.; Kim, Y.; Kline, R. J.; Richter, L. J.; Anthopoulos, T. D.; Sirringhaus, H.; Song, K.; et al. Molecular Origin of High Field-Effect Mobility in an Indacenodithiophene-Benzothiadiazole Copolymer. *Nat. Commun.* **2013**, *4*, 2238.
(55) Chang, M.; Choi, D.; Fu, B.; Reichmanis, E. Solvent Based Hydrogen Bonding: Impact on Poly(3-Hexylthiophene) Nanoscale Morphology and Charge Transport Characteristics. *ACS Nano* **2013**, *7*, 5402−5413.
(56) Chang, M.; Lee, J.; Kleinhenz, N.; Fu, B.; Reichmanis, E. Photoinduced Anisotropic Supramolecular Assembly and Enhanced Charge Transport of Poly(3-Hexylthiophene) Thin Films. *Adv. Funct. Mater.* **2014**, *24*, 4457−4465.
(57) Aiyar, A. R.; Hong, J.-I.; Nambiar, R.; Collard, D. M.; Reichmanis, E. Tunable Crystallinity in Regioregular Poly(3-Hexylthiophene) Thin Films and Its Impact on Field Effect Mobility. *Adv. Funct. Mater.* **2011**, *21*, 2652−2659.
(58) Neto, N. M. B.; Silva, M. D. R.; Araujo, P. T.; Sampaio, R. N. Photoinduced Self-Assembled Nanostructures and Permanent Polaron Formation in Regioregular Poly(3-Hexylthiophene). *Adv. Mater.* **2018**, *30*, 1705052.
(59) Gu, K.; Snyder, C. R.; Onorato, J.; Luscombe, C. K.; Bosse, A. W.; Loo, Y. L. Assessing the Huang-Brown Description of Tie Chains for Charge Transport in Conjugated Polymers. *ACS Macro Lett.* **2018**, *7*, 1333−1338.
(60) Duong, D. T.; Ho, V.; Shang, Z.; Mollinger, S.; Mannsfeld, S. C. B.; Dacuña, J.; Toney, M. F.; Segalman, R.; Salleo, A. Mechanism of Crystallization and Implications for Charge Transport in Poly(3-Ethylhexylthiophene) Thin Films. *Adv. Funct. Mater.* **2014**, *24*, 4515−4521.
(61) Tanaka, H.; Wakamatsu, A.; Kondo, M.; Kawamura, S.; Kuroda, S.-i.; Shimoi, Y.; Park, W.-T.; Noh, Y.-Y.; Takenobu, T. Microscopic Observation of Efficient Charge Transport Processes across Domain Boundaries in Donor-Acceptor-Type Conjugated Polymers. *Commun. Phys.* **2019**, *2*, 96.
(62) Deng, J.; Zheng, L.; Ding, C.; Guo, Y.; Xie, Y.; Wang, J.; Ke, Y.; Li, M.; Li, L.; Janssen, R. A. J. Determinant Role of Solution-State Supramolecular Assembly in Molecular Orientation of Conjugated Polymer Films. *Adv. Funct. Mater.* **2023**, *33*, 2209195.

https://doi.org/10.1021/acs.chemrev.2c00905
Chem. Rev. 2023, 123, 8395−8487

(63) Pandey, M.; Kumari, N.; Nagamatsu, S.; Pandey, S. S. Recent Advances in the Orientation of Conjugated Polymers for Organic Field-Effect Transistors. *J. Mater. Chem. C* **2019**, *7*, 13323−13351.
(64) Sirringhaus, H.; Brown, P. J.; Friend, R. H.; Nielsen, M. M.; Bechgaard, K.; Langeveld-Voss, B. M. W.; Spiering, A. J. H.; Janssen, R. A. J.; Meijer, E. W.; Herwig, P.; et al. Two-Dimensional Charge Transport in Self-Organized, High-Mobility Conjugated Polymers. *Nature* **1999**, *401*, 685−688.
(65) Wang, L.; Park, J. S.; Lee, H. G.; Kim, G. U.; Kim, D.; Kim, C.; Lee, S.; Kim, F. S.; Kim, B. J. Impact of Chlorination Patterns of Naphthalenediimide-Based Polymers on Aggregated Structure, Crystallinity, and Device Performance of All-Polymer Solar Cells and Organic Transistors. *ACS Appl. Mater. Interfaces* **2020**, *12*, 56240−56250.
(66) Wang, Y.; Hasegawa, T.; Matsumoto, H.; Mori, T.; Michinobu, T. High-Performance N-Channel Organic Transistors Using High-Molecular-Weight Electron-Deficient Copolymers and Amine-Tailed Self-Assembled Monolayers. *Adv. Mater.* **2018**, *30*, 1707164.
(67) Wang, S.; Zhang, T.; Zhang, L.; Liu, D.; Liu, X.; Li, J.; Li, H.; Zhang, Q.; Han, Y. The Continuous Fiber Networks with a Balanced Bimodal Orientation of P(Ndi2od-T2) by Controlling Solution Nucleation and Face-on and Edge-on Crystallization Rates. *Polymer* **2022**, *262*, 125435.
(68) Kang, S.-H.; Lee, H. R.; Dutta, G. K.; Lee, J.; Oh, J. H.; Yang, C. A Role of Side-Chain Regiochemistry of Thienylene-Vinylene-Thienylene (Tvt) in the Transistor Performance of Isomeric Polymers. *Macromolecules* **2017**, *50*, 884−890.
(69) Xue, G.; Zhao, X.; Qu, G.; Xu, T.; Gumyusenge, A.; Zhang, Z.; Zhao, Y.; Diao, Y.; Li, H.; Mei, J. Symmetry Breaking in Side Chains Leading to Mixed Orientations and Improved Charge Transport in Isoindigo-Alt-Bithiophene Based Polymer Thin Films. *ACS Appl. Mater. Interfaces* **2017**, *9*, 25426−25433.
(70) Liu, R.; Yang, W.; Xu, W.; Deng, J.; Ding, C.; Guo, Y.; Zheng, L.; Sun, J.; Li, M. Impact of Chemical Design on the Molecular Orientation of Conjugated Donor-Acceptor Polymers for Field-Effect Transistors. *ACS Appl. Polym. Mater.* **2022**, *4*, 2233−2250.
(71) Li, H.; Yang, H.; Zhang, L.; Wang, S.; Chen, Y.; Zhang, Q.; Zhang, J.; Tian, H.; Han, Y. Optimizing the Crystallization Behavior and Film Morphology of Donor-Acceptor Conjugated Semiconducting Polymers by Side-Chain-Solvent Interaction in Nonpolar Solvents. *Macromolecules* **2021**, *54*, 10557−10573.
(72) Khim, D.; Luzio, A.; Bonacchini, G. E.; Pace, G.; Lee, M. J.; Noh, Y. Y.; Caironi, M. Uniaxial Alignment of Conjugated Polymer Films for High-Performance Organic Field-Effect Transistors. *Adv. Mater.* **2018**, *30*, 1705463.
(73) Tseng, H. R.; Phan, H.; Luo, C.; Wang, M.; Perez, L. A.; Patel, S. N.; Ying, L.; Kramer, E. J.; Nguyen, T. Q.; Bazan, G. C.; et al. High-Mobility Field-Effect Transistors Fabricated with Macroscopic Aligned Semiconducting Polymers. *Adv. Mater.* **2014**, *26*, 2993−2998.
(74) Jimison, L. H.; Toney, M. F.; McCulloch, I.; Heeney, M.; Salleo, A. Charge-Transport Anisotropy Due to Grain Boundaries in Directionally Crystallized Thin Films of Regioregular Poly(3-Hexylthiophene). *Adv. Mater.* **2009**, *21*, 1568−1572.
(75) Crossland, E. J.; Tremel, K.; Fischer, F.; Rahimi, K.; Reiter, G.; Steiner, U.; Ludwigs, S. Anisotropic Charge Transport in Spherulitic Poly(3-Hexylthiophene) Films. *Adv. Mater.* **2012**, *24*, 839−844.
(76) O'Connor, B. T.; Reid, O. G.; Zhang, X.; Kline, R. J.; Richter, L. J.; Gundlach, D. J.; DeLongchamp, D. M.; Toney, M. F.; Kopidakis, N.; Rumbles, G. Morphological Origin of Charge Transport Anisotropy in Aligned Polythiophene Thin Films. *Adv. Funct. Mater.* **2014**, *24*, 3422−3431.
(77) Segatta, F.; Lattanzi, G.; Faccioli, P. Predicting Charge Mobility of Organic Semiconductors with Complex Morphology. *Macromolecules* **2018**, *51*, 9060−9068.
(78) Osaka, I.; Takimiya, K. Backbone Orientation in Semiconducting Polymers. *Polymer* **2015**, *59*, A1−A15.
(79) Vezie, M. S.; Few, S.; Meager, I.; Pieridou, G.; Dorling, B.; Ashraf, R. S.; Goni, A. R.; Bronstein, H.; McCulloch, I.; Hayes, S. C.; et al. Exploring the Origin of High Optical Absorption in Conjugated Polymers. *Nat. Mater.* **2016**, *15*, 746−753.
(80) Yan, J.; Rodriguez-Martinez, X.; Pearce, D.; Douglas, H.; Bili, D.; Azzouzi, M.; Eisner, F.; Virbule, A.; Rezasoltani, E.; Belova, V.; et al. Identifying Structure-Absorption Relationships and Predicting Absorption Strength of Non-Fullerene Acceptors for Organic Photovoltaics. *Energy Environ. Sci.* **2022**, *15*, 2958−2973.
(81) Li, W.; Chen, M.; Cai, J.; Spooner, E. L. K.; Zhang, H.; Gurney, R. S.; Liu, D.; Xiao, Z.; Lidzey, D. G.; Ding, L.; et al. Molecular Order Control of Non-Fullerene Acceptors for High-Efficiency Polymer Solar Cells. *Joule* **2019**, *3*, 819−833.
(82) Bai, F.; Zhang, J.; Zeng, A.; Zhao, H.; Duan, K.; Yu, H.; Cheng, K.; Chai, G.; Chen, Y.; Liang, J.; et al. A Highly Crystalline Non-Fullerene Acceptor Enabling Efficient Indoor Organic Photovoltaics with High Eqe and Fill Factor. *Joule* **2021**, *5*, 1231−1245.
(83) Park, K. S.; Kwok, J. J.; Dilmurat, R.; Qu, G.; Kafle, P.; Luo, X.; Jung, S. H.; Olivier, Y.; Lee, J. K.; Mei, J.; et al. Tuning Conformation, Assembly, and Charge Transport Properties of Conjugated Polymers by Printing Flow. *Sci. Adv.* **2019**, *5*, No. eaaw7757.
(84) Xu, Z.; Park, K. S.; Diao, Y. What Is the Assembly Pathway of a Conjugated Polymer from Solution to Thin Films? *Front. Chem.* **2020**, *8*, 583521.
(85) Zhokhavets, U.; Erb, T.; Gobsch, G.; Al-Ibrahim, M.; Ambacher, O. Relation between Absorption and Crystallinity of Poly(3-Hexylthiophene)/Fullerene Films for Plastic Solar Cells. *Chem. Phys. Lett.* **2006**, *418*, 347−350.
(86) Spano, F. C.; Silva, C. H- and J-Aggregate Behavior in Polymeric Semiconductors. *Annu. Rev. Phys. Chem.* **2014**, *65*, 477−500.
(87) Li, M.; Balawi, A. H.; Leenaers, P. J.; Ning, L.; Heintges, G. H. L.; Marszalek, T.; Pisula, W.; Wienk, M. M.; Meskers, S. C. J.; Yi, Y.; et al. Impact of Polymorphism on the Optoelectronic Properties of a Low-Bandgap Semiconducting Polymer. *Nat. Commun.* **2019**, *10*, 2867.
(88) Mikhnenko, O. V.; Blom, P. W. M.; Nguyen, T.-Q. Exciton Diffusion in Organic Semiconductors. *Energy Environ. Sci.* **2015**, *8*, 1867−1888.
(89) Menke, S. M.; Holmes, R. J. Exciton Diffusion in Organic Photovoltaic Cells. *Energy Environ. Sci.* **2014**, *7*, 499−512.
(90) Ren, H.; Chen, J.-D.; Li, Y.-Q.; Tang, J.-X. Recent Progress in Organic Photodetectors and Their Applications. *Adv. Sci.* **2021**, *8*, 2002418.
(91) Song, J.; Lee, H.; Jeong, E. G.; Choi, K. C.; Yoo, S. Organic Light-Emitting Diodes: Pushing toward the Limits and Beyond. *Adv. Mater.* **2020**, *32*, 1907539.
(92) Cicoira, F.; Santato, C. Organic Light Emitting Field Effect Transistors: Advances and Perspectives. *Adv. Funct. Mater.* **2007**, *17*, 3421−3434.
(93) Sudheendran Swayamprabha, S.; Dubey, D. K.; Shahnawaz; Yadav, R. A. K.; Nagar, M. R.; Sharma, A.; Tung, F.-C.; Jou, J.-H. Approaches for Long Lifetime Organic Light Emitting Diodes. *Adv. Sci.* **2021**, *8*, 2002254.
(94) Deibel, C.; Strobel, T.; Dyakonov, V. Role of the Charge Transfer State in Organic Donor-Acceptor Solar Cells. *Adv. Mater.* **2010**, *22*, 4097−4111.
(95) Zhu, L.; Yang, C.; Yi, Y.; Wei, Z. Effective Modulation of Exciton Binding Energies in Polymorphs of a Small-Molecule Acceptor for Organic Photovoltaics. *J. Phys. Chem. Lett.* **2020**, *11*, 10227−10232.
(96) Zhang, C.; Liu, R.; Mak, C. H.; Zou, X.; Shen, H.-H.; Leu, S.-Y.; Ji, L.; Hsu, H.-Y. Photophysics of Organic Photovoltaic Devices: A Review. *J. Photonics Energy* **2018**, *8*, 021001.
(97) Coropceanu, V.; Chen, X.-K.; Wang, T.; Zheng, Z.; Brédas, J.-L. Charge-Transfer Electronic States In organic Solar Cells. *Nat. Rev. Mater.* **2019**, *4*, 689−707.
(98) Zhang, Y.; Sajjad, M. T.; Blaszczyk, O.; Parnell, A. J.; Ruseckas, A.; Serrano, L. A.; Cooke, G.; Samuel, I. D. W. Large Crystalline Domains and an Enhanced Exciton Diffusion Length Enable Efficient Organic Solar Cells. *Chem. Mater.* **2019**, *31*, 6548−6557.
(99) Menke, S. M.; Luhman, W. A.; Holmes, R. J. Tailored Exciton Diffusion in Organic Photovoltaic Cells for Enhanced Power Conversion Efficiency. *Nat. Mater.* **2013**, *12*, 152−157.

https://doi.org/10.1021/acs.chemrev.2c00905
Chem. Rev. 2023, 123, 8395−8487

(100) Lin, J. D. A.; Mikhnenko, O. V.; Chen, J.; Masri, Z.; Ruseckas, A.; Mikhailovsky, A.; Raab, R. P.; Liu, J.; Blom, P. W. M.; Loi, M. A.; et al. Systematic Study of Exciton Diffusion Length in Organic Semiconductors by Six Experimental Methods. *Materials Horizons* **2014**, *1*, 280−285.
(101) Ward, A. J.; Ruseckas, A.; Samuel, I. D. W. A Shift from Diffusion Assisted to Energy Transfer Controlled Fluorescence Quenching in Polymer-Fullerene Photovoltaic Blends. *J. Phys. Chem. C* **2012**, *116*, 23931−23937.
(102) Wang, H.; Yue, B.; Xie, Z.; Gao, B.; Xu, Y.; Liu, L.; Sun, H.; Ma, Y. Controlled Transition Dipole Alignment of Energy Donor and Energy Acceptor Molecules in Doped Organic Crystals, and the Effect on Intermolecular Forster Energy Transfer. *Phys. Chem. Chem. Phys.* **2013**, *15*, 3527−3534.
(103) Sim, M.; Shin, J.; Shim, C.; Kim, M.; Jo, S. B.; Kim, J.-H.; Cho, K. Dependence of Exciton Diffusion Length on Crystalline Order in Conjugated Polymers. *J. Phys. Chem. C* **2014**, *118*, 760−766.
(104) Clarke, T. M.; Durrant, J. R. Charge Photogeneration in Organic Solar Cells. *Chem. Rev.* **2010**, *110*, 6736−6767.
(105) Onsager, L. Deviations from Ohm's Law in Weak Electrolytes. *J. Chem. Phys.* **1934**, *2*, 599−615.
(106) Karuthedath, S.; Gorenflot, J.; Firdaus, Y.; Chaturvedi, N.; De Castro, C. S. P.; Harrison, G. T.; Khan, J. I.; Markina, A.; Balawi, A. H.; Pena, T. A. D.; et al. Intrinsic Efficiency Limits in Low-Bandgap Non-Fullerene Acceptor Organic Solar Cells. *Nat. Mater.* **2021**, *20*, 378−384.
(107) Nakano, K.; Chen, Y.; Xiao, B.; Han, W.; Huang, J.; Yoshida, H.; Zhou, E.; Tajima, K. Anatomy of the Energetic Driving Force for Charge Generation in Organic Solar Cells. *Nat. Commun.* **2019**, *10*, 2520.
(108) Zhu, L.; Yi, Y.; Wei, Z. Exciton Binding Energies of Nonfullerene Small Molecule Acceptors: Implication for Exciton Dissociation Driving Forces in Organic Solar Cells. *J. Phys. Chem. C* **2018**, *122*, 22309−22316.
(109) Sun, H.; Hu, Z.; Zhong, C.; Zhang, S.; Sun, Z. Quantitative Estimation of Exciton Binding Energy of Polythiophene-Derived Polymers Using Polarizable Continuum Model Tuned Range-Separated Density Functional. *J. Phys. Chem. C* **2016**, *120*, 8048−8055.
(110) Kupgan, G.; Chen, X.-K.; Brédas, J.-L. Molecular Packing in the Active Layers of Organic Solar Cells Based on Non-Fullerene Acceptors: Impact of Isomerization on Charge Transport, Exciton Dissociation, and Nonradiative Recombination. *ACS Appl. Energy Mater.* **2021**, *4*, 4002−4011.
(111) Deibel, C.; Strobel, T.; Dyakonov, V. Origin of the Efficient Polaron-Pair Dissociation in Polymer-Fullerene Blends. *Phys. Rev. Lett.* **2009**, *103*, 036402.
(112) Han, G.; Guo, Y.; Ning, L.; Yi, Y. Improving the Electron Mobility of Itic by End-Group Modulation: The Role of Fluorination and Π-Extension. *Solar RRL* **2019**, *3*, 1800251.
(113) Rao, A.; Chow, P. C. Y.; Gélinas, S.; Schlenker, C. W.; Li, C.-Z.; Yip, H.-L.; Jen, A. K. Y.; Ginger, D. S.; Friend, R. H. The Role of Spin in the Kinetic Control of Recombination in Organic Photovoltaics. *Nature* **2013**, *500*, 435−439.
(114) Lübke, D.; Hartnagel, P.; Angona, J.; Kirchartz, T. Comparing and Quantifying Indoor Performance of Organic Solar Cells. *Adv. Energy Mater.* **2021**, *11*, 2101474.
(115) Menke, S. M.; Ran, N. A.; Bazan, G. C.; Friend, R. H. Understanding Energy Loss in Organic Solar Cells: Toward a New Efficiency Regime. *Joule* **2018**, *2*, 25−35.
(116) Scharber, M. C.; Mühlbacher, D.; Koppe, M.; Denk, P.; Waldauf, C.; Heeger, A. J.; Brabec, C. J. Design Rules for Donors in Bulk-Heterojunction Solar Cells—Towards 10% Energy-Conversion Efficiency. *Adv. Mater.* **2006**, *18*, 789−794.
(117) Yang, C.; Zhang, J.; Liang, N.; Yao, H.; Wei, Z.; He, C.; Yuan, X.; Hou, J. Effects of Energy-Level Offset between a Donor and Acceptor on the Photovoltaic Performance of Non-Fullerene Organic Solar Cells. *J. Mater. Chem. A* **2019**, *7*, 18889−18897.
(118) Zhang, X.; Yao, N.; Wang, R.; Li, Y.; Zhang, D.; Wu, G.; Zhou, J.; Li, X.; Zhang, H.; Zhang, J.; et al. On the Understanding of Energy Loss and Device Fill Factor Trade-Offs in Non-Fullerene Organic Solar Cells with Varied Energy Levels. *Nano Energy* **2020**, *75*, 105032.
(119) Naveed, H. B.; Zhou, K.; Ma, W. Interfacial and Bulk Nanostructures Control Loss of Charges in Organic Solar Cells. *Acc. Chem. Res.* **2019**, *52*, 2904−2915.
(120) Izawa, S.; Shintaku, N.; Kikuchi, M.; Hiramoto, M. Importance of Interfacial Crystallinity to Reduce Open-Circuit Voltage Loss in Organic Solar Cells. *Appl. Phys. Lett.* **2019**, *115*, 153301.
(121) Jao, M.-H.; Liao, H.-C.; Su, W.-F. Achieving a High Fill Factor for Organic Solar Cells. *J. Mater. Chem. A* **2016**, *4*, 5784−5801.
(122) Qi, B.; Wang, J. Fill Factor in Organic Solar Cells. *Phys. Chem. Chem. Phys.* **2013**, *15*, 8972−8982.
(123) Cui, C.; Li, Y. Morphology Optimization of Photoactive Layers in Organic Solar Cells. *Aggregate* **2021**, *2*, No. e31.
(124) Zhao, F.; Wang, C.; Zhan, X. Morphology Control in Organic Solar Cells. *Adv. Energy Mater.* **2018**, *8*, 1703147.
(125) Jiao, X.; Ye, L.; Ade, H. Quantitative Morphology-Performance Correlations in Organic Solar Cells: Insights from Soft X-Ray Scattering. *Adv. Energy Mater.* **2017**, *7*, 1700084.
(126) Park, J. S.; Kim, G. U.; Lee, D.; Lee, S.; Ma, B.; Cho, S.; Kim, B. J. Importance of Optimal Crystallinity and Hole Mobility of Bdt-Based Polymer Donor for Simultaneous Enhancements of Voc, Jsc, and Ff in Efficient Nonfullerene Organic Solar Cells. *Adv. Funct. Mater.* **2020**, *30*, 2005787.
(127) Zhang, L.; Xu, X.; Lin, B.; Zhao, H.; Li, T.; Xin, J.; Bi, Z.; Qiu, G.; Guo, S.; Zhou, K.; et al. Achieving Balanced Crystallinity of Donor and Acceptor by Combining Blade-Coating and Ternary Strategies in Organic Solar Cells. *Adv. Mater.* **2018**, *30*, 1805041.
(128) Zhang, L.; Hu, L.; Wang, X.; Mao, H.; Zeng, L.; Tan, L.; Zhuang, X.; Chen, Y. Regulation of Crystallinity and Vertical Phase Separation Enables High-Efficiency Thick Organic Solar Cells. *Adv. Funct. Mater.* **2022**, *32*, 2202103.
(129) Li, Q.; Wang, L.-M.; Liu, S.; Guo, L.; Dong, S.; Ma, G.; Cao, Z.; Zhan, X.; Gu, X.; Zhu, T.; et al. Vertical Composition Distribution and Crystallinity Regulations Enable High-Performance Polymer Solar Cells with > 17% Efficiency. *ACS Energy Lett.* **2020**, *5*, 3637−3646.
(130) Li, Y.; Zheng, N.; Yu, L.; Wen, S.; Gao, C.; Sun, M.; Yang, R. A Simple Phenyl Group Introduced at the Tail of Alkyl Side Chains of Small Molecular Acceptors: New Strategy to Balance the Crystallinity of Acceptors and Miscibility of Bulk Heterojunction Enabling Highly Efficient Organic Solar Cells. *Adv. Mater.* **2019**, *31*, 1807832.
(131) Heumueller, T.; Mateker, W. R.; Sachs-Quintana, I. T.; Vandewal, K.; Bartelt, J. A.; Burke, T. M.; Ameri, T.; Brabec, C. J.; McGehee, M. D. Reducing Burn-in Voltage Loss in Polymer Solar Cells by Increasing the Polymer Crystallinity. *Energy Environ. Sci.* **2014**, *7*, 2974−2980.
(132) Yang, J.-P.; Bussolotti, F.; Kera, S.; Ueno, N. Origin and Role of Gap States in Organic Semiconductor Studied by Ups: As the Nature of Organic Molecular Crystals. *J. Phys. D: Appl. Phys.* **2017**, *50*, 423002.
(133) Neupane, U.; Bahrami, B.; Biesecker, M.; Baroughi, M. F.; Qiao, Q. Kinetic Monte Carlo Modeling on Organic Solar Cells: Domain Size, Donor-Acceptor Ratio and Thickness. *Nano Energy* **2017**, *35*, 128−137.
(134) Lin, Y.; Zhao, F.; Prasad, S. K. K.; Chen, J. D.; Cai, W.; Zhang, Q.; Chen, K.; Wu, Y.; Ma, W.; Gao, F.; et al. Balanced Partnership between Donor and Acceptor Components in Nonfullerene Organic Solar Cells with > 12% Efficiency. *Adv. Mater.* **2018**, *30*, 1706363.
(135) Firdaus, Y.; Le Corre, V. M.; Karuthedath, S.; Liu, W.; Markina, A.; Huang, W.; Chattopadhyay, S.; Nahid, M. M.; Nugraha, M. I.; Lin, Y.; et al. Long-Range Exciton Diffusion in Molecular Non-Fullerene Acceptors. *Nat. Commun.* **2020**, *11*, 5220.
(136) Sajjad, M. T.; Ruseckas, A.; Jagadamma, L. K.; Zhang, Y.; Samuel, I. D. W. Long-Range Exciton Diffusion in Non-Fullerene Acceptors and Coarse Bulk Heterojunctions Enable Highly Efficient Organic Photovoltaics. *J. Mater. Chem. A* **2020**, *8*, 15687−15694.
(137) Mukherjee, S.; Proctor, C. M.; Bazan, G. C.; Nguyen, T.-Q.; Ade, H. Significance of Average Domain Purity and Mixed Domains on the Photovoltaic Performance of High-Efficiency Solution-Processed Small-Molecule Bhj Solar Cells. *Adv. Energy Mater.* **2015**, *5*, 1500877.

https://doi.org/10.1021/acs.chemrev.2c00905
Chem. Rev. 2023, 123, 8395−8487

(138) Lee, C.; Li, Y.; Lee, W.; Lee, Y.; Choi, J.; Kim, T.; Wang, C.; Gomez, E. D.; Woo, H. Y.; Kim, B. J. Correlation between Phase-Separated Domain Sizes of Active Layer and Photovoltaic Performances in All-Polymer Solar Cells. *Macromolecules* **2016**, *49*, 5051−5058.
(139) Zhang, Y.; Deng, D.; Wang, Z.; Wang, Y.; Zhang, J.; Fang, J.; Yang, Y.; Lu, G.; Ma, W.; Wei, Z. Enhancing the Photovoltaic Performance Via Vertical Phase Distribution Optimization in Small Molecule:Pc71bm Blends. *Adv. Energy Mater.* **2017**, *7*, 1701548.
(140) Li, S.; Zhan, L.; Yao, N.; Xia, X.; Chen, Z.; Yang, W.; He, C.; Zuo, L.; Shi, M.; Zhu, H.; et al. Unveiling Structure-Performance Relationships from Multi-Scales in Non-Fullerene Organic Photovoltaics. *Nat. Commun.* **2021**, *12*, 4627.
(141) Song, X.; Gasparini, N.; Baran, D. The Influence of Solvent Additive on Polymer Solar Cells Employing Fullerene and Non-Fullerene Acceptors. *Adv. Electron. Mater.* **2018**, *4*, 1700358.
(142) Sajjad, M. T.; Blaszczyk, O.; Jagadamma, L. K.; Roland, T. J.; Chowdhury, M.; Ruseckas, A.; Samuel, I. D. W. Engineered Exciton Diffusion Length Enhances Device Efficiency in Small Molecule Photovoltaics. *J. Mater. Chem. A* **2018**, *6*, 9445−9450.
(143) Lyons, B. P.; Clarke, N.; Groves, C. The Relative Importance of Domain Size, Domain Purity and Domain Interfaces to the Performance of Bulk-Heterojunction Organic Photovoltaics. *Energy Environ. Sci.* **2012**, *5*, 7657.
(144) Groves, C. Developing Understanding of Organic Photovoltaic Devices: Kinetic Monte Carlo Models of Geminate and Non-Geminate Recombination, Charge Transport and Charge Extraction. *Energy Environ. Sci.* **2013**, *6*, 3202.
(145) Lee, H.; Lee, D.; Sin, D. H.; Kim, S. W.; Jeong, M. S.; Cho, K. Effect of Donor-Acceptor Molecular Orientation on Charge Photogeneration in Organic Solar Cells. *NPG Asia Mater.* **2018**, *10*, 469−481.
(146) Kitchen, B.; Awartani, O.; Kline, R. J.; McAfee, T.; Ade, H.; O'Connor, B. T. Tuning Open-Circuit Voltage in Organic Solar Cells with Molecular Orientation. *ACS Appl. Mater. Interfaces* **2015**, *7*, 13208−13216.
(147) Ma, Y.; Zhang, M.; Wan, S.; Yin, P.; Wang, P.; Cai, D.; Liu, F.; Zheng, Q. Efficient Organic Solar Cells from Molecular Orientation Control of M-Series Acceptors. *Joule* **2021**, *5*, 197−209.
(148) Ma, W.; Tumbleston, J. R.; Wang, M.; Gann, E.; Huang, F.; Ade, H. Domain Purity, Miscibility, and Molecular Orientation at Donor/Acceptor Interfaces in High Performance Organic Solar Cells: Paths to Further Improvement. *Adv. Energy Mater.* **2013**, *3*, 864−872.
(149) Yang, L.; Zhang, S.; He, C.; Zhang, J.; Yang, Y.; Zhu, J.; Cui, Y.; Zhao, W.; Zhang, H.; Zhang, Y.; et al. Modulating Molecular Orientation Enables Efficient Nonfullerene Small-Molecule Organic Solar Cells. *Chem. Mater.* **2018**, *30*, 2129−2134.
(150) Tumbleston, J. R.; Collins, B. A.; Yang, L.; Stuart, A. C.; Gann, E.; Ma, W.; You, W.; Ade, H. The Influence of Molecular Orientation on Organic Bulk Heterojunction Solar Cells. *Nat. Photonics* **2014**, *8*, 385−391.
(151) Ye, L.; Weng, K.; Xu, J.; Du, X.; Chandrabose, S.; Chen, K.; Zhou, J.; Han, G.; Tan, S.; Xie, Z.; et al. Unraveling the Influence of Non-Fullerene Acceptor Molecular Packing on Photovoltaic Performance of Organic Solar Cells. *Nat. Commun.* **2020**, *11*, 6005.
(152) Feng, H.; Song, X.; Zhang, Z.; Geng, R.; Yu, J.; Yang, L.; Baran, D.; Tang, W. Molecular Orientation Unified Nonfullerene Acceptor Enabling 14% Efficiency as-Cast Organic Solar Cells. *Adv. Funct. Mater.* **2019**, *29*, 1903269.
(153) Vohra, V.; Kawashima, K.; Kakara, T.; Koganezawa, T.; Osaka, I.; Takimiya, K.; Murata, H. Efficient Inverted Polymer Solar Cells Employing Favourable Molecular Orientation. *Nat. Photonics* **2015**, *9*, 403−408.
(154) Zhou, K.; Wu, Y.; Liu, Y.; Zhou, X.; Zhang, L.; Ma, W. Molecular Orientation of Polymer Acceptor Dominates Open-Circuit Voltage Losses in All-Polymer Solar Cells. *ACS Energy Lett.* **2019**, *4*, 1057−1064.
(155) Ran, N. A.; Roland, S.; Love, J. A.; Savikhin, V.; Takacs, C. J.; Fu, Y. T.; Li, H.; Coropceanu, V.; Liu, X.; Bredas, J. L.; et al. Impact of Interfacial Molecular Orientation on Radiative Recombination and Charge Generation Efficiency. *Nat. Commun.* **2017**, *8*, 79.
(156) Adil, M. A.; Zhang, J.; Deng, D.; Wang, Z.; Yang, Y.; Wu, Q.; Wei, Z. Modulation of the Molecular Orientation at the Bulk Heterojunction Interface Via Tuning the Small Molecular Donor-Nonfullerene Acceptor Interactions. *ACS Appl. Mater. Interfaces* **2018**, *10*, 31526−31534.
(157) Yan, Y.; Liu, X.; Wang, T. Conjugated-Polymer Blends for Organic Photovoltaics: Rational Control of Vertical Stratification for High Performance. *Adv. Mater.* **2017**, *29*, 1601674.
(158) Wei, H. X.; Li, J.; Xu, Z. Q.; Cai, Y.; Tang, J. X.; Li, Y. Q. Thermal Annealing-Induced Vertical Phase Separation of Copper Phthalocyanine: Fullerene Bulk Heterojunction in Organic Photovoltaic Cells. *Appl. Phys. Lett.* **2010**, *97*, 083302.
(159) Xue, B.; Vaughan, B.; Poh, C.-H.; Burke, K. B.; Thomsen, L.; Stapleton, A.; Zhou, X.; Bryant, G. W.; Belcher, W.; Dastoor, P. C. Vertical Stratification and Interfacial Structure in P3ht:Pcbm Organic Solar Cells. *J. Phys. Chem. C* **2010**, *114*, 15797−15805.
(160) Onojima, N.; Ishima, Y.; Takahashi, K. Effects of Solvent-Vapor Annealing on Bulk-Heterojunction Morphology of Photoactive Layers Prepared by Electrostatic Spray Deposition. *Thin Solid Films* **2016**, *615*, 385−390.
(161) Xiao, Z.; Yuan, Y.; Yang, B.; VanDerslice, J.; Chen, J.; Dyck, O.; Duscher, G.; Huang, J. Universal Formation of Compositionally Graded Bulk Heterojunction for Efficiency Enhancement in Organic Photovoltaics. *Adv. Mater.* **2014**, *26*, 3068−3075.
(162) Kim, M.; Lee, J.; Jo, S. B.; Sin, D. H.; Ko, H.; Lee, H.; Lee, S. G.; Cho, K. Critical Factors Governing Vertical Phase Separation in Polymer-Pcbm Blend Films for Organic Solar Cells. *J. Mater. Chem. A* **2016**, *4*, 15522−15535.
(163) Han, J.; Xu, H.; Paleti, S. H. K.; Wen, Y.; Wang, J.; Wu, Y.; Bao, F.; Yang, C.; Li, X.; Jian, X.; et al. Vertical Stratification Engineering of Insulating Poly(Aryl Ether)S Enables 18.6% Organic Solar Cells with Improved Stability. *ACS Energy Lett.* **2022**, *7*, 2927−2936.
(164) Xu, Z.; Chen, L.-M.; Yang, G.; Huang, C.-H.; Hou, J.; Wu, Y.; Li, G.; Hsu, C.-S.; Yang, Y. Vertical Phase Separation in Poly(3-Hexylthiophene): Fullerene Derivative Blends and Its Advantage for Inverted Structure Solar Cells. *Adv. Funct. Mater.* **2009**, *19*, 1227−1234.
(165) Sun, R.; Wu, Q.; Guo, J.; Wang, T.; Wu, Y.; Qiu, B.; Luo, Z.; Yang, W.; Hu, Z.; Guo, J.; et al. A Layer-by-Layer Architecture for Printable Organic Solar Cells Overcoming the Scaling Lag of Module Efficiency. *Joule* **2020**, *4*, 407−419.
(166) Jee, M. H.; Ryu, H. S.; Lee, D.; Lee, W.; Woo, H. Y. Recent Advances in Nonfullerene Acceptor-Based Layer-by-Layer Organic Solar Cells Using a Solution Process. *Adv. Sci.* **2022**, *9*, 2201876.
(167) Faure, M. D. M.; Lessard, B. H. Layer-by-Layer Fabrication of Organic Photovoltaic Devices: Material Selection and Processing Conditions. *J. Mater. Chem. C* **2021**, *9*, 14−40.
(168) Forrest, S. R.; Thompson, M. E. Introduction: Organic Electronics and Optoelectronics. *Chem. Rev.* **2007**, *107*, 923−925.
(169) Duan, L.; Uddin, A. Progress in Stability of Organic Solar Cells. *Adv. Sci.* **2020**, *7*, 1903259.
(170) Xu, X.; Li, D.; Yuan, J.; Zhou, Y.; Zou, Y. Recent Advances in Stability of Organic Solar Cells. *EnergyChem.* **2021**, *3*, 100046.
(171) Li, Y.; Li, T.; Lin, Y. Stability: Next Focus in Organic Solar Cells Based on Non-Fullerene Acceptors. *Mater. Chem. Front.* **2021**, *5*, 2907−2930.
(172) Cheng, P.; Zhan, X. Stability of Organic Solar Cells: Challenges and Strategies. *Chem. Soc. Rev.* **2016**, *45*, 2544−2582.
(173) Manceau, M.; Bundgaard, E.; Carlé, J. E.; Hagemann, O.; Helgesen, M.; Søndergaard, R.; Jørgensen, M.; Krebs, F. C. Photochemical Stability of Π-Conjugated Polymers for Polymer Solar Cells: A Rule of Thumb. *J. Mater. Chem.* **2011**, *21*, 4132.
(174) Luke, J.; Speller, E. M.; Wadsworth, A.; Wyatt, M. F.; Dimitrov, S.; Lee, H. K. H.; Li, Z.; Tsoi, W. C.; McCulloch, I.; Bagnis, D.; et al. Twist and Degrade—Impact of Molecular Structure on the Photostability of Nonfullerene Acceptors and Their Photovoltaic Blends. *Adv. Energy Mater.* **2019**, *9*, 1803755.
(175) Hintz, H.; Egelhaaf, H. J.; Lüer, L.; Hauch, J.; Peisert, H.; Chassé, T. Photodegradation of P3ht-a Systematic Study of Environmental Factors. *Chem. Mater.* **2011**, *23*, 145−154.

https://doi.org/10.1021/acs.chemrev.2c00905
Chem. Rev. 2023, 123, 8395−8487

(176) Mateker, W. R.; Heumueller, T.; Cheacharoen, R.; Sachs-Quintana, I. T.; McGehee, M. D.; Warnan, J.; Beaujuge, P. M.; Liu, X.; Bazan, G. C. Molecular Packing and Arrangement Govern the Photo-Oxidative Stability of Organic Photovoltaic Materials. *Chem. Mater.* **2015**, *27*, 6345−6353.
(177) Guo, J.; Wu, Y.; Sun, R.; Wang, W.; Guo, J.; Wu, Q.; Tang, X.; Sun, C.; Luo, Z.; Chang, K.; et al. Suppressing Photo-Oxidation of Non-Fullerene Acceptors and Their Blends in Organic Solar Cells by Exploring Material Design and Employing Friendly Stabilizers. *J. Mater. Chem. A* **2019**, *7*, 25088−25101.
(178) Guo, J.; Wu, Y.; Sun, R.; Wang, W.; Li, J.; Zhou, E.; Guo, J.; Wang, T.; Wu, Q.; Luo, Z.; et al. Photooxidation Analysis of Two Isomeric Nonfullerene Acceptors: A Systematic Study of Conformational, Morphological, and Environmental Factors. *Solar RRL* **2021**, *5*, 2000704.
(179) Ghasemi, M.; Hu, H.; Peng, Z.; Rech, J. J.; Angunawela, I.; Carpenter, J. H.; Stuard, S. J.; Wadsworth, A.; McCulloch, I.; You, W.; et al. Delineation of Thermodynamic and Kinetic Factors That Control Stability in Non-Fullerene Organic Solar Cells. *Joule* **2019**, *3*, 1328−1348.
(180) Li, N.; Perea, J. D.; Kassar, T.; Richter, M.; Heumueller, T.; Matt, G. J.; Hou, Y.; Guldal, N. S.; Chen, H.; Chen, S.; et al. Abnormal Strong Burn-in Degradation of Highly Efficient Polymer Solar Cells Caused by Spinodal Donor-Acceptor Demixing. *Nat. Commun.* **2017**, *8*, 14541.
(181) Wong, H. C.; Li, Z.; Tan, C. H.; Zhong, H.; Huang, Z.; Bronstein, H.; McCulloch, I.; Cabral, J. T.; Durrant, J. R. Morphological Stability and Performance of Polymer-Fullerene Solar Cells under Thermal Stress: The Impact of Photoinduced Pc60bm Oligomerization. *ACS Nano* **2014**, *8*, 1297−1308.
(182) Zhu, Y.; Gadisa, A.; Peng, Z.; Ghasemi, M.; Ye, L.; Xu, Z.; Zhao, S.; Ade, H. Rational Strategy to Stabilize an Unstable High-Efficiency Binary Nonfullerene Organic Solar Cells with a Third Component. *Adv. Energy Mater.* **2019**, *9*, 1900376.
(183) Peng, Z.; Stingelin, N.; Ade, H.; Michels, J. J. A Materials Physics Perspective on Structure-Processing-Function Relations in Blends of Organic Semiconductors. *Nat. Rev. Mater.* **2023**. DOI: 10.1038/s41578-023-00541-5
(184) Rathi, P.; Huang, T.-M.; Dayal, P.; Kyu, T. Crystalline-Amorphous Interaction in Relation to the Phase Diagrams of Binary Polymer Blends Containing a Crystalline Constituent. *J. Phys. Chem. B* **2008**, *112*, 6460−6466.
(185) Ye, L.; Collins, B. A.; Jiao, X.; Zhao, J.; Yan, H.; Ade, H. Miscibility-Function Relations in Organic Solar Cells: Significance of Optimal Miscibility in Relation to Percolation. *Adv. Energy Mater.* **2018**, *8*, 1703058.
(186) Ghasemi, M.; Balar, N.; Peng, Z.; Hu, H.; Qin, Y.; Kim, T.; Rech, J. J.; Bidwell, M.; Mask, W.; McCulloch, I.; et al. A Molecular Interaction-Diffusion Framework for Predicting Organic Solar Cell Stability. *Nat. Mater.* **2021**, *20*, 525−532.
(187) Wang, Z.-G. 50th Anniversary Perspective: Polymer Conformation—a Pedagogical Review. *Macromolecules* **2017**, *50*, 9073−9114.
(188) Flory, P. J. *Principles of Polymer Chemistry*; Cornell University Press, 1953; p 399.
(189) Rubinstein, M.; Colby, R. H. *Polymer Physics*; Oxford University Press, 2003; pp 137−165.
(190) Hu, D.; Yu, J.; Wong, K.; Bagchi, B.; Rossky, P. J.; Barbara, P. F. Collapse of Stiff Conjugated Polymers with Chemical Defects into Ordered, Cylindrical Conformations. *Nature* **2000**, *405*, 1030−1033.
(191) Jackson, N. E.; Kohlstedt, K. L.; Savoie, B. M.; Olvera de la Cruz, M.; Schatz, G. C.; Chen, L. X.; Ratner, M. A. Conformational Order in Aggregates of Conjugated Polymers. *J. Am. Chem. Soc.* **2015**, *137*, 6254−6262.
(192) Lemaur, V.; Cornil, J.; Lazzaroni, R.; Sirringhaus, H.; Beljonne, D.; Olivier, Y. Resilience to Conformational Fluctuations Controls Energetic Disorder in Conjugated Polymer Materials: Insights from Atomistic Simulations. *Chem. Mater.* **2019**, *31*, 6889−6899.
(193) Cao, Z.; Leng, M.; Cao, Y.; Gu, X.; Fang, L. How Rigid Are Conjugated Non-Ladder and Ladder Polymers? *J. Polym. Sci.* **2022**, *60*, 298−310.
(194) Zhao, L.-H.; Png, R.-Q.; Zhuo, J.-M.; Wong, L.-Y.; Tang, J.-C.; Su, Y.-S.; Chua, L.-L. Role of Borderline Solvents to Induce Pronounced Extended-Chain Lamellar Order in Π-Stackable Polymers. *Macromolecules* **2011**, *44*, 9692−9702.
(195) Xiao, M.; Carey, R. L.; Chen, H.; Jiao, X.; Lemaur, V.; Schott, S.; Nikolka, M.; Jellett, C.; Sadhanala, A.; Rogers, S.; et al. Charge Transport Physics of a Unique Class of Rigid-Rod Conjugated Polymers with Fused-Ring Conjugated Units Linked by Double Carbon-Carbon Bonds. *Sci. Adv.* **2021**, *7*, No. eabe5280.
(196) Huang, H.; Yang, L.; Facchetti, A.; Marks, T. J. Organic and Polymeric Semiconductors Enhanced by Noncovalent Conformational Locks. *Chem. Rev.* **2017**, *117*, 10291−10318.
(197) Onwubiko, A.; Yue, W.; Jellett, C.; Xiao, M.; Chen, H. Y.; Ravva, M. K.; Hanifi, D. A.; Knall, A. C.; Purushothaman, B.; Nikolka, M.; et al. Fused Electron Deficient Semiconducting Polymers for Air Stable Electron Transport. *Nat. Commun.* **2018**, *9*, 416.
(198) Zhu, C.; Fang, L. Locking the Coplanar Conformation of Pi-Conjugated Molecules and Macromolecules Using Dynamic Non-covalent Bonds. *Macromol. Rapid Commun.* **2018**, *39*, 1700241.
(199) Yu, Z. D.; Lu, Y.; Wang, J. Y.; Pei, J. Conformation Control of Conjugated Polymers. *Chemistry* **2020**, *26*, 16194−16205.
(200) Kiriy, N.; Jähne, E.; Adler, H.-J.; Schneider, M.; Kiriy, A.; Gorodyska, G.; Minko, S.; Jehnichen, D.; Simon, P.; Fokin, A. A.; et al. One-Dimensional Aggregation of Regioregular Polyalkylthiophenes. *Nano Lett.* **2003**, *3*, 707−712.
(201) Zhang, W.; Gomez, E. D.; Milner, S. T. Predicting Chain Dimensions of Semiflexible Polymers from Dihedral Potentials. *Macromolecules* **2014**, *47*, 6453−6461.
(202) Farmer, B. L.; Chapman, B. R.; Dudis, D. S.; Adams, W. W. Molecular Dynamics of Rigid Rod Polymers. *Polymer* **1993**, *34*, 1588−1601.
(203) Harre, K.; Wegner, G. Solution Properties and Kinetics of Aggregation of an Alkyl-Substituted Poly(P-Phenylene). *Polymer* **2006**, *47*, 7312−7317.
(204) Petekidis, G.; Vlassopoulos, D.; Galda, P.; Rehahn, M.; Ballauff, M. Determination of Chain Conformation of Stiff Polymers by Depolarized Rayleigh Scattering in Solution. *Macromolecules* **1996**, *29*, 8948−8953.
(205) Wang, Z.-Y.; Yao, Z.-F.; Lu, Y.; Ding, L.; Yu, Z.-D.; You, H.-Y.; Wang, X.-Y.; Zhou, Y.-Y.; Zou, L.; Wang, J.-Y.; et al. Precise Tracking and Modulating Aggregation Structures of Conjugated Copolymers in Solutions. *Polym. Chem.* **2020**, *11*, 3716−3722.
(206) Wang, M.; Ford, M. J.; Zhou, C.; Seifrid, M.; Nguyen, T. Q.; Bazan, G. C. Linear Conjugated Polymer Backbones Improve Alignment in Nanogroove-Assisted Organic Field-Effect Transistors. *J. Am. Chem. Soc.* **2017**, *139*, 17624−17631.
(207) Rieger, R.; Beckmann, D.; Mavrinskiy, A.; Kastler, M.; Müllen, K. Backbone Curvature in Polythiophenes. *Chem. Mater.* **2010**, *22*, 5314−5318.
(208) Bridges, C. R.; Ford, M. J.; Bazan, G. C.; Segalman, R. A. Molecular Considerations for Mesophase Interaction and Alignment of Lyotropic Liquid Crystalline Semiconducting Polymers. *ACS Macro Lett.* **2017**, *6*, 619−624.
(209) Bridges, C. R.; Ford, M. J.; Popere, B. C.; Bazan, G. C.; Segalman, R. A. Formation and Structure of Lyotropic Liquid Crystalline Mesophases in Donor-Acceptor Semiconducting Polymers. *Macromolecules* **2016**, *49*, 7220−7229.
(210) Liu, D.; Lei, Y.; Ji, X.; Wu, Y.; Lin, Y.; Wang, Y.; Zhang, S.; Zheng, Y.; Chen, Y.; Lai, J. C.; et al. Tuning the Mechanical and Electric Properties of Conjugated Polymer Semiconductors: Side-Chain Design Based on Asymmetric Benzodithiophene Building Blocks. *Adv. Funct. Mater.* **2022**, *32*, 2203527.
(211) Mei, J.; Bao, Z. Side Chain Engineering in Solution-Processable Conjugated Polymers. *Chem. Mater.* **2014**, *26*, 604−615.
(212) Moser, M.; Savagian, L. R.; Savva, A.; Matta, M.; Ponder, J. F.; Hidalgo, T. C.; Ohayon, D.; Hallani, R.; Reisjalali, M.; Troisi, A.; et al.

Ethylene Glycol-Based Side Chain Length Engineering in Polythiophenes and Its Impact on Organic Electrochemical Transistor Performance. *Chem. Mater.* **2020**, *32*, 6618−6628.
(213) Andersson, M. R.; Thomas, O.; Mammo, W.; Svensson, M.; Theander, M.; Inganäs, O. Substituted Polythiophenes Designed for Optoelectronic Devices and Conductors. *J. Mater. Chem.* **1999**, *9*, 1933−1940.
(214) Ko, S.; Hoke, E. T.; Pandey, L.; Hong, S.; Mondal, R.; Risko, C.; Yi, Y.; Noriega, R.; McGehee, M. D.; Bredas, J. L.; et al. Controlled Conjugated Backbone Twisting for an Increased Open-Circuit Voltage While Having a High Short-Circuit Current in Poly(Hexylthiophene) Derivatives. *J. Am. Chem. Soc.* **2012**, *134*, 5222−5232.
(215) Pina, J.; B. Rodrigues, A. C.; Alnady, M.; Dong, W.; Scherf, U.; Seixas de Melo, J. S. Restricted Aggregate Formation on Tetraphenylethene-Substituted Polythiophenes. *J. Phys. Chem. C* **2020**, *124*, 13956−13965.
(216) Raithel, D.; Simine, L.; Pickel, S.; Schotz, K.; Panzer, F.; Baderschneider, S.; Schiefer, D.; Lohwasser, R.; Kohler, J.; Thelakkat, M.; et al. Direct Observation of Backbone Planarization Via Side-Chain Alignment in Single Bulky-Substituted Polythiophenes. *Proc. Natl. Acad. Sci. U. S. A.* **2018**, *115*, 2699−2704.
(217) Kim, B. G.; Jeong, E. J.; Chung, J. W.; Seo, S.; Koo, B.; Kim, J. A Molecular Design Principle of Lyotropic Liquid-Crystalline Conjugated Polymers with Directed Alignment Capability for Plastic Electronics. *Nat. Mater.* **2013**, *12*, 659−664.
(218) Reid, D. R.; Jackson, N. E.; Bourque, A. J.; Snyder, C. R.; Jones, R. L.; de Pablo, J. J. Aggregation and Solubility of a Model Conjugated Donor-Acceptor Polymer. *J. Phys. Chem. Lett.* **2018**, *9*, 4802−4807.
(219) Hong, W. D.; Lam, C. N.; Wang, Y.; He, Y.; Sanchez-Diaz, L. E.; Do, C.; Chen, W. R. Influence of Side Chain Isomerism on the Rigidity of Poly(3-Alkylthiophenes) in Solutions Revealed by Neutron Scattering. *Phys. Chem. Chem. Phys.* **2019**, *21*, 7745−7749.
(220) Ning, L.; Han, G.; Yi, Y. Conformational and Aggregation Properties of Pffbt4t Polymers: Atomistic Insight into the Impact of Alkyl-Chain Branching Positions. *J. Mater. Chem. C* **2019**, *7*, 14198−14204.
(221) You, H.; Kim, D.; Cho, H.-H.; Lee, C.; Chong, S.; Ahn, N. Y.; Seo, M.; Kim, J.; Kim, F. S.; Kim, B. J. Shift of the Branching Point of the Side-Chain in Naphthalenediimide (Ndi)-Based Polymer for Enhanced Electron Mobility and All-Polymer Solar Cell Performance. *Adv. Funct. Mater.* **2018**, *28*, 1803613.
(222) Lei, T.; Dou, J. H.; Pei, J. Influence of Alkyl Chain Branching Positions on the Hole Mobilities of Polymer Thin-Film Transistors. *Adv. Mater.* **2012**, *24*, 6457−6461.
(223) Lei, T.; Wang, J. Y.; Pei, J. Design, Synthesis, and Structure-Property Relationships of Isoindigo-Based Conjugated Polymers. *Acc. Chem. Res.* **2014**, *47*, 1117−1126.
(224) Meager, I.; Ashraf, R. S.; Mollinger, S.; Schroeder, B. C.; Bronstein, H.; Beatrup, D.; Vezie, M. S.; Kirchartz, T.; Salleo, A.; Nelson, J.; et al. Photocurrent Enhancement from Diketopyrrolopyrrole Polymer Solar Cells through Alkyl-Chain Branching Point Manipulation. *J. Am. Chem. Soc.* **2013**, *135*, 11537−11540.
(225) Dou, J.-H.; Zheng, Y.-Q.; Lei, T.; Zhang, S.-D.; Wang, Z.; Zhang, W.-B.; Wang, J.-Y.; Pei, J. Systematic Investigation of Side-Chain Branching Position Effect on Electron Carrier Mobility in Conjugated Polymers. *Adv. Funct. Mater.* **2014**, *24*, 6270−6278.
(226) Bridges, C. R.; Ford, M. J.; Thomas, E. M.; Gomez, C.; Bazan, G. C.; Segalman, R. A. Effects of Side Chain Branch Point on Self Assembly, Structure, and Electronic Properties of High Mobility Semiconducting Polymers. *Macromolecules* **2018**, *51*, 8597−8604.
(227) Kang, I.; Yun, H. J.; Chung, D. S.; Kwon, S. K.; Kim, Y. H. Record High Hole Mobility in Polymer Semiconductors Via Side-Chain Engineering. *J. Am. Chem. Soc.* **2013**, *135*, 14896−14899.
(228) Fu, B.; Baltazar, J.; Sankar, A. R.; Chu, P.-H.; Zhang, S.; Collard, D. M.; Reichmanis, E. Enhancing Field-Effect Mobility of Conjugated Polymers through Rational Design of Branched Side Chains. *Adv. Funct. Mater.* **2014**, *24*, 3734−3744.
(229) Adachi, T.; Brazard, J.; Ono, R. J.; Hanson, B.; Traub, M. C.; Wu, Z.-Q.; Li, Z.; Bolinger, J. C.; Ganesan, V.; Bielawski, C. W.; et al. Regioregularity and Single Polythiophene Chain Conformation. *J. Phys. Chem. Lett.* **2011**, *2*, 1400−1404.
(230) Hu, Z.; Adachi, T.; Lee, Y. G.; Haws, R. T.; Hanson, B.; Ono, R. J.; Bielawski, C. W.; Ganesan, V.; Rossky, P. J.; Vanden Bout, D. A. Effect of the Side-Chain-Distribution Density on the Single-Conjugated-Polymer-Chain Conformation. *ChemPhysChem* **2013**, *14*, 4143−4148.
(231) Snyder, C. R.; Henry, J. S.; DeLongchamp, D. M. Effect of Regioregularity on the Semicrystalline Structure of Poly(3-Hexylthiophene). *Macromolecules* **2011**, *44*, 7088−7091.
(232) Mauer, R.; Kastler, M.; Laquai, F. The Impact of Polymer Regioregularity on Charge Transport and Efficiency of P3ht:Pcbm Photovoltaic Devices. *Adv. Funct. Mater.* **2010**, *20*, 2085−2092.
(233) Bounos, G.; Ghosh, S.; Lee, A. K.; Plunkett, K. N.; DuBay, K. H.; Bolinger, J. C.; Zhang, R.; Friesner, R. A.; Nuckolls, C.; Reichman, D. R.; et al. Controlling Chain Conformation in Conjugated Polymers Using Defect Inclusion Strategies. *J. Am. Chem. Soc.* **2011**, *133*, 10155−10160.
(234) Nagai, M. Effect of Molecular Weight and Conformation on Photoluminescence Quantum Yield of Fluorene/Poly(2-Methoxy-5-(2′-Ethylhexyloxy)-1,4-Phenylene Vinylene) (Meh-Ppv) Copolymers. *ECS J. Solid State Sci. Technol.* **2013**, *2*, R218−R224.
(235) Nagai, M.; Liu, J.; Huang, W.; Kikuchi, M.; Kawaguchi, S.; Xie, L. Molecular Weight Induced Conformational Change and Its Impact on B-Phase Formation of Polydiarylfluorene in Dilute Solution. *J. Phys. Chem. C* **2020**, *124*, 6304−6310.
(236) Nagai, M.; Huang, J.; Zhou, T.; Huang, W. Effect of Molecular Weight on Conformational Characteristics of Poly(3-Hexyl Thiophene). *J. Polym. Sci., Part B: Polym. Phys.* **2017**, *55*, 1273−1277.
(237) Baysal, B. M.; Karasz, F. E. Coil-Globule Collapse in Flexible Macromolecules. *Macromol. Theory Simul.* **2003**, *12*, 627−646.
(238) Wang, D.; Yuan, Y.; Mardiyati, Y.; Bubeck, C.; Koynov, K. From Single Chains to Aggregates, How Conjugated Polymers Behave in Dilute Solutions. *Macromolecules* **2013**, *46*, 6217−6224.
(239) Daoud, M.; Cotton, J. P.; Farnoux, B.; Jannink, G.; Sarma, G.; Benoit, H.; Duplessix, C.; Picot, C.; de Gennes, P. G. Solutions of Flexible Polymers. Neutron Experiments and Interpretation. *Macromolecules* **1975**, *8*, 804−818.
(240) Boehm, B. J.; McNeill, C. R.; Huang, D. M. Competing Single-Chain Folding and Multi-Chain Aggregation Pathways Control Solution-Phase Aggregate Morphology of Organic Semiconducting Polymers. *Nanoscale* **2022**, *14*, 18070−18086.
(241) Kwok, J. J.; Park, K. S.; Patel, B. B.; Dilmurat, R.; Beljonne, D.; Zuo, X.; Lee, B.; Diao, Y. Understanding Solution State Conformation and Aggregate Structure of Conjugated Polymers Via Small Angle X-Ray Scattering. *Macromolecules* **2022**, *55*, 4353−4366.
(242) Xu, Z.; Tsai, H.; Wang, H. L.; Cotlet, M. Solvent Polarity Effect on Chain Conformation, Film Morphology, and Optical Properties of a Water-Soluble Conjugated Polymer. *J. Phys. Chem. B* **2010**, *114*, 11746−11752.
(243) Lee, F. L.; Barati Farimani, A.; Gu, K. L.; Yan, H.; Toney, M. F.; Bao, Z.; Pande, V. S. Solution-Phase Conformation and Dynamics of Conjugated Isoindigo-Based Donor-Acceptor Polymer Single Chains. *J. Phys. Chem. Lett.* **2017**, *8*, 5479−5486.
(244) Cohen, A. E.; Jackson, N. E.; de Pablo, J. J. Anisotropic Coarse-Grained Model for Conjugated Polymers: Investigations into Solution Morphologies. *Macromolecules* **2021**, *54*, 3780−3789.
(245) Wu, Y.; Ding, Z.; Zhang, Q.; Liang, X.; Yang, H.; Huang, W.; Su, Y.; Zhang, Y.; Hu, H.; Han, Y.; et al. Increasing H-Aggregates Via Sequential Aggregation to Enhance the Hole Mobility of Printed Conjugated Polymer Films. *Macromolecules* **2022**, *55*, 8609−8618.
(246) Schmidt, K.; Tassone, C. J.; Niskala, J. R.; Yiu, A. T.; Lee, O. P.; Weiss, T. M.; Wang, C.; Frechet, J. M.; Beaujuge, P. M.; Toney, M. F. A Mechanistic Understanding of Processing Additive-Induced Efficiency Enhancement in Bulk Heterojunction Organic Solar Cells. *Adv. Mater.* **2014**, *26*, 300−305.
(247) Zhao, K.; Zhang, Q.; Chen, L.; Zhang, T.; Han, Y. Nucleation and Growth of P(Ndi2od-T2) Nanowires Via Side Chain Ordering and Backbone Planarization. *Macromolecules* **2021**, *54*, 2143−2154.

https://doi.org/10.1021/acs.chemrev.2c00905
Chem. Rev. 2023, 123, 8395−8487

(248) Kwon, E. H.; Kim, G. W.; Kim, M.; Park, Y. D. Effect of Alcohol Polarity on the Aggregation and Film-Forming Behaviors of Poly(3-Hexylthiophene). *ACS Appl. Polym. Mater.* **2020**, *2*, 2980−2986.
(249) Keum, J. K.; Xiao, K.; Ivanov, I. N.; Hong, K.; Browning, J. F.; Smith, G. S.; Shao, M.; Littrell, K. C.; Rondinone, A. J.; Andrew Payzant, E.; et al. Solvent Quality-Induced Nucleation and Growth of Parallelepiped Nanorods in Dilute Poly(3-Hexylthiophene) (P3ht) Solution and the Impact on the Crystalline Morphology of Solution-Cast Thin Film. *CrystEngComm* **2013**, *15*, 1114−1124.
(250) Chu, P.-H.; Kleinhenz, N.; Persson, N.; McBride, M.; Hernandez, J. L.; Fu, B.; Zhang, G.; Reichmanis, E. Toward Precision Control of Nanofiber Orientation in Conjugated Polymer Thin Films: Impact on Charge Transport. *Chem. Mater.* **2016**, *28*, 9099−9109.
(251) Berson, S.; De Bettignies, R.; Bailly, S.; Guillerez, S. Poly(3-Hexylthiophene) Fibers for Photovoltaic Applications. *Adv. Funct. Mater.* **2007**, *17*, 1377−1384.
(252) Steyrleuthner, R.; Schubert, M.; Howard, I.; Klaumunzer, B.; Schilling, K.; Chen, Z.; Saalfrank, P.; Laquai, F.; Facchetti, A.; Neher, D. Aggregation in a High-Mobility N-Type Low-Bandgap Copolymer with Implications on Semicrystalline Morphology. *J. Am. Chem. Soc.* **2012**, *134*, 18303−18317.
(253) Balooch Qarai, M.; Chang, X.; Spano, F. C. Vibronic Exciton Model for Low Bandgap Donor-Acceptor Polymers. *J. Chem. Phys.* **2020**, *153*, 244901.
(254) Chang, M.-C.; Wei, Y.; Chen, W.-R.; Do, C. Deep Learning-Based Super-Resolution for Small-Angle Neutron Scattering Data: Attempt to Accelerate Experimental Workflow. *MRS Commun.* **2020**, *10*, 11−17.
(255) Stein, R. S.; Srinivasarao, M. Fifty Years of Light Scattering: A Perspective. *J. Polym. Sci., Part B: Polym. Phys.* **1993**, *31*, 2003−2010.
(256) Gettinger, C. L.; Heeger, A. J.; Drake, J. M.; Pine, D. J. A Photoluminescence Study of Poly(Phenylene Vinylene) Derivatives: The Effect of Intrinsic Persistence Length. *J. Chem. Phys.* **1994**, *101*, 1673−1678.
(257) Heffner, G. W.; Pearson, D. S. Molecular Characterization of Poly(3-Hexylthiophene). *Macromolecules* **1991**, *24*, 6295−6299.
(258) Liu, C.; Hu, W.; Jiang, H.; Liu, G.; Han, C. C.; Sirringhaus, H.; Boué, F.; Wang, D. Chain Conformation and Aggregation Structure Formation of a High Charge Mobility Dpp-Based Donor-Acceptor Conjugated Polymer. *Macromolecules* **2020**, *53*, 8255−8266.
(259) Wang, Z. Y.; Di Virgilio, L.; Yao, Z. F.; Yu, Z. D.; Wang, X. Y.; Zhou, Y. Y.; Li, Q. Y.; Lu, Y.; Zou, L.; Wang, H. I.; et al. Correlating Charge Transport Properties of Conjugated Polymers in Solution Aggregates and Thin-Film Aggregates. *Angew. Chem., Int. Ed. Engl.* **2021**, *60*, 20483−20488.
(260) Wang, Z.; Gao, M.; He, C.; Shi, W.; Deng, Y.; Han, Y.; Ye, L.; Geng, Y. Unraveling the Molar Mass Dependence of Shearing-Induced Aggregation Structure of a High-Mobility Polymer Semiconductor. *Adv. Mater.* **2022**, *34*, 2108255.
(261) Zhao, K.; Zhang, T.; Zhang, L.; Li, J.; Li, H.; Wu, F.; Chen, Y.; Zhang, Q.; Han, Y. Role of Molecular Weight in Microstructural Transition and Its Correlation to the Mechanical and Electrical Properties of P(Ndi2od-T2) Thin Films. *Macromolecules* **2021**, *54*, 10203−10215.
(262) Gross, Y. M.; Trefz, D.; Tkachov, R.; Untilova, V.; Brinkmann, M.; Schulz, G. L.; Ludwigs, S. Tuning Aggregation by Regioregularity for High-Performance N-Type P(Ndi2od-T2) Donor-Acceptor Copolymers. *Macromolecules* **2017**, *50*, 5353−5366.
(263) Matsidik, R.; Luzio, A.; Askin, O.; Fazzi, D.; Sepe, A.; Steiner, U.; Komber, H.; Caironi, M.; Sommer, M. Highly Planarized Naphthalene Diimide-Bifuran Copolymers with Unexpected Charge Transport Performance. *Chem. Mater.* **2017**, *29*, 5473−5483.
(264) Ziffer, M. E.; Jo, S. B.; Liu, Y.; Zhong, H.; Mohammed, J. C.; Harrison, J. S.; Jen, A. K. Y.; Ginger, D. S. Tuning H- and J-Aggregate Behavior in Π-Conjugated Polymers Via Noncovalent Interactions. *J. Phys. Chem. C* **2018**, *122*, 18860−18869.
(265) Liu, Y.; Wang, X.-Y.; Wang, Z.-Y.; Lu, Y.; Cheng, X.-F.; Tang, B.; Wang, J.-Y.; Pei, J. Systematically Investigating the Effect of the Aggregation Behaviors in Solution on the Charge Transport Properties of Bdopv-Based Polymers with Conjugation-Break Spacers. *Polym. Chem.* **2021**, *12*, 370−378.
(266) Scharsich, C.; Lohwasser, R. H.; Sommer, M.; Asawapirom, U.; Scherf, U.; Thelakkat, M.; Neher, D.; Köhler, A. Control of Aggregate Formation in Poly(3-Hexylthiophene) by Solvent, Molecular Weight, and Synthetic Method. *J. Polym. Sci., Part B: Polym. Phys.* **2012**, *50*, 442−453.
(267) Zheng, Y.-Q.; Yao, Z.-F.; Dou, J.-H.; Wang, Y.; Ma, W.; Zou, L.; Nikzad, S.; Li, Q.-Y.; Sun, Z.-H.; Yu, Z.-A.; et al. Influence of Solution-State Aggregation on Conjugated Polymer Crystallization in Thin Films and Microwire Crystals. *Giant* **2021**, *7*, 100064.
(268) Li, M.; Leenaers, P. J.; Wienk, M. M.; Janssen, R. A. J. The Effect of Alkyl Side Chain Length on the Formation of Two Semi-Crystalline Phases in Low Band Gap Conjugated Polymers. *J. Mater. Chem. C* **2020**, *8*, 5856−5867.
(269) Li, L.; Lu, G.; Yang, X. Improving Performance of Polymer Photovoltaic Devices Using an Annealing-Free Approach Via Construction of Ordered Aggregates in Solution. *J. Mater. Chem.* **2008**, *18*, 1984.
(270) Choi, D.; Chang, M.; Reichmanis, E. Controlled Assembly of Poly(3-Hexylthiophene): Managing the Disorder to Order Transition on the Nano- through Meso-Scales. *Adv. Funct. Mater.* **2015**, *25*, 920−927.
(271) Xi, Y.; Wolf, C. M.; Pozzo, L. D. Self-Assembly of Donor-Acceptor Conjugated Polymers Induced by Miscible 'Poor' Solvents. *Soft Matter* **2019**, *15*, 1799−1812.
(272) Li, M.; Bin, H.; Jiao, X.; Wienk, M. M.; Yan, H.; Janssen, R. A. J. Controlling the Microstructure of Conjugated Polymers in High-Mobility Monolayer Transistors Via the Dissolution Temperature. *Angew. Chem., Int. Ed. Engl.* **2020**, *59*, 846−852.
(273) Panzer, F.; Bassler, H.; Kohler, A. Temperature Induced Order-Disorder Transition in Solutions of Conjugated Polymers Probed by Optical Spectroscopy. *J. Phys. Chem. Lett.* **2017**, *8*, 114−125.
(274) Oh, J. Y.; Shin, M.; Lee, T. I.; Jang, W. S.; Min, Y.; Myoung, J.-M.; Baik, H. K.; Jeong, U. Self-Seeded Growth of Poly(3-Hexylthiophene) (P3ht) Nanofibrils by a Cycle of Cooling and Heating in Solutions. *Macromolecules* **2012**, *45*, 7504−7513.
(275) Hu, H.; Chow, P. C. Y.; Zhang, G.; Ma, T.; Liu, J.; Yang, G.; Yan, H. Design of Donor Polymers with Strong Temperature-Dependent Aggregation Property for Efficient Organic Photovoltaics. *Acc. Chem. Res.* **2017**, *50*, 2519−2528.
(276) Ashokan, A.; Wang, T.; Ravva, M. K.; Brédas, J.-L. Impact of Solution Temperature-Dependent Aggregation on the Solid-State Packing and Electronic Properties of Polymers for Organic Photovoltaics. *J. Mater. Chem. C* **2018**, *6*, 13162−13170.
(277) Zhao, J.; Li, Y.; Yang, G.; Jiang, K.; Lin, H.; Ade, H.; Ma, W.; Yan, H. Efficient Organic Solar Cells Processed from Hydrocarbon Solvents. *Nat. Energy* **2016**, *1*, 15027.
(278) Kohler, A.; Hoffmann, S. T.; Bassler, H. An Order-Disorder Transition in the Conjugated Polymer Meh-Ppv. *J. Am. Chem. Soc.* **2012**, *134*, 11594−11601.
(279) Du, B.; Yi, J.; Yan, H.; Wang, T. Temperature Induced Aggregation of Organic Semiconductors. *Chemistry* **2021**, *27*, 2908−2919.
(280) Liu, Y.; Zhao, J.; Li, Z.; Mu, C.; Ma, W.; Hu, H.; Jiang, K.; Lin, H.; Ade, H.; Yan, H. Aggregation and Morphology Control Enables Multiple Cases of High-Efficiency Polymer Solar Cells. *Nat. Commun.* **2014**, *5*, 5293.
(281) Yao, Z. F.; Wang, Z. Y.; Wu, H. T.; Lu, Y.; Li, Q. Y.; Zou, L.; Wang, J. Y.; Pei, J. Ordered Solid-State Microstructures of Conjugated Polymers Arising from Solution-State Aggregation. *Angew. Chem., Int. Ed. Engl.* **2020**, *59*, 17467−17471.
(282) Park, Y. D.; Lee, S. G.; Lee, H. S.; Kwak, D.; Lee, D. H.; Cho, K. Solubility-Driven Polythiophene Nanowires and Their Electrical Characteristics. *J. Phys. Chem. Lett.* **2011**, *21*, 2338−2343.
(283) Park, Y. D.; Park, J. K.; Seo, J. H.; Yuen, J. D.; Lee, W. H.; Cho, K.; Bazan, G. C. Solubility-Controlled Structural Ordering of Narrow Bandgap Conjugated Polymers. *Adv. Energy Mater.* **2011**, *1*, 63−67.

https://doi.org/10.1021/acs.chemrev.2c00905
Chem. Rev. 2023, 123, 8395−8487

(284) Nahid, M. M.; Matsidik, R.; Welford, A.; Gann, E.; Thomsen, L.; Sommer, M.; McNeill, C. R. Unconventional Molecular Weight Dependence of Charge Transport in the High Mobility N-Type Semiconducting Polymer P(Ndi2od-T2). *Adv. Funct. Mater.* **2017**, *27*, 1604744.
(285) Yao, Z. F.; Wang, J. Y.; Pei, J. Controlling Morphology and Microstructure of Conjugated Polymers Via Solution-State Aggregation. *Prog. Polym. Sci.* **2023**, *136*, 101626.
(286) Chung, K.; Yang, D. S.; Sul, W.-H.; Kim, B.-G.; Kim, J.; Jang, G.; Kwon, M. S.; Barłóg, M.; Lee, T. S.; Park, S.-Y.; et al. Molecular Design Approach for Directed Alignment of Conjugated Polymers. *Macromolecules* **2019**, *52*, 6485−6494.
(287) Hu, H.; Jiang, K.; Kim, J.-H.; Yang, G.; Li, Z.; Ma, T.; Lu, G.; Qu, Y.; Ade, H.; Yan, H. Influence of Fluorination on the Properties and Performance of Isoindigo-Quaterthiophene-Based Polymers. *J. Mater. Chem. A* **2016**, *4*, 5039−5043.
(288) Wang, T. H.; Bredas, J. L. Organic Photovoltaics: Understanding the Preaggregation of Polymer Donors in Solution and Its Morphological Impact. *J. Am. Chem. Soc.* **2021**, *143*, 1822−1835.
(289) Caddeo, C.; Fazzi, D.; Caironi, M.; Mattoni, A. Atomistic Simulations of P(Ndi2od-T2) Morphologies: From Single Chain to Condensed Phases. *J. Phys. Chem. B* **2014**, *118*, 12556−12565.
(290) Opoku, H.; Nketia-Yawson, B.; Shin, E. S.; Noh, Y.-Y. Controlling Organization of Conjugated Polymer Films from Binary Solvent Mixtures for High Performance Organic Field-Effect Transistors. *Org. Electron.* **2017**, *41*, 198−204.
(291) He, M.; Zhao, L.; Wang, J.; Han, W.; Yang, Y.; Qiu, F.; Lin, Z. Self-Assembly of All-Conjugated Poly(3-Alkylthiophene) Diblock Copolymer Nanostructures from Mixed Selective Solvents. *ACS Nano* **2010**, *4*, 3241−3247.
(292) Aiyar, A. R.; Hong, J. I.; Izumi, J.; Choi, D.; Kleinhenz, N.; Reichmanis, E. Ultrasound-Induced Ordering in Poly(3-Hexylthiophene): Role of Molecular and Process Parameters on Morphology and Charge Transport. *ACS Appl. Mater. Interfaces* **2013**, *5*, 2368−2377.
(293) Park, K. S.; Kwok, J. J.; Kafle, P.; Diao, Y. When Assembly Meets Processing: Tuning Multiscale Morphology of Printed Conjugated Polymers for Controlled Charge Transport. *Chem. Mater.* **2021**, *33*, 469−498.
(294) Yi, H. L.; Wu, C. H.; Wang, C. I.; Hua, C. C. Solvent-Regulated Mesoscale Aggregation Properties of Dilute Pbttt-C14 Solutions. *Macromolecules* **2017**, *50*, 5498−5509.
(295) Park, K. S.; Xue, Z.; Patel, B. B.; An, H.; Kwok, J. J.; Kafle, P.; Chen, Q.; Shukla, D.; Diao, Y. Chiral Emergence in Multistep Hierarchical Assembly of Achiral Conjugated Polymers. *Nat. Commun.* **2022**, *13*, 2738.
(296) Wang, H.; Liu, J.; Han, Y. Nano-Fibrils Formation of Pbttt Via Adding Alkylthiol into Solutions: Control Of morphology and Crystalline Structure. *Polymer* **2013**, *54*, 948−957.
(297) Newbloom, G. M.; Kim, F. S.; Jenekhe, S. A.; Pozzo, D. C. Mesoscale Morphology and Charge Transport in Colloidal Networks of Poly(3-Hexylthiophene). *Macromolecules* **2011**, *44*, 3801−3809.
(298) Newbloom, G. M.; Weigandt, K. M.; Pozzo, D. C. Structure and Property Development of Poly(3-Hexylthiophene) Organogels Probed with Combined Rheology, Conductivity and Small Angle Neutron Scattering. *Soft Matter* **2012**, *8*, 8854.
(299) Chen, C.-Y.; Chan, S.-H.; Li, J.-Y.; Wu, K.-H.; Chen, H.-L.; Chen, J.-H.; Huang, W.-Y.; Chen, S.-A. Formation and Thermally-Induced Disruption of Nanowhiskers in Poly(3-Hexylthiophene)/Xylene Gel Studied by Small-Angle X-Ray Scattering. *Macromolecules* **2010**, *43*, 7305−7311.
(300) Cao, Z.; Ma, G.; Leng, M.; Zhang, S.; Chen, J.; Do, C.; Hong, K.; Fang, L.; Gu, X. Variable-Temperature Scattering and Spectroscopy Characterizations for Temperature-Dependent Solution Assembly of Pffbt4t-Based Conjugated Polymers. *ACS Appl. Polym. Mater.* **2022**, *4*, 3023−3033.
(301) Khasbaatar, A.; Cheng, A.; Jones, A. L.; Kwok, J. J.; Park, S. K.; Komar, J. K.; Lin, O.; Jackson, N. E.; Chen, Q.; DeLongchamp, D. M.; et al. Solution Aggregate Structures of Donor Polymers Determine the Morphology and Processing Resiliency of Non-Fullerene Organic Solar Cells. *Chem. Mater.* **2023**, *35*, 2713−2729.
(302) Trefz, D.; Gross, Y. M.; Dingler, C.; Tkachov, R.; Hamidi-Sakr, A.; Kiriy, A.; McNeill, C. R.; Brinkmann, M.; Ludwigs, S. Tuning Orientational Order of Highly Aggregating P(Ndi2od-T2) by Solvent Vapor Annealing and Blade Coating. *Macromolecules* **2019**, *52*, 43−54.
(303) Knaapila, M.; Garamus, V. M.; Dias, F. B.; Almásy, L.; Galbrecht, F.; Charas, A.; Morgado, J.; Burrows, H. D.; Scherf, U.; Monkman, A. P. Influence of Solvent Quality on the Self-Organization of Archetypical Hairy Rods-Branched and Linear Side Chain Polyfluorenes: Rodlike Chains Versus "Beta-Sheets" in Solution. *Macromolecules* **2006**, *39*, 6505−6512.
(304) Knaapila, M.; Stepanyan, R.; Torkkeli, M.; Garamus, V. M.; Galbrecht, F.; Nehls, B. S.; Preis, E.; Scherf, U.; Monkman, A. P. Control over Phase Behavior and Solution Structure of Hairy-Rod Polyfluorene by Means of Side-Chain Length and Branching. *Phys. Rev. E Stat. Nonlin. Soft Matter Phys.* **2008**, *77*, 051803.
(305) Parent, L. R.; Gnanasekaran, K.; Korpanty, J.; Gianneschi, N. C. 100th Anniversary of Macromolecular Science Viewpoint: Polymeric Materials by in Situ Liquid-Phase Transmission Electron Microscopy. *ACS Macro Lett.* **2021**, *10*, 14−38.
(306) Newbloom, G. M.; Weigandt, K. M.; Pozzo, D. C. Electrical, Mechanical, and Structural Characterization of Self-Assembly in Poly(3-Hexylthiophene) Organogel Networks. *Macromolecules* **2012**, *45*, 3452−3462.
(307) Xu, W.; Tang, H.; Lv, H.; Li, J.; Zhao, X.; Li, H.; Wang, N.; Yang, X. Sol-Gel Transition of Poly(3-Hexylthiophene) Revealed by Capillary Measurements: Phase Behaviors, Gelation Kinetics and the Formation Mechanism. *Soft Matter* **2012**, *8*, 726−733.
(308) Koppe, M.; Brabec, C. J.; Heiml, S.; Schausberger, A.; Duffy, W.; Heeney, M.; McCulloch, I. Influence of Molecular Weight Distribution on the Gelation of P3ht and Its Impact on the Photovoltaic Performance. *Macromolecules* **2009**, *42*, 4661−4666.
(309) Yao, Z. F.; Zheng, Y. Q.; Li, Q. Y.; Lei, T.; Zhang, S.; Zou, L.; Liu, H. Y.; Dou, J. H.; Lu, Y.; Wang, J. Y.; et al. Wafer-Scale Fabrication of High-Performance N-Type Polymer Monolayer Transistors Using a Multi-Level Self-Assembly Strategy. *Adv. Mater.* **2019**, *31*, 1806747.
(310) Martelock, H.; Greiner, A.; Heitz, W. Structural Modifications of Poly(1,4-Phenylenevinylene) to Soluble, Fusible, Liquid-Crystalline Products. *Makromol. Chem.* **1991**, *192*, 967−979.
(311) Grell, M.; Bradley, D. D. C.; Inbasekaran, M.; Woo, E. P. A Glass-Forming Conjugated Main-Chain Liquid Crystal Polymer for Polarized Electroluminescence Applications. *Adv. Mater.* **1997**, *9*, 798−802.
(312) Schartel, B.; Wachtendorf, V.; Grell, M.; Bradley, D. D. C.; Hennecke, M. Polarized Fluorescence and Orientational Order Parameters of a Liquid-Crystalline Conjugated Polymer. *Phys. Rev. B* **1999**, *60*, 277−283.
(313) Grell, M.; Knoll, W.; Lupo, D.; Meisel, A.; Miteva, T.; Neher, D.; Nothofer, H.-G.; Scherf, U.; Yasuda, A. Blue Polarized Electroluminescence from a Liquid Crystalline Polyfluorene. *Adv. Mater.* **1999**, *11*, 671−675.
(314) Grell, M.; Bradley, D. D. C.; Ungar, G.; Hill, J.; Whitehead, K. S. Interplay of Physical Structure and Photophysics for a Liquid Crystalline Polyfluorene. *Macromolecules* **1999**, *32*, 5810−5817.
(315) Yu, L.; Bao, Z.; Cai, R. Konjugierte, Flüssigkristalline Polymere. *Angew. Chem.* **1993**, *105*, 1392−1394.
(316) Sirringhaus, H.; Wilson, R. J.; Friend, R. H.; Inbasekaran, M.; Wu, W.; Woo, E. P.; Grell, M.; Bradley, D. D. C. Mobility Enhancement in Conjugated Polymer Field-Effect Transistors through Chain Alignment in a Liquid-Crystalline Phase. *Appl. Phys. Lett.* **2000**, *77*, 406−408.
(317) DeLongchamp, D. M.; Kline, R. J.; Jung, Y.; Lin, E. K.; Fischer, D. A.; Gundlach, D. J.; Cotts, S. K.; Moad, A. J.; Richter, L. J.; Toney, M. F.; et al. Molecular Basis of Mesophase Ordering in a Thiophene-Based Copolymer. *Macromolecules* **2008**, *41*, 5709−5715.
(318) Banach, M. J.; Friend, R. H.; Sirringhaus, H. Influence of the Casting Solvent on the Thermotropic Alignment of Thin Liquid

https://doi.org/10.1021/acs.chemrev.2c00905
Chem. Rev. 2023, 123, 8395−8487

Crystalline Polyfluorene Copolymer Films. *Macromolecules* **2004**, *37*, 6079−6085.
(319) Lee, M. J.; Gupta, D.; Zhao, N.; Heeney, M.; McCulloch, I.; Sirringhaus, H. Anisotropy of Charge Transport in a Uniaxially Aligned and Chain-Extended, High-Mobility, Conjugated Polymer Semiconductor. *Adv. Funct. Mater.* **2011**, *21*, 932−940.
(320) McCulloch, I.; Heeney, M.; Bailey, C.; Genevicius, K.; Macdonald, I.; Shkunov, M.; Sparrowe, D.; Tierney, S.; Wagner, R.; Zhang, W.; et al. Liquid-Crystalline Semiconducting Polymers with High Charge-Carrier Mobility. *Nat. Mater.* **2006**, *5*, 328−333.
(321) Zhang, X.; Hudson, S. D.; DeLongchamp, D. M.; Gundlach, D. J.; Heeney, M.; McCulloch, I. In-Plane Liquid Crystalline Texture of High-Performance Thienothiophene Copolymer Thin Films. *Adv. Funct. Mater.* **2010**, *20*, 4098−4106.
(322) Zhang, W. L.; Gomez, E. D.; Milner, S. T. Using Surface-Induced Ordering to Probe the Isotropic-to-Nematic Transition for Semiflexible Polymers. *Soft Matter* **2016**, *12*, 6141−6147.
(323) Xie, R. X.; Aplan, M. P.; Caggiano, N. J.; Weisen, A. R.; Su, T.; Muller, C.; Segad, M.; Colby, R. H.; Gomez, E. D. Local Chain Alignment Via Nematic Ordering Reduces Chain Entanglement in Conjugated Polymers. *Macromolecules* **2018**, *51*, 10271−10284.
(324) Zhang, W. L.; Gomez, E. D.; Milner, S. T. Predicting Nematic Phases of Semiflexible Polymers. *Macromolecules* **2015**, *48*, 1454−1462.
(325) Wang, W.; Lieser, G.; Wegner, G. Lyotropic Liquid Crystals of a Soluble Polydiacetylene. A Comparative Investigation by Means of Optical and Electron Microscopy. *Liq. Cryst.* **1993**, *15*, 1−24.
(326) Zhu, Z.; Swager, T. M. Conjugated Polymer Liquid Crystal Solutions: Control of Conformation and Alignment. *J. Am. Chem. Soc.* **2002**, *124*, 9670−9671.
(327) Maki Hamaguchi, M. H.; Katsumi Yoshino, K. Y. Lyotropic Behavior of Poly(2,5-Dinonyloxy-P-Phenylenevinylene). *Jpn. J. Appl. Phys.* **1994**, *33*, L1689.
(328) Zhang, S.; Pfefferle, L. D.; Osuji, C. O. Lyotropic Hexagonal Ordering in Aqueous Media by Conjugated Hairy-Rod Supramolecules. *Macromolecules* **2010**, *43*, 7549−7555.
(329) Kleinhenz, N.; Rosu, C.; Chatterjee, S.; Chang, M.; Nayani, K.; Xue, Z.; Kim, E.; Middlebrooks, J.; Russo, P. S.; Park, J. O.; et al. Liquid Crystalline Poly(3-Hexylthiophene) Solutions Revisited: Role of Time-Dependent Self-Assembly. *Chem. Mater.* **2015**, *27*, 2687−2694.
(330) Park, M. S.; Aiyar, A.; Park, J. O.; Reichmanis, E.; Srinivasarao, M. Solvent Evaporation Induced Liquid Crystalline Phase in Poly(3-Hexylthiophene). *J. Am. Chem. Soc.* **2011**, *133*, 7244−7247.
(331) Steiger, D.; Smith, P.; Weder, C. Liquid Crystalline, Highly Luminescent Poly(2,5-Dialkoxy-P-Phenyleneethynylene). *Macromol. Rapid Commun.* **1997**, *18*, 643−649.
(332) Bunz, U. H. Poly(Aryleneethynylene)S: Syntheses, Properties, Structures, and Applications. *Chem. Rev.* **2000**, *100*, 1605−1644.
(333) Luzio, A.; Criante, L.; D'Innocenzo, V.; Caironi, M. Control of Charge Transport in a Semiconducting Copolymer by Solvent-Induced Long-Range Order. *Sci. Rep.* **2013**, *3*, 3425.
(334) Wu, D.; Kaplan, M.; Ro, H. W.; Engmann, S.; Fischer, D. A.; DeLongchamp, D. M.; Richter, L. J.; Gann, E.; Thomsen, L.; McNeill, C. R.; et al. Blade Coating Aligned, High-Performance, Semiconducting-Polymer Transistors. *Chem. Mater.* **2018**, *30*, 1924−1936.
(335) Qu, G.; Park, K. S.; Kafle, P.; Zhang, F.; Kwok, J. J.; Patel, B. B.; Smilgies, D.-M.; Thomsen, L.; McNeill, C. R.; Diao, Y. Lyotropic Liquid Crystalline Mesophase Governs Interfacial Molecular Orientation of Conjugated Polymer Thin Films. *Chem. Mater.* **2020**, *32*, 6043−6054.
(336) Schott, S.; Gann, E.; Thomsen, L.; Jung, S. H.; Lee, J. K.; McNeill, C. R.; Sirringhaus, H. Charge-Transport Anisotropy in a Uniaxially Aligned Diketopyrrolopyrrole-Based Copolymer. *Adv. Mater.* **2015**, *27*, 7356−7364.
(337) Knaapila, M.; Stepanyan, R.; Lyons, B. P.; Torkkeli, M.; Monkman, A. P. Towards General Guidelines for Aligned, Nanoscale Assemblies of Hairy-Rod Polyfluorene. *Adv. Funct. Mater.* **2006**, *16*, 599−609.
(338) Albano, G.; Pescitelli, G.; Di Bari, L. Chiroptical Properties in Thin Films of Pi-Conjugated Systems. *Chem. Rev.* **2020**, *120*, 10145−10243.
(339) Richter, L. J.; DeLongchamp, D. M.; Amassian, A. Morphology Development in Solution-Processed Functional Organic Blend Films: An in Situ Viewpoint. *Chem. Rev.* **2017**, *117*, 6332−6366.
(340) Chen, L.; Zhao, K.; Chi, S.; Liu, J.; Yu, X.; Han, Y. Improving Fiber Alignment by Increasing the Planar Conformation of Isoindigo-Based Conjugated Polymers. *Mater. Chem. Front.* **2017**, *1*, 286−293.
(341) Lee, J.; Shin, E.-S.; Kim, Y.-J.; Noh, Y.-Y.; Yang, C. Controlling the Ambipolarity of Thieno-Benzo-Isoindigo Polymer-Based Transistors: The Balance of Face-on and Edge-on Populations. *J. Mater. Chem. C* **2020**, *8*, 296−302.
(342) Lee, J.; Ko, H.; Song, E.; Kim, H. G.; Cho, K. Naphthodithiophene-Based Conjugated Polymer with Linear, Planar Backbone Conformation and Strong Intermolecular Packing for Efficient Organic Solar Cells. *ACS Appl. Mater. Interfaces* **2015**, *7*, 21159−21169.
(343) Chen, M. S.; Niskala, J. R.; Unruh, D. A.; Chu, C. K.; Lee, O. P.; Fréchet, J. M. J. Control of Polymer-Packing Orientation in Thin Films through Synthetic Tailoring of Backbone Coplanarity. *Chem. Mater.* **2013**, *25*, 4088−4096.
(344) Lee, H. W.; Kim, H. S.; Kim, D.; Yoon, M.; Lee, J.; Hwang, D.-H. Comparative Study of Charge-Transport Behavior of Edge-on- and Face-on-Oriented Diketopyrrolopyrrole-Based Conjugated Copolymers Bearing Chalcogenophene Units. *Chem. Mater.* **2022**, *34*, 314−324.
(345) Li, Y.; Lee, T. H.; Park, S. Y.; Uddin, M. A.; Kim, T.; Hwang, S.; Kim, J. Y.; Woo, H. Y. Straight Chain D-a Copolymers Based on Thienothiophene and Benzothiadiazole for Efficient Polymer Field Effect Transistors and Photovoltaic Cells. *Polym. Chem.* **2016**, *7*, 4638−4646.
(346) Jeon, S.; Lee, J. H.; Park, J. I.; Jo, B.; Whang, D. R.; Ahn, T. K.; Park, H. J.; Kim, S. D.; Lee, W. H.; Kim, B. G. Manipulation of Chain Conformation for Optimum Charge-Transport Pathways in Conjugated Polymers. *ACS Appl. Mater. Interfaces* **2017**, *9*, 22757−22763.
(347) Persson, N. E.; Engmann, S.; Richter, L. J.; DeLongchamp, D. M. In Situ Observation of Alignment Templating by Seed Crystals in Highly Anisotropic Polymer Transistors. *Chem. Mater.* **2019**, *31*, 4133−4147.
(348) Lin, Z.-Q.; Shi, N.-E.; Li, Y.-B.; Qiu, D.; Zhang, L.; Lin, J.-Y.; Zhao, J.-F.; Wang, C.; Xie, L.-H.; Huang, W. Preparation and Characterization of Polyfluorene-Based Supramolecular Π-Conjugated Polymer Gels. *J. Phys. Chem. C* **2011**, *115*, 4418−4424.
(349) Malik, S.; Nandi, A. K. Thermodynamic and Structural Investigation of Thermoreversible Poly(3-Dodecyl Thiophene) Gels in the Three Isomers of Xylene. *J. Phys. Chem. B* **2004**, *108*, 597−604.
(350) Malik, S.; Jana, T.; Nandi, A. K. Thermoreversible Gelation of Regioregular Poly(3-Hexylthiophene) in Xylene. *Macromolecules* **2001**, *34*, 275−282.
(351) Huang, W. Y.; Huang, P. T.; Han, Y. K.; Lee, C. C.; Hsieh, T. L.; Chang, M. Y. Aggregation and Gelation Effects on the Performance of Poly(3-Hexylthiophene)/Fullerene Solar Cells. *Macromolecules* **2008**, *41*, 7485−7489.
(352) Huang, P.-T.; Chang, Y.-S.; Chou, C.-W. Preparation of Porous Poly(3-Hexylthiophene) by Freeze-Dry Method and Its Application to Organic Photovoltaics. *J. Appl. Polym. Sci.* **2011**, *122*, 233−240.
(353) He, J.; Kong, X.; Wang, Y.; Delaney, M.; Kalyon, D. M.; Lee, S. S. Crystallization-Arrested Viscoelastic Phase Separation in Semiconducting Polymer Gels. *ACS Appl. Polym. Mater.* **2019**, *1*, 500−508.
(354) Kim, B. G.; Jeong, E. J.; Park, H. J.; Bilby, D.; Guo, L. J.; Kim, J. Effect of Polymer Aggregation on the Open Circuit Voltage in Organic Photovoltaic Cells: Aggregation-Induced Conjugated Polymer Gel and Its Application for Preventing Open Circuit Voltage Drop. *ACS Appl. Mater. Interfaces* **2011**, *3*, 674−680.
(355) Li, P.; Chen, L. J.; Pan, J.; Niu, G. X.; Zhang, T.; Xiang, J.; Cai, L.; Hu, Y.; Zhang, Y. J.; Wan, K. M.; et al. Dispersion of P3ht Gelation and Its Influence on the Performance of Bulk Heterojunction Organic

https://doi.org/10.1021/acs.chemrev.2c00905
Chem. Rev. 2023, 123, 8395−8487

Solar Cells Based on P3ht:Pcbm. *Sol. Energy Mater. Sol. Cells* **2014**, *125*, 96−101.
(356) Wicklein, A.; Ghosh, S.; Sommer, M.; Wurthner, F.; Thelakkat, M. Self-Assembly of Semiconductor Organogelator Nanowires for Photoinduced Charge Separation. *ACS Nano* **2009**, *3*, 1107−1114.
(357) Kumar, R. J.; MacDonald, J. M.; Singh, T. B.; Waddington, L. J.; Holmes, A. B. Hierarchical Self-Assembly of Semiconductor Functionalized Peptide Alpha-Helices and Optoelectronic Properties. *J. Am. Chem. Soc.* **2011**, *133*, 8564−8573.
(358) Richards, J. J.; Weigandt, K. M.; Pozzo, D. C. Aqueous Dispersions of Colloidal Poly(3-Hexylthiophene) Gel Particles with High Internal Porosity. *J. Colloid Interface Sci.* **2011**, *364*, 341−350.
(359) Yan, C.; Barlow, S.; Wang, Z.; Yan, H.; Jen, A. K. Y.; Marder, S. R.; Zhan, X. Non-Fullerene Acceptors for Organic Solar Cells. *Nat. Rev. Mater.* **2018**, *3*, 18003.
(360) Wadsworth, A.; Moser, M.; Marks, A.; Little, M. S.; Gasparini, N.; Brabec, C. J.; Baran, D.; McCulloch, I. Critical Review of the Molecular Design Progress in Non-Fullerene Electron Acceptors Towards Commercially Viable Organic Solar Cells. *Chem. Soc. Rev.* **2019**, *48*, 1596−1625.
(361) Lin, Y.; Wang, J.; Zhang, Z. G.; Bai, H.; Li, Y.; Zhu, D.; Zhan, X. An Electron Acceptor Challenging Fullerenes for Efficient Polymer Solar Cells. *Adv. Mater.* **2015**, *27*, 1170−1174.
(362) Yuan, J.; Zhang, Y.; Zhou, L.; Zhang, G.; Yip, H.-L.; Lau, T.-K.; Lu, X.; Zhu, C.; Peng, H.; Johnson, P. A.; et al. Single-Junction Organic Solar Cell with over 15% Efficiency Using Fused-Ring Acceptor with Electron-Deficient Core. *Joule* **2019**, *3*, 1140−1151.
(363) Cnops, K.; Zango, G.; Genoe, J.; Heremans, P.; Martinez-Diaz, M. V.; Torres, T.; Cheyns, D. Energy Level Tuning of Non-Fullerene Acceptors in Organic Solar Cells. *J. Am. Chem. Soc.* **2015**, *137*, 8991−8997.
(364) Nielsen, C. B.; Voroshazi, E.; Holliday, S.; Cnops, K.; Rand, B. P.; McCulloch, I. Efficient Truxenone-Based Acceptors for Organic Photovoltaics. *J. Mater. Chem. A* **2013**, *1*, 73−76.
(365) Cheng, P.; Zhao, X.; Zhan, X. Perylene Diimide-Based Oligomers and Polymers for Organic Optoelectronics. *Acc. Mater. Res.* **2022**, *3*, 309−318.
(366) Kim, Y.; Song, C. E.; Moon, S.-J.; Lim, E. Effect of Dye End Groups in Non-Fullerene Fluorene- and Carbazole-Based Small Molecule Acceptors on Photovoltaic Performance. *RSC Adv.* **2015**, *5*, 62739−62746.
(367) Lopez, S. A.; Sanchez-Lengeling, B.; de Goes Soares, J.; Aspuru-Guzik, A. Design Principles and Top Non-Fullerene Acceptor Candidates for Organic Photovoltaics. *Joule* **2017**, *1*, 857−870.
(368) Yoon, S.; Shin, E.-Y.; Cho, N.-K.; Park, S.; Woo, H. Y.; Son, H. J. Progress in Morphology Control from Fullerene to Nonfullerene Acceptors for Scalable High-Performance Organic Photovoltaics. *J. Mater. Chem. A* **2021**, *9*, 24729−24758.
(369) Zhong, W.; Zhang, M.; Zhu, L.; Zhang, Y.; Liu, F. Complex Multilength-Scale Morphology in Organic Photovoltaics. *Trends Chem.* **2022**, *4*, 699−713.
(370) Tsarfati, Y.; Rosenne, S.; Weissman, H.; Shimon, L. J. W.; Gur, D.; Palmer, B. A.; Rybtchinski, B. Crystallization of Organic Molecules: Nonclassical Mechanism Revealed by Direct Imaging. *ACS Cent. Sci.* **2018**, *4*, 1031−1036.
(371) Nielsen, C. B.; Holliday, S.; Chen, H. Y.; Cryer, S. J.; McCulloch, I. Non-Fullerene Electron Acceptors for Use in Organic Solar Cells. *Acc. Chem. Res.* **2015**, *48*, 2803−2812.
(372) Armin, A.; Li, W.; Sandberg, O. J.; Xiao, Z.; Ding, L.; Nelson, J.; Neher, D.; Vandewal, K.; Shoaee, S.; Wang, T.; et al. A History and Perspective of Non-Fullerene Electron Acceptors for Organic Solar Cells. *Adv. Energy Mater.* **2021**, *11*, 2003570.
(373) Hou, J.; Inganäs, O.; Friend, R. H.; Gao, F. Organic Solar Cells Based on Non-Fullerene Acceptors. *Nat. Mater.* **2018**, *17*, 119−128.
(374) Zhu, L.; Zhang, M.; Zhong, W.; Leng, S.; Zhou, G.; Zou, Y.; Su, X.; Ding, H.; Gu, P.; Liu, F.; et al. Progress and Prospects of the Morphology of Non-Fullerene Acceptor Based High-Efficiency Organic Solar Cells. *Energy Environ. Sci.* **2021**, *14*, 4341−4357.
(375) Cui, Y.; Yao, H.; Hong, L.; Zhang, T.; Tang, Y.; Lin, B.; Xian, K.; Gao, B.; An, C.; Bi, P.; et al. Organic Photovoltaic Cell with 17% Efficiency and Superior Processability. *Natl. Sci.* **2020**, *7*, 1239−1246.
(376) Liu, Z. X.; Yu, Z. P.; Shen, Z.; He, C.; Lau, T. K.; Chen, Z.; Zhu, H.; Lu, X.; Xie, Z.; Chen, H.; et al. Molecular Insights of Exceptionally Photostable Electron Acceptors for Organic Photovoltaics. *Nat. Commun.* **2021**, *12*, 3049.
(377) Winzenberg, K. N.; Kemppinen, P.; Scholes, F. H.; Collis, G. E.; Shu, Y.; Singh, T. B.; Bilic, A.; Forsyth, C. M.; Watkins, S. E. Indan-1,3-Dione Electron-Acceptor Small Molecules for Solution-Processable Solar Cells: A Structure-Property Correlation. *Chem. Commun.* **2013**, *49*, 6307−6309.
(378) Yu, P.; Zhen, Y.; Dong, H.; Hu, W. Crystal Engineering of Organic Optoelectronic Materials. *Chem.* **2019**, *5*, 2814−2853.
(379) Lai, H.; He, F. Crystal Engineering in Organic Photovoltaic Acceptors: A 3d Network Approach. *Adv. Energy Mater.* **2020**, *10*, 2002678.
(380) Desiraju, G. R. Crystal Engineering: From Molecule to Crystal. *J. Am. Chem. Soc.* **2013**, *135*, 9952−9967.
(381) Desiraju, G. R. Supramolecular Synthons in Crystal Engineering—a New Organic Synthesis. *Angew. Chem., Int. Ed. Engl.* **1995**, *34*, 2311−2327.
(382) Sun, K.; Xiao, Z.; Lu, S.; Zajaczkowski, W.; Pisula, W.; Hanssen, E.; White, J. M.; Williamson, R. M.; Subbiah, J.; Ouyang, J.; et al. A Molecular Nematic Liquid Crystalline Material for High-Performance Organic Photovoltaics. *Nat. Commun.* **2015**, *6*, 6013.
(383) He, T.; Leowanawat, P.; Burschka, C.; Stepanenko, V.; Stolte, M.; Wurthner, F. Impact of 2-Ethylhexyl Stereoisomers on the Electrical Performance of Single-Crystal Field-Effect Transistors. *Adv. Mater.* **2018**, *30*, 1804032.
(384) Bristow, H.; Thorley, K. J.; White, A. J. P.; Wadsworth, A.; Babics, M.; Hamid, Z.; Zhang, W.; Paterson, A. F.; Kosco, J.; Panidi, J.; et al. Impact of Nonfullerene Acceptor Side Chain Variation on Transistor Mobility. *Adv. Electron. Mater.* **2019**, *5*, 1900344.
(385) Zhao, X.; Liu, T.; Zhang, Y.; Wang, S.; Li, X.; Xiao, Y.; Hou, X.; Liu, Z.; Shi, W.; Dennis, T. J. S. Organic Single-Crystalline Donor-Acceptor Heterojunctions with Ambipolar Band-Like Charge Transport for Photovoltaics. *Adv. Mater. Interfaces* **2018**, *5*, 1800336.
(386) Swick, S. M.; Gebraad, T.; Jones, L.; Fu, B.; Aldrich, T. J.; Kohlstedt, K. L.; Schatz, G. C.; Facchetti, A.; Marks, T. J. Building Blocks for High-Efficiency Organic Photovoltaics: Interplay of Molecular, Crystal, and Electronic Properties in Post-Fullerene Itic Ensembles. *ChemPhysChem* **2019**, *20*, 2608−2626.
(387) Mannsfeld, S. C. B.; Virkar, A.; Reese, C.; Toney, M. F.; Bao, Z. Precise Structure of Pentacene Monolayers on Amorphous Silicon Oxide and Relation to Charge Transport. *Adv. Mater.* **2009**, *21*, 2294−2298.
(388) Grazulis, S.; Chateigner, D.; Downs, R. T.; Yokochi, A. F.; Quiros, M.; Lutterotti, L.; Manakova, E.; Butkus, J.; Moeck, P.; Le Bail, A. Crystallography Open Database - an Open-Access Collection of Crystal Structures. *J. Appl. Crystallogr.* **2009**, *42*, 726−729.
(389) Allen, F. H.; Bellard, S.; Brice, M. D.; Cartwright, B. A.; Doubleday, A.; Higgs, H.; Hummelink, T.; Hummelink-Peters, B. G.; Kennard, O.; Motherwell, W. D. S.; et al. The Cambridge Crystallographic Data Centre: Computer-Based Search, Retrieval, Analysis and Display of Information. *Acta. Crystallogr. B. Struct. Sci. Cryst. Eng. Mater.* **1979**, *35*, 2331−2339.
(390) Voigt, J. H.; Bienfait, B.; Wang, S.; Nicklaus, M. C. Comparison of the Nci Open Database with Seven Large Chemical Structural Databases. *J. Chem. Inf. Comput. Sci.* **2001**, *41*, 702−712.
(391) Cole, J. M. How the Shape of Chemical Data Can Enable Data-Driven Materials Discovery. *Trends Chem.* **2021**, *3*, 111−119.
(392) Dar, A. A.; Rashid, S. Organic Co-Crystal Semiconductors: A Crystal Engineering Perspective. *CrystEngComm* **2021**, *23*, 8007−8026.
(393) Hunter, C. A.; Sanders, J. K. M. The Nature Of.Pi.-.Pi. Interactions. *J. Am. Chem. Soc.* **1990**, *112*, 5525−5534.
(394) Yao, Z.-F.; Wang, J.-Y.; Pei, J. Control of Π-Π Stacking Via Crystal Engineering in Organic Conjugated Small Molecule Crystals. *Cryst. Growth Des.* **2018**, *18*, 7−15.

https://doi.org/10.1021/acs.chemrev.2c00905
Chem. Rev. 2023, 123, 8395−8487

(395) Dou, J. H.; Zheng, Y. Q.; Yao, Z. F.; Yu, Z. A.; Lei, T.; Shen, X.; Luo, X. Y.; Sun, J.; Zhang, S. D.; Ding, Y. F.; et al. Fine-Tuning of Crystal Packing and Charge Transport Properties of Bdopv Derivatives through Fluorine Substitution. *J. Am. Chem. Soc.* **2015**, *137*, 15947−15956.
(396) Burattini, S.; Colquhoun, H. M.; Fox, J. D.; Friedmann, D.; Greenland, B. W.; Harris, P. J.; Hayes, W.; Mackay, M. E.; Rowan, S. J. A Self-Repairing, Supramolecular Polymer System: Healability as a Consequence of Donor-Acceptor Pi-Pi Stacking Interactions. *Chem. Commun.* **2009**, 6717−6719.
(397) Li, S.; Bobbala, S.; Vincent, M. P.; Modak, M.; Liu, Y.; Scott, E. A. Pi-Stacking Enhances Stability, Scalability of Formation, Control over Flexibility and Circulation Time of Polymeric Filaments. *Adv. Nanobiomed Res.* **2021**, *1*, 2100063.
(398) Ma, Z.; Geng, H.; Wang, D.; Shuai, Z. Influence of Alkyl Side-Chain Length on the Carrier Mobility in Organic Semiconductors: Herringbone Vs. Pi-Pi Stacking. *J. Mater. Chem. C* **2016**, *4*, 4546−4555.
(399) Li, C.; Campillo-Alvarado, G.; Swenson, D. C.; MacGillivray, L. R. Photoreactive Salt Cocrystal: N+-H···N Hydrogen Bond and Cation-Π Interactions Support a Cascade-Like Photodimerization of a 4-Stilbazole. *CrystEngComm* **2021**, *23*, 1071−1074.
(400) Giese, M.; Albrecht, M.; Rissanen, K. Anion-Pi Interactions with Fluoroarenes. *Chem. Rev.* **2015**, *115*, 8867−8895.
(401) Grabowski, S. J.; Ugalde, J. M. Bond Paths Show Preferable Interactions: Ab Initio and Qtaim Studies on the X-H···Pi Hydrogen Bond. *J. Phys. Chem. A* **2010**, *114*, 7223−7229.
(402) Kertesz, M. Pancake Bonding: An Unusual Pi-Stacking Interaction. *Chemistry* **2019**, *25*, 400−416.
(403) Davies, D. W.; Park, S. K.; Kafle, P.; Chung, H.; Yuan, D.; Strzalka, J. W.; Mannsfeld, S. C. B.; Wang, S. G.; Chen, Y.-S.; Gray, D. L.; et al. Radically Tunable N-Type Organic Semiconductor Via Polymorph Control. *Chem. Mater.* **2021**, *33*, 2466−2477.
(404) Spruell, J. M.; Coskun, A.; Friedman, D. C.; Forgan, R. S.; Sarjeant, A. A.; Trabolsi, A.; Fahrenbach, A. C.; Barin, G.; Paxton, W. F.; Dey, S. K.; et al. Highly Stable Tetrathiafulvalene Radical Dimers in [3]Catenanes. *Nat. Chem.* **2010**, *2*, 870−879.
(405) Kwon, S.; Kang, H.; Lee, J.-H.; Lee, J.; Hong, S.; Kim, H.; Lee, K. Effect of Processing Additives on Organic Photovoltaics: Recent Progress and Future Prospects. *Adv. Energy Mater.* **2017**, *7*, 1601496.
(406) Zheng, W.; Liu, J.; Guo, Y.; Han, G.; Yi, Y. Regulation of Molecular Orientations of a-D-a Nonfullerene Acceptors for Organic Photovoltaics: The Role of End-Group Π-Π Stacking. *Adv. Funct. Mater.* **2022**, *32*, 2108551.
(407) Guo, J.; Hu, K.; Qiu, B.; Zhang, J.; Yang, D.; Zhou, L.; Li, S.; Meng, L.; Zhang, Z.; Li, Y. Fine-Tuning Miscibility and Pi-Pi Stacking by Alkylthio Side Chains of Donor Molecules Enables High-Performance All-Small-Molecule Organic Solar Cells. *ACS Appl. Mater. Interfaces* **2021**, *13*, 36033−36043.
(408) Aldrich, T. J.; Matta, M.; Zhu, W.; Swick, S. M.; Stern, C. L.; Schatz, G. C.; Facchetti, A.; Melkonyan, F. S.; Marks, T. J. Fluorination Effects on Indacenodithienothiophene Acceptor Packing and Electronic Structure, End-Group Redistribution, and Solar Cell Photovoltaic Response. *J. Am. Chem. Soc.* **2019**, *141*, 3274−3287.
(409) Ray, K. K.; Campillo-Alvarado, G.; Morales-Rojas, H.; Höpfl, H.; MacGillivray, L. R.; Tivanski, A. V. Semiconductor Cocrystals Based on Boron: Generated Electrical Response with Π-Rich Aromatic Molecules. *Cryst. Growth Des.* **2020**, *20*, 3−8.
(410) Desiraju, G. R. Hydrogen Bridges in Crystal Engineering: Interactions without Borders. *Acc. Chem. Res.* **2002**, *35*, 565−573.
(411) Arunan, E.; Desiraju, G. R.; Klein, R. A.; Sadlej, J.; Scheiner, S.; Alkorta, I.; Clary, D. C.; Crabtree, R. H.; Dannenberg, J. J.; Hobza, P.; et al. Definition of the Hydrogen Bond (Iupac Recommendations 2011). *Pure Appl. Chem.* **2011**, *83*, 1637−1641.
(412) Zhang, F.; Lemaur, V.; Choi, W.; Kafle, P.; Seki, S.; Cornil, J.; Beljonne, D.; Diao, Y. Repurposing DNA-Binding Agents as H-Bonded Organic Semiconductors. *Nat. Commun.* **2019**, *10*, 4217.
(413) Hendsbee, A. D.; Sun, J.-P.; Law, W. K.; Yan, H.; Hill, I. G.; Spasyuk, D. M.; Welch, G. C. Synthesis, Self-Assembly, and Solar Cell Performance of N-Annulated Perylene Diimide Non-Fullerene Acceptors. *Chem. Mater.* **2016**, *28*, 7098−7109.
(414) Li, X.; Zhou, L.; Lu, X.; Cao, L.; Du, X.; Lin, H.; Zheng, C.; Tao, S. Hydrogen Bond Induced High-Performance Quaternary Organic Solar Cells with Efficiency up to 17.48% and Superior Thermal Stability. *Mater. Chem. Front.* **2021**, *5*, 3850−3858.
(415) Yan, C.; Ma, R.; Cai, G.; Liu, T.; Zhu, J.; Wang, J.; Li, Y.; Huang, J.; Luo, Z.; Xiao, Y.; et al. Reducing Voc Loss Via Structure Compatible and High Lowest Unoccupied Molecular Orbital Nonfullerene Acceptors for over 17%-Efficiency Ternary Organic Photovoltaics. *EcoMat* **2020**, *2*, No. e12061.
(416) Aytun, T.; Barreda, L.; Ruiz-Carretero, A.; Lehrman, J. A.; Stupp, S. I. Improving Solar Cell Efficiency through Hydrogen Bonding: A Method for Tuning Active Layer Morphology. *Chem. Mater.* **2015**, *27*, 1201−1209.
(417) Sokolov, A. N.; Friscic, T.; MacGillivray, L. R. Enforced Face-to-Face Stacking of Organic Semiconductor Building Blocks within Hydrogen-Bonded Molecular Cocrystals. *J. Am. Chem. Soc.* **2006**, *128*, 2806−2807.
(418) Campillo-Alvarado, G.; Bernhardt, M.; Davies, D. W.; Soares, J.; Woods, T. J.; Diao, Y. Modulation of Pi-Stacking Modes and Photophysical Properties of an Organic Semiconductor through Isosteric Cocrystallization. *J. Chem. Phys.* **2021**, *155*, 071102.
(419) González-Rodríguez, D.; Schenning, A. P. H. J. Hydrogen-Bonded Supramolecular Π-Functional Materials. *Chem. Mater.* **2011**, *23*, 310−325.
(420) Shewmon, N. T.; Watkins, D. L.; Galindo, J. F.; Zerdan, R. B.; Chen, J.; Keum, J.; Roitberg, A. E.; Xue, J.; Castellano, R. K. Enhancement in Organic Photovoltaic Efficiency through the Synergistic Interplay of Molecular Donor Hydrogen Bonding and Π-Stacking. *Adv. Funct. Mater.* **2015**, *25*, 5166−5177.
(421) Liu, X.; Wang, X.; Xiao, Y.; Yang, Q.; Guo, X.; Li, C. H-Bonds-Assisted Molecular Order Manipulation of Nonfullerene Acceptors for Efficient Nonannealed Organic Solar Cells. *Adv. Energy Mater.* **2020**, *10*, 1903650.
(422) Politzer, P.; Murray, J. S.; Clark, T. Halogen Bonding: An Electrostatically-Driven Highly Directional Noncovalent Interaction. *Phys. Chem. Chem. Phys.* **2010**, *12*, 7748−7757.
(423) Desiraju, G. R.; Ho, P. S.; Kloo, L.; Legon, A. C.; Marquardt, R.; Metrangolo, P.; Politzer, P.; Resnati, G.; Rissanen, K. Definition of the Halogen Bond (Iupac Recommendations 2013). *Pure Appl. Chem.* **2013**, *85*, 1711−1713.
(424) Cavallo, G.; Metrangolo, P.; Milani, R.; Pilati, T.; Priimagi, A.; Resnati, G.; Terraneo, G. The Halogen Bond. *Chem. Rev.* **2016**, *116*, 2478−2601.
(425) Wang, R.; Yuan, J.; Wang, R.; Han, G.; Huang, T.; Huang, W.; Xue, J.; Wang, H. C.; Zhang, C.; Zhu, C.; et al. Rational Tuning of Molecular Interaction and Energy Level Alignment Enables High-Performance Organic Photovoltaics. *Adv. Mater.* **2019**, *31*, 1904215.
(426) Yang, Y. The Original Design Principles of the Y-Series Nonfullerene Acceptors, from Y1 to Y6. *ACS Nano* **2021**, *15*, 18679−18682.
(427) Zhang, H.; Yao, H.; Hou, J.; Zhu, J.; Zhang, J.; Li, W.; Yu, R.; Gao, B.; Zhang, S.; Hou, J. Over 14% Efficiency in Organic Solar Cells Enabled by Chlorinated Nonfullerene Small-Molecule Acceptors. *Adv. Mater.* **2018**, *30*, 1800613.
(428) Hu, H.; Fu, L.; Zhang, K.; Gao, K.; Ma, J.; Hao, X.; Yin, H. Observing Halogen-Bond-Assisted Electron Transport in High-Performance Polymer Solar Cells. *Appl. Phys. Lett.* **2021**, *119*, 183302.
(429) Fu, J.; Chen, S.; Yang, K.; Jung, S.; Lv, J.; Lan, L.; Chen, H.; Hu, D.; Yang, Q.; Duan, T.; et al. A "Sigma-Hole"-Containing Volatile Solid Additive Enabling 16.5% Efficiency Organic Solar Cells. *iScience* **2020**, *23*, 100965.
(430) Menekse, K.; Chen, P.; Mahlmeister, B.; Anhalt, O.; Kudzus, A.; Stolte, M.; Würthner, F. Quinoidal Dicyanomethylene-Endcapped Cyclopentadithiophenes as Vacuum-Processable N-Type Semiconductors. *J. Mater. Chem. C* **2020**, *8*, 15303−15311.

https://doi.org/10.1021/acs.chemrev.2c00905
Chem. Rev. 2023, 123, 8395−8487

(431) Kim, J. H.; Schembri, T.; Bialas, D.; Stolte, M.; Wurthner, F. Slip-Stacked J-Aggregate Materials for Organic Solar Cells and Photodetectors. *Adv. Mater.* **2022**, *34*, 2104678.
(432) Zhao, J.; Xu, X.; Yu, L.; Li, R.; Li, Y.; Peng, Q. Highly Efficient Non-Fused-Ring Electron Acceptors Enabled by the Conformational Lock and Structural Isomerization Effects. *ACS Appl. Mater. Interfaces* **2021**, *13*, 25214−25223.
(433) Halaby, S.; Martynowycz, M. W.; Zhu, Z.; Tretiak, S.; Zhugayevych, A.; Gonen, T.; Seifrid, M. Microcrystal Electron Diffraction for Molecular Design of Functional Non-Fullerene Acceptor Structures. *Chem. Mater.* **2021**, *33*, 966−977.
(434) Steed, J. W.; Turner, D. R.; Wallace, K. J. *Core Concepts in Supramolecular Chemistry and Nanochemistry*; John Wiley & Sons, 2007; pp 17−26.
(435) Li, D.; Zhang, X.; Liu, D.; Wang, T. Aggregation of Non-Fullerene Acceptors in Organic Solar Cells. *J. Mater. Chem. A* **2020**, *8*, 15607−15619.
(436) Han, G.; Guo, Y.; Song, X.; Wang, Y.; Yi, Y. Terminal Π-Π Stacking Determines Three-Dimensional Molecular Packing and Isotropic Charge Transport in an a-Π-a Electron Acceptor for Non-Fullerene Organic Solar Cells. *J. Mater. Chem. C* **2017**, *5*, 4852−4857.
(437) Sutton, C.; Risko, C.; Brédas, J.-L. Noncovalent Intermolecular Interactions in Organic Electronic Materials: Implications for the Molecular Packing Vs Electronic Properties of Acenes. *Chem. Mater.* **2016**, *28*, 3−16.
(438) Xu, J.; Jo, S. B.; Chen, X.; Zhou, G.; Zhang, M.; Shi, X.; Lin, F.; Zhu, L.; Hao, T.; Gao, K.; et al. The Molecular Ordering and Double-Channel Carrier Generation of Nonfullerene Photovoltaics within Multi-Length-Scale Morphology. *Adv. Mater.* **2022**, *34*, 2108317.
(439) Zhang, Z.; Cui, X.; Li, M.; Liu, Y.; Li, D.; Jiang, P.; Bo, Z. Nonfullerene Acceptors Comprising a Naphthalene Core for High Efficiency Organic Solar Cells. *RSC Adv.* **2019**, *9*, 39163−39169.
(440) Liu, H.; Wang, W.; Zhou, Y.; Li, Z. a. A Ring-Locking Strategy to Enhance the Chemical and Photochemical Stability of a-D-a-Type Non-Fullerene Acceptors. *J. Mater. Chem. A* **2021**, *9*, 1080−1088.
(441) Liu, D.; Kan, B.; Ke, X.; Zheng, N.; Xie, Z.; Lu, D.; Liu, Y. Extended Conjugation Length of Nonfullerene Acceptors with Improved Planarity Via Noncovalent Interactions for High-Performance Organic Solar Cells. *Adv. Energy Mater.* **2018**, *8*, 1801618.
(442) Ma, L.; Zhang, S.; Zhu, J.; Wang, J.; Ren, J.; Zhang, J.; Hou, J. Completely Non-Fused Electron Acceptor with 3d-Interpenetrated Crystalline Structure Enables Efficient and Stable Organic Solar Cell. *Nat. Commun.* **2021**, *12*, 5093.
(443) Yang, J.; Ding, W. L.; Li, Q. S.; Li, Z. S. Theoretical Study of Non-Fullerene Acceptors Using End-Capped Groups with Different Electron-Withdrawing Abilities toward Efficient Organic Solar Cells. *J. Phys. Chem. Lett.* **2022**, *13*, 916−922.
(444) Cao, H.; Bauer, N.; Pang, C.; Rech, J.; You, W.; Rupar, P. A. End-Cap Group Engineering of a Small Molecule Non-Fullerene Acceptor: The Influence of Benzothiophene Dioxide. *ACS Appl. Energy Mater.* **2018**, *1*, 7146−7152.
(445) Suman, S.; Singh, S. P. Impact of End Groups on the Performance of Non-Fullerene Acceptors for Organic Solar Cell Applications. *J. Mater. Chem. A* **2019**, *7*, 22701−22729.
(446) Wang, N.; Zhan, L.; Li, S.; Shi, M.; Lau, T.-K.; Lu, X.; Shikler, R.; Li, C.-Z.; Chen, H. Enhancement of Intra- and Inter-Molecular Π-Conjugated Effects for a Non-Fullerene Acceptor to Achieve High-Efficiency Organic Solar Cells with an Extended Photoresponse Range and Optimized Morphology. *Mater. Chem. Front.* **2018**, *2*, 2006−2012.
(447) Li, G.; Zhang, X.; Jones, L. O.; Alzola, J. M.; Mukherjee, S.; Feng, L. W.; Zhu, W.; Stern, C. L.; Huang, W.; Yu, J.; et al. Systematic Merging of Nonfullerene Acceptor Pi-Extension and Tetrafluorination Strategies Affords Polymer Solar Cells with > 16% Efficiency. *J. Am. Chem. Soc.* **2021**, *143*, 6123−6139.
(448) Shi, X.; Liao, X.; Gao, K.; Zuo, L.; Chen, J.; Zhao, J.; Liu, F.; Chen, Y.; Jen, A. K. Y. An Electron Acceptor with Broad Visible-Nir Absorption and Unique Solid State Packing for as-Cast High Performance Binary Organic Solar Cells. *Adv. Funct. Mater.* **2018**, *28*, 1802324.
(449) Swick, S. M.; Alzola, J. M.; Sangwan, V. K.; Amsterdam, S. H.; Zhu, W.; Jones, L. O.; Powers-Riggs, N.; Facchetti, A.; Kohlstedt, K. L.; Schatz, G. C.; et al. Fluorinating Π-Extended Molecular Acceptors Yields Highly Connected Crystal Structures and Low Reorganization Energies for Efficient Solar Cells. *Adv. Energy Mater.* **2020**, *10*, 2000635.
(450) Luo, Z.; Liu, T.; Xiao, Y.; Yang, T.; Chen, Z.; Zhang, G.; Zhong, C.; Ma, R.; Chen, Y.; Zou, Y.; et al. Significantly Improving the Performance of Polymer Solar Cells by the Isomeric Ending-Group Based Small Molecular Acceptors: Insight into the Isomerization. *Nano Energy* **2019**, *66*, 104146.
(451) Xiao, S.; Zhang, Q.; You, W. Molecular Engineering of Conjugated Polymers for Solar Cells: An Updated Report. *Adv. Mater.* **2017**, *29*, 1601391.
(452) Zhang, Z.; Li, M.; Liu, Y.; Zhang, J.; Feng, S.; Xu, X.; Song, J.; Bo, Z. Simultaneous Enhancement of the Molecular Planarity and the Solubility of Non-Fullerene Acceptors: Effect of Aliphatic Side-Chain Substitution on the Photovoltaic Performance. *J. Mater. Chem. A* **2017**, *5*, 7776−7783.
(453) Zhang, C.; Feng, S.; Liu, Y.; Hou, R.; Zhang, Z.; Xu, X.; Wu, Y.; Bo, Z. Effect of Non-Fullerene Acceptors' Side Chains on the Morphology and Photovoltaic Performance of Organic Solar Cells. *ACS Appl. Mater. Interfaces* **2017**, *9*, 33906−33912.
(454) Li, C.; Zhou, J.; Song, J.; Xu, J.; Zhang, H.; Zhang, X.; Guo, J.; Zhu, L.; Wei, D.; Han, G.; et al. Non-Fullerene Acceptors with Branched Side Chains and Improved Molecular Packing to Exceed 18% Efficiency in Organic Solar Cells. *Nat. Energy* **2021**, *6*, 605−613.
(455) Liang, J.; Pan, M.; Wang, Z.; Zhang, J.; Bai, F.; Ma, R.; Ding, L.; Chen, Y.; Li, X.; Ade, H.; et al. Branched Alkoxy Side Chain Enables High-Performance Non-Fullerene Acceptors with High Open-Circuit Voltage and Highly Ordered Molecular Packing. *Chem. Mater.* **2022**, *34*, 2059−2068.
(456) Reichenbacher, K.; Suss, H. I.; Hulliger, J. Fluorine in Crystal Engineering-"the Little Atom That Could". *Chem. Soc. Rev.* **2005**, *34*, 22−30.
(457) Wang, H.; Liu, T.; Zhou, J.; Mo, D.; Han, L.; Lai, H.; Chen, H.; Zheng, N.; Zhu, Y.; Xie, Z.; et al. Bromination: An Alternative Strategy for Non-Fullerene Small Molecule Acceptors. *Adv. Sci.* **2020**, *7*, 1903784.
(458) Lai, H.; Chen, H.; Zhou, J.; Qu, J.; Chao, P.; Liu, T.; Chang, X.; Zheng, N.; Xie, Z.; He, F. Isomer-Free: Precise Positioning of Chlorine-Induced Interpenetrating Charge Transfer for Elevated Solar Conversion. *iScience* **2019**, *17*, 302−314.
(459) Lai, H.; Chen, H.; Zhou, J.; Qu, J.; Wang, M.; Xie, W.; Xie, Z.; He, F. 3d Interpenetrating Network for High-Performance Non-fullerene Acceptors Via Asymmetric Chlorine Substitution. *J. Phys. Chem. Lett.* **2019**, *10*, 4737−4743.
(460) Yu, H.; Qi, Z.; Zhang, J.; Wang, Z.; Sun, R.; Chang, Y.; Sun, H.; Zhou, W.; Min, J.; Ade, H.; et al. Tailoring Non-Fullerene Acceptors Using Selenium-Incorporated Heterocycles for Organic Solar Cells with over 16% Efficiency. *J. Mater. Chem. A* **2020**, *8*, 23756−23765.
(461) Cruz-Cabeza, A. J.; Reutzel-Edens, S. M.; Bernstein, J. Facts and Fictions About Polymorphism. *Chem. Soc. Rev.* **2015**, *44*, 8619−8635.
(462) Gentili, D.; Gazzano, M.; Melucci, M.; Jones, D.; Cavallini, M. Polymorphism as an Additional Functionality of Materials for Technological Applications at Surfaces and Interfaces. *Chem. Soc. Rev.* **2019**, *48*, 2502−2517.
(463) Dunitz, J. D.; Bernstein, J. Disappearing Polymorphs. *Acc. Chem. Res.* **1995**, *28*, 193−200.
(464) Zhu, L.; Zhang, M.; Zhou, G.; Hao, T.; Xu, J.; Wang, J.; Qiu, C.; Prine, N.; Ali, J.; Feng, W.; et al. Efficient Organic Solar Cell with 16.88% Efficiency Enabled by Refined Acceptor Crystallization and Morphology with Improved Charge Transfer and Transport Properties. *Adv. Energy Mater.* **2020**, *10*, 1904234.
(465) Mai, J.; Xiao, Y.; Zhou, G.; Wang, J.; Zhu, J.; Zhao, N.; Zhan, X.; Lu, X. Hidden Structure Ordering Along Backbone of Fused-Ring Electron Acceptors Enhanced by Ternary Bulk Heterojunction. *Adv. Mater.* **2018**, *30*, 1802888.

https://doi.org/10.1021/acs.chemrev.2c00905
Chem. Rev. 2023, 123, 8395−8487

(466) Boschetto, G.; Krompiec, M.; Skylaris, C.-K. How Does Polymorphism Affect the Interfacial Charge-Transfer States in Organic Photovoltaics? *J. Phys. Chem. C* **2019**, *123*, 25585−25595.
(467) Mondelli, P.; Boschetto, G.; Horton, P. N.; Tiwana, P.; Skylaris, C.-K.; Coles, S. J.; Krompiec, M.; Morse, G. Meta-Analysis: The Molecular Organization of Non-Fullerene Acceptors. *Mater. Horiz.* **2020**, *7*, 1062−1072.
(468) Diao, Y.; Lenn, K. M.; Lee, W. Y.; Blood-Forsythe, M. A.; Xu, J.; Mao, Y.; Kim, Y.; Reinspach, J. A.; Park, S.; Aspuru-Guzik, A.; et al. Understanding Polymorphism in Organic Semiconductor Thin Films through Nanoconfinement. *J. Am. Chem. Soc.* **2014**, *136*, 17046−17057.
(469) Jones, A. O. F.; Chattopadhyay, B.; Geerts, Y. H.; Resel, R. Substrate-Induced and Thin-Film Phases: Polymorphism of Organic Materials on Surfaces. *Adv. Funct. Mater.* **2016**, *26*, 2233−2255.
(470) Marina, S.; Scaccabarozzi, A. D.; Gutierrez-Fernandez, E.; Solano, E.; Khirbat, A.; Ciammaruchi, L.; Iturrospe, A.; Balzer, A.; Yu, L.; Gabirondo, E.; et al. Polymorphism in Non-Fullerene Acceptors Based on Indacenodithienothiophene. *Adv. Funct. Mater.* **2021**, *31*, 2103784.
(471) Gutierrez-Fernandez, E.; Scaccabarozzi, A. D.; Basu, A.; Solano, E.; Anthopoulos, T. D.; Martin, J. Y6 Organic Thin-Film Transistors with Electron Mobilities of 2.4 Cm(2) V(−1) S(−1) Via Microstructural Tuning. *Adv. Sci.* **2022**, *9*, 2104977.
(472) Sharma, V.; Koenig, J. D. B.; Welch, G. C. Perylene Diimide Based Non-Fullerene Acceptors: Top Performers and an Emerging Class Featuring N-Annulation. *J. Mater. Chem. A* **2021**, *9*, 6775−6789.
(473) Macedo, A. G.; Christopholi, L. P.; Gavim, A. E. X.; de Deus, J. F.; Teridi, M. A. M.; Yusoff, A. R. b. M.; da Silva, W. J. Perylene Derivatives for Solar Cells and Energy Harvesting: A Review of Materials, Challenges and Advances. *J. Mater. Sci. Mater. Electron.* **2019**, *30*, 15803−15824.
(474) Nowak-Krol, A.; Shoyama, K.; Stolte, M.; Wurthner, F. Naphthalene and Perylene Diimides - Better Alternatives to Fullerenes for Organic Electronics? *Chem. Commun.* **2018**, *54*, 13763−13772.
(475) Liu, Z.; Wu, Y.; Zhang, Q.; Gao, X. Non-Fullerene Small Molecule Acceptors Based on Perylene Diimides. *J. Mater. Chem. A* **2016**, *4*, 17604−17622.
(476) Li, C.; Wonneberger, H. Perylene Imides for Organic Photovoltaics: Yesterday, Today, and Tomorrow. *Adv. Mater.* **2012**, *24*, 613−636.
(477) Hartnett, P. E.; Timalsina, A.; Matte, H. S.; Zhou, N.; Guo, X.; Zhao, W.; Facchetti, A.; Chang, R. P.; Hersam, M. C.; Wasielewski, M. R.; et al. Slip-Stacked Perylenediimides as an Alternative Strategy for High Efficiency Nonfullerene Acceptors in Organic Photovoltaics. *J. Am. Chem. Soc.* **2014**, *136*, 16345−16356.
(478) Felter, K. M.; Caselli, V. M.; Gunbas, D. D.; Savenije, T. J.; Grozema, F. C. Interplay between Charge Carrier Mobility, Exciton Diffusion, Crystal Packing, and Charge Separation in Perylene Diimide-Based Heterojunctions. *ACS Appl. Energy Mater.* **2019**, *2*, 8010−8021.
(479) Zhong, Y.; Trinh, M. T.; Chen, R.; Purdum, G. E.; Khlyabich, P. P.; Sezen, M.; Oh, S.; Zhu, H.; Fowler, B.; Zhang, B.; et al. Molecular Helices as Electron Acceptors in High-Performance Bulk Heterojunction Solar Cells. *Nat. Commun.* **2015**, *6*, 8242.
(480) Zhong, Y.; Kumar, B.; Oh, S.; Trinh, M. T.; Wu, Y.; Elbert, K.; Li, P.; Zhu, X.; Xiao, S.; Ng, F.; et al. Helical Ribbons for Molecular Electronics. *J. Am. Chem. Soc.* **2014**, *136*, 8122−8130.
(481) Pan, Y. Q.; Sun, G. Y. Star-Shaped Non-Fullerene Small Acceptors for Organic Solar Cells. *ChemSusChem* **2019**, *12*, 4570−4600.
(482) Meng, D.; Fu, H.; Xiao, C.; Meng, X.; Winands, T.; Ma, W.; Wei, W.; Fan, B.; Huo, L.; Doltsinis, N. L.; et al. Three-Bladed Rylene Propellers with Three-Dimensional Network Assembly for Organic Electronics. *J. Am. Chem. Soc.* **2016**, *138*, 10184−10190.
(483) Chen, S.; Meng, D.; Huang, J.; Liang, N.; Li, Y.; Liu, F.; Yan, H.; Wang, Z. Symmetry-Induced Orderly Assembly Achieving High-Performance Perylene Diimide-Based Nonfullerene Organic Solar Cells. *CCS Chem.* **2021**, *3*, 78−84.
(484) Ding, K.; Shan, T.; Xu, J.; Li, M.; Wang, Y.; Zhang, Y.; Xie, Z.; Ma, Z.; Liu, F.; Zhong, H. A Perylene Diimide-Containing Acceptor Enables High Fill Factor in Organic Solar Cells. *Chem. Commun.* **2020**, *56*, 11433−11436.
(485) Xie, D.; Liu, T.; Gao, W.; Zhong, C.; Huo, L.; Luo, Z.; Wu, K.; Xiong, W.; Liu, F.; Sun, Y.; et al. A Novel Thiophene-Fused Ending Group Enabling an Excellent Small Molecule Acceptor for High-Performance Fullerene-Free Polymer Solar Cells with 11.8% Efficiency. *Solar RRL* **2017**, *1*, 1700044.
(486) Li, S.; Ye, L.; Zhao, W.; Liu, X.; Zhu, J.; Ade, H.; Hou, J. Design of a New Small-Molecule Electron Acceptor Enables Efficient Polymer Solar Cells with High Fill Factor. *Adv. Mater.* **2017**, *29*, 1704051.
(487) Ciammaruchi, L.; Zapata-Arteaga, O.; Gutiérrez-Fernández, E.; Martin, J.; Campoy-Quiles, M. Structure Dependent Photostability of Itic and Itic-4f. *Mater. Adv.* **2020**, *1*, 2846−2861.
(488) Boothroyd, S.; Kerridge, A.; Broo, A.; Buttar, D.; Anwar, J. Why Do Some Molecules Form Hydrates or Solvates? *Cryst. Growth Des.* **2018**, *18*, 1903−1908.
(489) Zhang, W.; Smith, J.; Watkins, S. E.; Gysel, R.; McGehee, M.; Salleo, A.; Kirkpatrick, J.; Ashraf, S.; Anthopoulos, T.; Heeney, M.; et al. Indacenodithiophene Semiconducting Polymers for High-Performance, Air-Stable Transistors. *J. Am. Chem. Soc.* **2010**, *132*, 11437−11439.
(490) McCulloch, I.; Ashraf, R. S.; Biniek, L.; Bronstein, H.; Combe, C.; Donaghey, J. E.; James, D. I.; Nielsen, C. B.; Schroeder, B. C.; Zhang, W. Design of Semiconducting Indacenodithiophene Polymers for High Performance Transistors and Solar Cells. *Acc. Chem. Res.* **2012**, *45*, 714−722.
(491) Holliday, S.; Ashraf, R. S.; Wadsworth, A.; Baran, D.; Yousaf, S. A.; Nielsen, C. B.; Tan, C. H.; Dimitrov, S. D.; Shang, Z.; Gasparini, N.; et al. High-Efficiency and Air-Stable P3ht-Based Polymer Solar Cells with a New Non-Fullerene Acceptor. *Nat. Commun.* **2016**, *7*, 11585.
(492) Classen, A.; Chochos, C. L.; Lüer, L.; Gregoriou, V. G.; Wortmann, J.; Osvet, A.; Forberich, K.; McCulloch, I.; Heumüller, T.; Brabec, C. J. The Role of Exciton Lifetime for Charge Generation in Organic Solar Cells at Negligible Energy-Level Offsets. *Nat. Energy* **2020**, *5*, 711−719.
(493) Yuan, J.; Zou, Y. The History and Development of Y6. *Org. Electron.* **2022**, *102*, 106436.
(494) Lin, F.; Jiang, K.; Kaminsky, W.; Zhu, Z.; Jen, A. K. A Non-Fullerene Acceptor with Enhanced Intermolecular Pi-Core Interaction for High-Performance Organic Solar Cells. *J. Am. Chem. Soc.* **2020**, *142*, 15246−15251.
(495) Zhang, G.; Chen, X. K.; Xiao, J.; Chow, P. C. Y.; Ren, M.; Kupgan, G.; Jiao, X.; Chan, C. C. S.; Du, X.; Xia, R.; et al. Delocalization of Exciton and Electron Wavefunction in Non-Fullerene Acceptor Molecules Enables Efficient Organic Solar Cells. *Nat. Commun.* **2020**, *11*, 3943.
(496) Xiao, Y.; Yuan, J.; Zhou, G.; Ngan, K. C.; Xia, X.; Zhu, J.; Zou, Y.; Zhao, N.; Zhan, X.; Lu, X. Unveiling the Crystalline Packing of Y6 in Thin Films by Thermally Induced "Backbone-on" Orientation. *J. Mater. Chem. A* **2021**, *9*, 17030−17038.
(497) Xiao, C.; Li, C.; Liu, F.; Zhang, L.; Li, W. Single-Crystal Field-Effect Transistors Based on a Fused-Ring Electron Acceptor with High Ambipolar Mobilities. *J. Mater. Chem. C* **2020**, *8*, 5370−5374.
(498) Hedley, G. J.; Ward, A. J.; Alekseev, A.; Howells, C. T.; Martins, E. R.; Serrano, L. A.; Cooke, G.; Ruseckas, A.; Samuel, I. D. Determining the Optimum Morphology in High-Performance Polymer-Fullerene Organic Photovoltaic Cells. *Nat. Commun.* **2013**, *4*, 2867.
(499) Chen, W.; Xu, T.; He, F.; Wang, W.; Wang, C.; Strzalka, J.; Liu, Y.; Wen, J.; Miller, D. J.; Chen, J.; et al. Hierarchical Nanomorphologies Promote Exciton Dissociation in Polymer/Fullerene Bulk Heterojunction Solar Cells. *Nano Lett.* **2011**, *11*, 3707−3713.
(500) Yang, X.; Loos, J.; Veenstra, S. C.; Verhees, W. J.; Wienk, M. M.; Kroon, J. M.; Michels, M. A.; Janssen, R. A. Nanoscale Morphology of High-Performance Polymer Solar Cells. *Nano Lett.* **2005**, *5*, 579−583.
(501) Lou, S. J.; Szarko, J. M.; Xu, T.; Yu, L.; Marks, T. J.; Chen, L. X. Effects of Additives on the Morphology of Solution Phase Aggregates

https://doi.org/10.1021/acs.chemrev.2c00905
Chem. Rev. 2023, 123, 8395−8487

Formed by Active Layer Components of High-Efficiency Organic Solar Cells. *J. Am. Chem. Soc.* **2011**, *133*, 20661−20663.
(502) Lu, L.; Zheng, T.; Wu, Q.; Schneider, A. M.; Zhao, D.; Yu, L. Recent Advances in Bulk Heterojunction Polymer Solar Cells. *Chem. Rev.* **2015**, *115*, 12666−12731.
(503) Ro, H. W.; Downing, J. M.; Engmann, S.; Herzing, A. A.; DeLongchamp, D. M.; Richter, L. J.; Mukherjee, S.; Ade, H.; Abdelsamie, M.; Jagadamma, L. K.; et al. Morphology Changes Upon Scaling a High-Efficiency, Solution-Processed Solar Cell. *Energy Environ. Sci.* **2016**, *9*, 2835−2846.
(504) Yao, H.; Li, Y.; Hu, H.; Chow, P. C. Y.; Chen, S.; Zhao, J.; Li, Z.; Carpenter, J. H.; Lai, J. Y. L.; Yang, G.; et al. A Facile Method to Fine-Tune Polymer Aggregation Properties and Blend Morphology of Polymer Solar Cells Using Donor Polymers with Randomly Distributed Alkyl Chains. *Adv. Energy Mater.* **2018**, *8*, 1701895.
(505) Qian, D.; Ye, L.; Zhang, M.; Liang, Y.; Li, L.; Huang, Y.; Guo, X.; Zhang, S.; Tan, Z. a.; Hou, J. Design, Application, and Morphology Study of a New Photovoltaic Polymer with Strong Aggregation in Solution State. *Macromolecules* **2012**, *45*, 9611−9617.
(506) Yi, X.; Peng, Z.; Xu, B.; Seyitliyev, D.; Ho, C. H. Y.; Danilov, E. O.; Kim, T.; Reynolds, J. R.; Amassian, A.; Gundogdu, K.; et al. Critical Role of Polymer Aggregation and Miscibility in Nonfullerene-Based Organic Photovoltaics. *Adv. Energy Mater.* **2020**, *10*, 1902430.
(507) Ye, L.; Hu, H.; Ghasemi, M.; Wang, T.; Collins, B. A.; Kim, J. H.; Jiang, K.; Carpenter, J. H.; Li, H.; Li, Z.; et al. Quantitative Relations between Interaction Parameter, Miscibility and Function in Organic Solar Cells. *Nat. Mater.* **2018**, *17*, 253−260.
(508) Gibbs, J. W. On the Equilibrium of Heterogeneous Substances. *Am. J. Sci.* **1878**, *3*, 441−458.
(509) Erdemir, D.; Lee, A. Y.; Myerson, A. S. Nucleation of Crystals from Solution: Classical and Two-Step Models. *Acc. Chem. Res.* **2009**, *42*, 621−629.
(510) Lee, J.; Yang, J.; Kwon, S. G.; Hyeon, T. Nonclassical Nucleation and Growth of Inorganic Nanoparticles. *Nat. Rev. Mater.* **2016**, *1*, 16034.
(511) Davey, R. J.; Schroeder, S. L. M.; ter Horst, J. H. Nucleation of Organic Crystals—a Molecular Perspective. *Angew. Chem., Int. Ed.* **2013**, *52*, 2166−2179.
(512) Mullin, J. W. *Crystallization*, 4th ed.; Butterworth-Heinemann, 2001; pp 181−215.
(513) Michels, J. J.; Zhang, K.; Wucher, P.; Beaujuge, P. M.; Pisula, W.; Marszalek, T. Predictive Modelling of Structure Formation in Semiconductor Films Produced by Meniscus-Guided Coating. *Nat. Mater.* **2021**, *20*, 68−75.
(514) Liu, J.; Arif, M.; Zou, J.; Khondaker, S. I.; Zhai, L. Controlling Poly(3-Hexylthiophene) Crystal Dimension: Nanowhiskers and Nanoribbons. *Macromolecules* **2009**, *42*, 9390−9393.
(515) Gu, X.; Shaw, L.; Gu, K.; Toney, M. F.; Bao, Z. The Meniscus-Guided Deposition of Semiconducting Polymers. *Nat. Commun.* **2018**, *9*, 534.
(516) Peterlin, A. Crystalline Character in Polymers. *J. Polym. Sci., Part C: Polym. Symp.* **1965**, *9*, 61−89.
(517) Lauritzen, J. I.; Hoffman, J. D. Theory of Formation of Polymer Crystals with Folded Chains in Dilute Solution. *J. Res. Natl. Bur. Stand. (U. S.)* **1960**, *64A*, 73−102.
(518) De Yoreo, J. J.; Gilbert, P. U. P. A.; Sommerdijk, N. A. J. M.; Penn, R. L.; Whitelam, S.; Joester, D.; Zhang, H.; Rimer, J. D.; Navrotsky, A.; Banfield, J. F.; et al. Crystallization by Particle Attachment in Synthetic, Biogenic, and Geologic Environments. *Science* **2015**, *349*, aaa6760.
(519) Gebauer, D.; Kellermeier, M.; Gale, J. D.; Bergström, L.; Cölfen, H. Pre-Nucleation Clusters as Solute Precursors in Crystallisation. *Chem. Soc. Rev.* **2014**, *43*, 2348−2371.
(520) Zhang, T. H.; Liu, X. Y. How Does a Transient Amorphous Precursor Template Crystallization. *J. Am. Chem. Soc.* **2007**, *129*, 13520−13526.
(521) Vekilov, P. G. The Two-Step Mechanism of Nucleation of Crystals in Solution. *Nanoscale* **2010**, *2*, 2346−2357.
(522) Baumgartner, J.; Dey, A.; Bomans, P. H. H.; Le Coadou, C.; Fratzl, P.; Sommerdijk, N. A. J. M.; Faivre, D. Nucleation and Growth of Magnetite from Solution. *Nat. Mater.* **2013**, *12*, 310−314.
(523) Dumetz, A. C.; Chockla, A. M.; Kaler, E. W.; Lenhoff, A. M. Protein Phase Behavior in Aqueous Solutions: Crystallization, Liquid-Liquid Phase Separation, Gels, and Aggregates. *Biophys. J.* **2008**, *94*, 570−583.
(524) Savage, J. R.; Dinsmore, A. D. Experimental Evidence for Two-Step Nucleation in Colloidal Crystallization. *Phys. Rev. Lett.* **2009**, *102*, 198302.
(525) Shahar, C.; Dutta, S.; Weissman, H.; Shimon, L. J. W.; Ott, H.; Rybtchinski, B. Precrystalline Aggregates Enable Control over Organic Crystallization in Solution. *Angew. Chem., Int. Ed.* **2016**, *55*, 179−182.
(526) Zhang, T.; Sun, D.; Ren, X.; Liu, L.; Wen, G.; Ren, Z.; Li, H.; Yan, S. Synthesis and Properties of Siloxane Modified Perylene Bisimide Discotic Liquid Crystals. *Soft Matter* **2013**, *9*, 10739−10745.
(527) Wang, F.; Richards, V. N.; Shields, S. P.; Buhro, W. E. Kinetics and Mechanisms of Aggregative Nanocrystal Growth. *Chem. Mater.* **2014**, *26*, 5−21.
(528) Patel, B. B.; Diao, Y. Multiscale Assembly of Solution-Processed Organic Electronics: The Critical Roles of Confinement, Fluid Flow, and Interfaces. *Nanotechnology* **2018**, *29*, 044004.
(529) García-Ojalvo, J.; Lacasta, A. M.; Sancho, J. M.; Toral, R. Phase Separation Driven by External Fluctuations. *Europhys. Lett.* **1998**, *42*, 125−130.
(530) Kouijzer, S.; Michels, J. J.; van den Berg, M.; Gevaerts, V. S.; Turbiez, M.; Wienk, M. M.; Janssen, R. A. Predicting Morphologies of Solution Processed Polymer:Fullerene Blends. *J. Am. Chem. Soc.* **2013**, *135*, 12057−12067.
(531) Stein, R. S. Crystallization from Polymer Blends. *MRS Online Proceedings Library (OPL)* **1993**, *321*, 531.
(532) Samanta, P.; Srivastava, R.; Nandan, B.; Chen, H. L. Crystallization Behavior of Crystalline/Crystalline Polymer Blends under Confinement in Electrospun Nanofibers of Polystyrene/Poly(Ethylene Oxide)/Poly(Epsilon-Caprolactone) Ternary Mixtures. *Soft Matter* **2017**, *13*, 1569−1582.
(533) Nilsson, S.; Bernasik, A.; Budkowski, A.; Moons, E. Morphology and Phase Segregation of Spin-Casted Films of Polyfluorene/Pcbm Blends. *Macromolecules* **2007**, *40*, 8291−8301.
(534) Michels, J. J.; Moons, E. Simulation of Surface-Directed Phase Separation in a Solution-Processed Polymer/Pcbm Blend. *Macromolecules* **2013**, *46*, 8693−8701.
(535) van Franeker, J. J.; Turbiez, M.; Li, W.; Wienk, M. M.; Janssen, R. A. A Real-Time Study of the Benefits of Co-Solvents in Polymer Solar Cell Processing. *Nat. Commun.* **2015**, *6*, 6229.
(536) van Franeker, J. J.; Heintges, G. H.; Schaefer, C.; Portale, G.; Li, W.; Wienk, M. M.; van der Schoot, P.; Janssen, R. A. Polymer Solar Cells: Solubility Controls Fiber Network Formation. *J. Am. Chem. Soc.* **2015**, *137*, 11783−11794.
(537) Bartelt, J. A.; Douglas, J. D.; Mateker, W. R.; Labban, A. E.; Tassone, C. J.; Toney, M. F.; Fréchet, J. M. J.; Beaujuge, P. M.; McGehee, M. D. Controlling Solution-Phase Polymer Aggregation with Molecular Weight and Solvent Additives to Optimize Polymer-Fullerene Bulk Heterojunction Solar Cells. *Adv. Energy Mater.* **2014**, *4*, 1301733.
(538) Wang, Z.; Gao, K.; Kan, Y.; Zhang, M.; Qiu, C.; Zhu, L.; Zhao, Z.; Peng, X.; Feng, W.; Qian, Z.; et al. The Coupling and Competition of Crystallization and Phase Separation, Correlating Thermodynamics and Kinetics in Opv Morphology and Performances. *Nat. Commun.* **2021**, *12*, 332.
(539) Saito, H.; Stuehn, B. Exclusion of Noncrystalline Polymer from the Interlamellar Region in Poly(Vinylidene Fluoride)/Poly(Methyl Methacrylate) Blends. *Macromolecules* **1994**, *27*, 216−218.
(540) Okabe, Y.; Murakami, H.; Osaka, N.; Saito, H.; Inoue, T. Morphology Development and Exclusion of Noncrystalline Polymer During Crystallization in Pvdf/Pmma Blends. *Polymer* **2010**, *51*, 1494−1500.
(541) Arai, F.; Shinohara, K.; Nagasawa, N.; Takeshita, H.; Takenaka, K.; Miya, M.; Shiomi, T. Crystallization Behavior and Higher-Order

https://doi.org/10.1021/acs.chemrev.2c00905
Chem. Rev. 2023, 123, 8395−8487

Structure in Miscible Crystalline/Crystalline Polymer Blends. *Polym. J.* **2013**, *45*, 921−928.
(542) Hu, S.-R.; Kyu, T.; Stein, R. S. Characterization and Properties of Polyethylene Blends I. Linear Low-Density Polyethylene with High-Density Polyethylene. *J. Polym. Sci., Part B: Polym. Phys.* **1987**, *25*, 71−87.
(543) Kyu, T.; Hu, S.-R.; Stein, R. S. Characterization and Properties of Polyethylene Blends Ii. Linear Low-Density with Conventional Low-Density Polyethylene. *J. Polym. Sci., Part B: Polym. Phys.* **1987**, *25*, 89−103.
(544) Kohn, P.; Rong, Z.; Scherer, K. H.; Sepe, A.; Sommer, M.; Müller-Buschbaum, P.; Friend, R. H.; Steiner, U.; Hüttner, S. Crystallization-Induced 10-Nm Structure Formation in P3ht/Pcbm Blends. *Macromolecules* **2013**, *46*, 4002−4013.
(545) Kozub, D. R.; Vakhshouri, K.; Kesava, S. V.; Wang, C.; Hexemer, A.; Gomez, E. D. Direct Measurements of Exciton Diffusion Length Limitations on Organic Solar Cell Performance. *Chem. Commun.* **2012**, *48*, 5859−5861.
(546) Amb, C. M.; Chen, S.; Graham, K. R.; Subbiah, J.; Small, C. E.; So, F.; Reynolds, J. R. Dithienogermole as a Fused Electron Donor in Bulk Heterojunction Solar Cells. *J. Am. Chem. Soc.* **2011**, *133*, 10062−10065.
(547) Woo, C. H.; Beaujuge, P. M.; Holcombe, T. W.; Lee, O. P.; Frechet, J. M. Incorporation of Furan into Low Band-Gap Polymers for Efficient Solar Cells. *J. Am. Chem. Soc.* **2010**, *132*, 15547−15549.
(548) Negi, V.; Wodo, O.; van Franeker, J. J.; Janssen, R. A. J.; Bobbert, P. A. Simulating Phase Separation During Spin Coating of a Polymer-Fullerene Blend: A Joint Computational and Experimental Investigation. *ACS Appl. Energy Mater.* **2018**, *1*, 725−735.
(549) Ye, L.; Li, S.; Liu, X.; Zhang, S.; Ghasemi, M.; Xiong, Y.; Hou, J.; Ade, H. Quenching to the Percolation Threshold in Organic Solar Cells. *Joule* **2019**, *3*, 443−458.
(550) Albrecht, S.; Janietz, S.; Schindler, W.; Frisch, J.; Kurpiers, J.; Kniepert, J.; Inal, S.; Pingel, P.; Fostiropoulos, K.; Koch, N.; et al. Fluorinated Copolymer Pcpdtbt with Enhanced Open-Circuit Voltage and Reduced Recombination for Highly Efficient Polymer Solar Cells. *J. Am. Chem. Soc.* **2012**, *134*, 14932−14944.
(551) Tvingstedt, K.; Vandewal, K.; Gadisa, A.; Zhang, F.; Manca, J.; Inganas, O. Electroluminescence from Charge Transfer States in Polymer Solar Cells. *J. Am. Chem. Soc.* **2009**, *131*, 11819−11824.
(552) Marsh, R. A.; Hodgkiss, J. M.; Friend, R. H. Direct Measurement of Electric Field-Assisted Charge Separation in Polymer:-Fullerene Photovoltaic Diodes. *Adv. Mater.* **2010**, *22*, 3672−3676.
(553) Mihailetchi, V. D.; Koster, L. J.; Hummelen, J. C.; Blom, P. W. Photocurrent Generation in Polymer-Fullerene Bulk Heterojunctions. *Phys. Rev. Lett.* **2004**, *93*, 216601.
(554) Xu, B.; Pelse, I.; Agarkar, S.; Ito, S.; Zhang, J.; Yi, X.; Chujo, Y.; Marder, S.; So, F.; Reynolds, J. R. Randomly Distributed Conjugated Polymer Repeat Units for High-Efficiency Photovoltaic Materials with Enhanced Solubility and Processability. *ACS Appl. Mater. Interfaces* **2018**, *10*, 44583−44588.
(555) Hamid, Z.; Wadsworth, A.; Rezasoltani, E.; Holliday, S.; Azzouzi, M.; Neophytou, M.; Guilbert, A. A. Y.; Dong, Y.; Little, M. S.; Mukherjee, S.; et al. Influence of Polymer Aggregation and Liquid Immiscibility on Morphology Tuning by Varying Composition in Pffbt4t-2dt/Nonfullerene Organic Solar Cells. *Adv. Energy Mater.* **2020**, *10*, 1903248.
(556) Yang, B.; Zhang, S.; Chen, Y.; Cui, Y.; Liu, D.; Yao, H.; Zhang, J.; Wei, Z.; Hou, J. Investigation of Conjugated Polymers Based on Naphtho[2,3-C]Thiophene-4,9-Dione in Fullerene-Based and Fullerene-Free Polymer Solar Cells. *Macromolecules* **2017**, *50*, 1453−1462.
(557) Jiang, K.; Zhang, G.; Yang, G.; Zhang, J.; Li, Z.; Ma, T.; Hu, H.; Ma, W.; Ade, H.; Yan, H. Multiple Cases of Efficient Nonfullerene Ternary Organic Solar Cells Enabled by an Effective Morphology Control Method. *Adv. Energy Mater.* **2018**, *8*, 1701370.
(558) Naveed, H. B.; Ma, W. Miscibility-Driven Optimization of Nanostructures in Ternary Organic Solar Cells Using Non-Fullerene Acceptors. *Joule* **2018**, *2*, 621−641.
(559) Wu, Y.; Schneider, S.; Walter, C.; Chowdhury, A. H.; Bahrami, B.; Wu, H. C.; Qiao, Q.; Toney, M. F.; Bao, Z. Fine-Tuning Semiconducting Polymer Self-Aggregation and Crystallinity Enables Optimal Morphology and High-Performance Printed All-Polymer Solar Cells. *J. Am. Chem. Soc.* **2020**, *142*, 392−406.
(560) Li, Z.; Jiang, K.; Yang, G.; Lai, J. Y.; Ma, T.; Zhao, J.; Ma, W.; Yan, H. Donor Polymer Design Enables Efficient Non-Fullerene Organic Solar Cells. *Nat. Commun.* **2016**, *7*, 13094.
(561) Eastham, N. D.; Dudnik, A. S.; Aldrich, T. J.; Manley, E. F.; Fauvell, T. J.; Hartnett, P. E.; Wasielewski, M. R.; Chen, L. X.; Melkonyan, F. S.; Facchetti, A.; et al. Small Molecule Acceptor and Polymer Donor Crystallinity and Aggregation Effects on Microstructure Templating: Understanding Photovoltaic Response in Fullerene-Free Solar Cells. *Chem. Mater.* **2017**, *29*, 4432−4444.
(562) Liu, J.; Ma, L.-K.; Li, Z.; Hu, H.; Sheong, F. K.; Zhang, G.; Ade, H.; Yan, H. Donor Polymer Based on Alkylthiophene Side Chains for Efficient Non-Fullerene Organic Solar Cells: Insights into Fluorination and Side Chain Effects on Polymer Aggregation and Blend Morphology. *J. Mater. Chem. A* **2018**, *6*, 23270−23277.
(563) Liu, T.; Huo, L.; Chandrabose, S.; Chen, K.; Han, G.; Qi, F.; Meng, X.; Xie, D.; Ma, W.; Yi, Y.; et al. Optimized Fibril Network Morphology by Precise Side-Chain Engineering to Achieve High-Performance Bulk-Heterojunction Organic Solar Cells. *Adv. Mater.* **2018**, *30*, 1707353.
(564) Chen, S.; Zhang, L.; Ma, C.; Meng, D.; Zhang, J.; Zhang, G.; Li, Z.; Chow, P. C. Y.; Ma, W.; Wang, Z.; et al. Alkyl Chain Regiochemistry of Benzotriazole-Based Donor Polymers Influencing Morphology and Performances of Non-Fullerene Organic Solar Cells. *Adv. Energy Mater.* **2018**, *8*, 1702427.
(565) Wu, J.; Li, G.; Fang, J.; Guo, X.; Zhu, L.; Guo, B.; Wang, Y.; Zhang, G.; Arunagiri, L.; Liu, F.; et al. Random Terpolymer Based on Thiophene-Thiazolothiazole Unit Enabling Efficient Non-Fullerene Organic Solar Cells. *Nat. Commun.* **2020**, *11*, 4612.
(566) Zheng, Z.; Yao, H.; Ye, L.; Xu, Y.; Zhang, S.; Hou, J. Pbdb-T and Its Derivatives: A Family of Polymer Donors Enables over 17% Efficiency in Organic Photovoltaics. *Mater. Today* **2020**, *35*, 115−130.
(567) Sun, H.; Liu, T.; Yu, J.; Lau, T.-K.; Zhang, G.; Zhang, Y.; Su, M.; Tang, Y.; Ma, R.; Liu, B.; et al. A Monothiophene Unit Incorporating Both Fluoro and Ester Substitution Enabling High-Performance Donor Polymers for Non-Fullerene Solar Cells with 16.4% Efficiency. *Energy Environ. Sci.* **2019**, *12*, 3328−3337.
(568) Xie, B.; Zhang, K.; Hu, Z.; Fang, H.; Lin, B.; Yin, Q.; He, B.; Dong, S.; Ying, L.; Ma, W.; et al. Polymer Pre-Aggregation Enables Optimal Morphology and High Performance in All-Polymer Solar Cells. *Solar RRL* **2020**, *4*, 1900385.
(569) Zhang, L.; Ding, Z.; Zhao, R.; Jirui, F.; Ma, W.; Liu, J.; Wang, L. Effect of Polymer Donor Aggregation on the Active Layer Morphology of Amorphous Polymer Acceptor-Based All-Polymer Solar Cells. *J. Mater. Chem. C* **2020**, *8*, 5613−5619.
(570) Zhang, Q.; Chen, Z.; Ma, W.; Xie, Z.; Han, Y. Optimizing Domain Size and Phase Purity in All-Polymer Solar Cells by Solution Ordered Aggregation and Confinement Effect of the Acceptor. *J. Mater. Chem. C* **2019**, *7*, 12560−12571.
(571) Zhao, H.; Naveed, H. B.; Lin, B.; Zhou, X.; Yuan, J.; Zhou, K.; Wu, H.; Guo, R.; Scheel, M. A.; Chumakov, A.; et al. Hot Hydrocarbon-Solvent Slot-Die Coating Enables High-Efficiency Organic Solar Cells with Temperature-Dependent Aggregation Behavior. *Adv. Mater.* **2020**, *32*, 2002302.
(572) Seo, S.; Kim, J.; Kang, H.; Lee, J.-W.; Lee, S.; Kim, G.-U.; Kim, B. J. Polymer Donors with Temperature-Insensitive, Strong Aggregation Properties Enabling Additive-Free, Processing Temperature-Tolerant High-Performance All-Polymer Solar Cells. *Macromolecules* **2021**, *54*, 53−63.
(573) Li, S.; Ye, L.; Zhao, W.; Zhang, S.; Ade, H.; Hou, J. Significant Influence of the Methoxyl Substitution Position on Optoelectronic Properties and Molecular Packing of Small-Molecule Electron Acceptors for Photovoltaic Cells. *Adv. Energy Mater.* **2017**, *7*, 1700183.
(574) Dai, S.; Zhao, F.; Zhang, Q.; Lau, T. K.; Li, T.; Liu, K.; Ling, Q.; Wang, C.; Lu, X.; You, W.; et al. Fused Nonacyclic Electron Acceptors

https://doi.org/10.1021/acs.chemrev.2c00905
Chem. Rev. 2023, 123, 8395−8487

for Efficient Polymer Solar Cells. *J. Am. Chem. Soc.* **2017**, *139*, 1336−1343.
(575) Zhang, Y.; Liu, Z.; Shan, T.; Wang, Y.; Zhu, L.; Li, T.; Liu, F.; Zhong, H. Tuning the Molecular Geometry and Packing Mode of Non-Fullerene Acceptors by Altering the Bridge Atoms Towards Efficient Organic Solar Cells. *Mater. Chem. Front.* **2020**, *4*, 2462−2471.
(576) Dai, S.; Zhou, J.; Chandrabose, S.; Shi, Y.; Han, G.; Chen, K.; Xin, J.; Liu, K.; Chen, Z.; Xie, Z.; et al. High-Performance Fluorinated Fused-Ring Electron Acceptor with 3d Stacking and Exciton/Charge Transport. *Adv. Mater.* **2020**, *32*, 2000645.
(577) Zhang, X.; Li, G.; Mukherjee, S.; Huang, W.; Zheng, D.; Feng, L. W.; Chen, Y.; Wu, J.; Sangwan, V. K.; Hersam, M. C.; et al. Systematically Controlling Acceptor Fluorination Optimizes Hierarchical Morphology, Vertical Phase Separation, and Efficiency in Non-Fullerene Organic Solar Cells. *Adv. Energy Mater.* **2022**, *12*, 2102172.
(578) Zhang, Z.; Yuan, J.; Wei, Q.; Zou, Y. Small-Molecule Electron Acceptors for Efficient Non-Fullerene Organic Solar Cells. *Front. Chem.* **2018**, *6*, 414.
(579) Kamm, V.; Battagliarin, G.; Howard, I. A.; Pisula, W.; Mavrinskiy, A.; Li, C.; Müllen, K.; Laquai, F. Organic Solar Cells: Polythiophene: Perylene Diimide Solar Cells - the Impact of Alkyl-Substitution on the Photovoltaic Performance (Adv. Energy Mater. 2/2011). *Adv. Energy Mater.* **2011**, *1*, 137−137.
(580) Cai, Y.; Huo, L.; Sun, X.; Wei, D.; Tang, M.; Sun, Y. High Performance Organic Solar Cells Based on a Twisted Bay-Substituted Tetraphenyl Functionalized Perylenediimide Electron Acceptor. *Adv. Energy Mater.* **2015**, *5*, 1500032.
(581) Zhang, X.; Lu, Z.; Ye, L.; Zhan, C.; Hou, J.; Zhang, S.; Jiang, B.; Zhao, Y.; Huang, J.; Zhang, S.; et al. A Potential Perylene Diimide Dimer-Based Acceptor Material for Highly Efficient Solution-Processed Non-Fullerene Organic Solar Cells with 4.03% Efficiency. *Adv. Mater.* **2013**, *25*, 5791−5797.
(582) Li, S.; Liu, W.; Li, C.-Z.; Liu, F.; Zhang, Y.; Shi, M.; Chen, H.; Russell, T. P. A Simple Perylene Diimide Derivative with a Highly Twisted Geometry as an Electron Acceptor for Efficient Organic Solar Cells. *J. Mater. Chem. A* **2016**, *4*, 10659−10665.
(583) Liu, J.; Xie, S.; Feng, S.; Li, M.; Wu, L.; Xu, X.; Chen, X.; Li, C.; Bo, Z. A Propeller-Shaped Perylene Diimide Hexamer as a Non-fullerene Acceptor for Organic Solar Cells. *J. Mater. Chem. C* **2018**, *6*, 9336−9340.
(584) Lin, Y.; Wang, Y.; Wang, J.; Hou, J.; Li, Y.; Zhu, D.; Zhan, X. A Star-Shaped Perylene Diimide Electron Acceptor for High-Performance Organic Solar Cells. *Adv. Mater.* **2014**, *26*, 5137−5142.
(585) Hong, L.; Yao, H.; Wu, Z.; Cui, Y.; Zhang, T.; Xu, Y.; Yu, R.; Liao, Q.; Gao, B.; Xian, K.; et al. Eco-Compatible Solvent-Processed Organic Photovoltaic Cells with over 16% Efficiency. *Adv. Mater.* **2019**, *31*, 1903441.
(586) Jiang, K.; Wei, Q.; Lai, J. Y. L.; Peng, Z.; Kim, H. K.; Yuan, J.; Ye, L.; Ade, H.; Zou, Y.; Yan, H. Alkyl Chain Tuning of Small Molecule Acceptors for Efficient Organic Solar Cells. *Joule* **2019**, *3*, 3020−3033.
(587) Wang, Y.; Wang, X.; Lin, B.; Bi, Z.; Zhou, X.; Naveed, H. B.; Zhou, K.; Yan, H.; Tang, Z.; Ma, W. Achieving Balanced Crystallization Kinetics of Donor and Acceptor by Sequential-Blade Coated Double Bulk Heterojunction Organic Solar Cells. *Adv. Energy Mater.* **2020**, *10*, 2000826.
(588) Lin, B.; Zhou, X.; Zhao, H.; Yuan, J.; Zhou, K.; Chen, K.; Wu, H.; Guo, R.; Scheel, M. A.; Chumakov, A.; et al. Balancing the Pre-Aggregation and Crystallization Kinetics Enables High Efficiency Slot-Die Coated Organic Solar Cells with Reduced Non-Radiative Recombination Losses. *Energy Environ. Sci.* **2020**, *13*, 2467−2479.
(589) Liu, Q.; Fang, J.; Wu, J.; Zhu, L.; Guo, X.; Liu, F.; Zhang, M. Tuning Aggregation Behavior of Polymer Donor Via Molecular-Weight Control for Achieving 17.1% Efficiency Inverted Polymer Solar Cells. *Chin. J. Chem.* **2021**, *39*, 1941−1947.
(590) Zhou, N.; Dudnik, A. S.; Li, T. I.; Manley, E. F.; Aldrich, T. J.; Guo, P.; Liao, H. C.; Chen, Z.; Chen, L. X.; Chang, R. P.; et al. All-Polymer Solar Cell Performance Optimized Via Systematic Molecular Weight Tuning of Both Donor and Acceptor Polymers. *J. Am. Chem. Soc.* **2016**, *138*, 1240−1251.
(591) Hu, H.; Jiang, K.; Chow, P. C. Y.; Ye, L.; Zhang, G.; Li, Z.; Carpenter, J. H.; Ade, H.; Yan, H. Influence of Donor Polymer on the Molecular Ordering of Small Molecular Acceptors in Nonfullerene Polymer Solar Cells. *Adv. Energy Mater.* **2018**, *8*, 1701674.
(592) Liang, Q.; Han, J.; Song, C.; Yu, X.; Smilgies, D.-M.; Zhao, K.; Liu, J.; Han, Y. Reducing the Confinement of Pbdb-T to Itic to Improve the Crystallinity of Pbdb-T/Itic Blends. *J. Mater. Chem. A* **2018**, *6*, 15610−15620.
(593) Ma, R.; Li, G.; Li, D.; Liu, T.; Luo, Z.; Zhang, G.; Zhang, M.; Wang, Z.; Luo, S.; Yang, T.; et al. Understanding the Effect of End Group Halogenation in Tuning Miscibility and Morphology of High-Performance Small Molecular Acceptors. *Solar RRL* **2020**, *4*, 2000250.
(594) Li, W.; Ye, L.; Li, S.; Yao, H.; Ade, H.; Hou, J. A High-Efficiency Organic Solar Cell Enabled by the Strong Intramolecular Electron Push-Pull Effect of the Nonfullerene Acceptor. *Adv. Mater.* **2018**, *30*, 1707170.
(595) Wang, T.; Brédas, J.-L. Organic Solar Cells Based on Non-Fullerene Small-Molecule Acceptors: Impact of Substituent Position. *Matter* **2020**, *2*, 119−135.
(596) Ma, R.; Liu, T.; Luo, Z.; Gao, K.; Chen, K.; Zhang, G.; Gao, W.; Xiao, Y.; Lau, T.-K.; Fan, Q.; et al. Adding a Third Component with Reduced Miscibility and Higher Lumo Level Enables Efficient Ternary Organic Solar Cells. *ACS Energy Lett.* **2020**, *5*, 2711−2720.
(597) Dong, S.; Zhang, K.; Jia, T.; Zhong, W.; Wang, X.; Huang, F.; Cao, Y. Suppressing the Excessive Aggregation of Nonfullerene Acceptor in Blade-Coated Active Layer by Using N-Type Polymer Additive to Achieve Large-Area Printed Organic Solar Cells with Efficiency over 15%. *EcoMat* **2019**, *1*, No. e12006.
(598) Liao, X.; Xie, Q.; Guo, Y.; He, Q.; Chen, Z.; Yu, N.; Zhu, P.; Cui, Y.; Ma, Z.; Xu, X.; et al. Inhibiting Excessive Molecular Aggregation to Achieve Highly Efficient and Stabilized Organic Solar Cells by Introducing a Star-Shaped Nitrogen Heterocyclic-Ring Acceptor. *Energy Environ. Sci.* **2022**, *15*, 384−394.
(599) Yi, N.; Ai, Q.; Zhou, W.; Huang, L.; Zhang, L.; Xing, Z.; Li, X.; Zeng, J.; Chen, Y. Miscibility Matching and Bimolecular Crystallization Affording High-Performance Ternary Nonfullerene Solar Cells. *Chem. Mater.* **2019**, *31*, 10211−10224.
(600) Abdelsamie, M.; Zhao, K.; Niazi, M. R.; Chou, K. W.; Amassian, A. In Situ Uv-Visible Absorption During Spin-Coating of Organic Semiconductors: A New Probe for Organic Electronics and Photovoltaics. *J. Mater. Chem. C* **2014**, *2*, 3373.
(601) Schmidt-Hansberg, B.; Sanyal, M.; Klein, M. F.; Pfaff, M.; Schnabel, N.; Jaiser, S.; Vorobiev, A.; Muller, E.; Colsmann, A.; Scharfer, P.; et al. Moving through the Phase Diagram: Morphology Formation in Solution Cast Polymer-Fullerene Blend Films for Organic Solar Cells. *ACS Nano* **2011**, *5*, 8579−8590.
(602) Li, W.; Chen, M.; Zhang, Z.; Cai, J.; Zhang, H.; Gurney, R. S.; Liu, D.; Yu, J.; Tang, W.; Wang, T. Retarding the Crystallization of a Nonfullerene Electron Acceptor for High-Performance Polymer Solar Cells. *Adv. Funct. Mater.* **2018**, 1807662.
(603) Li, Y.; Liu, H.; Wu, J.; Tang, H.; Wang, H.; Yang, Q.; Fu, Y.; Xie, Z. Additive and High-Temperature Processing Boost the Photovoltaic Performance of Nonfullerene Organic Solar Cells Fabricated with Blade Coating and Nonhalogenated Solvents. *ACS Appl. Mater. Interfaces* **2021**, *13*, 10239−10248.
(604) Zhang, S.; Qin, Y.; Zhu, J.; Hou, J. Over 14% Efficiency in Polymer Solar Cells Enabled by a Chlorinated Polymer Donor. *Adv. Mater.* **2018**, *30*, 1800868.
(605) Lee, J. K.; Ma, W. L.; Brabec, C. J.; Yuen, J.; Moon, J. S.; Kim, J. Y.; Lee, K.; Bazan, G. C.; Heeger, A. J. Processing Additives for Improved Efficiency from Bulk Heterojunction Solar Cells. *J. Am. Chem. Soc.* **2008**, *130*, 3619−3623.
(606) Collins, B. A.; Li, Z.; Tumbleston, J. R.; Gann, E.; McNeill, C. R.; Ade, H. Absolute Measurement of Domain Composition and Nanoscale Size Distribution Explains Performance in Ptb7:Pc71bm Solar Cells. *Adv. Energy Mater.* **2013**, *3*, 65−74.
(607) Richter, L. J.; DeLongchamp, D. M.; Bokel, F. A.; Engmann, S.; Chou, K. W.; Amassian, A.; Schaible, E.; Hexemer, A. In Situ Morphology Studies of the Mechanism for Solution Additive Effects on

https://doi.org/10.1021/acs.chemrev.2c00905
Chem. Rev. 2023, 123, 8395−8487

the Formation of Bulk Heterojunction Films. *Adv. Energy Mater.* **2015**, *5*, 1400975.
(608) Liu, F.; Zhao, W.; Tumbleston, J. R.; Wang, C.; Gu, Y.; Wang, D.; Briseno, A. L.; Ade, H.; Russell, T. P. Understanding the Morphology of Ptb7:Pcbm Blends in Organic Photovoltaics. *Adv. Energy Mater.* **2014**, *4*, 1301377.
(609) Liu, F.; Gu, Y.; Wang, C.; Zhao, W.; Chen, D.; Briseno, A. L.; Russell, T. P. Efficient Polymer Solar Cells Based on a Low Bandgap Semi-Crystalline Dpp Polymer-Pcbm Blends. *Adv. Mater.* **2012**, *24*, 3947−3951.
(610) Wienhold, K. S.; Korstgens, V.; Grott, S.; Jiang, X.; Schwartzkopf, M.; Roth, S. V.; Muller-Buschbaum, P. Effect of Solvent Additives on the Morphology and Device Performance of Printed Nonfullerene Acceptor Based Organic Solar Cells. *ACS Appl. Mater. Interfaces* **2019**, *11*, 42313−42321.
(611) Ren, G.; Ahmed, E.; Jenekhe, S. A. Non-Fullerene Acceptor-Based Bulk Heterojunction Polymer Solar Cells: Engineering the Nanomorphology Via Processing Additives. *Adv. Energy Mater.* **2011**, *1*, 946−953.
(612) Ye, L.; Zhao, W.; Li, S.; Mukherjee, S.; Carpenter, J. H.; Awartani, O.; Jiao, X.; Hou, J.; Ade, H. High-Efficiency Nonfullerene Organic Solar Cells: Critical Factors That Affect Complex Multi-Length Scale Morphology and Device Performance. *Adv. Energy Mater.* **2017**, *7*, 1602000.
(613) Alqahtani, O.; Lv, J.; Xu, T.; Murcia, V.; Ferron, T.; McAfee, T.; Grabner, D.; Duan, T.; Collins, B. A. High Sensitivity of Non-Fullerene Organic Solar Cells Morphology and Performance to a Processing Additive. *Small* **2022**, *18*, 2202411.
(614) Song, X.; Gasparini, N.; Ye, L.; Yao, H.; Hou, J.; Ade, H.; Baran, D. Controlling Blend Morphology for Ultrahigh Current Density in Nonfullerene Acceptor-Based Organic Solar Cells. *ACS Energy Lett.* **2018**, *3*, 669−676.
(615) Sun, J.; Zhang, Z.; Yin, X.; Zhou, J.; Yang, L.; Geng, R.; Zhang, F.; Zhu, R.; Yu, J.; Tang, W. High Performance Non-Fullerene Polymer Solar Cells Based on Ptb7-Th as the Electron Donor with 10.42% Efficiency. *J. Mater. Chem. A* **2018**, *6*, 2549−2554.
(616) Ye, L.; Xiong, Y.; Li, S.; Ghasemi, M.; Balar, N.; Turner, J.; Gadisa, A.; Hou, J.; O'Connor, B. T.; Ade, H. Precise Manipulation of Multilength Scale Morphology and Its Influence on Eco-Friendly Printed All-Polymer Solar Cells. *Adv. Funct. Mater.* **2017**, *27*, 1702016.
(617) Zhang, X.; Wang, H.; Li, D.; Chen, M.; Mao, Y.; Du, B.; Zhuang, Y.; Tan, W.; Huang, W.; Zhao, Y.; et al. Modulation of J-Aggregation of Nonfullerene Acceptors toward near-Infrared Absorption and Enhanced Efficiency. *Macromolecules* **2020**, *53*, 3747−3755.
(618) Fidder, H. Absorption and Emission Studies on Pure and Mixed J-Aggregates of Pseudoisocyanine. *Chem. Phys.* **2007**, *341*, 158−168.
(619) Yan, D.; Liu, W.; Yao, J.; Zhan, C. Fused-Ring Nonfullerene Acceptor Forming Interpenetrating J-Architecture for Fullerene-Free Polymer Solar Cells. *Adv. Energy Mater.* **2018**, *8*, 1800204.
(620) Yao, C. J.; Zhang, H. L.; Zhang, Q. Recent Progress in Thermoelectric Materials Based on Conjugated Polymers. *Polymers (Basel)* **2019**, *11*, 107.
(621) Wang, S.; Zuo, G.; Kim, J.; Sirringhaus, H. Progress of Conjugated Polymers as Emerging Thermoelectric Materials. *Prog. Polym. Sci.* **2022**, *129*, 101548.
(622) Zhang, G.; Lan, Z. A.; Wang, X. Conjugated Polymers: Catalysts for Photocatalytic Hydrogen Evolution. *Angew. Chem., Int. Ed. Engl.* **2016**, *55*, 15712−15727.
(623) Dai, C.; Liu, B. Conjugated Polymers for Visible-Light-Driven Photocatalysis. *Energy Environ. Sci.* **2020**, *13*, 24−52.
(624) Qiao, S.; Di, M.; Jiang, J.; Han, B. Conjugated Porous Polymers for Photocatalysis: The Road from Catalytic Mechanism, Molecular Structure to Advanced Applications. *EnergyChem.* **2022**, *4*, 100094.
(625) Bogani, L.; Wernsdorfer, W. Molecular Spintronics Using Single-Molecule Magnets. *Nat. Mater.* **2008**, *7*, 179−186.
(626) Bujak, P.; Kulszewicz-Bajer, I.; Zagorska, M.; Maurel, V.; Wielgus, I.; Pron, A. Polymers for Electronics and Spintronics. *Chem. Soc. Rev.* **2013**, *42*, 8895−8999.
(627) Guo, L.; Qin, Y.; Gu, X.; Zhu, X.; Zhou, Q.; Sun, X. Spin Transport in Organic Molecules. *Front Chem.* **2019**, *7*, 428.
(628) Li, D.; Yu, G. Innovation of Materials, Devices, and Functionalized Interfaces in Organic Spintronics. *Adv. Funct. Mater.* **2021**, *31*, 2100550.
(629) Zhu, Y.; Jiang, Q.; Zhang, J.; Ma, Y. Recent Progress of Organic Semiconductor Materials in Spintronics. *Chem. Asian J.* **2023**, *18*, No. e202201125.
(630) Martin, D. C.; Subramanian, V. Direct Observation of Liquid-to-Solid Phase Transformations During the Electrochemical Deposition of Poly(3,4-Ethylenedioxythiophene) (Pedot) by Liquid-Phase Transmission Electron Microscopy (Lptem). *Macromolecules* **2021**, *54*, 6956−6967.
(631) Subramanian, V.; Martin, D. C. In Situ Observations of Nanofibril Nucleation and Growth During the Electrochemical Polymerization of Poly(3,4-Ethylenedioxythiophene) Using Liquid-Phase Transmission Electron Microscopy. *Nano Lett.* **2021**, *21*, 9077−9084.
(632) Isaacson, K. J.; Van Devener, B. R.; Steinhauff, D. B.; Jensen, M. M.; Cappello, J.; Ghandehari, H. Liquid-Cell Transmission Electron Microscopy for Imaging of Thermosensitive Recombinant Polymers. *J. Controlled Release* **2022**, *344*, 39−49.
(633) Janasz, L.; Chlebosz, D.; Gradzka, M.; Zajaczkowski, W.; Marszalek, T.; Mullen, K.; Ulanski, J.; Kiersnowski, A.; Pisula, W. Improved Charge Carrier Transport in Ultra Thin Poly(3-Hexylthiophene) Films Via Solution Aggregation. *J. Mater. Chem. C* **2016**, *4*, 11488.
(634) Ding, L.; Wang, Z. Y.; Yao, Z. F.; Liu, N. F.; Wang, X. Y.; Zhou, Y. Y.; Luo, L. F.; Shen, Z. H.; Wang, J. Y.; Pei, J. Controllable Transformation between the Kinetically and Thermodynamically Stable Aggregates in a Solution of Conjugated Polymers. *Macromolecules* **2021**, *54*, 5815−5824.
(635) Bronstein, H. A.; Luscombe, C. K. Externally Initiated Regioregular P3ht with Controlled Molecular Weight and Narrow Polydispersity. *J. Am. Chem. Soc.* **2009**, *131*, 12894.
(636) Curtarolo, S.; Hart, G. L.; Nardelli, M. B.; Mingo, N.; Sanvito, S.; Levy, O. The High-Throughput Highway to Computational Materials Design. *Nat. Mater.* **2013**, *12*, 191−201.
(637) Hachmann, J.; Olivares-Amaya, R.; Atahan-Evrenk, S.; Amador-Bedolla, C.; Sánchez-Carrera, R. S.; Gold-Parker, A.; Vogt, L.; Brockway, A. M.; Aspuru-Guzik, A. The Harvard Clean Energy Project: Large-Scale Computational Screening and Design of Organic Photovoltaics on the World Community Grid. *J. Phys. Chem. Lett.* **2011**, *2*, 2241−2251.
(638) Nagasawa, S.; Al-Naamani, E.; Saeki, A. Computer-Aided Screening of Conjugated Polymers for Organic Solar Cell: Classification by Random Forest. *J. Phys. Chem. Lett.* **2018**, *9*, 2639−2646.
(639) Sokolov, A. N.; Atahan-Evrenk, S.; Mondal, R.; Akkerman, H. B.; Sanchez-Carrera, R. S.; Granados-Focil, S.; Schrier, J.; Mannsfeld, S. C.; Zoombelt, A. P.; Bao, Z.; et al. From Computational Discovery to Experimental Characterization of a High Hole Mobility Organic Crystal. *Nat. Commun.* **2011**, *2*, 437.
(640) Sun, W.; Zheng, Y.; Yang, K.; Zhang, Q.; Shah, A. A.; Wu, Z.; Sun, Y.; Feng, L.; Chen, D.; Xiao, Z.; et al. Machine Learning-Assisted Molecular Design and Efficiency Prediction for High-Performance Organic Photovoltaic Materials. *Sci. Adv.* **2019**, *5*, No. eaay4275.
(641) McBride, M.; Liu, A.; Reichmanis, E.; Grover, M. A. Toward Data-Enabled Process Optimization of Deformable Electronic Polymer-Based Devices. *Curr. Opin. Chem. Eng.* **2020**, *27*, 72−80.
(642) Callaway, C. P.; Liu, A. L.; Venkatesh, R.; Zheng, Y.; Lee, M.; Meredith, J. C.; Grover, M.; Risko, C.; Reichmanis, E. The Solution Is the Solution: Data-Driven Elucidation of Solution-to-Device Feature Transfer for Π-Conjugated Polymer Semiconductors. *ACS Appl. Mater. Interfaces* **2022**, *14*, 3613−3620.
(643) Rodríguez-Martínez, X.; Sánchez-Díaz, A.; Liu, G.; Niño, M. A.; Cabanillas-Gonzalez, J.; Campoy-Quiles, M. Combinatorial Optimization of Evaporated Bilayer Small Molecule Organic Solar Cells through Orthogonal Thickness Gradients. *Org. Electron.* **2018**, *59*, 288−292.

https://doi.org/10.1021/acs.chemrev.2c00905
Chem. Rev. 2023, 123, 8395−8487

(644) Glaser, K.; Beu, P.; Bahro, D.; Sprau, C.; Pütz, A.; Colsmann, A. Rapid Experimental Optimization of Organic Tandem Solar Cells: 200 Absorber Layer Thickness Combinations on a 4 × 4 Cm2 Substrate. *J. Mater. Chem. A* **2018**, *6*, 9257−9263.
(645) Alstrup, J.; Jorgensen, M.; Medford, A. J.; Krebs, F. C. Ultra Fast and Parsimonious Materials Screening for Polymer Solar Cells Using Differentially Pumped Slot-Die Coating. *ACS Appl. Mater. Interfaces* **2010**, *2*, 2819−2827.
(646) Lee, J.-h.; Sagawa, T.; Yoshikawa, S. Fast Screening of the Optimal Polymer Ratio for Organic Solar Cells Using a Spray-Coating Deposition Method for the Fullerene Mixture. *Energy Technol.* **2013**, *1*, 85−93.
(647) Rodríguez-Martínez, X.; Sevim, S.; Xu, X.; Franco, C.; Pamies-Puig, P.; Córcoles-Guija, L.; Rodriguez-Trujillo, R.; Campo, F. J.; Rodriguez San Miguel, D.; deMello, A. J.; et al. Microfluidic-Assisted Blade Coating of Compositional Libraries for Combinatorial Applications: The Case of Organic Photovoltaics. *Adv. Energy Mater.* **2020**, *10*, 2001308.
(648) An, N. G.; Kim, J. Y.; Vak, D. Machine Learning-Assisted Development of Organic Photovoltaics Via High-Throughput in Situ Formulation. *Energy Environ. Sci.* **2021**, *14*, 3438−3446.
(649) Liu, A. L.; Dogan-Guner, E. M.; McBride, M.; Venkatesh, R.; Gonzalez, M. A.; Reichmanis, E.; Grover, M.; Meredith, J. C. Composition Gradient High-Throughput Polymer Libraries Enabled by Passive Mixing and Elevated Temperature Operability. *Chem. Mater.* **2022**, *34*, 6659−6670.
(650) Savagatrup, S.; Printz, A. D.; O'Connor, T. F.; Kim, I.; Lipomi, D. J. Efficient Characterization of Bulk Heterojunction Films by Mapping Gradients by Reversible Contact with Liquid Metal Top Electrodes. *Chem. Mater.* **2017**, *29*, 389−398.
(651) Pascual-San-José, E.; Rodríguez-Martínez, X.; Adel-Abdelaleim, R.; Stella, M.; Martínez-Ferrero, E.; Campoy-Quiles, M. Blade Coated P3ht:Non-Fullerene Acceptor Solar Cells: A High-Throughput Parameter Study with a Focus on up-Scalability. *J. Mater. Chem. A* **2019**, *7*, 20369−20382.
(652) MacLeod, B. P.; Parlane, F. G. L.; Morrissey, T. D.; Hase, F.; Roch, L. M.; Dettelbach, K. E.; Moreira, R.; Yunker, L. P. E.; Rooney, M. B.; Deeth, J. R.; et al. Self-Driving Laboratory for Accelerated Discovery of Thin-Film Materials. *Sci. Adv.* **2020**, *6*, No. eaaz8867.
(653) Langner, S.; Hase, F.; Perea, J. D.; Stubhan, T.; Hauch, J.; Roch, L. M.; Heumueller, T.; Aspuru-Guzik, A.; Brabec, C. J. Beyond Ternary Opv: High-Throughput Experimentation and Self-Driving Laboratories Optimize Multicomponent Systems. *Adv. Mater.* **2020**, *32*, 1907801.
(654) Du, X.; Lüer, L.; Heumueller, T.; Wagner, J.; Berger, C.; Osterrieder, T.; Wortmann, J.; Langner, S.; Vongsaysy, U.; Bertrand, M.; et al. Elucidating the Full Potential of Opv Materials Utilizing a High-Throughput Robot-Based Platform and Machine Learning. *Joule* **2021**, *5*, 495−506.
(655) Vriza, A.; Chan, H.; Xu, J. Self-Driving Laboratory for Polymer Electronics. *Chem. Mater.* **2023**, *35*, 3046−3056.

https://doi.org/10.1021/acs.chemrev.2c00905
Chem. Rev. 2023, 123, 8395−8487